The Determination and Application of In Situ Stresses in Petroleum Exploration and Production

Jeremy J Meyer B.Sc (Hons.)

National Centre for Petroleum Geology and Geophysics

The University of Adelaide

This thesis is submitted in fulfilment of the
requirements for the degree of Doctor of Philosophy
in the Faculty of Science, The University of Adelaide

August 2002

**THE UNIVERSITY
OF ADELAIDE**
AUSTRALIA

SUB CRUCE LUMEN

Contents

The Determination and Application of In Situ Stresses in

Petroleum Exploration and Production

Abstract

This thesis applies standard techniques, and develops new techniques for in situ stress determination from data acquired in petroleum exploration. The techniques are applied in four case studies and the impact of the resultant in situ stress data on exploration and development plans is assessed.

Flexible software (SWIFT) was developed to facilitate both the application of existing stress determination techniques and the development of new techniques. The SWIFT software is used to constrain the in situ stress tensor based on the occurrence of horizontal fractures open under the near wellbore stresses, and by forward modelling the variation of leak-off pressures in deviated wells. The occurrence of horizontal drilling-induced fractures, in the Swan Lake Field, Cooper Basin, South Australia, places tight constraints on both the minimum and maximum horizontal stress magnitudes, indicating a stress regime on the boundary of strike-slip and thrust faulting ($S_v \approx S_{hmin} < S_{Hmax}$). Forward modelling of leak-off pressures in deviated wells, in the Pattani Basin, Gulf of Thailand, restricts the range of feasible maximum horizontal stress magnitudes, and indicates a stress regime on the boundary of normal and strike-slip faulting ($S_{hmin} < S_v \approx S_{Hmax}$). Standard techniques are used to determine the stress regime of the Mereenie Field, Amadeus Basin, central Australia ($S_{hmin} < S_v < S_{Hmax}$) and the Penola Trough, Otway Basin, South Australia ($S_{hmin} < S_v < S_{Hmax}$).

The in situ stress tensor in the Swan Lake Field suggests that under-balanced drilling is feasible in order to minimise formation damage, especially in favourable trajectories, and that the problems encountered with fracture stimulation are the result of stimulation in a non-optimal in situ stress environment. In the Mereenie Field, although fracture density is low, certain sets are suitably oriented to be open and hydraulically conductive and these present a target for improved production and exploitation of the gas cap. Further depletion prior to fracture stimulation in the Mereenie Field may help alleviate problems associated with stimulating the high stress areas. The in situ stress tensor in the Pattani Basin, Gulf of Thailand, suggests

that reactivation of pre-existing faults within the in situ stress field may provide conduits for hydrocarbon migration. The in situ stress tensor in the Penola Trough, combined with fault strength data, for fault rocks, suggests that fault reactivation is probably not the cause of observed seal breach in the area. Pervasive fracturing of the intact cap rock may be the cause of seal breach.

Statement

This thesis contains no material which has been accepted for the award of any other degree or diploma in any university or other tertiary institution and, to the best of my knowledge and belief, contains no material previously published or written by another person except where due reference has been made in the text.

I give consent to this copy of my thesis, when deposited in the University Library, being available for loan and photocopying.

Jeremy Meyer

9/12/2002
Date

Acknowledgements

List of Symbols

α clockwise rotation (Equation 4.2)

β clockwise rotation (Equation 4.2)

γ clockwise rotation (Equation 4.2)

ΔP difference between wellbore and pore pressure (Equation 3.3)

δ borehole azimuth (Equation 4.4)

δ_{ij} Kronecker delta

μ coefficient of friction (Equation 2.7)

ν Poisson's ratio (Equation 3.8)

ρ density (Equation 3.1)

σ_1 maximum effective wellbore stress

σ_2 intermediate effective wellbore stress

σ_3 minimum effective wellbore stress

σ_{ij} stress component acting in the j direction in the plane normal to the i direction (Equation 2.1)

σ_n normal stress (Equation 2.5)

σ_{rr} effective radial stress (Equation 3.4)

$\sigma_{\theta\theta}$ effective circumferential stress (Equation 3.3)

$\sigma_{\theta\theta min}$ minimum of the effective circumferential stress (Equation 3.15)

σ_{tmax} maximum effective stress tangential to the wellbore wall (Equation 4.10)

σ_{tmin} minimum effective stress tangential to the wellbore wall (Equation 4.11)

σ_{zzmin} minimum of the effective axial stress (Equation 5.2)

σ_{zz} effective axial stress (Equation 3.8)

τ shear stress (Equation 2.6)

τ_0 cohesive strength (Equation 2.8)

$\tau_{r\theta}$ tangential shear stress (Equation 3.5)

ϕ borehole deviation (Equation 4.4)

ω angle between σ_{tmax} and the borehole axis (Equation 4.12)

C compressive strength (Equation 3.11)

C_0 uniaxial compressive strength (Equation 2.9)

C_b biaxial compressive strength (Equation 3.14)

d_{tvd} true vertical depth (Equation 3.2)

d_i along hole depth for deviation survey i (Equation 3.2)

g acceleration due to gravity (Equation 3.1)

h_{rt} height of rotary table (Equation 3.2)

P stress tensor due to pore pressure (Equation 2.12)

P_c fracture closure pressure (Equation 3.18)

P_i fracture initiation pressure (Equation 3.17)

P_p pore pressure (Equation 2.11)

P_r fracture reopening pressure (Equation 3.19)

P_w wellbore fluid pressure (Equation 3.9)

R_b coordinate transform matrix (Equation 4.4)

R_S coordinate transform matrix (Equation 4.2)

S applied stress tensor (Equation 2.1)

S_1 maximum principal stress (Equation 2.3)

S_2 intermediate principal stress (Equation 2.3)

S_3 minimum principal stress (Equation 2.3)

S' effective stress tensor (Equation 2.11)

S'_{hmin} effective minimum horizontal stress magnitude (Equation 3.3)

S'_{Hmax} effective maximum horizontal stress magnitude (Equation 3.3)

S'_v effective vertical stress magnitude (Equation 3.3)

S_b stress tensor in the borehole coordinate system (Equation 4.5)

S_g stress tensor in the geographic coordinate system (Equation 4.3)

S_{Hmax} maximum horizontal stress magnitude (Equation 2.4)

S_{hmin} minimum horizontal stress magnitude (Equation 2.4)

S_v vertical stress magnitude (Equation 2.4)

S_S stress tensor in principal stress coordinate system (Equation 4.1)

T tensile strength (Equation 2.10)

1. Introduction

1.1. Project Background

The last decade has seen a dramatic increase in the application of in situ stress data to problems in petroleum exploration and production. Borehole breakouts were only so-named, and recognised as being due to unequal horizontal stresses acting on the wellbore, in the late 1970s (Bell and Gough, 1979). Now breakouts are routinely used to determine in situ horizontal stress directions (Bell and Gough, 1979; Zoback and Zoback, 1980; Plumb and Cox, 1987).

Initially, breakouts gained prominence as a cause of wellbore instability and related drilling problems (Bradley, 1979; Aadnoy and Chenevert, 1987). However, utilising the breakouts themselves to help ascertain the in situ stress field has led to drilling strategies that minimise such wellbore stability problems (Peska and Zoback, 1995). More recently, there has been growing recognition that the in situ stress field also controls both natural and induced fluid flow in the subsurface, impacting on:

- reservoir flooding and drainage patterns (Heffer and Dowokpor, 1990);
- hydraulic fracture stimulation (Shlyapobersky and Chudnovsky, 1994);
- fluid flow in naturally fractured reservoirs (Sibson, 1996), and;
- seal integrity of fault-bound prospects (Hillis, 1998).

Furthermore, the in situ state-of-stress can be used to constrain the fault condition, and therefore provide evidence, independent from seismic interpretations, on the style of recent tectonic activity/fault reactivation.

One key driver for the increased application of in situ stress data to problems in petroleum exploration and production has been the increasing quality and use of borehole imaging tools, and the geomechanical information yielded by these tools. Furthermore, the increased incidence of deviated drilling has provided both new techniques for constraining the in situ stress tensor, as discussed in this thesis (Chapter 4), and increased demand for solutions to problems related to the state-of-stress in inclined wellbores, such as wellbore stability and fracture stimulation.

1.2. Project Aims and Philosophy

The aim of this project is to apply existing, and develop new techniques for in situ stress determination from oil field data, and to utilise these techniques within several case studies examining the wide range of implications of in situ stress data to petroleum exploration and production. In situ stress determination in any oil field or sedimentary basin involves some aspects that are essentially routine, such as determination of the vertical stress and the horizontal stress orientation, and other aspects that are non-routine, often related to constraining the magnitude of the maximum horizontal stress. The approach to the non-routine aspects of stress determination is dependent upon the dataset that is available, and the philosophy of this project was to modify techniques as required for specific problems and by specific datasets in the case studies (Chapters 5-8). The importance of image logs and deviated wellbores to in situ stress determination has been recognised, and a significant part of this project has involved developing software (SWIFT) that facilitates the determination of the in situ stress tensor from image logs run in deviated wellbores. The SWIFT software also facilitates application of knowledge of the in situ stress tensor to problems related to the state-of-stress in inclined wellbores, such as wellbore stability and fracture stimulation.

This project was undertaken as part of a group working on in situ stress and related issues at the NCPGG (National Centre for Petroleum Geology and Geophysics) ó the ëstress groupí. Many of the case studies discussed in Chapters 5-8 were analysed at least in part by the ëstress groupí as a whole. Where necessary, for example to fully describe all components of the stress tensor in the individual case studies, the results of the group are incorporated in this thesis. However, any results that are not solely the authorís are clearly noted as such in the text.

1.3. Review

There has been extensive research on the determination of in situ stresses, particularly in the oil industry. Consequently a review of existing techniques is presented here to provide a contextual framework for the more detailed discussion of new and existing techniques in subsequent chapters

In sedimentary basins, where most petroleum activity occurs, the stress tensor can be reduced to four components. These components are the vertical stress magnitude (S_v), the orientation of the maximum horizontal stress, the minimum horizontal stress magnitude (S_{hmin}) and the maximum horizontal stress magnitude (S_{Hmax}; see Chapter 2 for further discussion). The vertical stress magnitude is the weight of the overburden (McGarr and Gay, 1978), which can be calculated using density logs and checkshot velocity surveys. Density logs are routinely run during petroleum exploration and conventionally provide a density measurement every 15 cm. However, density logs are rarely run to the surface resulting in a lack of shallow data. Density can be estimated in the shallow section by transforming sonic velocity from a checkshot velocity survey to density using the Nafe-Drake velocity transform (Ludwig et al., 1970; see Section 3.2 for further discussion).

The orientation of the maximum horizontal stress can be determined from observations of stress-induced wellbore elongations (breakouts). Breakouts were first described by Bell and Gough (1979) as stress-induced compressive failure of the wellbore, and have subsequently been used to determine maximum horizontal stress orientations throughout the world (Zoback and Zoback, 1980; Mount and Suppe, 1987; Plumb and Cox, 1987; Sections 3.4, 5.2.2, 6.2.2, and 7.2.2). The advent of borehole imaging tools has confirmed the nature of breakouts and has led to the recognition of stress-induced tensile wellbore failure known as drilling induced tensile fractures (DITFs). DITFs are oriented orthogonal to breakouts and can also be used to determine the orientation of the maximum horizontal stress (Aadnoy, 1990b; Brudy and Zoback, 1993, Section 3.4).

An early and reliable method for determining in situ horizontal stress magnitudes and directions is the hydraulic fracture test (Haimson and Fairhurst, 1967). Hydraulic fracture tests involve isolating a section of the wellbore and increasing the pressure in the isolated interval by pumping fluid into it, and thereby creating a fracture in the wellbore wall. This fracture forms parallel to the wellbore axis (for a vertical wellbore) and orthogonal to the minimum horizontal stress. In general the fracture propagates away from the wellbore in this orientation as fluid continues to be pumped into the interval. In a thrust faulting stress regime the fracture may rotate to horizontal, as it propagates away from the wellbore, complicating the analysis.

However, in general it is the minimum horizontal stress that acts to close the fracture (i.e. the minimum principal stress; Hubbert and Willis, 1957), and consequently the pressure at which the fracture closes is a measure of the minimum horizontal stress and can be determined from the pressure versus time record (Haimson and Fairhurst, 1967). Hydraulic fracture tests are not generally undertaken in petroleum drilling, but the leak-off test (LOT) is somewhat similar in procedure to the initial stages of a hydraulic fracture test and is routinely conducted during petroleum drilling. Leak-off tests are conducted to determine the maximum fluid density that can be used in the next drilling section (i.e. fracture gradient) and not for stress determination per se. During a LOT the pressure is increased until a decrease in the rate of pressurisation (leak-off) is observed (Section 3.5). Consequently the induced fracture is comparatively small compared to that induced during a hydraulic fracture test, resulting in fracture closure not generally being observed. However, Breckels and van Eeklen (1982) showed that leak-off test pressures provide an estimate of the S_{hmin}, but not as accurate an estimate as that yielded by hydraulic fracture tests (for further discussion see Section 3.5).

Kunze and Steiger (1991), recognising the similarity between LOTs and hydraulic fracture tests, proposed the Extended Leak-Off Test (XLOT). This test uses the same equipment as a LOT, but a procedure more similar to the hydraulic fracture test, with multiple cycles of pressurization and de-pressurization, resulting in a pressure versus time record that can be used to determine the S_{hmin} with increased confidence (Section 3.5). The orientation of the maximum horizontal stress may be determined by observing the orientation of the induced fracture using an impression packer or a borehole imaging tool (Engelder, 1993; Haimson, 1993). The magnitude of the maximum horizontal stress can be determined from XLOTs and hydraulic fracture tests in some circumstances where a re-opening pressure can be interpreted (Haimson and Fairhurst, 1967; Enever et al., 1996; for further discussion see Section 3.5).

With the introduction of wellbore imaging tools, breakouts can be more accurately interpreted and their geometry observed. This increased knowledge of breakout geometry led Zoback *et al.* (1985) to propose a method for determining the magnitude of the maximum horizontal stress using the angular width of breakouts around the wellbore. This technique was used to obtain S_{Hmax} in New Mexico (Barton et al.,

1988). However, this technique is controversial because attempts to relate size and shape of breakouts to stress magnitudes requiring consideration of the geometrical effects of breakout development and the failure mechanisms of the material (Detournay and Roegiers, 1986). Nonetheless if breakouts are observed and compressive rock strength measurements available, a lower bound for S_{Hmax} can be determined (Moos and Zoback, 1990; Section 3.6.2).

Like breakout occurrence, DITF occurrence can be used to constrain S_{Hmax}, in this instance given knowledge of tensile rock strength (Moos and Zoback, 1990). Tensile rock strength is typically low compared to compressive rock strength and rocks typically contain planes of weakness on which the tensile rock strength is negligible. Consequently the tensile rock strength can be assumed to be negligible (Brudy and Zoback, 1999). The tighter constraint on tensile than compressive rock strength makes the use of DITFs to constrain S_{Hmax} less susceptible to errors than the use of breakouts (Section 3.6.3).

Widespread application of deviated drilling led to new techniques being utilised for stress determination. Aadnoy (1990a) proposed a method for inverting three or more LOTs from wellbores of different trajectories to determine the complete stress tensor (Section 7.3.1). Gj□nnes *et al.* (1998) suggested the original method was inaccurate, because it ignored shear stress stresses, and proposed an improved method. However, Gj□nnes *et al.* (1998) found the improved inversion also contained large uncertainties, in part due to the inaccuracy of LOTs and suggested the use of multiple techniques to determine the in situ stresses.

Image logging in deviated wells led to the observation that breakout orientations rotate as deviation increases, depending on the stress regime and hole azimuth (Mastin, 1988). Qian and Pedersen (1991) developed a technique for inverting the variation in breakout orientations with hole deviation and azimuth to determine the complete stress tensor. Peska and Zoback (1995) developed a similar technique for using rotation of breakout azimuths with deviation to constrain the stress tensor. However, Peska and Zoback (1995) also considered rotation of DITF azimuths and variations in the occurrence of both breakouts and DITFs to constrain the stress tensor. Using observations of both DITF and breakout occurrence and change in

orientation, the stress tensor can be determined from a single deviated borehole (Peska and Zoback, 1995).

Finally, frictional failure provides a theoretical limit to the ratio of the maximum to minimum effective stress beyond which failure of optimally-oriented pre-existing faults occurs (Sibson, 1974). This is known as the frictional limit to stress. A large number of in situ stress measurements in seismically active regions have shown stresses to be at frictional limit (Brace and Kohlstedt, 1980; McGarr, 1980; Zoback and Healy, 1984). Where one or more of the stress magnitudes are known, frictional limits can be used to constrain stress magnitudes in seismically inactive regions and estimate stress magnitudes in seismically active regions (Section 2.5). Most commonly S_v and S_{hmin} are known and the frictional limit is used to provide an upper limit to S_{Hmax}.

1.4. Thesis Plan

Chapter 2 of this thesis presents an introduction to the stress tensor and rock failure. This is necessary background for the discussion of stress determination techniques used in the petroleum industry in Chapter 3, which covers methods for determining S_v, horizontal stress direction, S_{hmin}, S_{Hmax}, and pore pressure.

A key part of this thesis was the development of software (SWIFT) to apply the techniques described in Chapter 3. Furthermore, SWIFT was developed to apply stress determination techniques in deviated wellbores, and to investigate the consequences of the in situ stress field for petroleum exploration and production (Chapter 4).

The stress determination techniques and software outlined in Chapters 1-4 are used to determine the stress tensor and its implications for fault reactivation/structural permeability, wellbore stability and fracture stimulation in four case studies. The impetus for investigating the stress tensor differs in each case study.

Reservoir permeability is low (< 1 mD) in the Swan Lake Field, Cooper Basin, South Australia. Fracture stimulation, natural fracture plays and under-balanced drilling have been proposed to improve production. Under-balanced drilling has been proposed because drilling-related formation damage is considered to negatively

influence already low permeabilities. The feasibility of fracture stimulation and under-balanced drilling are affected by the in situ stress tensor. Consequently in Chapter 5 the stress tensor in the Swan Lake Field is determined and its implications for under balanced drilling and fracture stimulation are investigated.

The Mereenie Field, Amadeus Basin, central Australia, contains an unexploited gas cap that the operators plan to develop. This gas cap is characterised by permeabilities of typically 5-10 mD, which are further lowered during production by fines migration. Targeting hydraulically conductive natural fractures and fracture stimulation have both been proposed to overcome this problem. Both these approaches are affected by the in situ stress tensor. Consequently in Chapter 6 the stress tensor in the Mereenie Field is determined and its implications for targeting open natural fractures and fracture stimulation are investigated.

The Gulf of Thailand is a region of active exploration and production in which contemporary tectonics and fluid flow pathways (migration and seal breach) are not fully understood. The in situ stress tensor exerts a major control on contemporary tectonics and fluid flow. Consequently a key tool for improving understanding of these issues is to determine the in situ stress tensor. In Chapter 7 the in situ stress tensor in the Gulf of Thailand is determined and its implications for contemporary tectonics and fluid flow are investigated.

The Otway Basin, South Australia, contains many fault-bound prospects of which some are breached, containing only residual hydrocarbon columns (Jones et al., 2000). Fault deformation processes, across-fault reservoir-seal juxtaposition and fault reactivation all control the sealing potential of faults (Jones et al., 2000). However, in the Otway Basin faults reactivation appears to be the critical control. Fault reactivation is in turn controlled by the stress tensor. Consequently in Chapter 8 the stress tensor in the Otway Basin is determined and fault geometries most prone to reactivation are determined.

2. The Stress Tensor and Rock Failure

2.1. Introduction

The stresses within the lithosphere have been of interest for many years at scales ranging from continental to microscopic. Lithospheric stresses are responsible for processes ranging from the formation of mountain belts (~1000 km) to wellbore failure (~ cm). In situ stress data are critical to a number of areas such as understanding the driving forces of plate tectonics (Coblentz et al., 1995), seismic hazard assessment (Horner et al., 1994) and mine stability (Hoek and Brown, 1980), in addition to the petroleum-related applications discussed in this thesis. The in situ stress field is the current day stress field and is responsible for contemporary failure. It is the result of a variety of forces acting at differing scales. These forces can be separated into first and second order forces (Zoback, 1992). First order forces are the result of plate boundary interactions and are responsible for the continental-scale stress field. Second order forces are the result of topography, lithospheric flexure, lateral density and strength variations and geologic structure. These forces result in variations in the stress field at the scales of several hundred kilometres to less than a kilometre (Zoback, 1992).
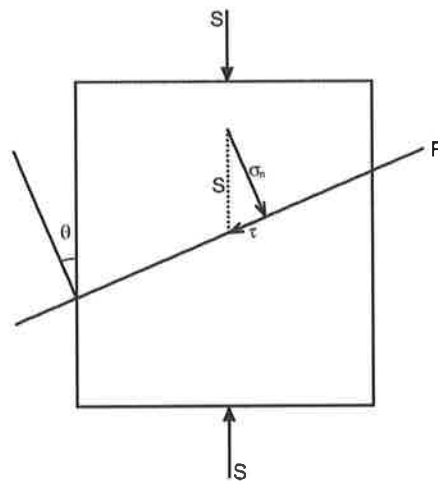
Figure 2.1. The shear (τ) and normal (σ_n) stress acting on a plane (P) at an angle θ to the applied stress.

The quantitative investigation of the phenomena discussed above requires a mathematical representation of the in situ stress within the lithosphere. The state of stress can be mathematically described using the stress tensor as discussed in the following section.
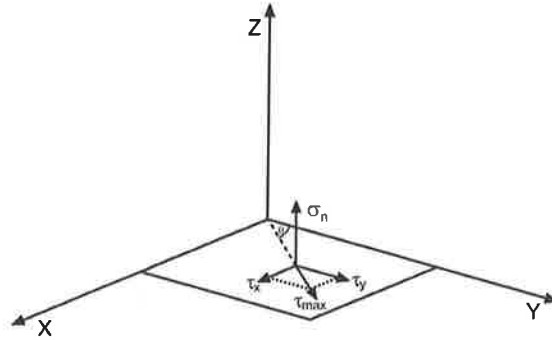
Figure 2.2. The components of stress acting on a plane. These are the normal stress (σ_n), the shear stress component in the x-direction (τ_x) and the shear stress component in the y-direction (τ_y) or the maximum shear stress (τ_{max}) and its orientation in the plane.

2.2. The Stress Tensor

Stress (S) is defined as force per unit area and can be divided into two components, shear and normal stress. The shear stress (τ) is the stress component acting parallel to a plane (P), inducing sliding along that plane (Figure 2.1). The normal stress (σ_n) is the stress component acting normal to the plane (Figure 2.1). The stresses acting on a plane can be completely described by the normal stress acting on the plane, the maximum shear stress (τ_{max}) acting on the plane and the orientation of that shear stress (Figure 2.2). Alternatively, the stresses can be completely described by the normal stress (σ_n) acting on the plane and the shear stress acting in two perpendicular directions (τ_x and τ_y) on the plane (Figure 2.2). The stress field in three-dimensions can be described by the normal stress acting on each of three orthogonal planes and the two orthogonal components of shear stress acting on those planes (Figure 2.3). These nine values of the three-dimensional stress tensor can be written:

$$S = \begin{pmatrix} \sigma_{xx} & \sigma_{xy} & \sigma_{xz} \\ \sigma_{yx} & \sigma_{yy} & \sigma_{yz} \\ \sigma_{zx} & \sigma_{zy} & \sigma_{zz} \end{pmatrix} \qquad \text{Eq. 2.1,}$$

where S is the stress tensor, σ_{ii} is the normal stress in the i direction, σ_{ij} is the shear stress acting in the j direction in the plane containing the j and k directions and $\sigma_{ij} = \sigma_{ji}$. The stress tensor can be simplified by choosing a coordinate system such that the planes have no shear stress acting upon them. The normals to these planes are principal stress directions. In this case the complete stress tensor can be completely defined by the magnitudes of the three principal stresses and the orientations of two of the principal stresses. The stress tensor becomes:

$$S = \begin{pmatrix} \sigma_{xx} & 0 & 0 \\ 0 & \sigma_{yy} & 0 \\ 0 & 0 & \sigma_{zz} \end{pmatrix}$$

Eq. 2.2.

Alternatively, the stress tensor can be written:

$$S = \begin{pmatrix} S_1 & 0 & 0 \\ 0 & S_2 & 0 \\ 0 & 0 & S_3 \end{pmatrix}$$

Eq. 2.3,

where S_1 is the maximum principal stress, S_2 is the intermediate principal stress and S_3 is the minimum principal stress.
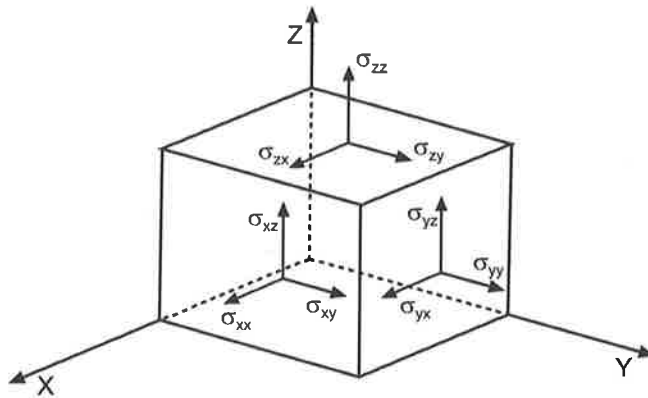
Figure 2.3. Components of stress acting on the faces of a cube. These nine values form the complete stress tensor.

This study considers the stresses within the earthís crust. The earthís surface is a free surface on which no shear stress acts and is consequently a principal plane. The earthís surface is normal to the vertical direction to a first order approximation,

particularly in sedimentary basins where little topographic relief exists. Therefore the vertical direction can be assumed to be a principal stress direction. Consequently the two remaining principal stress directions are in the horizontal plane. In this case the stress tensor can be written:

$$S = \begin{pmatrix} S_{Hmax} & 0 & 0 \\ 0 & S_{hmin} & 0 \\ 0 & 0 & S_v \end{pmatrix} \qquad \text{Eq. 2.4,}$$

where S_v is the vertical principal stress, S_{hmin} is the minimum horizontal principal stress and S_{Hmax} is the maximum horizontal principal stress (note that the positions of S_{Hmax}, S_{hmin} and S_v on the diagonal are interchangeable depending on which is larger). Hence, if the vertical stress is assumed to be a principal stress, the stress tensor can be completely constrained by the orientation of one of the horizontal stresses and the magnitudes of the vertical and two principal stresses. In this thesis compressive stresses are defined to be positive and tensile stresses are negative.

Anderson (1951) developed a classification of three different stress regimes, thrust faulting, strike-slip faulting and normal faulting:

- $S_{Hmax} > S_{hmin} > S_v$ thrust;
- $S_{Hmax} > S_v > S_{hmin}$ strike-slip, and;
- $S_v > S_{Hmax} > S_{hmin}$ normal.

These three states of stress correspond to the three commonly seen modes of faulting in the earthís crust and are used throughout this thesis to describe relative stress magnitudes in the earthís crust.

2.3. Stresses and Rock Failure

The rock properties and the stress tensor control rock failure. Failure occurs on planes as a function of the shear and normal stress acting on a plane, its frictional properties and any strength it may possess.

The normal and shear stress acting on a plane in a two-dimensional stress field can be calculated using:

$$\sigma_n = \frac{1}{2}(S_1 + S_2) + \frac{1}{2}(S_1 - S_2)\cos 2\theta \qquad \text{Eq. 2.5 and,}$$

$$\tau = \frac{1}{2}(S_2 - S_1)\sin 2\theta \qquad \text{Eq. 2.6,}$$

where σ_n is the normal stress, τ is the shear stress, S_1 is the maximum principal stress, S_2 is the minimum principal stress and θ is the angle between S_1 and the normal to the plane (Jaeger and Cook, 1979). The shear and normal stress calculated from equations 2.5 and 2.6 can be simply displayed on a Mohr diagram (Figure 2.4; Mohr, 1900). Plotting the shear and normal stresses on a Mohr diagram for θ varying between 0° and 90° and a given S_1 and S_2, forms a circle the centre of which is at a normal stress of $(S_1 + S_2)/2$ and shear stress of zero, and the radius of which is $(S_1 - S_2)/2$ (Figure 2.4). All two-dimensional states-of-stress lie on the perimeter of this circle.
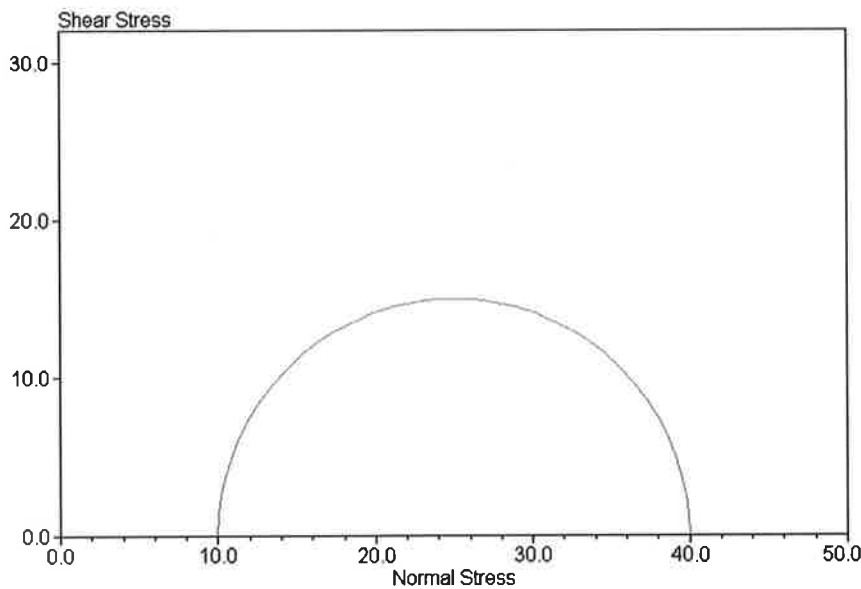
Figure 2.4. Two-dimensional Mohr circle with $S_1 = 40$ MPa and $S_2 = 10$ MPa.

Mohr diagrams can also be used to represent three-dimensional stress fields. In this case the diagram contains three Mohr circles with centres at $\{(S_1 + S_2)/2,0\}$, $\{(S_1 + S_3)/2,0\}$ and $\{(S_2 + S_3)/2,0\}$, and radii of $(S_1 - S_2)/2$, $(S_1 - S_3)/2$ and $(S_2 - S_3)/2$ respectively (Figure 2.5). All three-dimensional states of stress lie within the shaded area defined by the three Mohr circles (Figure 2.5).
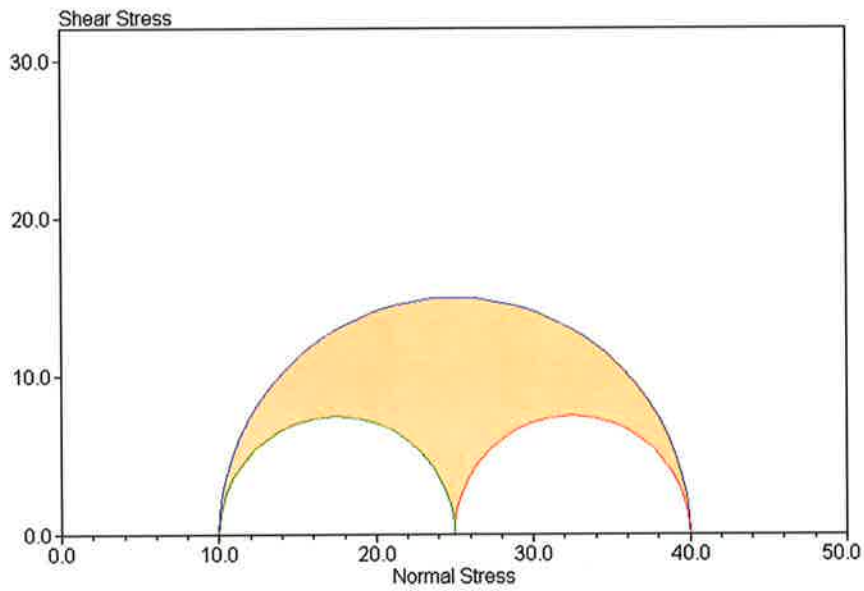
Figure 2.5. Three-dimensional Mohr circle with $S_1 = 40$ MPa, $S_2 = 25$ MPa and $S_3 = 10$ MPa.
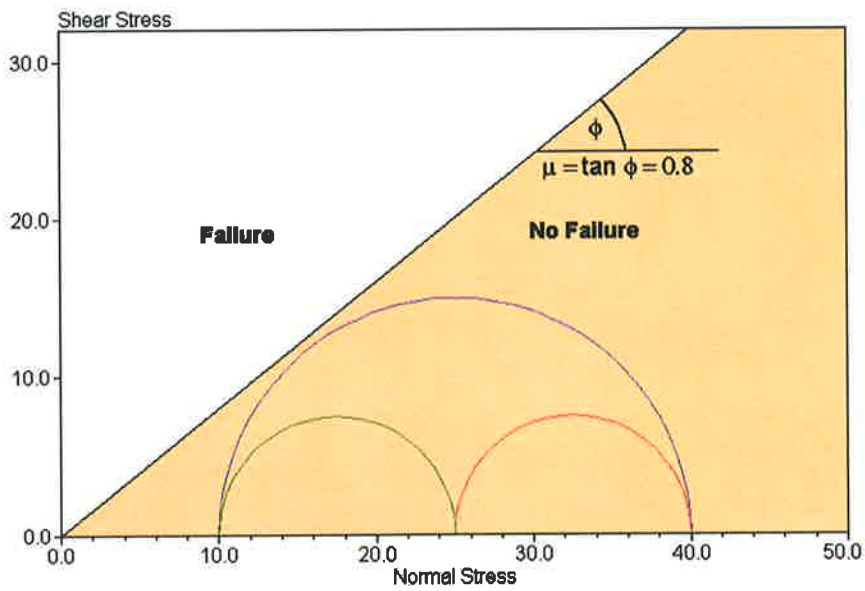
Figure 2.6. Three-Dimensional Mohr circle with $S_1 = 40$ MPa, $S_2 = 25$ MPa, $S_3 = 10$ MPa and a failure envelope for a coefficient of friction (μ) of 0.8 and zero cohesion.

The rock properties can also be displayed on a Mohr diagram, in the form of a failure envelope (Figure 2.6). A failure envelope separates two shear/normal stress regions. Normal stress/shear stress combinations within the region below the failure envelope do not result in failure while those above the failure envelope do result in failure. In

Figure 2.6 there are no points (planes) within the three-dimensional stress field that are at failure.

Failure envelopes can either be theoretically or empirically determined. An empirical failure envelope is based on laboratory rock tests, in which the maximum stress applied to a rock is increased until failure occurs. This results in a shear and normal stress value for failure, which can be plotted as a point on a Mohr diagram (Figure 2.7). A series of points, which form a failure envelope, can be determined by failing the rock under many different stress states (Figure 2.7). A widely used failure envelope is the Mohr-Coulomb failure criteria that can be written in its simplest form as:

$$\frac{\tau}{\sigma_n} = \mu \qquad \text{Eq. 2.7,}$$

where μ is the coefficient of friction (Figure 2.6; Jaeger and Cook, 1979). Laboratory rock tests indicate the coefficient of friction generally lies between 0.5 and 1.0 (Byerlee, 1978). This failure envelope represents frictional sliding on a pre-existing failure plain with no cohesive strength i.e. for a normal stress of zero, any shear stress greater than zero causes sliding. Where the cohesive strength is non-zero, Equation 2.7 can be written:

$$\tau = \tau_0 + \mu\sigma_n \qquad \text{Eq. 2.8,}$$

where τ_0 is the cohesive strength (Byerlee, 1978). However, commonly the uniaxial rock strength rather than cohesion is determined in laboratory testing. Consequently Equation 2.8 can be written:

$$\tau = \frac{C_0}{\left(2(\mu^2 + 1)^{\frac{1}{2}} + \mu\right)} + \mu\sigma_n \qquad \text{Eq. 2.9,}$$

where C_0 is the uniaxial compressive strength (Jaeger and Cook, 1979).

Another commonly used failure envelope is the Griffith failure criterion, which can be written:

$$\tau = \left(4T^2 + 4T\sigma_n\right)^{\frac{1}{2}}$$
Eq. 2.10,

where T is the tensile strength (Griffith, 1924). The Griffith criterion incorporates the role of flaws, which may propagate under applied stresses and can account for the weakness of rocks under tension.
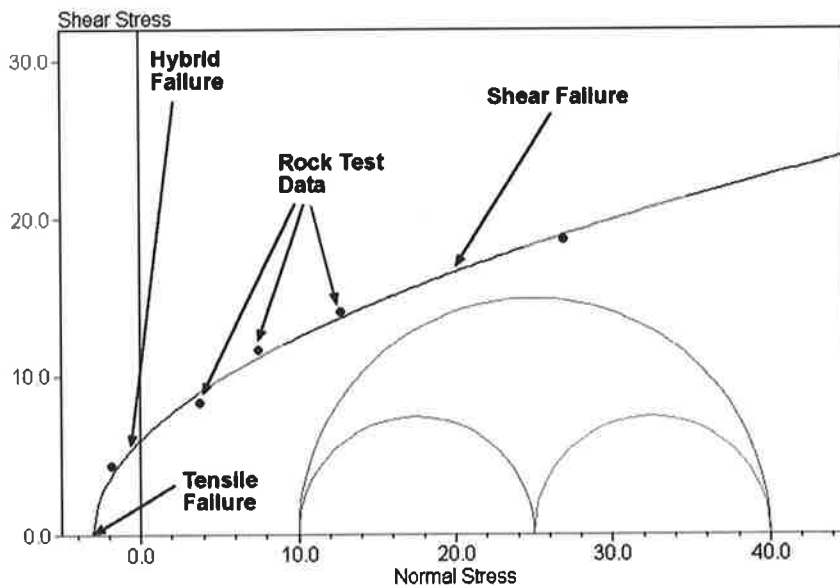
Figure 2.7. Mohr diagram with a Griffith failure envelope (T = 3 MPa) that fits closely to laboratory rock testing data. Rock testing data are normal and shear stress values at failure.

The mode of failure that occurs is constrained by where the Mohr circle touches the failure envelope. If the Mohr circle touches the failure envelope such that $\tau > 0$ and $\sigma_n \geq 0$, compressional shear failure occurs (Figure 2.7). If the Mohr circle touches the failure envelope such that $\tau = 0$ and $\sigma_n < 0$ tensile failure occurs (Figure 2.7). If the Mohr circle touches the failure envelope such that $\tau > 0$ and $\sigma_n < 0$ hybrid tensile/shear failure occurs (Figure 2.7). Hence assuming a composite Griffith (in tension) ñ Coulomb (in compression) failure envelope (Brace, 1960; Secor, 1965), if:

- $(S_1-S_3) < 4T$ $\Rightarrow$ tensile failure;
- $4T < (S_1-S_3) < 5.66T$ $\Rightarrow$ hybrid tensile/shear failure, and;

- $(S_1-S_3) > 5.66T$ $\Rightarrow$ shear failure (Sibson, 1996).

2.4. Effect of Pore Pressure

The presence of pore fluid under pressure has a profound effect on the physical properties of the porous solids (Terzaghi, 1943; Hubbert and Rubey, 1959; Figure 2.8). Most physical properties of porous rocks obey a law of effective stress wherein the effective stress (S') is the applied stress (S) minus the pore pressure (P_p):

$$S' = S - P_p \qquad \text{Eq. 2.11.}$$

It has been demonstrated both by laboratory testing (eg. Handin, 1958) and in oil fields by the compaction of sediments from which oil has been drained and P_p reduced (Teufel et al., 1991) that rock deformation and failure occurs in response to effective, not total stress.
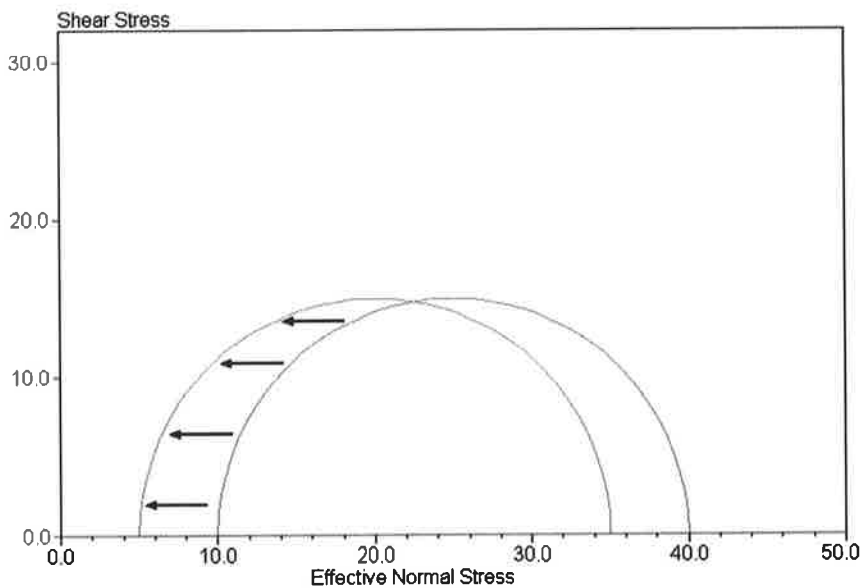
Figure 2.8. Mohr circle showing shift of Mohr circle from that in Figure 2.4 due to P_p of 5 MPa.

Pore fluid pressure is isotropic and the stress tensor associated with pore fluid pressure is given by:

$$P = \begin{pmatrix} P_p & 0 & 0 \\ 0 & P_p & 0 \\ 0 & 0 & P_p \end{pmatrix} \qquad \text{Eq. 2.12.}$$

From Equation 2.11, the effective stress tensor is given by:

$$S' = \begin{pmatrix} S_{Hmax} - P_P & 0 & 0 \\ 0 & S_{hmin} - P_P & 0 \\ 0 & 0 & S_v - P_P \end{pmatrix} \qquad \text{Eq. 2.13.}$$

Since rock failure obeys an effective stress law, the abscissa of the Mohr diagram is given by effective, not total stress (Figure 2.8).

2.5. Frictional Limits to Stress

Coulomb frictional failure provides a useful theoretical limit to stress magnitudes. It is assumed that the ratio of the maximum to minimum effective stress cannot exceed that required to cause faulting on an optimally-oriented, cohesionless, pre-existing fault (Sibson, 1974). It can be shown, based on Coulomb failure criterion (Equation 2.8), that the frictional limit, above which sliding occurs, is given by:

$$\frac{(S_1 - P_P)}{(S_3 - P_p)} = f(\mu) \qquad \text{Eq. 2.14,}$$

$$f(\mu) = \left[\left(1 + \mu^2\right)^{\frac{1}{2}} + \mu \right]^2 \qquad \text{Eq. 2.15.}$$

If the ratio exceeds the above function of μ, then slip occurs in order to reduce that ratio to within frictional limits. A large number of in situ stress measurements in seismically active regions have shown stresses to be at frictional limit (Brace and Kohlstedt, 1980; McGarr, 1980; Zoback and Healy, 1984). Consequently this ratio can be used to constrain the ratio of the magnitudes of the maximum and minimum stress in seismically active regions. Furthermore this ratio can be used to place upper or lower bounds on the maximum and minimum stress magnitude respectively in seismically inactive regions. Commonly S_{hmin} and S_v are known and the relationship can be used to place a limit on the more poorly constrained value of S_{Hmax}.

3. In Situ Stress Determination Using Petroleum Exploration Data

3.1. Introduction

The high cost of drilling in petroleum exploration and production requires that the risk is minimised and production maximised. Hence, it is necessary to maximise the value of information obtained from each well drilled. Large amounts of data are acquired in association with drilling. Little of this data is acquired for the purpose of stress determination. Nonetheless, extra value can be yielded from some of this data, because it can be used to determine the in situ stress tensor. Knowledge of the in situ stress tensor can in turn be used to reduce risk and increase production. The purpose of this chapter is to describe the exploration and production data that can be used to determine in situ stresses and the theory and methodology required.

As discussed in Section 2.2, the complete in situ stress tensor, in a sedimentary basin, comprises S_v, the maximum horizontal stress orientation, S_{hmin}, S_{Hmax} and P_P. Consequently the data and methods used to determine S_v (Section 3.2), the maximum horizontal stress orientation (Section 3.4), S_{hmin} (Section 3.5), S_{Hmax} (Section 3.6) and P_P (Section 3.7) are discussed in this Chapter.

3.2. Vertical Stress

The vertical stress is the weight of the overburden and can be calculated using knowledge of the rock densities (McGarr and Gay, 1978). Vertical stress is determined using the formula:

$$S_v = \int_0^h \rho(h).g.dh \qquad\qquad \text{Eq. 3.1,}$$

where h is the vertical depth, $\rho(h)$ is the function of density with vertical depth, and g is the acceleration due to gravity.

Density logs and check shot velocity surveys/vertical seismic profiles (VSPs) are the two main sources of density data.

Density logs are generally recorded relative to the depth along the hole below the rotary table. Depths in deviated wells must be converted to true vertical depth below the surface in order to calculate the S_v. The rotary table is a fixed height above the surface and can be corrected for by simply subtracting the height of the rotary table above the surface from the logging depth. The vertical depth is a function of along-hole depth and wellbore deviation, which is surveyed at regular intervals. Logging depth can be converted to true vertical depth using:

$$d_{tvd} = \left(\sum_{i=0}^{i=n} (d_i - d_{i-1}) \cos(\theta_i) \right) - h_{rt}$$
Eq. 3.2,

where d_{tvd} is the true vertical depth, n is the number of deviation surveys, d_i is the along hole depth for deviation survey i, θ_i is the deviation recorded at deviation survey i and h_{rt} is the height of the rotary table.

The density logging tool relies on good contact with the wellbore wall. Consequently wellbore rugosity may result in spurious density measurements (Figure 3.1). Most modern density logging tools correct errors in the density measurements and record the magnitude of the correction (DRHO). However, this correction is only accurate for values of DRHO $\leq$ 0.2 g/cc (Asquith and Gibson, 1983). Therefore, removing density values for which DRHO $\geq$ 0.2 g/cc results in the removal of spurious data. This needs to be undertaken before vertical stress is evaluated from the density log.

The character of the density log can be used to remove spurious data if neither DRHO nor caliper logs are available (Figure 3.1). Sudden large changes in density over short distance are unlikely to reflect actual changes in density and appear as large amplitude spikes in the density log. These can be removed by applying a de-spiking filter to the density log.

Density logs are commonly run as part of the wireline-logging suite and provide a detailed density profile, but they are rarely run to the surface. Sonic velocities from check shot velocity surveys/VSPs can be used to estimate average density from the

top of the density log to the surface, using the Nafe-Drake sonic velocity/density transform (Ludwig et al., 1970; Figure 3.2).
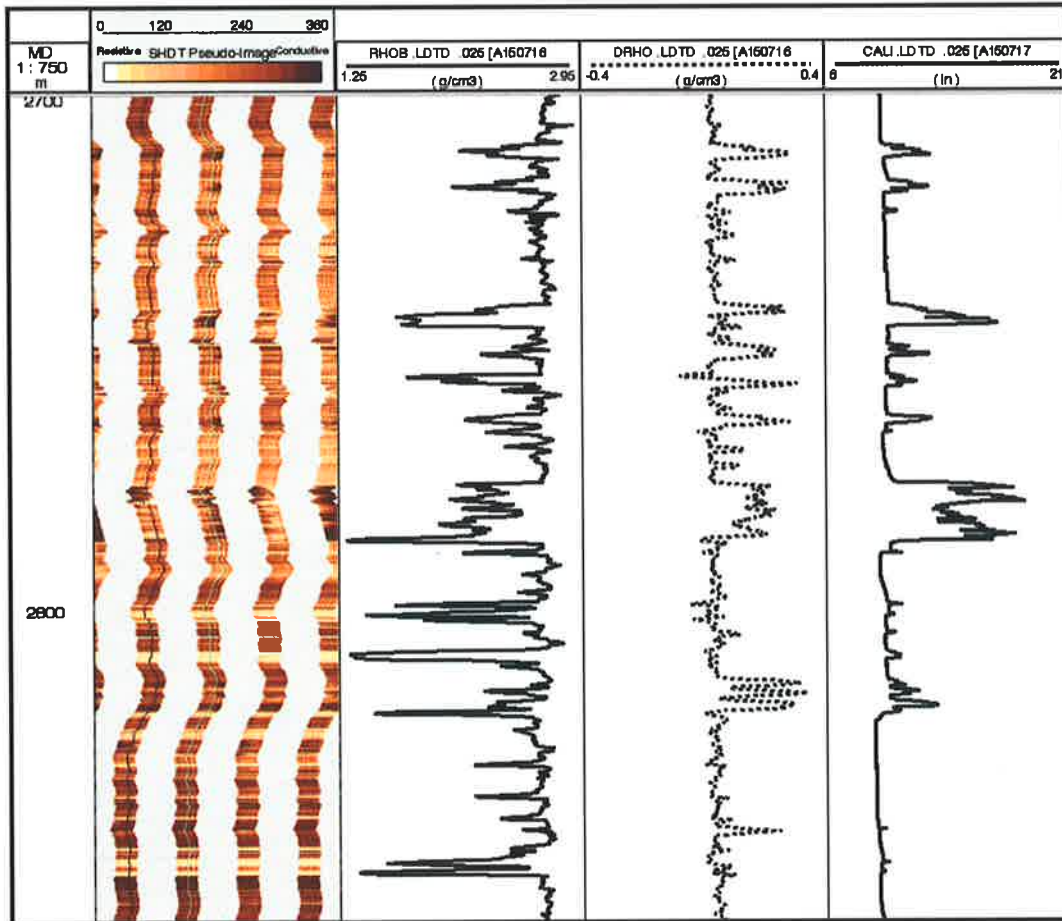
Figure 3.1. Resistivity image, density log (RHOB), density correction log (DRHO) and caliper log (CALI). Spikes in the density log are coincident with large spikes in the density correction and caliper logs as well as a poorly resolved, ëblobbyí conductive intervals in the resistivity image, all being indicative of wellbore rugosity. In this example, wellbore rugosity is due to wellbore breakout.

Ludwig et al. (1970) compared sonic velocity and density measurements and proposed the Nafe-Drake velocity/density transform (Figure 3.2). This transform can be locally re-calibrated using density and sonic log data from the area under consideration and shifting the transform to match the observed data. This locally calibrated Nafe-Drake velocity/density transform can then be applied to sonic velocities obtained from vertical seismic profiles (VSP) or check shot velocity surveys, providing an average density from the top of the density run to the surface.

The average density from the check shot survey/VSP and the density from the corrected density log can be used to calculate the vertical stress using Equation 3.1.
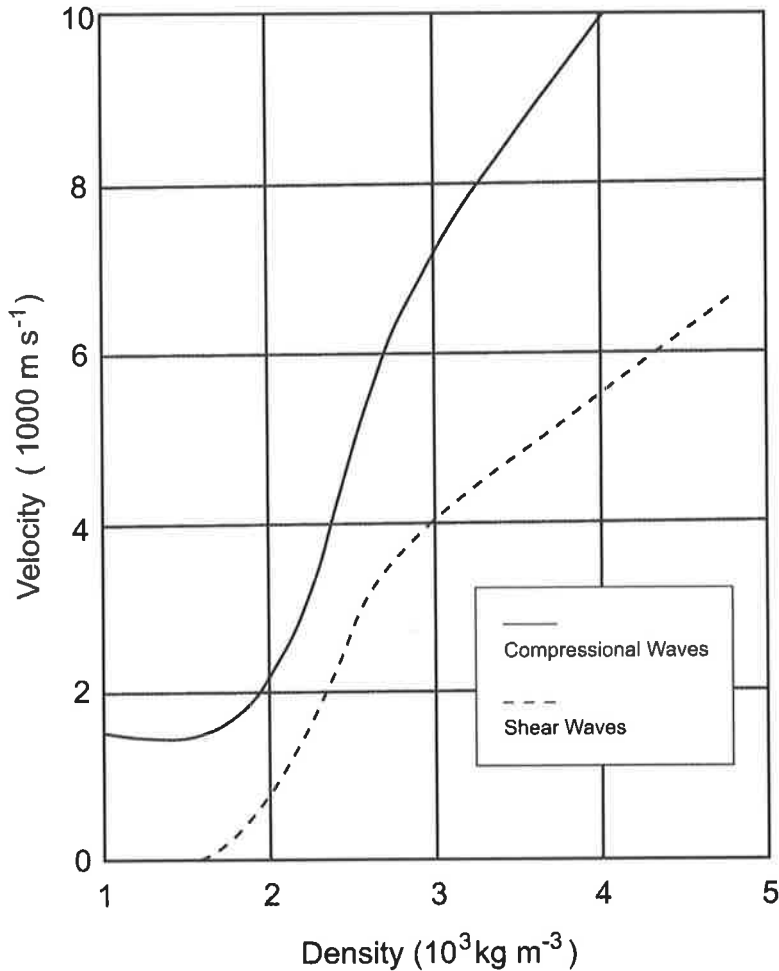
Figure 3.2. Nafe-Drake sonic velocity/density transform (after Ludwig et al., 1970).

3.3. Stresses Around Vertical Wellbores

3.3.1. Introduction

Drilling petroleum wells removes material from the subsurface, which previously carried stresses. As a result, the surrounding material (the wellbore wall) must support the stresses previously carried by the removed material, causing a stress concentration in the vicinity of the borehole. The stress concentration, in an elastic material, depends on the far field in situ stresses (Kirsch, 1898) and can result in wellbore failure (Bell and Gough, 1979). Observations of wellbore failure have been

proposed to determine both stress orientations and magnitudes (Bell and Gough, 1979; Zoback et al., 1985). The following discussion assumes the borehole is vertical, the vertical stress is a principal stress and the rock behaves elastically.
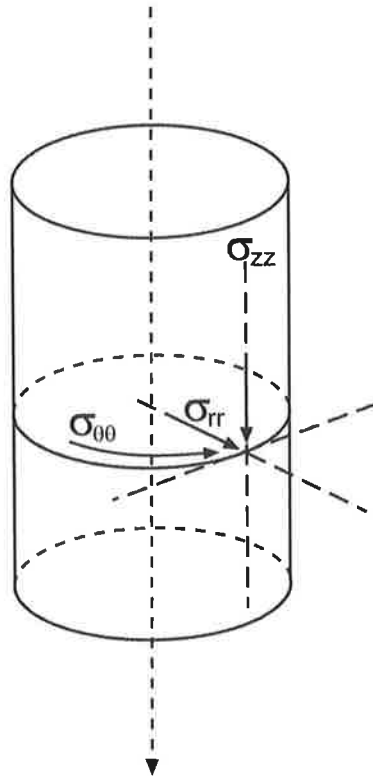
Figure 3.3. Wellbore showing the orientations of the circumferential ($\sigma_{\theta\theta}$), axial (σ_{zz}) and radial (σ_{rr}) stresses.

3.3.2. Basic Theory

Kirsch (1898) developed a set of equations for calculating the stresses acting in a thick, homogenous, isotropic elastic plate, containing a cylindrical hole, subject to effective minimum and maximum far field principal stresses. Assuming the wellbore is vertical, the three principal wellbore stresses are the effective radial stress (σ_{rr}), the effective axial stress (σ_{zz}) and the effective circumferential stress ($\sigma_{\theta\theta}$; Figure 3.3). The radial stress acts normal to the wellbore wall. The axial stress acts parallel to the wellbore axis. The circumferential stress acts orthogonal to σ_{rr} and σ_{zz} (in the horizontal direction in the plane tangential to the wellbore wall). The Kirsch (1898) equations can be written as:

$$\sigma_{\theta\theta} = \frac{1}{2}(S'_{Hmax} + S'_{hmin})\left(1 + \frac{R^2}{r^2}\right) - \frac{1}{2}(S'_{Hmax} - S'_{hmin})\left(1 + 3\frac{R^4}{r^4}\right)\cos2\theta - \frac{\Delta PR^2}{r^2}$$

Eq. 3.3,

$$\sigma_{rr} = \frac{1}{2}(S'_{Hmax} + S'_{hmin})\left(1 - \frac{R^2}{r^2}\right) + \frac{1}{2}(S'_{Hmax} - S'_{hmin})\left(1 - 4\frac{R^2}{r^2} + 3\frac{R^4}{r^4}\right)\cos2\theta + \frac{\Delta PR^2}{r^2}$$

Eq. 3.4 and,

$$\tau_{r\theta} = -\frac{1}{2}(S'_{Hmax} + S'_{hmin})\left(1 + 2\frac{R^2}{r^2} - 3\frac{R^4}{r^4}\right)\sin2\theta$$

Eq. 3.5,

where $\tau_{r\theta}$ is the tangential shear stress, R is the radius of the hole, r is the distance from the centre of the hole, θ is the azimuth measured from the orientation of S_{Hmax}, S'_{Hmax} is the effective maximum horizontal stress, S'_{hmin} is the effective minimum horizontal stress and ΔP is the difference between mud pressure (P_w) in the wellbore and P_p in the surrounding formation. The stress concentration predicted by these equations is illustrated in Figures 3.4 and 3.5.
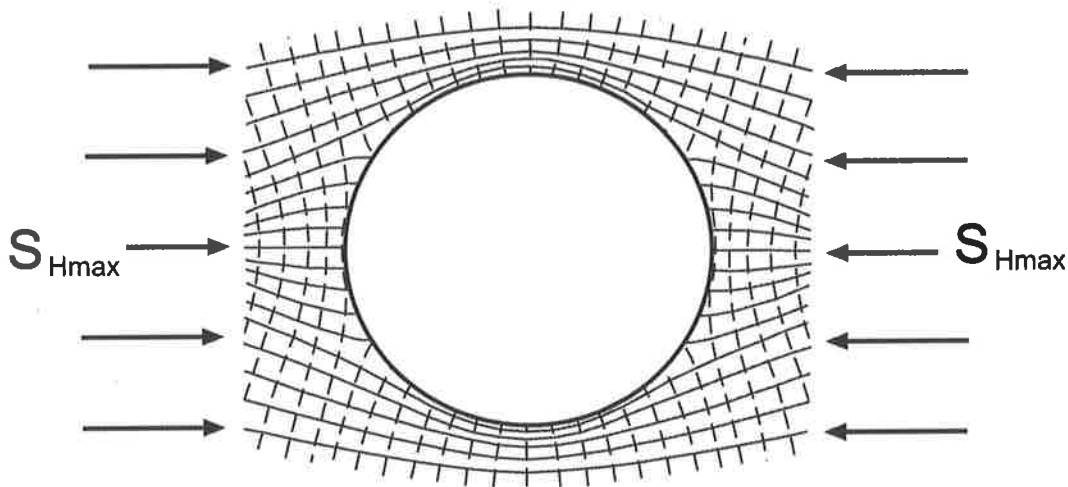
Figure 3.4. Stress concentration about a wellbore predicted using the Kirsch (1898) equations.

At the wellbore wall where R = r, Equations 3.3 and 3.4 become:

$$\sigma_{\theta\theta} = S'_{Hmax} + S'_{hmin} \ \tilde{n} \ 2(S'_{Hmax} - S'_{hmin})\cos2\theta - \Delta P \qquad \text{Eq. 3.6 and,}$$

$$\sigma_{rr} = \Delta P \qquad \text{Eq. 3.7.}$$

Equation 3.5 becomes zero. The axial stress at the wellbore wall can be calculated using:

$$\sigma_{zz} = S_V' - 2\nu(S_{Hmax}' - S_{hmin}')\cos2\theta \qquad\qquad \text{Eq. 3.8,}$$

where ν is Poisson's ratio and S_V' is the effective vertical stress (Fairhurst, 1968).

The above equations are written in terms of the effective far field principal stresses. Equations 3.6 to 3.8 can be rewritten:

$$\sigma_{\theta\theta} = S_{Hmax} + S_{hmin} - 2(S_{Hmax} - S_{hmin})\cos2\theta - P_W - P_P \qquad \text{Eq. 3.9,}$$

$$\sigma_{rr} = \Delta P \qquad\qquad\qquad\qquad\qquad \text{Eq. 3.7 and,}$$

$$\sigma_{zz} = S_V - 2\nu(S_{Hmax} - S_{hmin})\cos2\theta - P_P \qquad\quad \text{Eq. 3.10,}$$

where P_w is the wellbore fluid (mud) pressure.
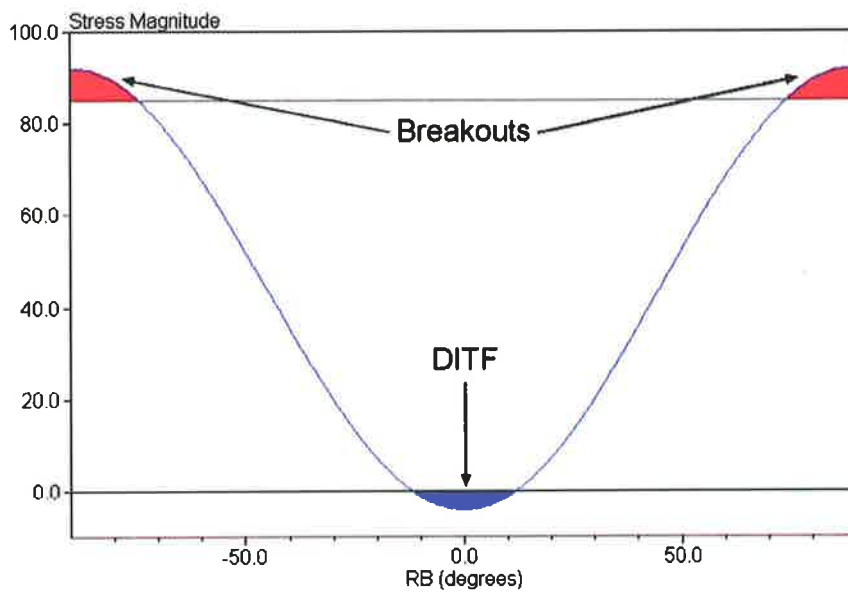
Figure 3.5. The circumferential wellbore stress magnitude ($\sigma_{\theta\theta}$) as a function of relative bearing (θ) around the wellbore from the orientation of S_{Hmax}, $S_{Hmax} = 54$ MPa, $S_{hmin} = 30$ MPa and $P_p = P_w = 20$ MPa. The red regions show the relative bearing at which breakouts form, for a compressive rock strength of 85 MPa. The blue region shows the relative bearing at which DITFs form, for tensile rock strength of zero.

3.3.3. Wellbore Breakouts

Borehole breakouts are stress-induced ovalisations of the cross-sectional shape of the wellbore (Bell and Gough, 1979). Ovalisation is caused by compressive shear failure on intersecting conjugate shear planes resulting in pieces of rock spalling off the wellbore wall (Figure 3.6). This occurs when the wellbore stress concentration exceeds that required to cause compressive failure of intact rock (Figure 3.5).
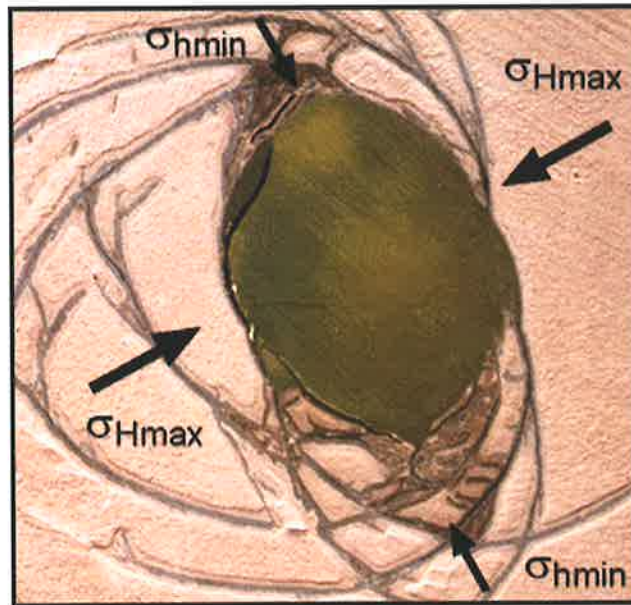
Figure 3.6. Hollow cylinder lab test showing conjugate shear failure planes resulting in ovalisation of the cross-sectional shape of the wellbore.

The Mohr-Coulomb failure criterion, expressed in terms of principal stresses is (Jaeger and Cook, 1979):

$$\sigma_1 \ \tilde{n} \ f(\mu).\sigma_3 \geq C. \qquad \text{Eq. 3.11,}$$

where C is the appropriated compressive rock strength discussed later in this section. In general σ_1 is the circumferential stress and σ_3 is the radial stress (Moos and Zoback, 1990). From Equation 3.9 the maximum of the circumferential stress occurs at $\theta = \pm 90°$ (Figure 3.5) and can be rewritten in the form:

$$\sigma_{\theta\theta max} = 3S_{Hmax} - S_{hmin} - P_W - P_P \qquad \text{Eq. 3.12.}$$

For the simple case where σ_3 is zero (i.e. σ_3 is σ_{rr} and the wellbore is in balance, $P_w = P_p$) and σ_1 is the circumferential stress, Equation 3.12 can be substituted into Equation 3.11 resulting in a simple failure criterion:

$$\sigma_{\theta\theta max} = 3S_{Hmax} - S_{hmin} - 2P_P \geq C \qquad \text{Eq. 3.13.}$$

Compressive failure occurs when the circumferential stress exceeds the rock strength, for an in balance wellbore ($P_w = P_p$; Figure 3.5). The significance of Equation 3.11 to the situation where the wellbore is not in balance ($P_w \neq P_p$) is discussed in Section 3.6.2.

The appropriate rock strength (C; Equation 3.11) considered in breakout calculations is typically the uniaxial compressive rock strength (C_0). However, the stress components at the wellbore wall resulting in wellbore failure are typically polyaxial ($\sigma_1 > \sigma_2 > \sigma_3 = 0$). Rocks under polyaxial conditions are stronger than under uniaxial ($\sigma_1 > \sigma_2 = \sigma_3 = 0$) conditions, but weaker than under biaxial conditions ($\sigma_1 > \sigma_2 = \sigma_3 \neq 0$; Wiebels and Cook, 1968). The relationship between uniaxial and biaxial rock strength can be written:

$$C_b = C_0(1.0 + 0.6\mu) \qquad \text{Eq. 3.14,}$$

where C_b is the biaxial rock strength and μ is the coefficient of friction (Wiebels and Cook, 1968). Consequently, for a typical μ of 0.6 (Byerlee, 1978), the rock strength relevant in the context of breakout formation is $C_0 \leq C \leq 1.36C_0$ (Moos and Zoback, 1990).

3.3.4. Drilling Induced Tensile Fractures

Drilling induced tensile fractures (DITFs) are stress-induced tensile fractures of the wellbore wall (Figure 3.7; Aadnoy, 1990b). Tensile failure occurs when the wellbore stress concentration is less than the tensile strength of the rock. The circumferential stress is minimized for $\theta = 0$ (Figure 3.5), and Equation 3.9 can be rewritten:

$$\sigma_{\theta\theta min} = 3S_{hmin} - S_{Hmax} - P_W - P_P \qquad \text{Eq. 3.15.}$$

DITFs form when:

$$\sigma_{\theta\theta min} = 3S_{hmin} \; \tilde{n} \; S_{Hmax} - P_W - P_P \leq T \qquad\qquad \text{Eq. 3.16,}$$

where T is the rock tensile strength and $T \leq 0$. The tensile rock strength is typically small compared to the compressive rock strength and rocks typically contain plains of weakness on which the tensile rock strength is negligible. Consequently, tensile rock strength can be assumed to be negligible (Brudy and Zoback, 1999). Hence, DITFs tend to occur when $\sigma_{\theta\theta min}$ is less than zero (Figure 3.5).
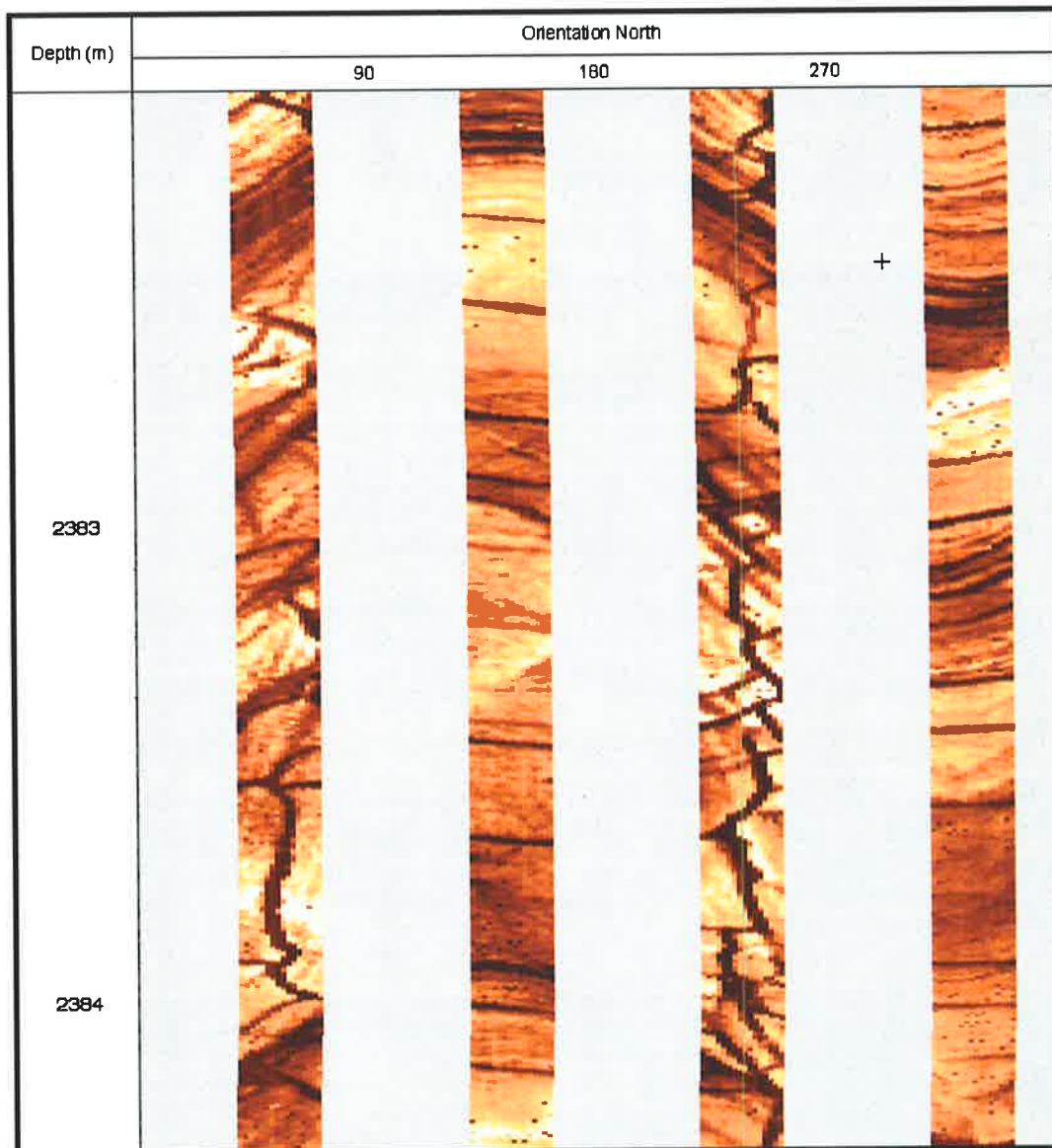
Figure 3.7. Formation Micro Scanner (FMS) resistivity image of the wellbore showing DITFs on two orthogonal pads. The DITFs are sub vertical, conductive (black) and contain drilling fluid. Along hole depth (m) is shown on the y-axis, while the x-axis is the angle around the wellbore.

Under certain unusual circumstances the minimum of σ_{zz} is less than $\sigma_{\theta\theta min}$ and under such circumstances DITFs may form transverse to the wellbore. This case is discussed in detail in Chapter 5.

3.4. Horizontal Stress Orientations

The observation of wellbore deformation (wellbore breakouts and DITFs) is the most common method for the determination of horizontal stress orientations in the oil patch (Bell, 1996a). As discussed in the previous section, breakouts and DITFs in vertical wells form at 90° and 0° from the orientation of S_{Hmax} respectively, and consequently can be used to determine the orientation of S_{Hmax} (Bell and Gough, 1979; Brudy and Zoback, 1999). Alternatively, horizontal stress orientations can be determined from the orientation of fractures induced by hydraulic fracture, leak-off or extended leak-off tests (Hubbert and Willis, 1957); discussed in Section 3.5). Such testing-induced fractures form in the same orientation as DITFs and can thus similarly be used to indicate the orientation of S_{Hmax}.

o The tool rotation stops ± 15° in the zone of elongation.

o The tool must rotate at least 30° in the 30 m immediately beneath the breakout.

o The smaller caliper width is within 5% of bit size.

o The difference between the caliper widths is greater than 6 mm.

o The length of the elongation zone is greater than 1.5 m.

o The direction of elongation should not coincide within ± 5° of the high side of the tool if deviation is > 5°.

Table 3.1. Criteria used in the recognition of wellbore breakout on four-arm caliper data (Mildren et al., 1994)

Breakouts can be recognized, and their orientation determined, using dipmeter-type tools. Four arm dipmeter tools are designed to measure stratigraphic dips, by depth

correlating formation resistivity measured on four orthogonal that are pads pushed against the wellbore wall. The raw data recorded is:

- pad one azimuth;
- wellbore deviation;
- wellbore azimuth;
- the distance between pads one and three (C1);
- the distance between pads two and four (C2), and;
- the formation resistivity measured by each pad.

C1 and C2 measure the wellbore diameter in two orthogonal directions. Dipmeter tools are typically lowered to the base of the borehole and data recorded while the tool
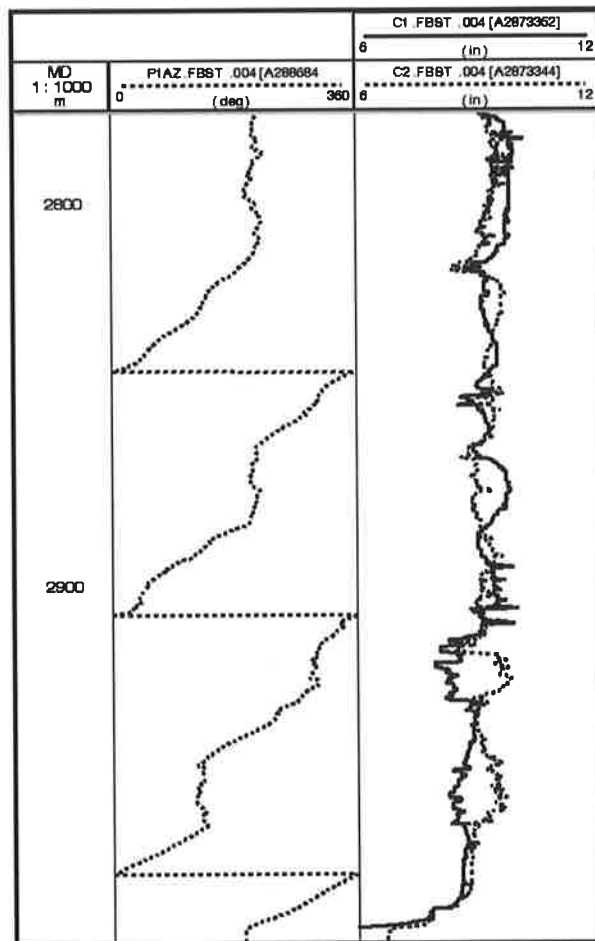
Figure 3.8. Full Bore Scanner Tool (FBST) log data showing pad one azimuth (P1AZ), distance between pads one and three (C1) and distance between pads two and four (C2). P1AZ shows cessation of rotation coincident with a large difference between C1 and C2 indicating wellbore breakout.

is pulled back up the borehole. Dipmeter tools typically rotate, as they are pulled up the hole, due to cable torque. When the tool reaches a zone of wellbore breakout, in which the hole is ovalised (Section 3.3.3), one pair of pads may become stuck in the breakout (i.e. the tool stops rotating). The caliper width between the pads in the wellbore breakout is greater than the distance between the orthogonal pads. As the tool continues up the hole, the tool may free itself and resume rotation sometimes becoming stuck again further up the hole (Figure 3.8). Wellbore breakouts can thus be interpreted from raw dipmeter logs, where rotation is observed below and above the breakout zone and rotation ceases within it. One caliper width reading should be greater than bit size and the orthogonal reading equal to bit size (Plumb and Hickman, 1985; Figure 3.8; Table 3.1). Furthermore if the hole is deviated, the elongation should not parallel the azimuth of deviation. This ensures that asymmetric ákey seatsí (caused by abrasion of drill pipe on the lower side of the hole) are not misinterpreted as wellbore breakouts.

Wellbore imaging tools are used to obtain stratigraphic and structural information from the wellbore. Resistivity and acoustic imaging tools are the two main types of imaging tool. Resistivity imaging tools evolved from the dipmeter tools and consist of four to eight pads with each pad containing 16 to 32 resistivity measuring buttons. Combining the measurements from all the buttons produces a resistivity image of the wellbore. Acoustic imaging tools contain a rotating piezoelectric crystal transducer, which emits and receives ultrasonic pulses (frequency: 250 kHz -1 MHz; Zemack and Caldwell, 1967). The travel time and amplitude of the pulse reflected from the wellbore wall are measured and can be used to create images of the wellbore wall. The amplitude image shows the acoustic reflectivity of the formation, while the travel time image shows the shape of the wellbore.

The pads of the resistivity image-logging tool make poor contact with the wellbore wall in zones of wellbore breakout, due to wellbore wall rugosity, resulting in an un-focused blobby image (Figure 3.9; Hillis et al., 1995). This rugosity also results in poor acoustic reflectivity (Plumb, 1989). By definition, breakouts are hole-enlargements and hence can be seen on the acoustic travel time image (Plumb, 1989).

DITFs are small fractures in the wellbore filled with conductive drilling fluid, resulting in large resistivity and acoustic reflectivity differences between the fracture
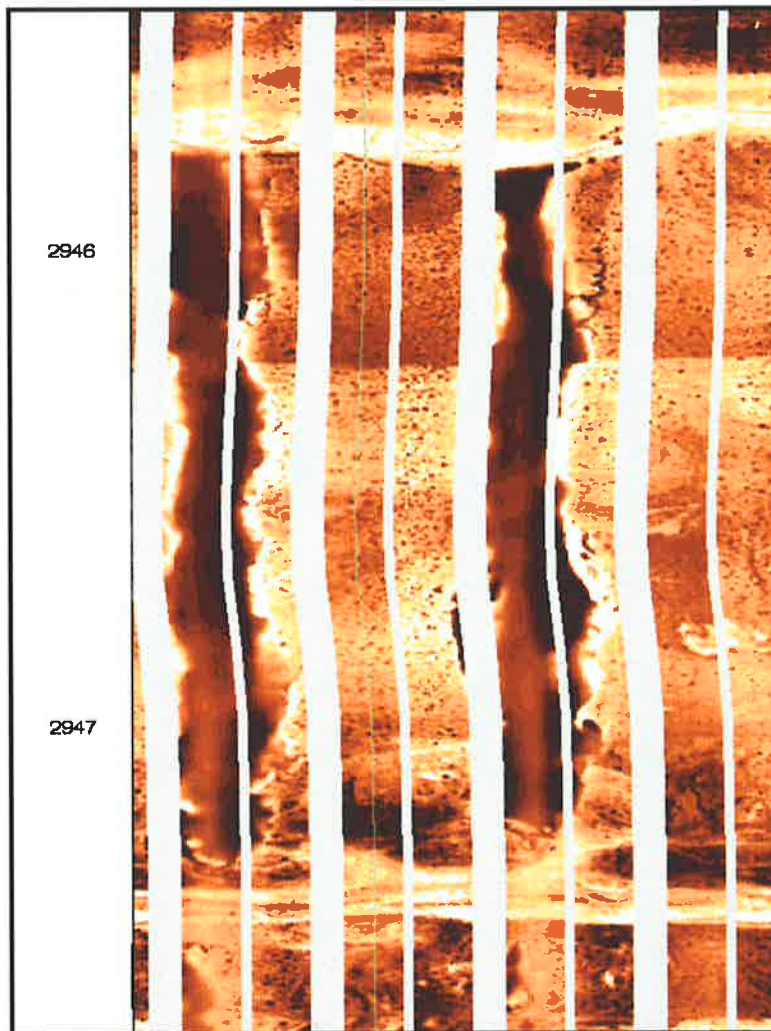
Figure 3.9. Fullbore Formation MicroImager (FMI) resistivity image of the wellbore showing breakouts truncated by lithological boundaries. The breakouts are axial, conductive (black) and contain drilling fluid. Along hole depth is shown on the y-axis, while the x-axis is the angle around the wellbore.

and the wellbore wall that are easily observable using resistivity and acoustic imaging tools (Brudy and Zoback, 1999). DITFs are often not exactly axial to the wellbore wall forming on echelon sets centred at the azimuth of the far field maximum horizontal stress. DITFs can generally be distinguished from natural fractures because they are always conductive, have a consistent orientation, are generally non-planar and are only conductive over a small section of the wellbore (Barton, 2000).

3.5.   Minimum Horizontal Stress Magnitudes

Leak-off tests (LOT), extended leak-off tests (XLOT) and minifracture tests can be used to constrain horizontal stress magnitudes (Haimson and Fairhurst, 1967;

Breckels and van Eeklen, 1982; Kunze and Steiger, 1991). All the tests involve increasing fluid pressure in the wellbore until a fracture is created at the wellbore wall. The LOT is the most commonly undertaken and simplest of these tests. LOTs are conducted not for the purpose of making stress estimates, but in order to determine the maximum mud weight that can be used when drilling ahead. An XLOT is conducted when information on the stress tensor is of interest (Kunze and Steiger, 1991). As the name suggests an XLOT is an extended version of a LOT, using the same basic equipment, but a different test procedure. The third type of test discussed in this section is the minifracture or hydraulic fracture test, which is specifically designed to determine horizontal stress magnitudes. LOTs can be used to estimate S_{hmin}. XLOTs and minifracture tests provide a more reliable estimate of S_{hmin} and, under certain circumstances, an estimate of S_{Hmax}.

3.5.1. Leak-Off Tests

Leak-off tests are performed, for engineering purposes, to determine the maximum mud weight that can be used drilling ahead. Leak-off tests are performed after casing has been set and when a new section of hole is about to be drilled. The casing shoe
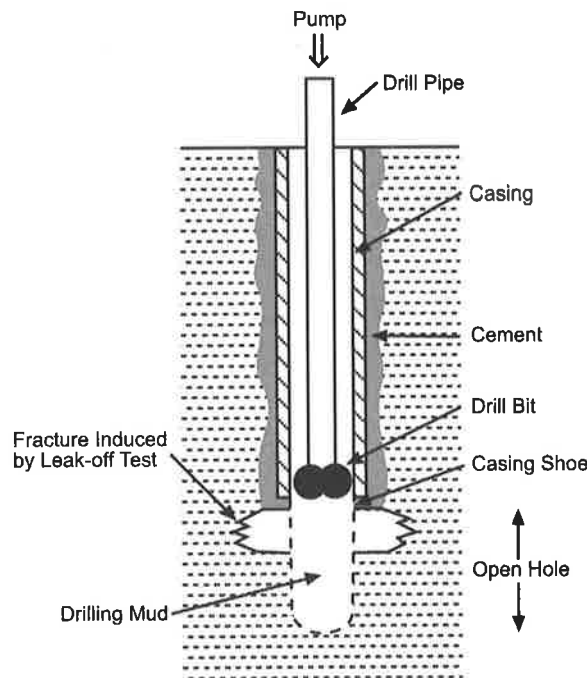
Figure 3.10. Downhole schematic for LOT/XLOT showing open hole section and induced fracture (after Bell, 1996a).

and cement are drilled out and several metres of new hole are drilled (Figure 3.10). Fluid is pumped into the wellbore, increasing the pressure, until the rate of pressurisation decreases i.e. leak-off occurs. Leak-off pressure (LOP) is defined as the point on the pressure-time curve at which the pressure build up deviates from linearity (Figure 3.11), and is interpreted as the point at which a fracture is initiated at the wellbore wall. The test is referred to as a Formation Integrity Test (FIT) if no leak-off is observed, i.e. test is stopped at pre-determined pressure that does not generate a fracture.
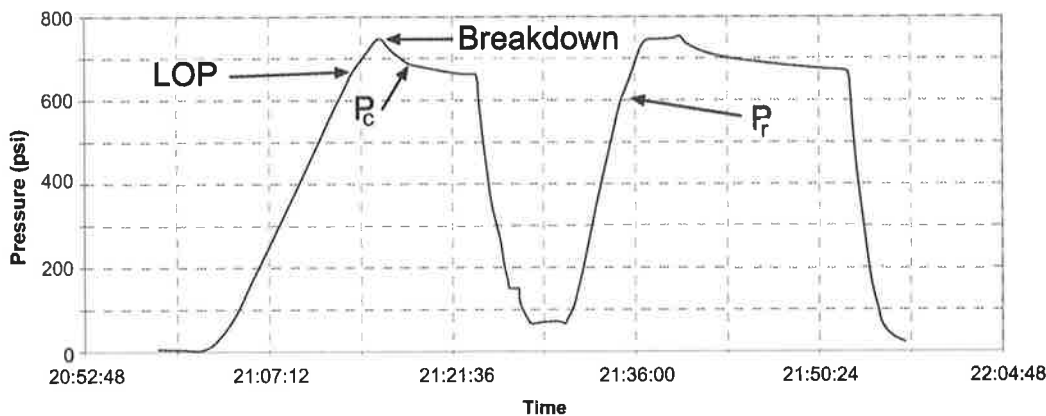
Figure 3.11. XLOT pressure versus time record showing LOP, breakdown, P_c and Pr.

The fluid pressure in the wellbore must overcome the near wellbore stress concentration and tensile rock strength in order to initiate a fracture. Consequently, the wellbore fluid pressure at which the fracture is initiated depends on the tensile rock strength, P_p, S_{Hmax} and S_{hmin} (Section 3.3). Nonetheless, Breckels and van Eeklen (1982) observed that values of S_{hmin} determined from minifracture tests form the lower bound to LOPs in several basins worldwide. Consequently, LOPs can be used to estimate S_{hmin}, but contains large uncertainties due to the wellbore stress concentration and unknown tensile rock strength (Addis et al., 1998). Furthermore it is necessary to verify original pressure versus time records for the test to ensure that an FIT has not been described as an LOT and indeed to verify the quality of the test.

3.5.2. Extended Leak-Off and Minifracture Tests

Extended leak-off tests and minifracture tests are conducted specifically for the purpose of stress determination (Haimson and Fairhurst, 1967; Kunze and Steiger,

1991; Enever et al., 1996). These tests are similar in procedure, each involving multiple cycles of pressurisation and de-pressurisation (Enever et al., 1996), but use different equipment. An XLOT can be conducted in place of a LOT during drilling when better quality stress information is required (Kunze and Steiger, 1991; Enever et al., 1996). The only practical difference between a LOT and an XLOT is the extra time taken to conduct the multiple cycles of an XLOT.

XLOTs and minifracture tests are conducted in an isolated section of wellbore. In an XLOT the test interval is the same as that in an LOT, usually being ~3m of fresh borehole (Figure 3.10), while a minifracture test, like a hydraulic fracture test, uses a packer system lowered into an uncased borehole (Figure 3.12; Engelder, 1993).
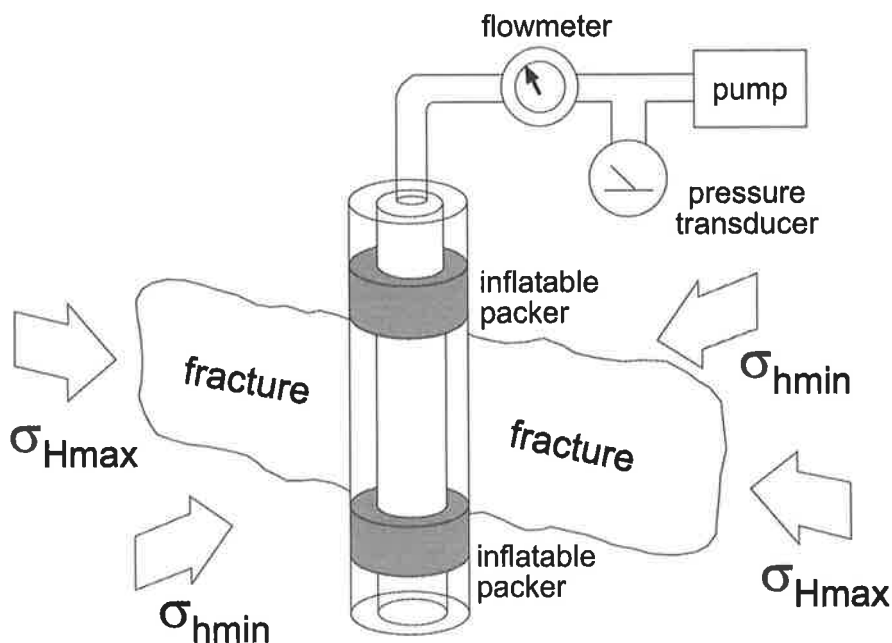
Figure 3.12. Schematic of a minifracture or hydraulic fracture test, showing the initiated fracture and packer system (after Bell, 1996a).

In both tests fluid is pumped into the isolated section of wellbore increasing the pressure. The pressure is increased beyond LOP until breakdown is reached (Figure 3.11). Breakdown is the pressure at which a fracture is propagated into the far field and no further pressure increase is possible. At this point, pumping is stopped, the section is shut in (no fluid is allowed to escape back through the pump) and the pressure decline is monitored. Once the pressure has stabilised the section is opened and the amount of fluid return is measured. Subsequently, in the second cycle, the

section is shut in and pumping is recommenced. The pressure increase is again monitored. When the pressure stabilises, after fracture reopening, a fixed amount of fluid (one litre to several barrels) is pumped before shutting off the pump and shutting in the section. The amount of fluid depends on the test being conducted and is pumped in order to propagate the fracture away from the near wellbore stress concentration. The pumping is then stopped and the pressure decline monitored. Once the pressure has stabilised, the section is opened and the amount of fluid returned recorded. This pressurisation/de-pressurisation cycle is repeated one or more additional times (Figure 3.11). The multiple cycles ensure (i) the fracture is propagated into the far field stress tensor (ii) tensile strength has been overcome and (iii) reliable, repeatable re-opening and closure pressures are obtained.
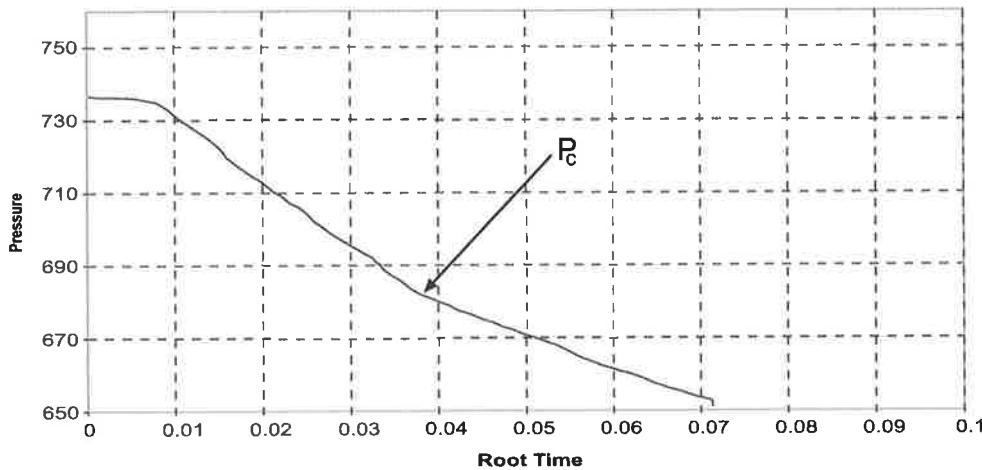
Figure 3.13. Pressure versus root time plot showing P_c. Plotting pressure versus root of time since pumping is stopped removes the effect of radial flow allowing P_c to be identified in permeable formations.

The fracture closure pressure (P_c) is the minimum pressure required to hold the fracture open against S_{hmin} and therefore equals S_{hmin} (Gronseth, 1982; Gronseth and Kry, 1983). The fracture closure pressure is interpreted from the pressure record, as the point after shut in at which there is a sudden decrease in the rate of pressure decline (Figure 3.11). This is interpreted as being due to the change from fluid loss through the entire length of the fracture and wellbore wall while the fracture is open, to fluid loss only through the wellbore wall after the fracture is closed. In an impermeable formation this is a rapid change readily apparent on the standard pressure record. As the permeability of the formation increases, radial flow into the

formation can mask the fracture closure on the pressure record. Several methods including tangent diversion (Gronseth and Kry, 1983), tangent intersection (Enever and Chopra, 1986) and the logarithmic method (Doe et al., 1983) can be used to facilitate identification of P_c, especially in permeable formations. The most common method is a plot of pressure versus the square root of time after shut in (Enever, 1993). This removes the effect of radial flow and allows P_c hence S_{hmin} to be determined (Figure 3.13).

3.6. Maximum Horizontal Stress Magnitudes

3.6.1. Extended Leak-Off and Minifracture Tests

The procedures used to conduct XLOTs and minifracture tests, and methods by which they can be used to measure S_{hmin} are described in Section 3.5. However, these tests can also be used to estimate S_{Hmax}.

S_{Hmax} can be determined from these tests using the fracture initiation and/or reopening pressure (Hubbert and Willis, 1957; Haimson and Fairhurst, 1967; Bredehoeft et al., 1976). The fracture initiation and/or reopening pressures depend on the stress concentration around an open hole. From Section 3.3 the minimum stress concentration around the wellbore is given by:

$$\sigma_{\theta\theta min} = 3S_{hmin} \tilde{n} \ S_{Hmax} - P_W - P_P \qquad \text{Eq. 3.15.}$$

Tensile failure occurs when this concentration exceeds the tensile strength of the rock (in an absolute sense, tensile stresses have been defined as negative). Hence for tensile failure of the wellbore wall:

$$\sigma_{\theta\theta min} = 3S_{hmin} \tilde{n} \ S_{Hmax} - P_W - P_P \le T \qquad \text{Eq. 3.16.}$$

The fracture initiation pressure (P_i, LOP) is P_w at fracture initiation, hence:

$$3S_{hmin} \ \tilde{n} \ S_{Hmax} \ \tilde{n} \ P_i - P_P = T \qquad \text{Eq. 3.17.}$$

The fracture initiation pressure can be read directly from the pressure record, as can S_{hmin} which is P_c (Figure 3.11). Hence Equation 3.17 can be rewritten:

$$S_{Hmax} = 3P_c \ \tilde{n} \ P_i - P_P \ \tilde{n} \ T \qquad \text{Eq. 3.18.}$$

The unknowns in Equation 3.18 can be determined from the pressure record, with the exception of the tensile rock strength which can be determined from lab testing of samples from the test interval. The fracture reopening pressure (P_r) is the pressure at which the fracture reopens in the subsequent cycles and can be read directly from the pressure record (Figure 3.11). Since the initial fracturing cycle overcomes tensile rock strength, for subsequent cycles Equation 3.18 can be rewritten:

$$S_{Hmax} = 3P_c \text{ ñ } P_r - P_P \qquad\qquad \text{Eq. 3.19.}$$

Using Equation 3.19 it is possible to determine S_{Hmax} from the pressure record. The above equations apply only to the open hole and not to tests conducted through casing perforations, as casing and cement disturbs the stress field around the wellbore.

Estimates of S_{Hmax} based on the above are subject to greater uncertainty than estimates of S_{hmin} because there is uncertainty in P_c, and P_r and it may not be unequivocally clear in which cycle tensile strength has been completely overcome. Repeating the test until consistent P_r and P_c are obtained can reduce these errors. Another potential source of error in S_{Hmax} determination is due to the permeability of the formation. The equations above assume impermeable rocks. If the formation is permeable, the increased P_w during testing may cause an increase in the pore fluid pressure in the formation. Assuming S_{Hmax} is not altered by the change in P_p and following Equation 3.19, this results in the artificial lowering of the P_c and P_r and an inaccurate estimate of P_p (Evans et al., 1989). However, Enever (1993) suggested this increase in P_p causes an increase in P_c. These changes can have a significant effect on the estimates of both S_{hmin} and S_{Hmax}. This problem can be overcome by using high pumping rates and fluids of high viscosity. Another uncertainty in S_{Hmax} determination is associated with the fact that for a variety of stress states, particularly strike-slip stress regimes, P_r in vertical wellbores is small, resulting in an inability to correctly interpret P_r and hence preventing S_{Hmax} from being accurately estimated (Evans et al., 1989).

3.6.2. Breakout Occurrence and Rock Strength

As discussed in Section 3.3.3, breakouts occur if the wellbore stresses exceed the rock strength (Equation 3.13). Therefore breakout occurrence depends on the far field in situ stresses, P_p, and the rock strength. Commonly S_v, S_{hmin} and P_p are known (Sections 3.2, 3.5 and 3.7 respectively). Therefore the only unknowns in Equation

3.13 are S_{Hmax} and the compressive rock strength. Where samples are available, laboratory rock strength measurements can be made, making S_{Hmax} the only unknown. Rewriting Equation 3.13, for breakout occurrence:

$$S_{H\,max} \geq (C - S_{h\,min} + 2P_P)/3 \qquad\qquad \text{Eq. 3.20.}$$

This relation enables a lower bound for S_{Hmax} to be determined, where breakouts are observed.

Equation 3.20 applies where the wellbore is drilled in balance (i.e. $P_w = P_p$). Due to issues related to wellbore stability, formation damage or anticipated changes in P_p, the borehole may not be drilled in balance, making Equation 3.20 invalid. In the case where the wellbore is not in balance, σ_3 in Equation 3.11 is non-zero (σ_3 is generally the radial stress which is given by ΔP). If we assume that σ_3 is the radial stress (this is not always the case, but is in general true) and σ_1 is the circumferential stress, Equation 3.11 becomes:

$$3S_{Hmax} - S_{hmin} - P_W - P_P \text{ ñ } f(\mu).\Delta P \geq C \qquad\qquad \text{Eq. 3.21.}$$

In this case Equation 3.20 becomes:

$$S_{H\,max} \geq (C - S_{h\,min} + P_P + P_w + f(\mu)\Delta P)/3 \qquad\qquad \text{Eq. 3.22.}$$

Equation 3.22 can be used to determine the lower bound to S_{Hmax} if breakouts are observed in boreholes drilled out of balance.

The above equations assume impermeable and elastic rocks. Drilling target horizons are typically reservoir sandstones. Sandstones tend to especially permeable. However, drilling mud is designed to minimise fluid loss to the formation and as drilling fluid flows into the formation when drilling over-balanced a mud cake forms at the wellbore wall, forming an impermeable barrier to further fluid loss. Mud cake formation maintains the assumption of impermeability. However, fluid flow is into the wellbore if the borehole is drilled under-balanced. In this case no mud cake forms and the rate of fluid flow into the wellbore depends on the permeability, P_p and P_w. This into-wellbore flow acts to equalise P_p and P_w. Equalisation occurs rapidly in the immediate vicinity of the wellbore, if the formation is highly permeable, and when

this occurs the wellbore can be assumed to be in balance. If the formation is of low permeability (still allowing flow into the wellbore), there is some, but not complete pressure equalisation. Hence there may be uncertainty in the pore fluid pressure in the vicinity of the wellbore, leading to uncertainty in the lower bound to S_{Hmax} determined using Equation 3.22.

3.6.3. Drilling Induced Tensile Fracture Occurrence and Rock Strength

As discussed in Section 3.3.4, DITFs occur if the wellbore stresses are less than the tensile rock strength (Equation 3.16). Therefore DITF occurrence depends on the far field in situ stresses and the rock strength. Commonly S_v, S_{hmin} and P_p are known (Sections 3.2, 3.5 and 3.7 respectively). Therefore the only unknowns in Equation 3.16 are S_{Hmax} and the tensile rock strength. If tensile rock strength is assumed to be negligible, Equation 3.16 can be rewritten:

$$\sigma_{\theta\theta min} = 3S_{hmin} \text{ ñ } S_{Hmax} - P_W - P_P \leq 0 \qquad \text{Eq. 3.23.}$$

Thus, a lower bound to S_{Hmax} can be determined where DITFs are observed, by rewriting Equation 3.23:

$$S_{H max} \geq 3S_{h min} - P_p - P_w \qquad \text{Eq. 3.24.}$$

Equations 3.23 and 3.24 do not assume that the wellbore is in balance, but do assume elastic, impermeable rocks and thereby suffer the same shortcomings as Equation 3.22. However, from inspection of Equation 3.24 it can be seen that DITFs are more likely to occur when P_w is high. Consequently, DITFs typically occur if wells are drilled over-balanced, in which case a mud cake forms and Equation 3.24 remains valid. The propensity for DITF formation may also be increased by increased down hole pressure both due to pumping pressure and running in the hole too quickly (surge pressure), and due to thermal stresses (Moos and Zoback, 1990).

Pumping pressure increases the effective circulating density (ECD). Effective circulating density is dependent on the pump rate, the inside diameter of the drill pipe, the fluid viscosity and the length of drill pipe. Where possible ECD should be used to calculate the down hole pressure. However, the required information to calculate ECD is not always available, in which case the static mud pressure is used.

The effect of surge pressure is dependent on the rate the drill string is run into the hole, which is typically unknown preventing the calculation of surge pressures.

The thermal stress depends on the difference between the temperature of the mud and the temperature of the formation (Coussy et al., 1991). As drilling mud is pumped down the drill pipe, it is heated by the mud flowing up the outside of the pipe and consequently the difference in temperature is greatly reduced and the actual temperature difference is not known.

The lack of information about the parameters controlling the thermal stress, surge pressures and pumping pressure, precludes their incorporation in S_{Hmax} determination except where specific and detailed data is available.

3.6.4. Frictional Limits

The frictional limits to stress are discussed in Section 2.5. For an optimally-oriented cohesionless fault plane, there exists a maximum ratio of maximum to minimum effective principal stresses above which sliding occurs (Sibson, 1974). In the case where S_v, S_{hmin} and P_p are known, and assuming a value for the coefficient of friction (μ), Equation 2.14 can be used to provide an upper bound to the S_{Hmax}. This method assumes that, on a large scale optimally-oriented cohesionless faults exist.

3.7. Pore Pressure

Pore pressure is required to determine the effective stress tensor (Section 2.4) and to successfully design petroleum wells. Although P_p is often hydrostatic (i.e. the same as that exerted by a column of water of given density), this is not always the case. Changes in P_p not only affect the effective stress by the amount of P_p change, but may also cause a change in the total applied stresses (Hillis, 2000). Hence, knowledge of the P_p is important to fully constrain the stress tensor.

There are several different methods for determining P_p in petroleum wells. These include transient pressure tests and mud weight records. Transient pressure tests include drill stem tests (DST) and measurements from wireline formation interval tests (WFITs) such as Schlumbergeri s repeat formation tester (RFT) and modular dynamic tester (MDT), and Haliburtoni s sequential formation tester.

3.7.1. Mud Weights

Drilling engineers continually vary the properties of drilling mud in order to prevent mud loss into the formation, to prevent formation fluids entering the well, to minimise damage to the formation and to mechanically stabilise the wellbore. One of the key mud properties is the mud density (known as mud weight). Mud weight is primarily varied to prevent formation fluids from entering the wellbore (i.e. preventing hazardous kicks or even blowouts). Consequently, the pressure resulting from the weight of the mud needs to be approximately equal to, or slightly in excess of Pp. If the pressure due to the mud weight is excessive, fractures may form (i.e. LOP exceeded) and mud may be lost into the formation. This loss of drilling fluid is undesirable, as drilling fluid is expensive and can damage the permeability of the reservoir horizon. Furthermore, it is expensive to increase the mud density and excess over-balanced slows the rate of penetration. Hence mud weight is generally kept just above, and is representative of P_p. It should be noted that mud weight can be raised to maintain wellbore stability (prevent breakout) in the absence of P_p increase. Hence mud weight is not always representative of P_p. Furthermore, in impermeable formations, drilling under-balanced or over-balanced may not result in significant kicks or mud loss requiring a change in mud weight. Consequently mud weight may not reflect pore pressure. Van Ruth et al. (2000) showed that in the Australia North West Shelf mud weights are close to pressures yielded by transient pressure tests in permeable formations, but that they may not be representative of P_p in impermeable formations.

Mud weight not P_w is recorded while drilling. Mud weights can be simply converted to pressures using:

$$P_{mw} = \rho.g.h \qquad \qquad \text{Eq. 3.25,}$$

where ρ is the mud weight, g is the acceleration due to gravity and h is the depth. Mud weights are measured in pound per gallon, specific gravity, kg/m^3 and and g/cm^3. Consequently, care must be taken to ensure all measurements are in the correct units.

Although mud weights do not provide a very reliable estimate of Pp, they are widely available and recorded throughout all wells, often being the only available indicator of

P_p. The accuracy of mud weights as an indicator of P_p can be improved by comparing them to the more reliable transient pressure tests (van Ruth et al., 2000).

3.7.2. Wireline Formation Interval Tests

Wireline formation interval tests (WFITs) are wireline tests designed to measure P_p and obtain fluid samples at specific depths in a well (Smolen, 1993). Testing involves forcing a probe against the wellbore wall, sealing it with a packer and then reducing the pressure in the test chamber, causing formation fluids to be drawn into the tool from the formation. The rate at which the pressure stabilises in the test chamber provides a measure of the permeability, and the equilibrium pressure corresponds to the pore fluid pressure (Smolen, 1993). Consequently, WFITs are only effective for formations with permeabilities > 5 mD. In general, WFITs are run over a short section of expected pay with many readings being taken over a small distance, in order to find the change in the pressure gradient corresponding to the gas-oil-water contact. The main disadvantages of WFITs are their limited coverage, their reliance on high permeability formations and the fact that only a small section of wellbore is tested at each depth.

3.7.3. Drill Stem Tests

Drill stem tests (DSTs) are conducted in isolated sections of wellbore, usually covering several metres, in which logging has indicated the presence of hydrocarbons. DSTs provide (Borah, 1993):

- fluid samples;
- pore fluid pressure;
- formation permeability;
- skin factor;
- radius of investigation;
- productivity estimates, and;
- hydrodynamic information.

The section of interest is sealed off using packers and allowed to flow for several minutes (3-5 minutes) to remove any drilling effects. The section is then shut in to allow pressure to build up for approximately one hour to determine a valid pore fluid

pressure. The section is then flowed for 60-120 minutes in order to cause a pressure disturbance well away from the wellbore. The section is then shut in again and the pressure recorded. Pore fluid pressure, fluid samples, formation properties and production estimates are made from this test (for further detail see Borah, 1993). DSTs provide very accurate estimates of pore fluid pressures, due to the size of the interval tested and the duration of the test. However, DSTs are only conducted on intervals in which logs have indicated the presence of hydrocarbons. Consequently, the number per well is generally low.

4. Stresses Around Arbitrarily Inclined Boreholes and Development of the SWIFT Software

4.1. Introduction

Technological advances in drilling techniques such as logging while drilling methods, combined with the benefits of deviated drilling, significantly increased the drilling of deviated petroleum production wells in recent years. In 1987 51 horizontal wells were drilled worldwide, while in 1997 4000 horizontal wells were drilled worldwide (Shirley, 2000). Technological advances have improved the positioning of the wellbore within reservoir units. The benefits of deviated holes include flexibility in surface location, a single surface location for multiple subsurface targets and trajectories that maximise productivity. These advantages commonly outweigh the increased cost of deviated drilling. However, wellbore stability is a major concern in drilling deviated wellbores and thus is of particular interest to the petroleum industry (Cooper, 1994). Mechanical wellbore stability depends on the in situ stress field, the wellbore geometry and the in situ rock strength. Consequently, the drilling of deviated boreholes has resulted in an increased interest in the in situ stress field and the resulting stress concentration around deviated wellbores.

The calculation of the stresses around an arbitrarily inclined wellbore requires that the far field in situ stress tensor is transformed into the borehole coordinate system. In this coordinate system, the stress tensor may no longer be represented by the principal stress magnitudes and directions of Equation 2.4. The shear stress components may be non-zero and the transformed stress tensor must be represented by Equation 2.1. The transformed stress tensor is required to calculate the wellbore stress concentration.

The necessity to repeatedly calculate the wellbore stresses on varying wellbore trajectories led to the development of software to simplify calculation of the stress around arbitrarily inclined wellbores. This software can be used to determine both the stress tensor using information such as that described in Chapter 3 and also to use that same stress tensor to investigate the implications for petroleum exploration and

production. The theory and development of the SWIFT (Stressed Wellbore Interactive Failure Tool) software are described in this chapter, while its use is tested in four case studies in Chapters 5-8.

4.2. Coordinate Transform

Peska and Zoback (1995) described a system of transformations to transform the three principal stresses into the borehole coordinate system. This system is described below. It is useful to choose a reference coordinate system with respect to which both the stress tensor and wellbore trajectory can be measured. Following Peska and Zoback (1995), a geographic coordinate system with north as a reference is chosen.

The stress tensor as described in Chapter 2 can be written:

$$S_S = \begin{pmatrix} S_{Hmax} & 0 & 0 \\ 0 & S_{hmin} & 0 \\ 0 & 0 & S_V \end{pmatrix} \qquad \text{Eq. 4.1.}$$

The matrix required to transform the stress tensor into the geographic coordinate system is:

$$R_S = \begin{pmatrix} \cos\alpha\cos\beta & \sin\alpha\cos\beta & -\sin\beta \\ \cos\alpha\sin\beta\sin\gamma-\sin\alpha\cos\gamma & \sin\alpha\sin\beta\sin\gamma+\cos\alpha\cos\gamma & \cos\beta\sin\gamma \\ \cos\alpha\sin\beta\cos\gamma+\sin\alpha\sin\gamma & \sin\alpha\sin\beta\cos\gamma-\cos\alpha\sin\gamma & \cos\beta\cos\gamma \end{pmatrix}$$
$$\text{Eq. 4.2,}$$

where α defines the clockwise rotation about the vertical axis from geographic north to the orientation of the maximum horizontal stress, β defines the rotation about the minimum horizontal stress direction towards the vertical down, and γ defines the rotation about the maximum horizontal stress direction.

The stress tensor in the geographic coordinate system (S_g) can be described by:

$$S_g = R_S^T S_S R_S \qquad \text{Eq. 4.3.}$$

The trajectory of a borehole can be described in the geographic coordinate system by δ and ϕ, where δ is the azimuth of the horizontal projection of the borehole measured clockwise from geographic north and ϕ is the angle between the borehole and the vertical. The matrix required to transform the stress tensor in the geographic coordinate system into the borehole coordinate system is:

$$R_b = \begin{pmatrix} -\cos\delta\cos\phi & -\sin\delta\cos\phi & \sin\phi \\ \sin\delta & -\cos\delta & 0 \\ \cos\delta\sin\phi & \sin\delta\sin\phi & \cos\phi \end{pmatrix} \qquad \text{Eq. 4.4.}$$

The stress tensor in the borehole coordinate system (S_b) can be described by:

$$S_b = R_b R_S^T S_S R_s R_b^T \qquad \text{Eq. 4.5.}$$

When considering effective stresses, the stress tensor becomes:

$$\sigma_{ij} = S_{b,ij} - \delta_{ij} P_P \qquad \text{Eq. 4.6}$$

where $S_{b,ij}$ is the i,j^{th} component of the stress tensor S_b and δ_{ij} is the Kronecker. Using the effective stresses described in Equation 4.6, the effective stresses at the wellbore wall become (Hiramatsu and Oka, 1962):

$$\sigma_{\theta\theta} = \sigma_{11} + \sigma_{22} - 2(\sigma_{11} - \sigma_{22})\cos 2\theta - 4\sigma_{12}\sin 2\theta - \Delta P$$

$$\text{Eq. 4.7,}$$

$$\sigma_{zz} = \sigma_{33} - 2\nu(\sigma_{11} - \sigma_{22})\cos 2\theta - 4\nu\sigma_{12}\sin 2\theta \qquad \text{Eq. 4.8,}$$

$$\tau_{\theta z} = 2(\sigma_{23}\cos\theta - \sigma_{13}\sin\theta) \qquad \text{Eq. 4.9 and,}$$

$$\sigma_{rr} = \Delta P \qquad \text{Eq. 3.7.}$$

For a borehole arbitrarily inclined with respect to the principal stresses, $\tau_{\theta z}$ is non-zero i.e. the axial and circumferential stresses are not principal stresses. In this case, the three principal stresses at the wellbore wall can be calculated using:

$$\sigma_{t\,max} = \frac{1}{2}\left(\sigma_{zz} + \sigma_{\theta\theta} + \sqrt{(\sigma_{zz} - \sigma_{\theta\theta})^2 + 4\tau_{\theta z}^2}\right) \qquad \text{Eq. 4.10,}$$

$$\sigma_{t\,min} = \frac{1}{2}\left(\sigma_{zz} + \sigma_{\theta\theta} - \sqrt{(\sigma_{zz} - \sigma_{\theta\theta})^2 + 4\tau_{\theta z}^2}\right)$$ Eq. 4.11 and,

$$\sigma_{rr} = \Delta P$$ Eq. 3.7,

where σ_{tmax} and σ_{tmin} are the maximum and minimum effective stresses in the plane tangential to the borehole wall (Figure 4.1). The angle ω defines the angle between σ_{tmax} and the borehole axis in the plane tangential to the borehole wall and is defined:

$$\tan 2\omega = \frac{2\tau_{\theta z}}{\sigma_{zz} - \sigma_{\theta\theta}}$$ Eq. 4.12.

Thus the stress tensor at the wellbore wall can be described using Equations 3.7, 4.10, 4.11 and 4.12.
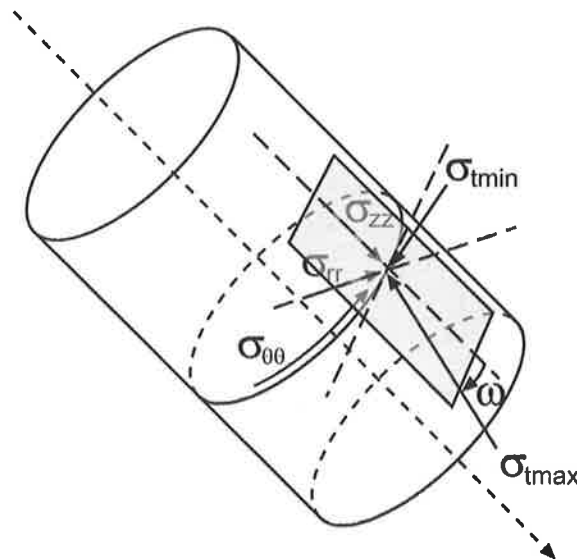
Figure 4.1. Arbitarily inclined wellbore showing the orientations of the cirumferential ($\sigma_{\theta\theta}$), axial (σ_{zz}), radial (σ_{rr}), minimum (σ_{tmin}) and maximum (σ_{tmax}) stresses, where ω is the angle between σ_{tmax} and the wellbore axis (after Peska and Zoback, 1995).

4.3.   Breakouts

The formation of breakouts in vertical boreholes was described in Chapter 3. Breakouts in deviated boreholes also occur due to compressional shear failure of the wellbore wall. In vertical boreholes compressional shear failure occurs, in general, due to the difference between the maximum circumferential stress and the radial

stress. However in deviated boreholes, breakouts occur due to the difference between σ_{tmax} and the lesser of the σ_{rr} and σ_{tmin}. Hence Equation 3.11 can be written:

$$\sigma_{t\,max} - f(\mu)\sigma_3 \geq C \qquad\qquad \text{Eq. 4.13.}$$

As discussed in Section 3.3.3, these equations assume that rocks are impermeable and behave elastically. While the assumption of elastic behaviour may be reasonable, the assumption of impermeability is not (Section 3.3.3). If the borehole is drilled over-balanced the assumption of impermeability can be maintained due to mud cake formation (Section 3.3.3). However, if the borehole is drilled under-balanced the assumption of impermeability may not be maintained and a value for the near wellbore P_p must be assumed depending on formation permeability (Section 3.3.3).

4.4. DITFs

The formation of DITFs in vertical boreholes was described in Section 3.3.4. DITFs in deviated boreholes also occur due to tensile failure of the wellbore wall. However, this occurs when σ_{tmin} is less than the tensile strength of the rock, in deviated wellbores. Hence DITFs in deviated wells develop at an angle ω to the borehole axis in the plane tangential to the wellbore wall, where ω is defined in Equation 4.12.

4.5. SWIFT Software

4.5.1. Introduction

In situ stress determination based on the observation of wellbore failure requires modelling observed wellbore failure using certain known parameters thereby constraining unknown parameters. For example, if DITFs are observed and S_v, S_{hmin} and ΔP are known, and T is assumed to be equal to zero, then S_{Hmax} can be constrained to that required to produce $\sigma_{tmin} \leq 0$ (Sections 6.3.1 and 8.3.2). Such can be readily undertaken by means of forward modelling using software capable of accessing existing information, varying the unknown parameters and predicting the type of failure. The SWIFT software was developed for this and related purposes and the remainder of this Chapter outlines the SWIFT Software.

Typically, the available information consists of observations of wellbore deformation (breakouts and DITFs), LOTs, XLOTs, minifractures, mud weights, WFITs, DSTs and vertical stress (Chapter 3). Information of this type can be stored in a database, enabling relevant data to be queried.

The main aim of the SWIFT software is to determine the stress tensor and investigate its implications for petroleum exploration and production, thereby requiring repeated calculation of the equations described in Section 4.2. Consequently, a programming language that simplifies the implementation of these calculations is needed. The platform on which the software is implemented is Microsoft Windowsô . The main features required to achieve the aims of the software are database access and the ability to visualise results. These aims can be achieved by using the Borland C++ programming environment, which uses the C++ programming language. The use of classes in C++ enables calculations to be programmed in a relatively simple and scalable manner. Borland C++ facilitates database access and visualisation of results using inbuilt and third party components.

4.5.2. Stress Classes

Programming classes provide a structure capable of encapsulating data and related functions required for a particular task and thus provide the ideal mechanism for implementation of the equations described in Section 4.2. A class allows programming code to be written without reference to the actual calculations, with data being input and results retrieved. Furthermore C++ classes feature inheritance, allowing a new class to be constructed incorporating all the features of an existing (base) class. This allows complex classes to be constructed by combining more simple classes and adding functionality to create a new (derived) class. The use of classes results in scalable programming code that can be easily improved upon and added to without affecting the original functionality.

The calculations performed by the SWIFT software are achieved by the use of three classes, a base class (class stress), a child class (class cstress) and further child class (wbfstress) based on class cstress.

Class stress transforms a stress tensor in an arbitrary coordinate system to a stress tensor in the wellbore coordinate system. This is achieved by using the

transformations described in Section 4.2. This class requires the input of the principal stresses (S_{Hmax}, S_{hmin} and S_v), P_P and the rotations (α, β and γ) and outputs the complete stress tensor (Equation 2.1) in the new coordinate system. A default value of zero is used if no value is entered. For a list of the functions and parameters available in class stress see Appendix A.

Class cstress is derived from class stress and contains all the functionality of class stress while also calculating the stress concentration about an arbitrarily inclined wellbore using Equations 3.7, and 4.7 - 4.12. This class requires the input of the wellbore trajectory (δ and ϕ) and P_w and outputs the wellbore stresses calculated from Equations 3.7, and 4.7 - 4.12. For a list of the functions and parameters available in class cstress see Appendix A.

Class wbfstress is derived from class cstress and contains all the functionality of classes cstress and stress while also calculating the shear and normal stresses acting on a fracture at the wellbore wall. This class requires the input of the fracture geometry. For a list of the functions and parameters available in class cstress see Appendix A.

These three stress classes work together to simplify implementation of the wellbore stress calculations. Figure 4.2 contains example code for calculating the wellbore stresses and a flow diagram illustrating the way in which they are calculated. Figure 4.2 highlights the manner in which the results can be obtained without knowledge of the calculations. Furthermore, as the parameters are stored within the classes, future calculations are further simplified. For example, to change a single parameter only that parameter needs to be re-entered and the results retrieved.

These three stress classes provide the necessary functions to investigate the occurrence of borehole breakouts and drilling induced tensile fractures, and can be used to investigate a wide variety of stress-related issues.

4.5.3. User Interface

The classes described above provide the ëengineí for calculating the stresses around an arbitrarily inclined wellbore. However, a method of inputting and manipulating the required data and visualising the results is also required. This is achieved by a

```
local_stress  =  new wbfstress();              //creates a new instances of class wbfstress
local_stress_>SetSHmax(20);                    //sets the maximum horizontal stress
local_stress_>SetShmin(10);                    //sets the minimum horizontal stress
local_stress_>SetSv(15);                       //sets the vertical stress
Local_stress_>SetPp(7);                        //sets the pore pressure
local_stress_>SetOrient(90);                   //sets the orientation of the maximum horizontal stress
Local_stress_>SetHazi(45);                     //sets the wellbore orientation
local_stress_>SetDevi(15);                     //sets the wellbore deviation
Circumf = local_stress_>GetSigTT();            //retrieves the circumferential stress around the wellbore
Wellboremax = local_stress_>GetSigTMax();      //retrieves the maximum wellbore
```
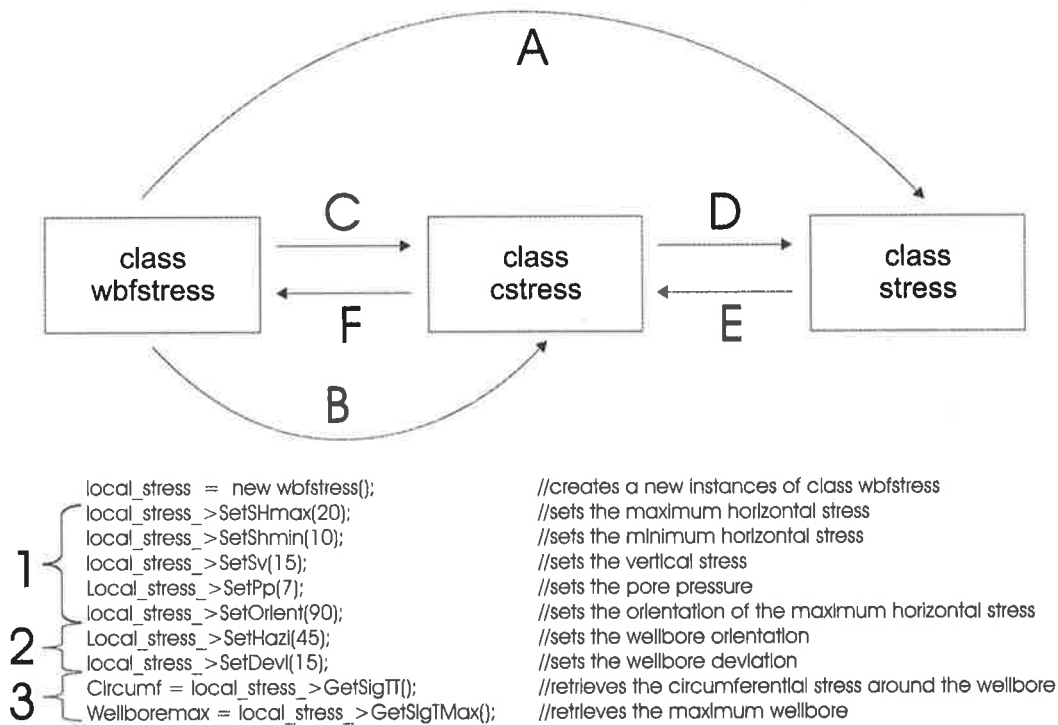
Figure 4.2. Example code and flow diagram showing how the stress classes function. The first line of code creates a new instance of the class wbfstress. Section 1 of the code sets the principal stress values (contained in class stress) and is represented by A. Section 2 of the code sets the wellbore trajectory (contained in class cstress) and is represented by B. Section 3 of the code retreives the circumferential stress and maximum stress in the plane normal to the wellbore wall around the wellbore. This is represented by C, D, E and F. C represents class wbfstress requesting the wellbore stress from class cstress. D represents class cstress requesting the transformed stress tensor from class stress. E represents class stress returning the transformed stress tensor. F represents the wellbore stresses being returned to class wbfstress and subsequently returned to the variables Circumf and Wellboremax in Section 3 of the example code.

graphical user interface (GUI). The GUI needs to simplify data manipulation and visualisation and provide access to all the functionality of the stress classes, and also provide the ability to save and load data, copy data and results and print the results. These features greatly enhance the effectiveness and useability of the software. The features that apply to all types of display and the basic GUI are described in this section. The GUI consists of a menu bar, a toolbar, a program window area and the main form (Figure 4.3). To aid in the description a font scheme is used for GUI components (Table 4.1)
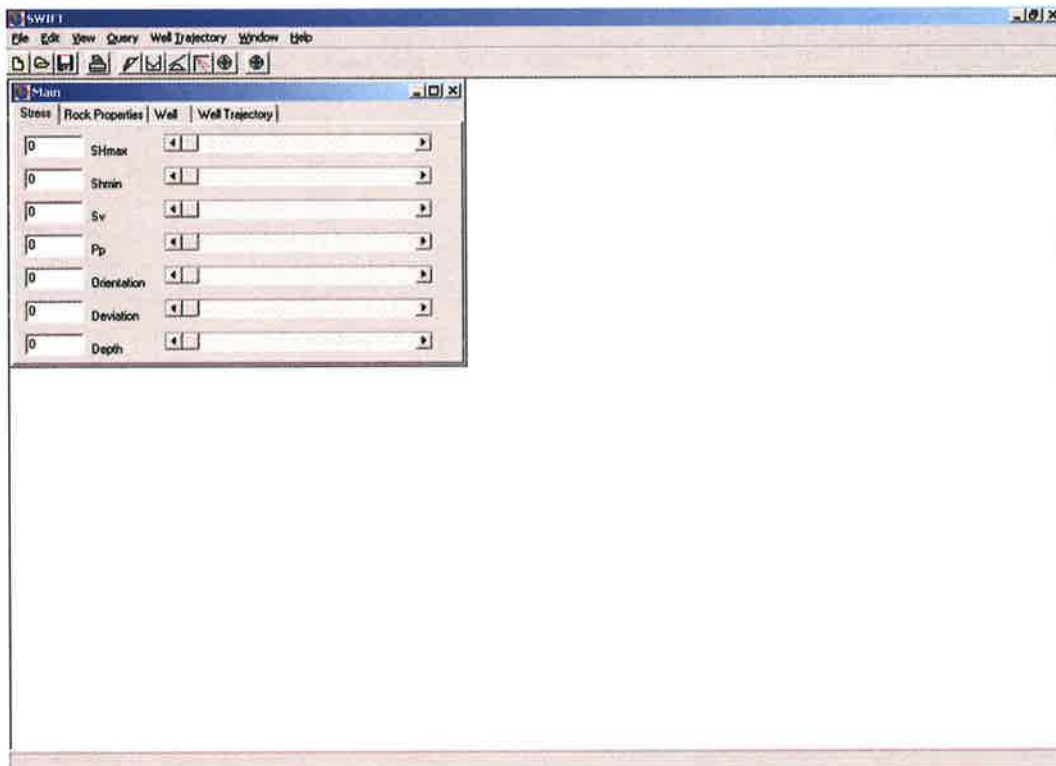
Figure 4.3. SWIFT software graphical user interface (GUI) provides an interface between the user and the data and stress classes.

Component	Font Type
Window/Form	**Main**
Window Tab	*Stress*
Window Item	*Automatic Scaling*
Menu	**File**
Menu Item	*Open Session*

Table 4.1. Font scheme used for GUI components.

Main Form

The **Main** form contains the **Stress**, **Rock Properties**, **Well** and **Well Trajectory** tabs (Figure 4.4). These tabs are used to enter information on those parameters.

The **Stress** tab contains slider bars and text boxes for altering S_{Hmax}, S_{hmin}, S_v, P_P and the orientation and dip of S_{Hmax} (Figure 4.4).
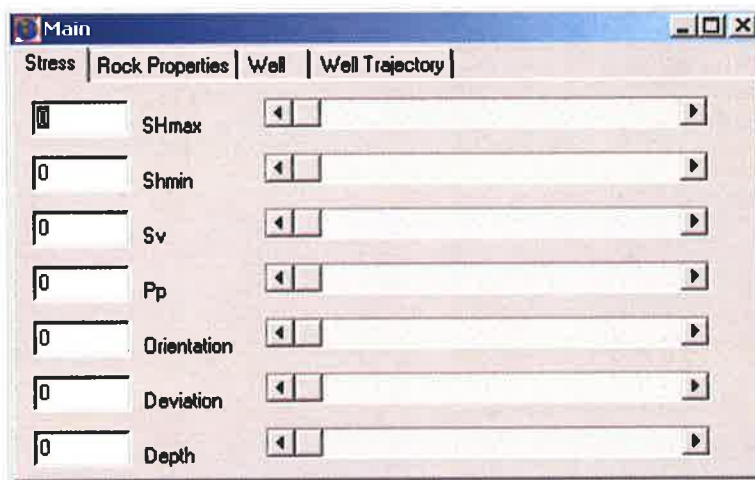

Figure 4.4. Main Form containing Stress, Rock Properties, Well and Well Trajectory tabs for entering information on those parameters. The Stress tab on the Main form contains slider bars and text boxes for altering S_{Hmax}, S_{hmin}, S_v, P_P and the orientation and dip of S_{Hmax}.

The **Rock Properties** tab contains text boxes and slider bars for altering the coefficient of friction, the coefficient of internal friction, Poisson's ratio, the uniaxial compressive rock strength and the tensile rock strength, as well as radio buttons to select the type of failure envelope (Figure 4.5). The data entered in the **Rock Properties** tab is used for investigation of rock failure and is required for breakout risk and structural permeability calculations (Sections 4.5.8 - 4.5.10).

The **Well** tab contains text boxes and slider bars for altering the wellbore azimuth, deviation and P_w (Figure 4.6).

The **Well Trajectory** tab contains a spreadsheet for viewing and editing wellbore trajectory properties, such as inclination and deviation, P_w, P_p and whether DITFs or wellbore breakouts are observed (Figure 4.7). This information can be saved and loaded using the **Well Trajectory** menu.
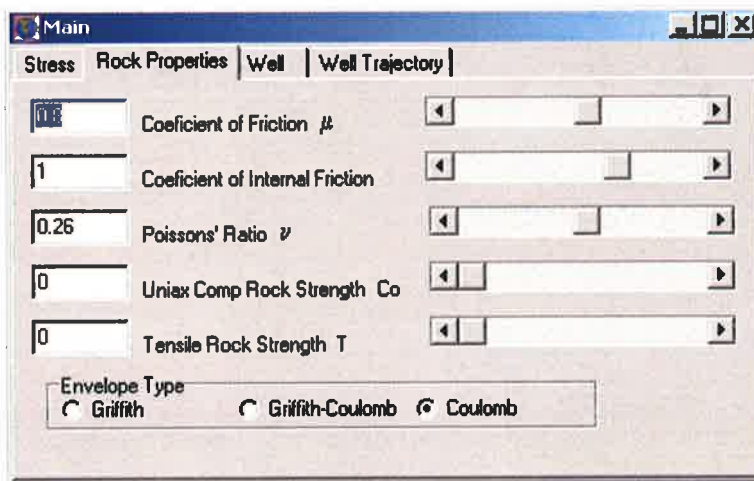
Figure 4.5. The Rock Properties tab on the Main form contains the parameters and options for the method in which failure envelopes are calculated.
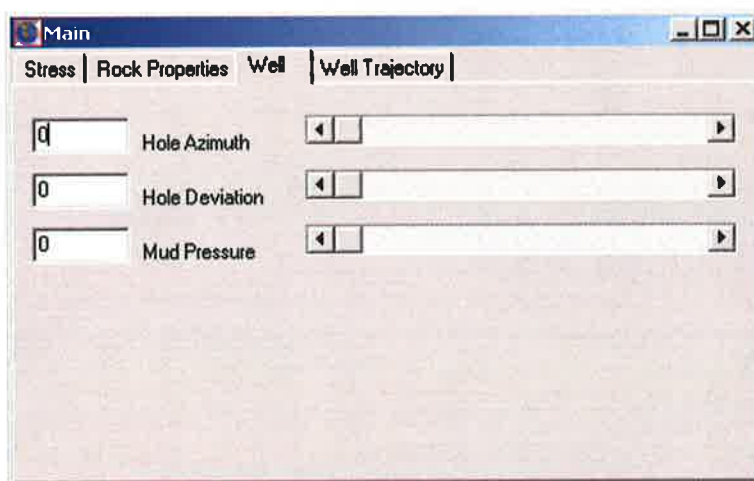

Figure 4.6. The Well tab on the Main forms contains text boxes and slider bars for altering the wellbore azimuth, deviation and fluid pressure.

Menu Bar

The menu bar contains **File, Edit, View, Query, Well Trajectory, Window** and **Help** menus. The **File** menu contains *New Session, Open Session, Save Session, Save StrucPerm, Save Breakout, Save DITF, Print* and *Exit* menu items (Figure 4.8).

The *New Session* menu item is used to reset all values back to their default values. The *Open Session* menu item is used to open a previously saved session. A session stores the values of all the variables, many of the program settings and all the open

queries. Sessions can be saved using the *Save Session* menu item. The ability to save and open sessions enables values to be stored, reducing the time to restore a stress state and reduces the likelihood of errors as values do not have to be re-entered. By default, the current session is saved when SWIFT is shut down and the session reloaded when SWIFT is restarted. This feature can be deactivated.

Figure 4.7. The Well Trajectory tab on the Main form contains a spreadsheet for viewing and editing wellbore trajectory information.

Figure 4.8. File menu.

The *Save StrucPerm*, *Save Breakout* and *Save DITF* menu items are used to save the results from structural permeability risk, breakout risk and DITF risk analysis respectively to file. The structural permeability risk, breakout risk and DITF risk are discussed in Sections 4.5.9 - 4.5.11. The *Print* menu item is used to print all the

current windows to the selected printer. The *Exit* menu item is used to shut down the program.

The **Edit** menu contains the *Cut, Copy, Paste* and *Options* menu items (Figure 4.9). The *Cut* menu item cuts the selected item to the clipboard. The *Cut, Copy* and *Paste* menu items operate similarly to those in standard application software. The *Options* menu item displays the **Options** window (Figure 4.10).
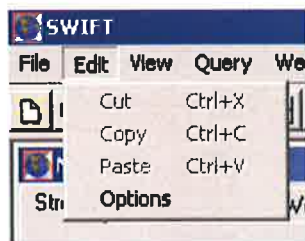

Figure 4.9. Edit menu.

The **Options** window allows options relating to calculations, displays and program settings to be selected. The *General* tab on the options window allows the maximum stress value and step size for the stress slider bars on the main form (Figure 4.3) to be set and enables the database to be chosen (Figure 4.10).
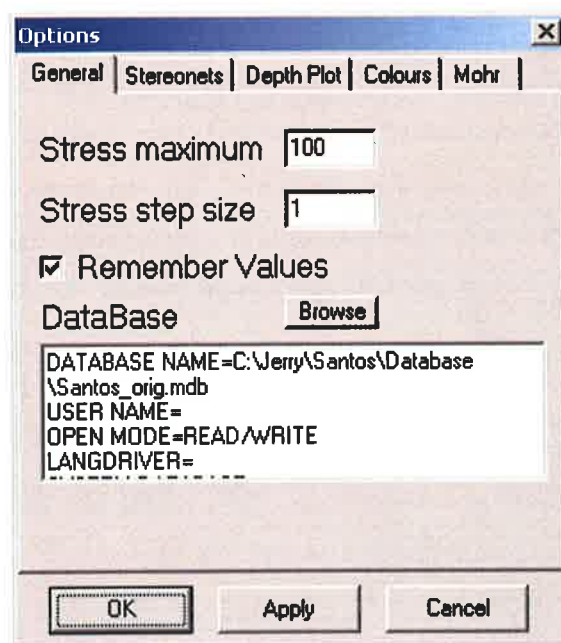

Figure 4.10. Options window.

The **Stereonets** tab contains options for the *Number of Circles, Radial Angle*, the *Max* and *Min* values for the stereonet, *Automatic Scaling, Use C₀, Use ppg, Breakout Width, Link to Wellbore Stresses, Invert DITF colours* and *Near Wellbore Depletion* (Figure 4.11). The *Number of Circles* and *Radial Angle* control the number of axial and radial gridlines on the plots. The *Max* value, *Min* value and *Automatic Scaling* options control whether maximum and minimum values displayed on the stereonet are user defined or automatically calculated. The *Use C₀, Breakout Width* and *Near Well*bore Depletion options control the way in which breakout risk is calculated and displayed, and are discussed in Section 4.5.10. The *Use ppg* option controls whether results are displayed as change in pressure divided by the vertical stress ($\Delta P/S_v$) or as a mud weight gradient in pounds per gallon (ppg). The *Link to Wellbore Stresses* option determines whether the wellbore stresses plot is linked to the breakout risk and DITF risk plots. When this option is selected and both the wellbore stresses plot, and either the breakout risk or DITF risk plots are displayed, as the mouse is moved over the risk plot, the wellbore stresses plot changes representing the hole azimuth and deviation of the point over which the mouse is moved. The *Invert DITF colours* option simply inverts the colours displayed on the DITF risk plot.
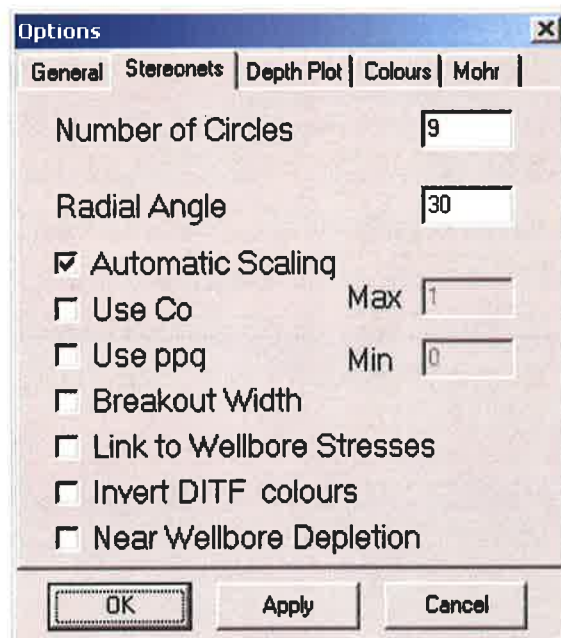
Figure 4.11. Stereonets options tab on the Options window.

The **Depth Plot** tab contains *automatic scale, lines, X max, X min, Y max, Y min, LOT max devi* and, *Horizontal* and *Vertical* size options. These options are discussed in Section 4.5.6. The **Colours** tab contains the *Chart Background colour* option which allows the chart background colours to be set. The **Mohr** tab contains *automatic scale, Max Norm, Min Norm, Max Shear, Min Shear* and, *Horizontal* and *Vertical* size options. These options are discussed in Section 4.5.7.

The **View** menu contains *Allowable Region, Wellbore Fractures, Legend* and *Rock Failure Data* menu items and **Wellbore Stresses, Mohr Circle, Stereonets** and **Depth Plot** submenus (Figure 4.12). These menu items and submenus are used to display each of the plots described in Sections 4.5.4 - 4.5.11 and their use is described in those sections.
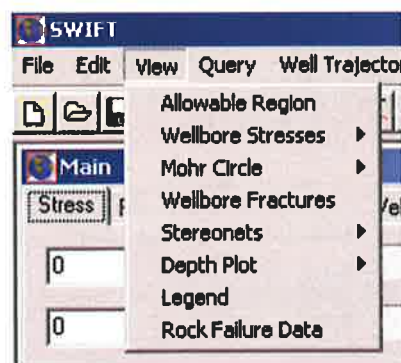
Figure 4.12. View menu.

The **Query** menu contains **Fractures, WBFractures, Breakouts, DITFs, LOT, Mud Weight, WFIT, DST, Vertical Stress** and **Mini Fracture Tests** submenus (Figure 4.13). Each of these submenus contains a *Query* and *Show* menu item (Figure 4.13).

The *Query* menu item displays the **Query** window (Section 4.5.4). The results of a query can be viewed in tabular form by selecting the *Show* menu item on the **Query** menu corresponding to the type of data queried (Figure 4.13), alternatively the data can be visualised using the appropriate plot type.

The **Well Trajectory** menu contains the *Add Row, Open* and *Save* menu items (Figure 4.14). The *Add Row* menu item allows rows to be added to the well trajectory

spreadsheet on the ***Well Trajectory*** tab in the **Main** form. The *Open* and *Save* menu items are used to save and open the contents of the well trajectory spreadsheet.
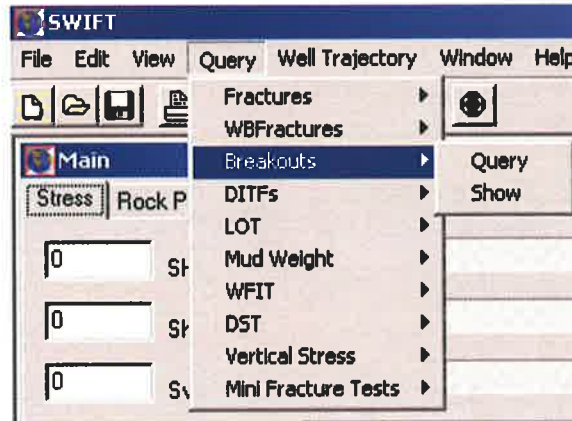
Figure 4.13. Query menu.

Figure 4.14. Well trajectory menu.

The **Window** menu contains the *Tile, Cascade, Arrange All* and *Hide* menu items as well as a menu item for each plot type that is displayed and the **Main** form (Figure 4.15). These menu items operate similarly to those in standard application software.

The **Help** menu is used to display the **About** window. The **About** window displays the build number, copyright information and the number of days before the license expires.

Toolbar

The toolbar contains *New Session* ( ), *Open Session* ( ), *Save Session* ( ), *Print* ( ), *Allowable Region* ( ), *Wellbore Stresses* ( ), *Mohr Circle* ( ), *Depth Plot* ( ), *Fracture Stereonet* ( ) and *Risk of Reactivation* ( ) buttons (Figure 4.3). The *New Session, Open Session, Save Session* and *Print* buttons

correspond to the *New Session*, *Open Session*, *Save Session* and *Print* in the **File** menu. The *Wellbore Stresses*, *Mohr Circle* and *Depth Plot* buttons correspond to the *Show* menu item on each of the **Wellbore Stresses**, **Mohr circle** and **Depth Plot** submenus in the **View** menu. The *Fracture Stereonet* and *Risk of Reactivation* buttons correspond to the *Show* menu item on the **Fracture** and **Strucperm** submenus in the **Stereonets** submenu on the **View** menu.
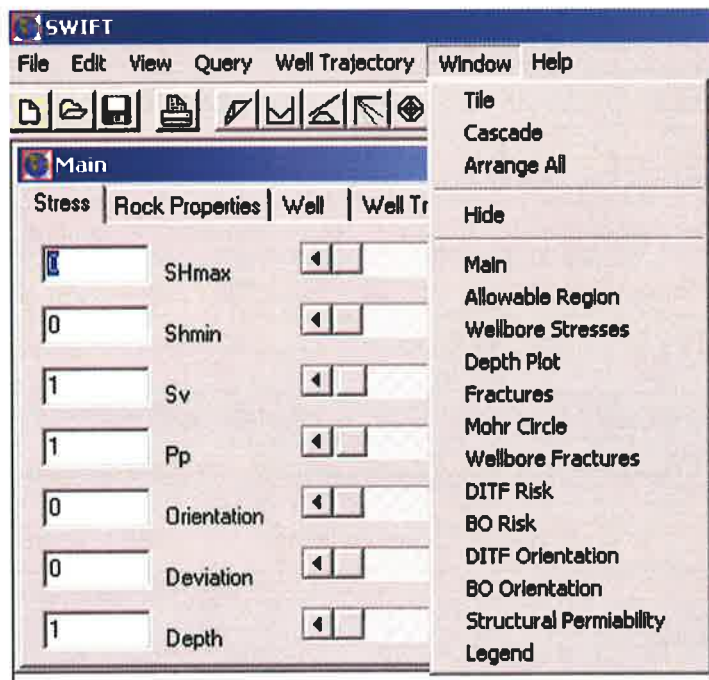
Figure 4.15. Window Menu.

4.5.4. Query Tool
The query tool is used to query data from a specifically designed Microsoft ACCESS 97ô database. When SWIFT is started it automatically creates a link to the database.

The database is used to store a wide variety of data used in geomechanics and provides a means by which a large amount of data can be stored and recovered in a logical and rapid manner. The easy and rapid access to this data is a key feature of the SWIFT software in simplifying stress determination by allowing reference to all available data. Furthermore, the database alone provides a consistent and accessible repository for storing data for the entire ëStress Groupí, ensuring no duplication of

effort and allowing easy access to each others data and interpretations. SWIFT provides access to the database using the **Query** window (Figure 4.16).

To use the **Query** window, first, a location type is selected in the *Wells* section of the query window. This can either be an individual *Well*, a *Field*, a *Basin* or a user-defined *Group* of wells. When the type of location is selected, a list of all possible selections is automatically created in the drop down box below the list of location types. Once the location has been selected, the depth range of data can be specified. This is achieved by either selecting *All*, *Depth* or *Formation* in the *Depth* section at the bottom right of the query window. If either *Depth* or *Formation* are selected a depth range or formation must be chosen. The Formation drop down box contains a list of all the available formations for the location specified in the *Wells* section of the window. If fractures are queried the *Fractures* section appears in the top right of the query window (Figure 4.16) and either all fractures or only specific fracture types can be selected.
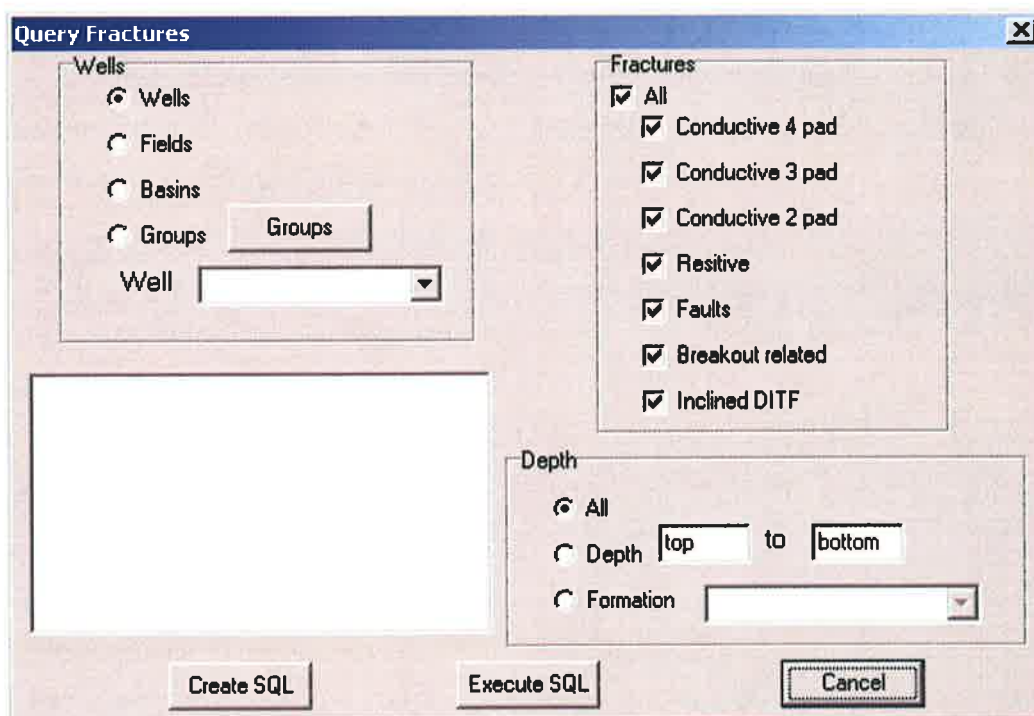

Figure 4.16. Query window.

Once all the options have been selected, the *Create SQL* button is clicked. This generates the structured query language (SQL) required for the query and displays it

in the text box at the bottom left of the query window (Figure 4.16). The query can then be executed or the SQL code altered in order to further customise the query and then executed using the *Execute SQL* button, retrieving the relevant data from the database. If the SQL code is executed successfully the query window disappears, if not the query window remains open after the *Execute SQL* button is clicked. The results of the query can be viewed in tabular form by selecting the *Show* menu item on the **Query** menu corresponding to the type of data queried (Figure 4.13), alternatively the data can be visualised using the appropriate plot type.

4.5.5. Allowable Region Diagram

The **Allowable Region** diagram displays the frictional limits to stress (Section 2.5) and the relative magnitudes of the three principal stresses (Moos and Zoback, 1990; Figure 4.17). This plot is used to visualise the relative stress magnitudes and to maintain them within frictional limits while altering the stress magnitudes in the **Main** form. The **Allowable Region** diagram is displayed using either the *Allowable Region* ( ) button or the *Allowable Region* menu item in the **View** menu (Figure 4.12).
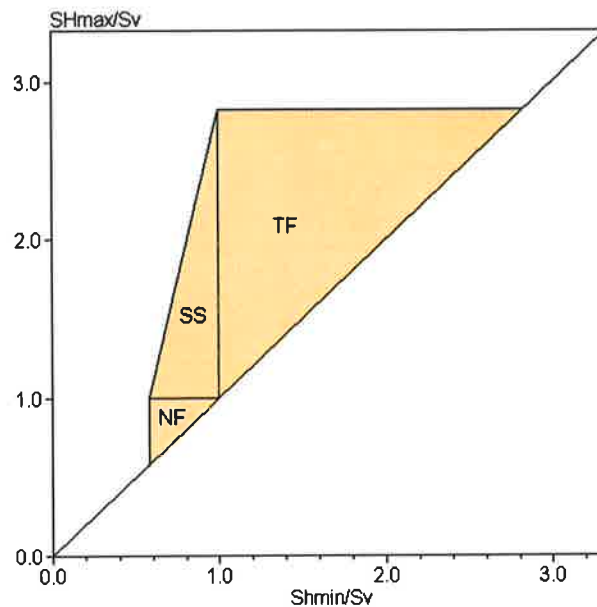
Figure 4.17. Allowable region diagram showing the frictional limits to stress and relative magnitudes of the three principal stresses. The shaded region represents stress magnitudes within frictional limits. TF represents a thrust faulting stress regime. SS represents a strike-slip faulting stress regime. NF represents a normal faulting stress regime. Figure assumes a μ of 0.8 and hydrostatic P_P.

4.5.6. Depth Plots

The **Depth Plot** (Figure 4.18) is used to visualise information on stress magnitudes, stored in the database, such as, S_{hmin}, S_v, and P_p, which are selected using the **Query** window (Figure 4.16; Section 4.5.3). The **Depth Plot** is displayed either by selecting the *Show* menu item in the **Depth Plot** submenu (Figure 4.19) or clicking the *Depth Plot* ( ) button on the toolbar. The items displayed in, and the format of the **Depth Plot**, are controlled using the *Depth Plot* tab (Figure 4.20) in the **Options** window and the **Depth Plot** submenu (Figure 4.19) in the **View** menu.
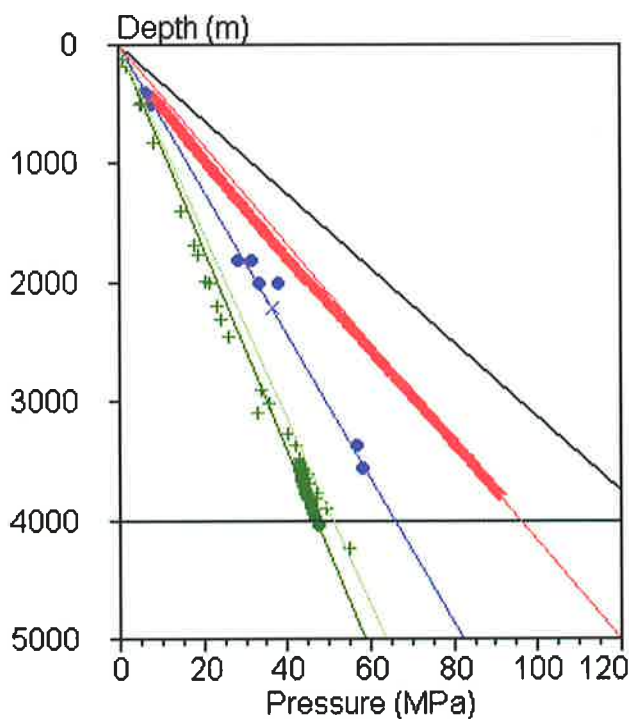
Figure 4.18. Depth plot showing vertical stress (+), LOTs (•), minifractures and XLOTs (×), mud weights (+), WFITs (•), S_v gradient (–), S_{hmin} gradient (–), P_p gradient (–), P_w gradient ( ) and S_{Hmax} gradient (–).

The **Depth Plot** submenu is used to display the **Depth Plot** and to control the types of data that are displayed (Figure 4.19). Data queried, using the **Query** window, is displayed on the **Depth Plot** when the corresponding menu item on the **Depth Plot** submenu is selected.

The *Depth Plot* tab on the **Options** window is used to control the plot scaling, the size of the plot, the maximum deviation of wells in which LOTs were undertaken to

be displayed, and whether or not gradient lines are displayed (Figure 4.20). If *Automatic Scale* is checked, the scaling is automatic, otherwise *X max, X min, Y max and Y min* must be set. The size of the plot can be altered using the *Horizontal* and *Vertical* edit boxes. Gradient lines are displayed if *Lines* is checked.
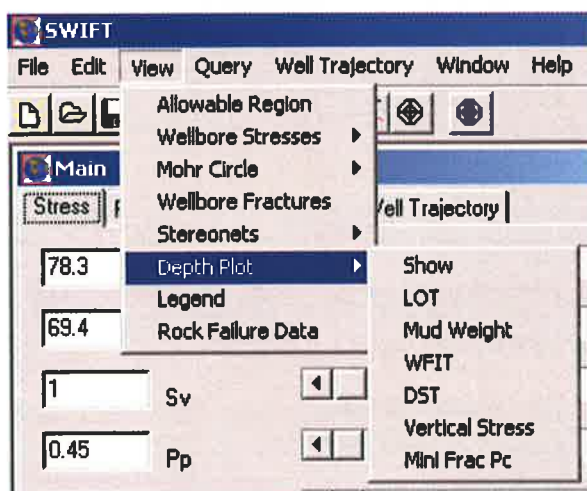
Figure 4.19. Depth Plot submenu.
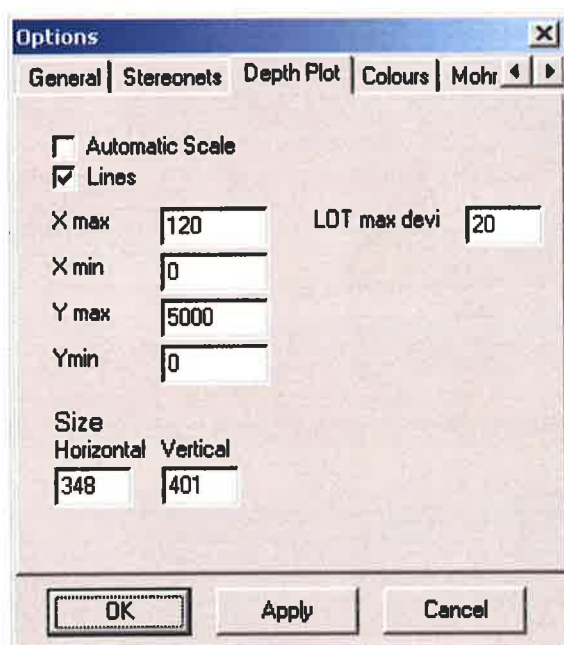
Figure 4.20. Depth Plot tab in the Options window.

4.5.7. Mohr Circles

The **Mohr Circle** diagram is used to display Mohr circles, failure envelopes and the shear and normal stress acting on fractures (Figure 4.21; Section 2.3). The **Mohr Circle** diagram is displayed either by selecting the *Show* menu item in the **Mohr Circle** submenu (Figure 4.22) or clicking the *Mohr Circle* (◿) button on the toolbar. The items displayed in, and the format of the **Mohr Circle** diagrams are controlled using the *Mohr* tab (Figure 4.23) in the **Options** window and the **Mohr Circle** submenu (Figure 4.22) in the **View** menu.

The *Mohr* tab on the **Options** window is used to control the plot scaling and the size of the plot (Figure 4.23). If *Automatic Scale* is checked the scaling is automatic, otherwise *Max Norm, Min Norm, Max Shear* and *Min Shear* must be set. The size of the plot can be altered using the *Horizontal* and *Vertical* edit boxes.
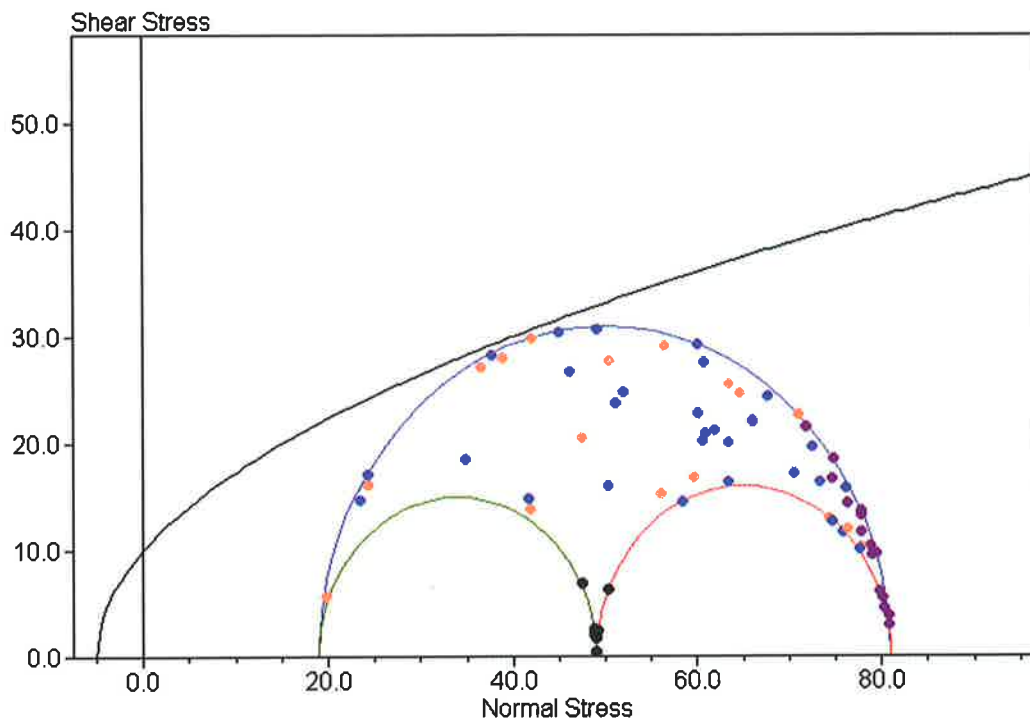
Figure 4.21. Mohr circle diagram showing Griffith failure envelope and fractures. A single fracture (dip/dip direction combination) plots as a single shear stress-normal stress point representing the shear and normal stress acting on that fracture. See Jaeger and Cook (1979)

The **Mohr Circle** submenu is used to display the **Mohr Circle** diagram and to control the types of data that are displayed (Figure 4.22). Fractures queried, using the **Query** window, are displayed on the **Mohr Circle** diagram when the *Fractures*

menu item on the **Mohr Circle** submenu is selected. The failure envelope is displayed when the *Failure Line* menu item is selected. Laboratory-derived rock failure data, entered in the **Rock Failure Values** window (Figure 4.24), are displayed if the *Rock Failure* menu item (Figure 4.22) is selected. The **Rock Failure** window is displayed by selecting the *Rock Failure Data* menu item on the **View** menu (Figure 4.12) and is used to enter laboratory rock failure data. This allows a failure envelope to be adjusted to match the laboratory rock failure data.
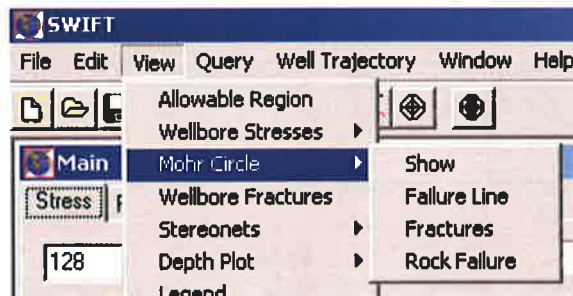
Figure 4.22. Mohr Circle submenu.
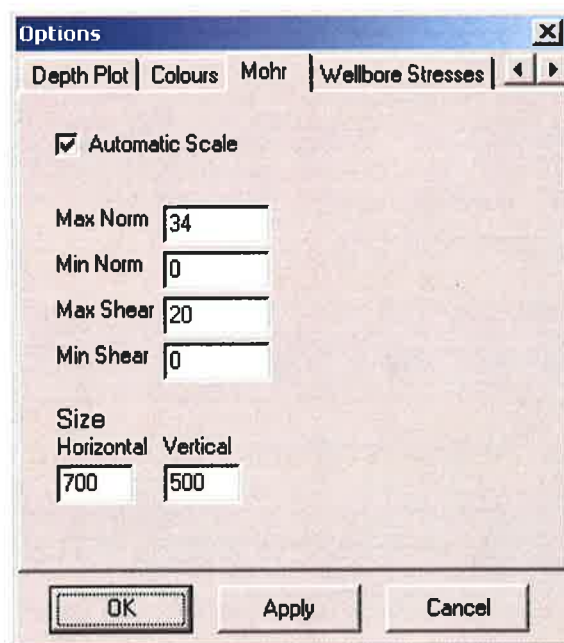
Figure 4.23. Mohr Circle tab in the options window.

Figure 4.24. Rock Failure Values window used to enter laboratory-derived rock test failure data.

4.5.8. Wellbore Stresses

The **Wellbore Stresses** diagram is used to display the stresses around an arbitrarily inclined wellbore (Figure 4.25; Section 4.2). The **Wellbore Stresses** diagrams are displayed either by selecting the *Show* menu item in the **Wellbore Stresses** submenu (Figure 4.26) or clicking the *Wellbore Stresses* (⌦) button on the toolbar. The wellbore azimuth, deviation and P_w are set using the *Well* tab on the **Main** form (Figure 4.6). The items displayed in, and the format of the **Wellbore Stresses** diagrams are controlled using the *Wellbore Stresses* tab (Figure 4.27) in the **Options** window and the **Wellbore Stresses** submenu (Figure 4.26) in the **View** menu.

The **Wellbore Stresses** submenu is used to display the **Wellbore Stresses** diagram and to control the types of data that are displayed (Figure 4.26). The circumferential stress, axial stress, maximum stress, minimum stress, breakout failure line and shear stress (Section 4.2) are displayed on the **Wellbore Stresses** diagram if the corresponding menu item on the **Wellbore Stresses** submenu is selected (Figure 4.26).
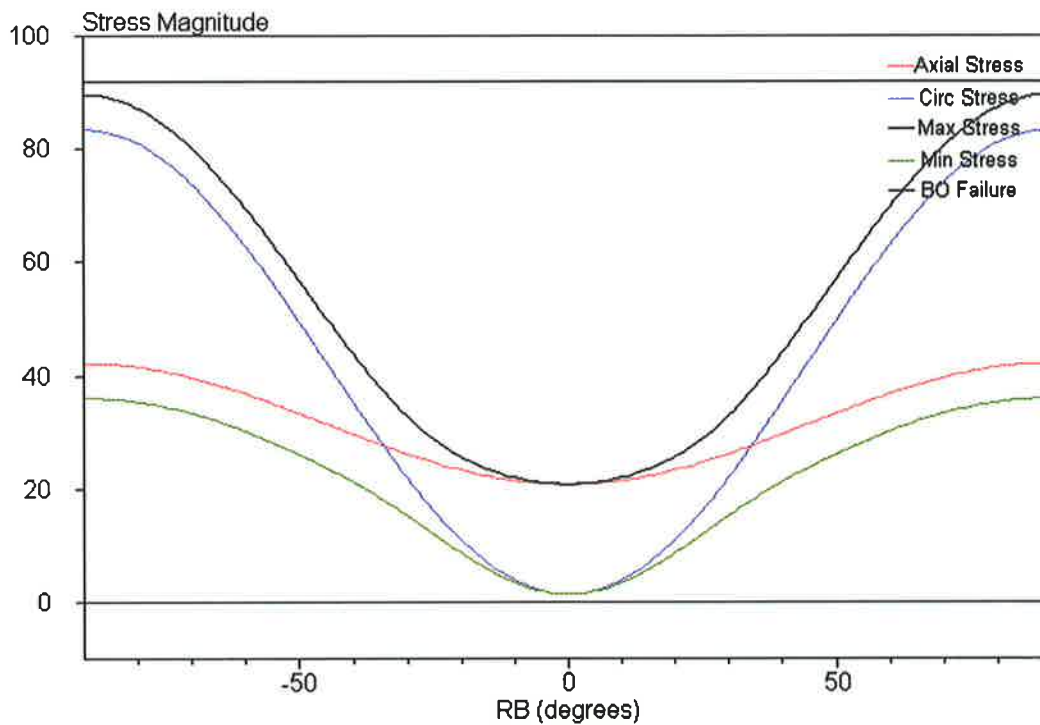
Figure 4.25. Wellbore stress diagram showing the axial stress (σ_{zz}), the circumferential stress ($\sigma_{\theta\theta}$), the maximum stress (σ_{tmax}), the minimum stress (σ_{tmin}) and breakout failure line as a function of relative bearing around the wellbore.
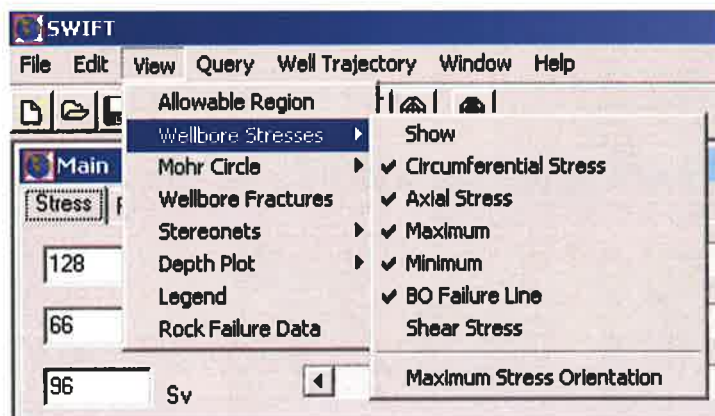
Figure 4.26. Wellbore Stresses submenu.

The **Wellbore Stresses** tab on the **Options** window is used to control the plot scaling and the size of the plot (Figure 4.27). If *Automatic Scale* is checked, the scaling is automatic, otherwise *Max* and *Min* must be set. The size of the plot can be altered using the *Horizontal* and *Vertical* edit boxes.
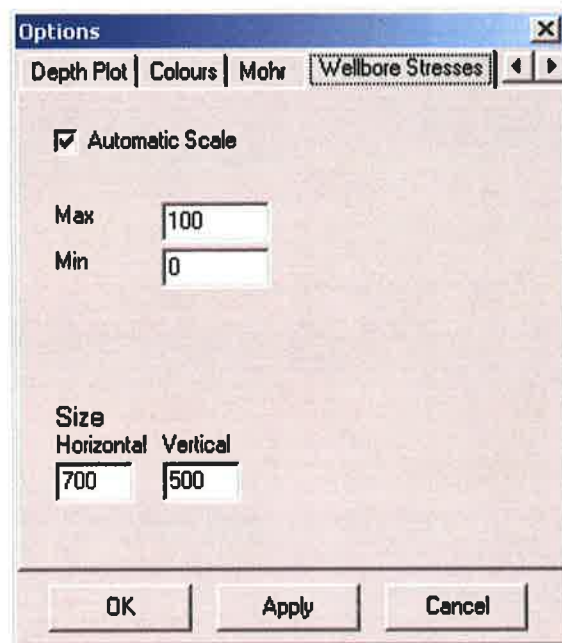
Figure 4.27. Wellbore Stresses tab in the options window.

The orientation of the maximum stress relative to the axial stress (Section 4.2; Equation 4.12) can be visualized with the **Maximum Stress Orientation** plot (Figure 4.28), displayed using the *Maximum Stress Orientation* menu item on the **Wellbore Stresses** submenu. This is useful for calculating the angle ω at which DITFs form on the wellbore wall, which is also the angle at which fractures induced by minifracture tests and XLOTs form at the wellbore wall, allowing investigation of potential fracture twisting problems (Chapters 5 and 6).

4.5.9. Structural Permeability Diagram

The **Structural Permeability** diagram (Figure 4.29) is used to investigate the likelihood of fractures/faults being reactivated within the in situ stress field. Structural permeability diagrams are contoured polar plots of poles to fracture planes coloured by the risk of reactivation. The risk of reactivation is measured in terms of the change in P_p (ΔP_p) required to reactivate a fracture/fault of given geometry (Figure 4.30). This analysis assumes no pore pressure stress coupling (sensu Hillis, 2000). The change in P_p required to reactivate a fracture of given geometry depends on the failure envelope and stresses acting on the fracture (Figure 4.30). The failure envelope is chosen using the *Rock Properties* tab (Figure 4.5) on the **Main** form, while the stresses acting on the fracture are chosen using the *Stress* tab (Figure 4.4)
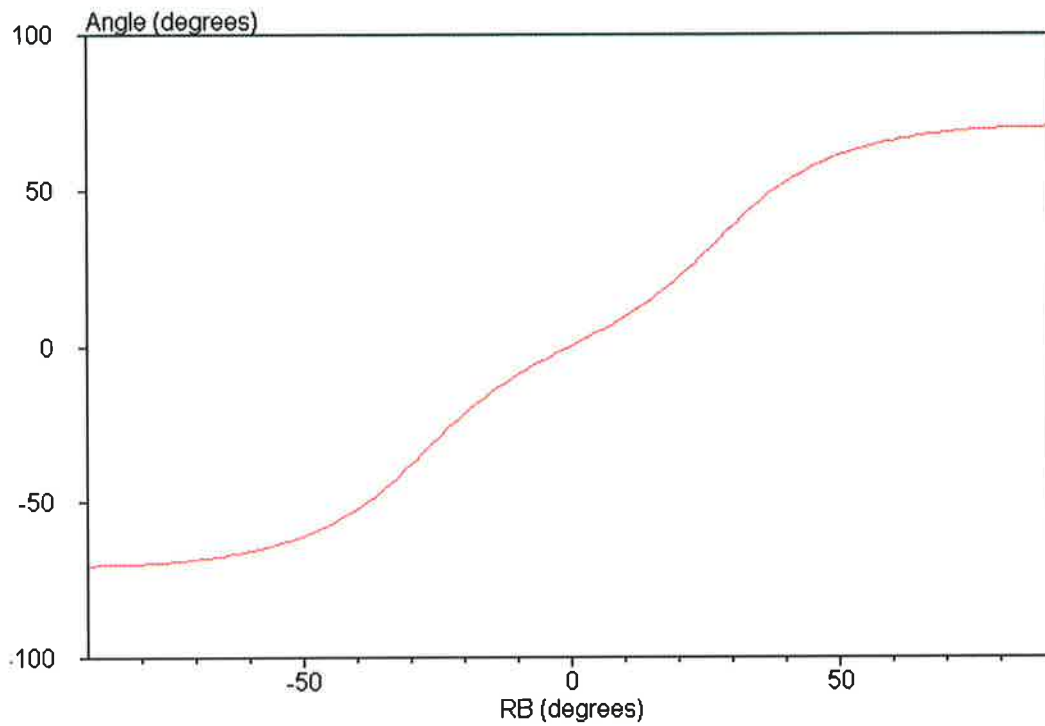
Figure 4.28. The angle between the maximum wellbore stress and the axial stress as a function of relative bearing around the wellbore.
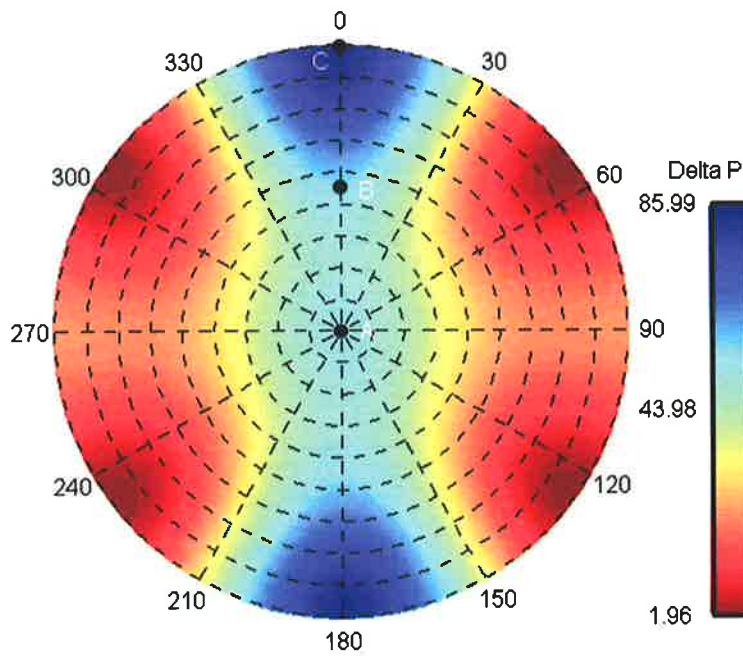
Figure 4.29 Structural Permiability Diagram: contoured polar diagram of poles to fracture planes coloured by the P_p change required to reactivate that fracture. The fracture/fault (A) is horizontal. The fracture/fault (B) is dipping 45° towards 180°N. The fracture/fault (C) is dipping 90° towards 180°N

on the **Main** form. The **Structural Permeability** diagram is displayed, once a failure envelope and stress tensor have been chosen, using either the *Risk of Reactivation* button ( ) or the *Show* menu item on the **StrucPerm** submenu (Figure 4.31). The display options for the stereonets are set using the *Stereonets* tab in the **Option** window (Figure 4.11;Section 4.5.3). Fractures, queried using the **Query** window, can be displayed on the **Structural Permeability** diagram if the *Fractures* menu item (Figure 4.31) is selected in the **StrucPerm** submenu prior to the **Structural Permeability** diagram being displayed. The application of structural permeability diagrams to fracture conductivity and fault seal risk in the Mereenie Field, Central Australia, the Otway Basin, southern Australia and the Pattani Basin, Gulf of Thailand are discussed in Chapters 6 - 8.
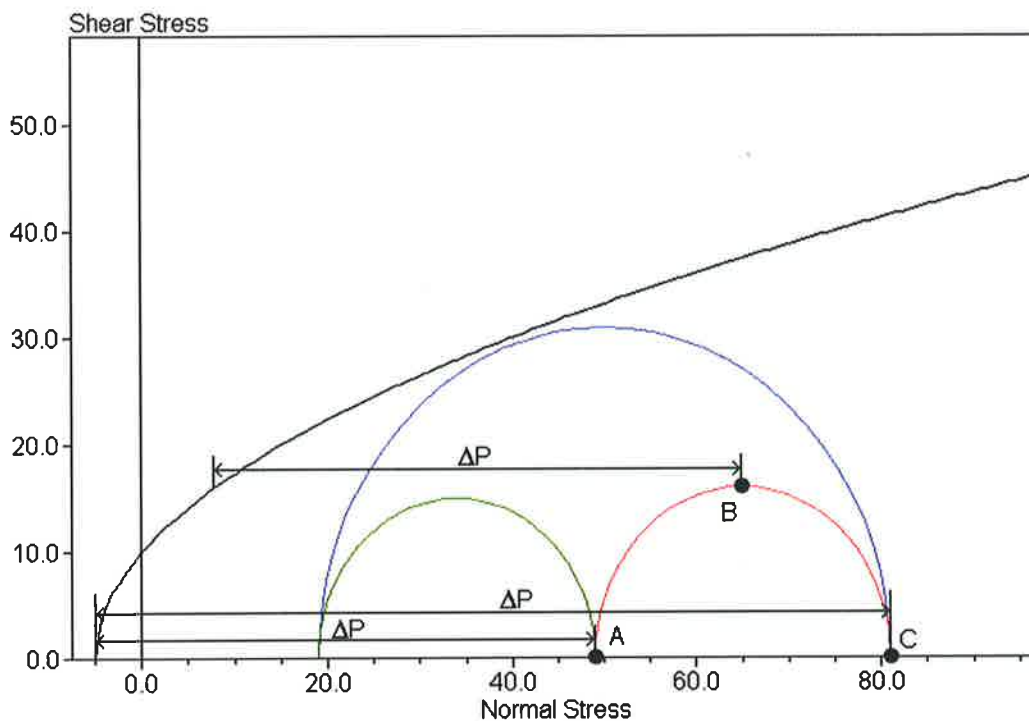
Figure 4.30. Mohr diagram with Griffith failure envelope showing three fractures (orientation of A, B and C as in Figure 4.29) and the change in P_p (ΔP) required to reactivate those fractures. From the stresses acting on each fracture it can be seen that the stress regime is strile-slip (A, the horizontal fracture is acted on by S_V' which is S_2 hence strike-slip stress regime) and that S_{Hmax} is oriented north-south (C, the vertical fractures striking east-west is acted on by S'_{Hmax}). The risk of reactivation for these fractures is shown in Figure 4.29.
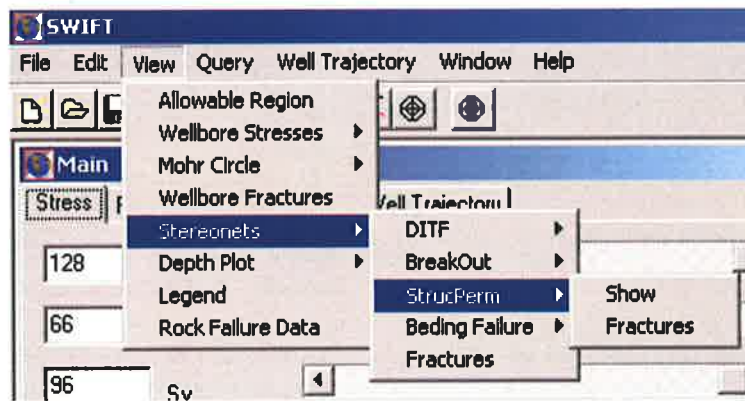
Figure 4.31. Strucperm submenu.

4.5.10. Breakout Diagrams

Breakout diagrams are used to examine the risk of wellbore breakout formation and the azimuth at which breakouts form. This is undertaken, respectively, using breakout **Risk** (Figure 4.32) and **Orientation** (Figure 4.33) plots. **Risk** and **Orientation** diagrams are displayed by checking the *Orientation* and/or *Risk* menu items and then selecting the *Show* menu item on the **Breakout** submenu on the **Stereonet** submenu (Figure 4.34). Risk can be calculated as rock strength, P_w difference, required mud weight or breakout width. Risk calculated in terms of rock strength provides the only method of breakout risk determination for which a rock strength estimate is not required. The rock strength at which breakout related failure initiates is calculated from the known stress tensor and wellbore trajectory, using Equations 3.20 and 4.1 - 4.11. If this rock strength is calculated for a single stress tensor and a range of azimuth and deviations, a risk diagram can be constructed (Figure 4.32). This type of risk diagram is calculated if *Use Co, Use ppg*, and *Breakout Width* are not selected on the *Stereonets* tab in the **Options** window (Figure 4.11).

Mud pressure difference and required mud weight can be used to measure breakout risk (Figure 4.35). This technique requires rock strength to be measured or estimated. The mud pressure is varied until the wellbore stresses exceed that required to cause failure (Figure 4.36). The change in pressure is recorded as either a P_w difference or a mud weight. If *Use ppg*, on the *Stereonet* tab in the **Option** window (Figure 4.11) is checked, the required mud weight is calculated. These types of risk diagram are calculated if *Use Co* on the *Stereonet* tab is checked.
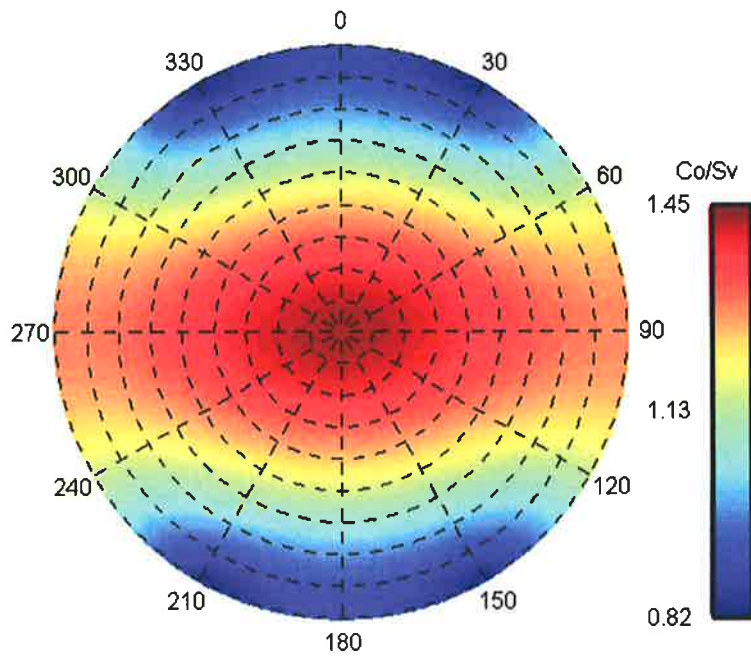
Figure 4.32. Breakout risk diagam: polar diagram of wellbore azimuth and deviation coloured by rock strength required to prevent breakout formation. Vertical well plots at centre of plot, horizontal well plots at the perimeter at the azimuth of its deviation.

Figure 4.33. Breakout orientation diagram: polar diagram of wellbore azimuths and deviations marked with the orientation of breakout formation using the along hole convention. For example, breakout form in the horizontal plane for a well deviated 90° towards 000°N, but at the top and bottom of the wellbore for a well deviated 90° towards 090°N. Well trajectories plot as in Figure 4.32.
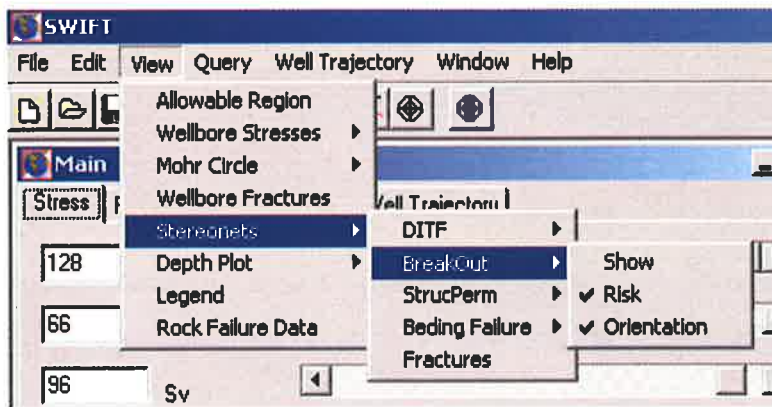
Figure 4.34. Breakout submenu.
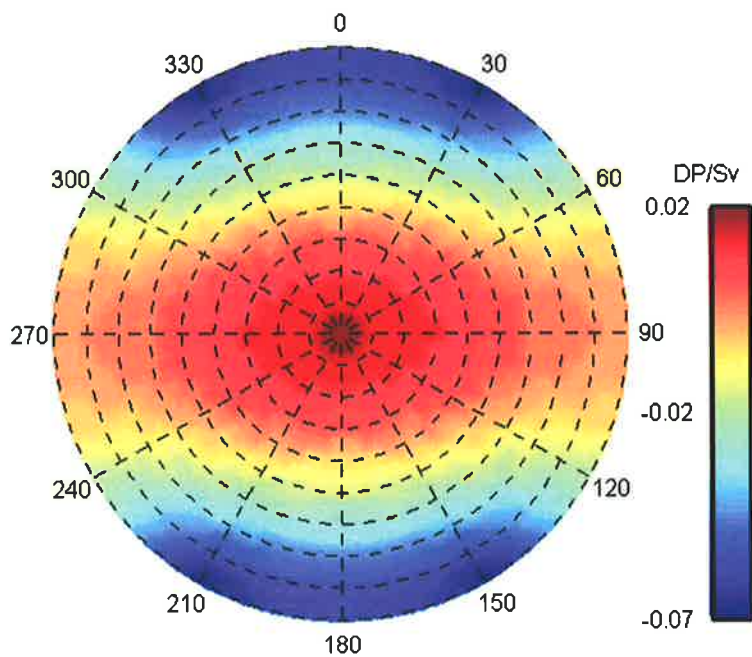
Figure 4.35. Breakout risk diagram: polar diagram of wellbore azimuth and deviation coloured by P_w change required to prevent breakout formation. Well trajectories plot as in Figure 4.32.

A)

B)
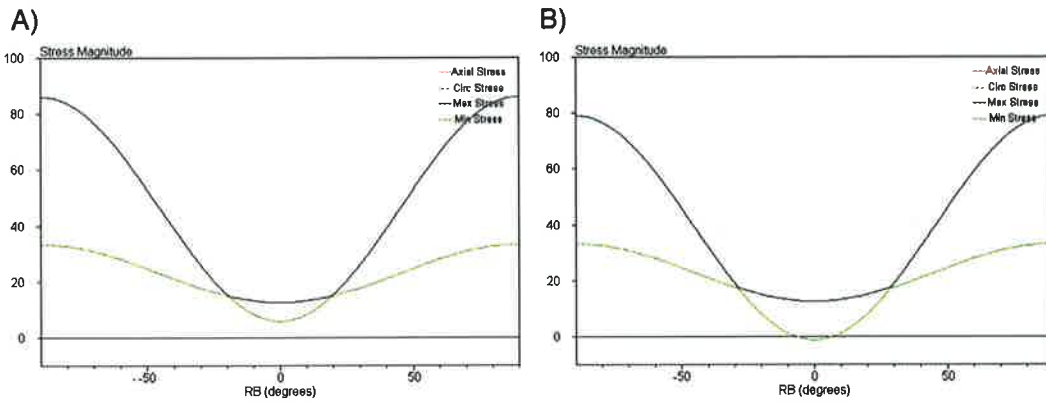
Figure 4.36. A) For a P$_w$ of 47 MPa no breakout is predicted. B) For a P$_w$ decrease of 1 MPa breakout initiation is predicted.

The final method for measuring breakout risk is breakout width (Figure 4.37). This technique also requires rock strength measurements or estimates. The breakout width is calculated, using a given stress tensor, well trajectory and rock strength, by measuring the width of the region for which the wellbore stress concentration exceeds that required to cause failure (Figure 4.38). This type of risk diagram is calculated if *Breakout Width* on the **Stereonet** tab is checked.
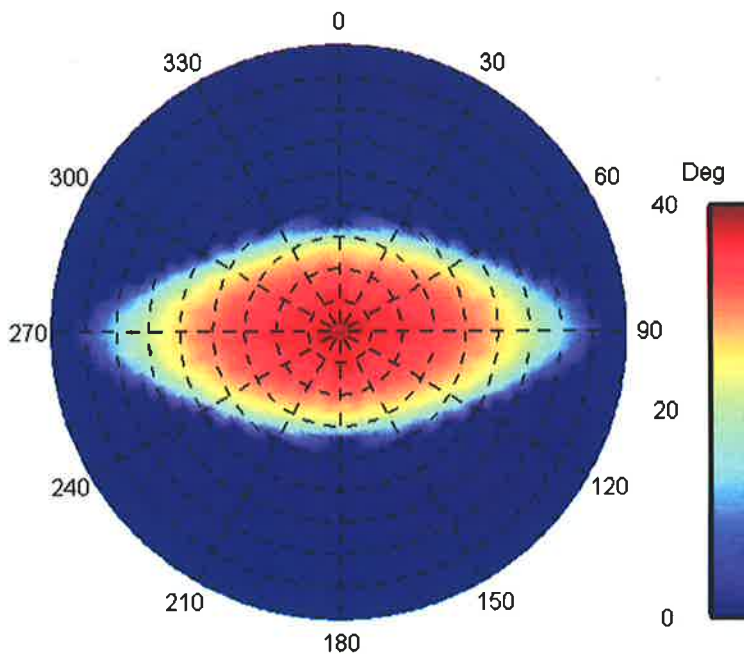
Figure 4.37. Breakout risk diagam: polar diagram of wellbore azimuth and deviation coloured by predicted breakout width. Well trajectories plot as in Figure 4.32.
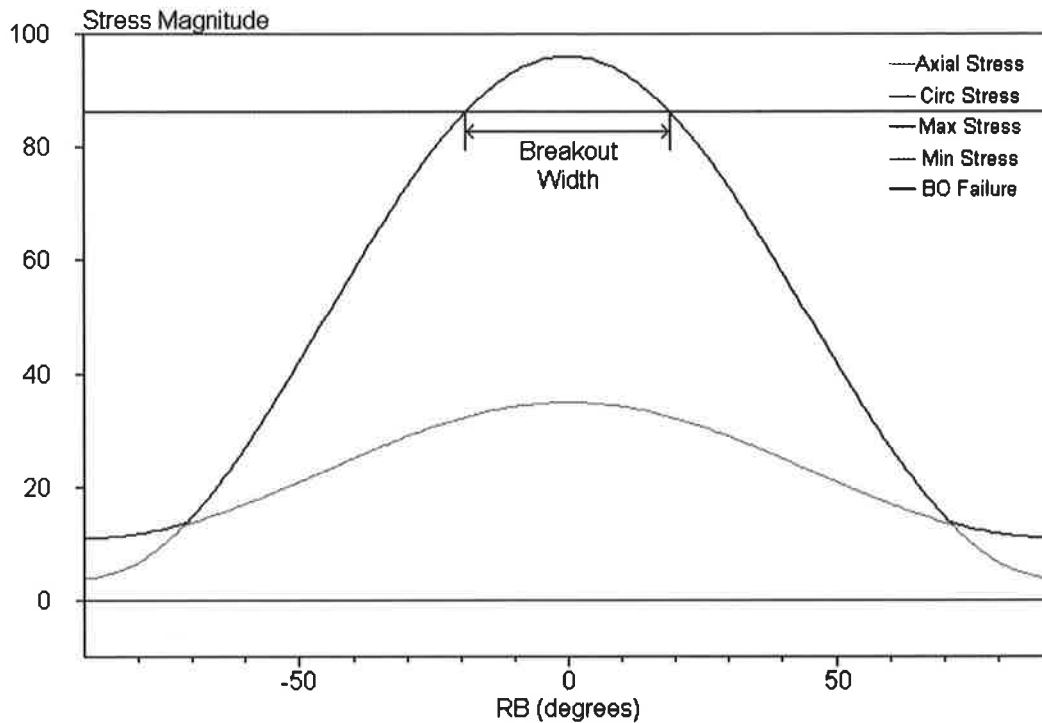
Figure 4.38. Wellbore stresses and breakout failure line showing the predicted width of breakout formation.

4.5.11. DITF Diagrams

DITF diagrams are used to examine the risk of DITF formation and the azimuth at which DITFs will form. This is undertaken, respectively, using DITF **Risk** (Figure 4.39) and **Orientation** (Figure 4.40) plots. **Risk** and **Orientation** diagrams are displayed by checking the *Orientation* and/or *Risk* menu items and then selecting the *Show* menu item on the **DITF** submenu on the **Stereonet** submenu (Figure 4.41).

Mud pressure difference or required mud weight can be used to measure DITF risk (Figure 4.39). This technique assumes no tensile rock strength (Section 3.3.4). The mud pressure is varied until the minimum wellbore stress becomes tensile (Figure 4.42). The change in pressure is recorded as either a P_w difference or a mud weight. If *Use ppg*, on the *Stereonet* tab in the **Option** window (Figure 4.11) is checked, the required mud weight is calculated.
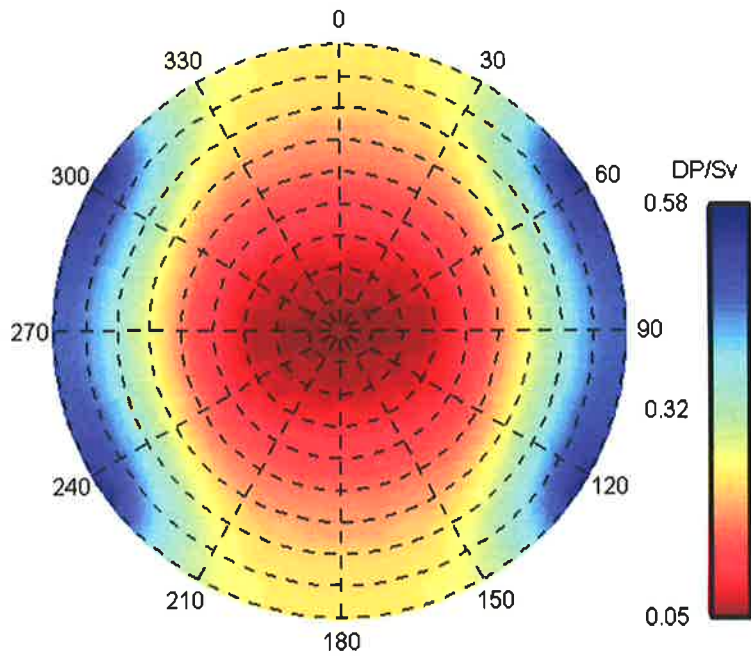
Figure 4.39. DITF risk diagram: polar diagram of wellbore azimuth and deviation coloured by P_w change required to prevent DITF formation. Well trajectories plot as in Figure 4.32.

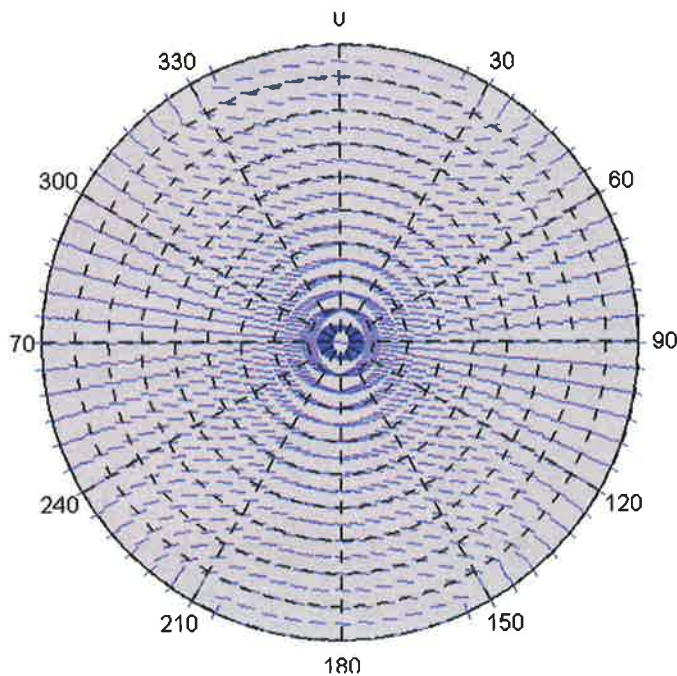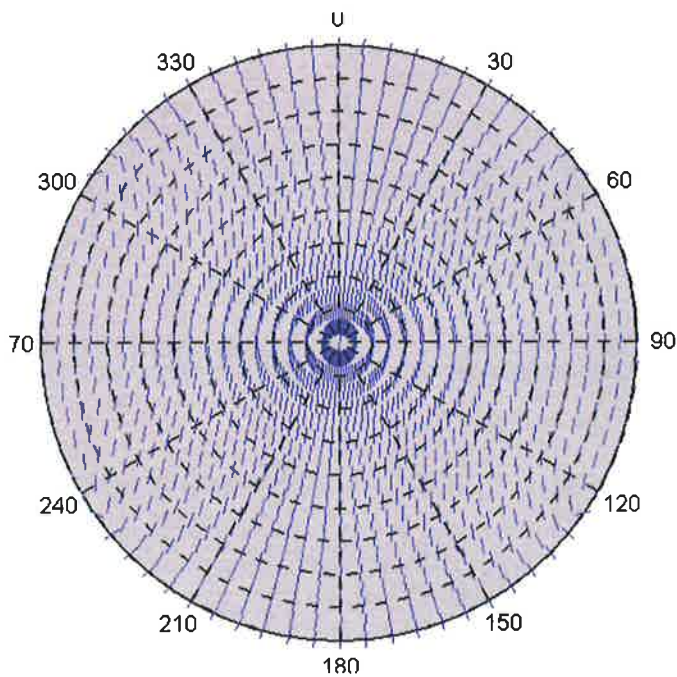**Figure 4.40. DITF orientation diagram: polar diagram of wellbore azimuths and deviations marked with the orientation of DITF formation using the along hole convention. For example DITFs form in the horizontal plane for a well deviated 90° towards 090°N, but at the top and bottom of the wellbore for a well deviated 90° towards 000°N. Well trajectories plot as in Figure 4.32.**
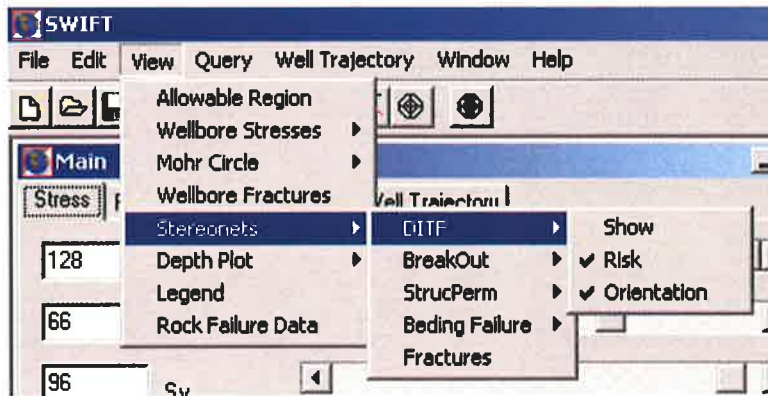
Figure 4.41. DITF submenu.
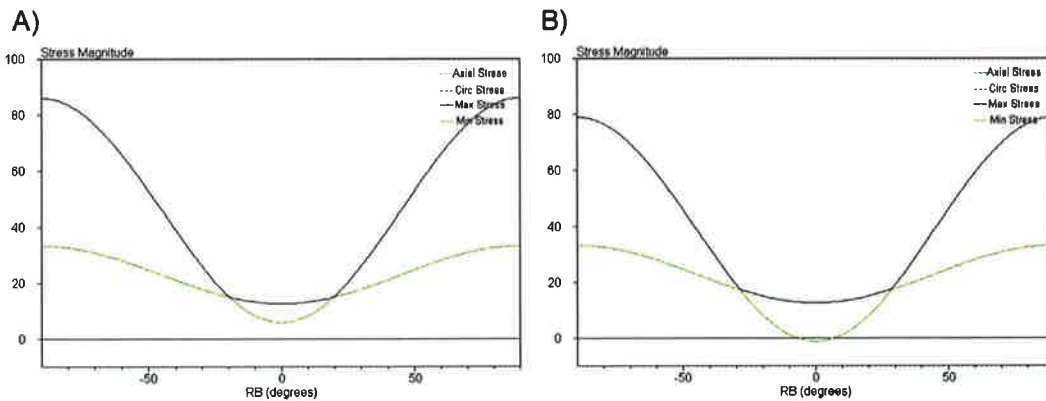
Figure 4.42. A) For a P$_w$ of 47 MPa no DITF is predicted. B) For a P$_w$ increase of 7 MPa DITF initiation is predicted.

4.5.12. Roses: Azimuthal Data Visualisation Component

A SWIFT component called Roses was created specifically for the purpose of generating rose diagrams, stereonets and azimuthal depth plots of directional information stored in the database (Figure 4.43). Roses is a separate program, using the same databases settings and code to access the database and is opened by selecting the Roses item beneath the SWIFT item in the windows start menu.

Breakouts, DITFs, fractures and LOTs can be queried and their dips and azimuths plotted on stereonets, rose diagrams and depth plots. The menu items are used to query data, copy, paste, and exit the program. The items in the **Roses** window are used to control the queried data that is displayed, and the manner in which it is displayed. The *Scale* section, in the top right corner, controls the scale of the rose diagrams. The *Show Frame*, *SHmax* and *Formation* checkboxes control whether

the frame on the rose diagram/stereonet is displayed, whether breakout rose diagrams are plotted in terms of breakout azimuths or inferred S_{Hmax} orientations and whether formation tops are displayed on the depth plot respectively. The Azimuth and Dip radio buttons control whether the x-axis on the depth plot represents fracture strike or fracture dip respectively. The *Bin Width, Azi int* and *Radial int* textboxes control the angular width of the bins used in the rose diagrams, the azimuthal interval of the plot frame and the radial interval of the plot frame respectively. The *Weighting* section allows the choice of breakout rose diagrams to be un-weighted, length-weighted or eccentricity-weighted. The *Selection* section controls what is displayed on the plots. The *Depth Plot* section allows the scale of the depth ploy to be chosen. The *Statistics* section displays the circular statistics of the displayed data.
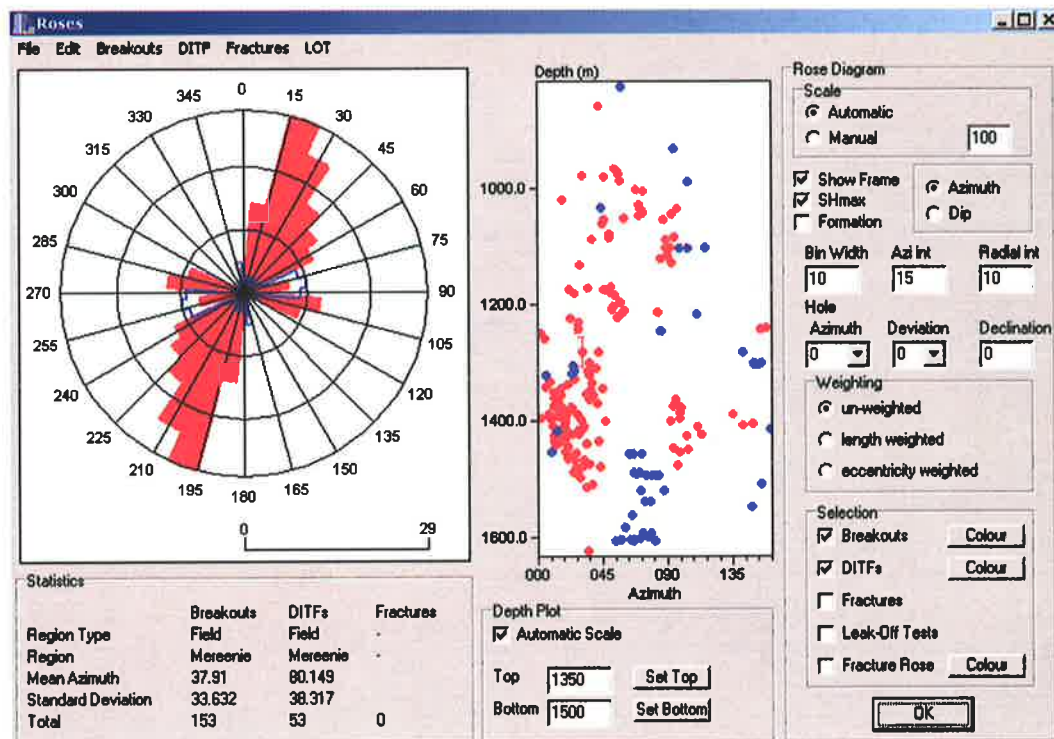
Figure 4.43. Roses component of SWIFT.

4.6. Conclusion

The SWIFT software described in this chapter is applied, in the following chapters, to four case studies, investigating wellbore stability, fracture stimulation, natural fracture conductivity and risk of fault reactivation, in various Australian and Asian Basins.

5. Swan Lake Field, South Australia: Fracture Stimulation and Under-balanced Drilling

5.1. The Problem

The Swan Lake Field, Nappamerri Trough, Cooper Basin, South Australia (Figure 5.1) contains low permeability (< 1 mD) gas reservoirs in the Permian Patchawarra Formation (the key reservoir interval; Figure 5.2). Low reservoir permeability severely reduces gas deliverability. Fracture stimulation, the targeting of natural fractures and under-balanced drilling have all been proposed to improve gas deliverability in the area. Fracture stimulation improves gas deliverability by artificially creating a large fracture, thereby providing a conduit through which gas can flow to the wellbore (Fjaer et al., 1992). Similarly, natural fractures provide a conduit for gas to flow into the wellbore, if open, hydraulically-conductive natural fractures are intersected by the wellbore (Nelson, 1985). Under-balanced drilling may
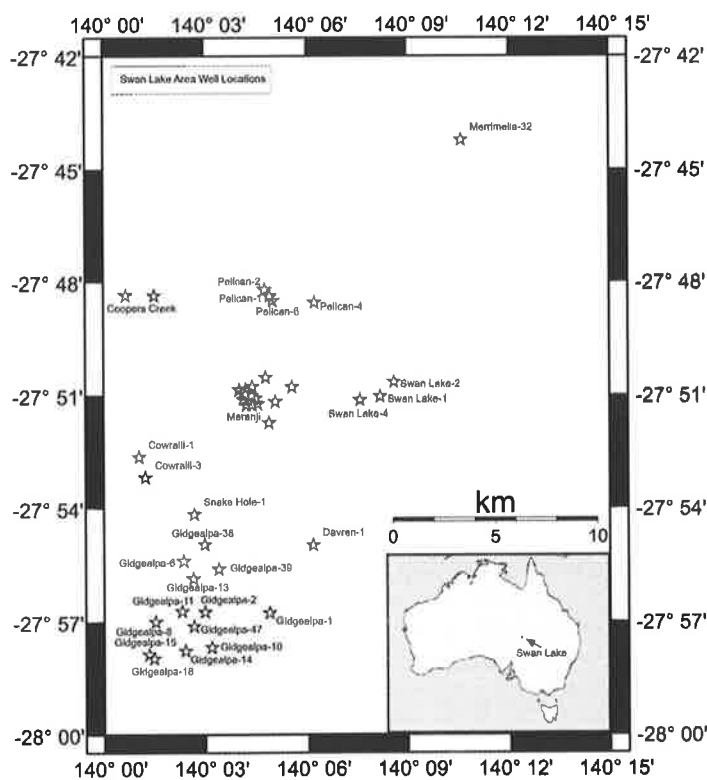
Figure 5.1. Swan Lake area location map.

reduce near wellbore formation damage, resulting in improved near wellbore permeability and hence improved gas deliverability (Bennion, 1996). The feasibility of fracture stimulation, targeting open natural fractures, and under-balanced drilling are all critically dependent on the in situ stress tensor.
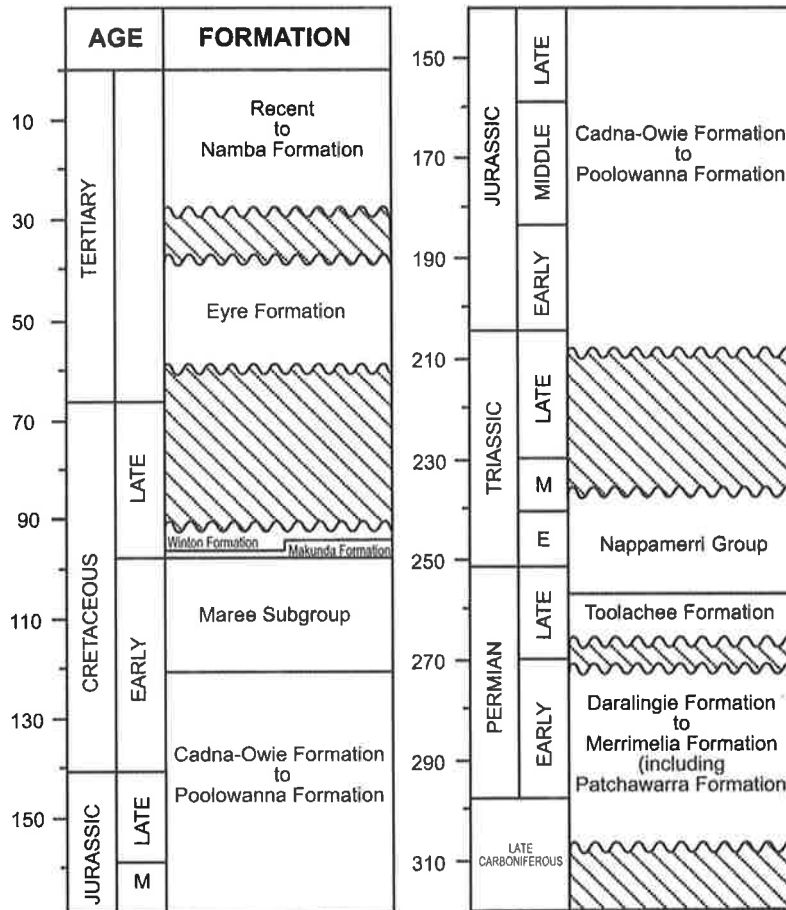
Figure 5.2. Cooper Basin stratigraphy (after van Ruth and Hillis, 2000).

The in situ stress tensor controls the geometry of a fracture induced during fracture stimulation (Hubbert and Willis, 1957). Poor fracture geometry, such as fractures that are non-axial to the wellbore or twist when propagating away from the wellbore, can result from a non-optimal stress tensor and/or wellbore trajectory (Shlyapobersky and Chudnovsky, 1994). Poor fracture geometry can preclude a successful fracture treatment, for example by preventing the placement of proppant within the fracture, resulting in little or no improvement in gas deliverability (Finch et al., 1997). Fracture stimulation has been conducted in the Swan Lake Field. However, problems

have been encountered in hydraulic fracture stimulation, often resulting in little or no improvement in gas deliverability.

Interactions between drilling muds and the formation can ëdamageí its permeability (Porter, 1989). If mud weight is minimised then such interactions, and possible formation damage, may be minimised. However, the low mud weights used in under-balanced drilling can significantly increase the risk of wellbore instability. Wellbore stability, like hydraulic fracture geometry, is strongly influenced by the in situ stress tensor. Hence under-balanced drilling needs to be planned with knowledge of the in situ stress tensor.

This chapter determines the in situ stress tensor in the Swan Lake Field by combining the available data with routine and non-routine stress determination techniques. Knowledge of the in situ stress tensor is applied to fracture stimulation and under-balanced drilling for improved gas deliverability in the field. Application of the in situ stress tensor to the intersection of open natural fractures, although relevant to the Swan Lake Field, is not discussed in this Chapter, but rather in the case study on the Mereenie Field, central Australia (Chapter 6).

5.2. Routine Stress Determination Techniques

5.2.1. Vertical Stress

Hillis (1996) calculated the vertical stress in the Swan Lake Field, from data acquired in Swan Lake-1, using the techniques described in Section 3.2 (Figure 5.3). The vertical stress in the Swan Lake Field is closely approximated by the power law function:

$$S_v = 0.005497 \times z^{1.1742} \qquad \text{Eq. 5.1,}$$

where S_v is in MPa and z is depth in m.

5.2.2. Horizontal Stress Orientations

A single FMS image log obtained in Swan Lake-4 is the only available information with which to constrain stress orientations within the Swan Lake Field. A declination (8°E) corrected S_{Hmax} orientation of 124°N was determined from observation of 23
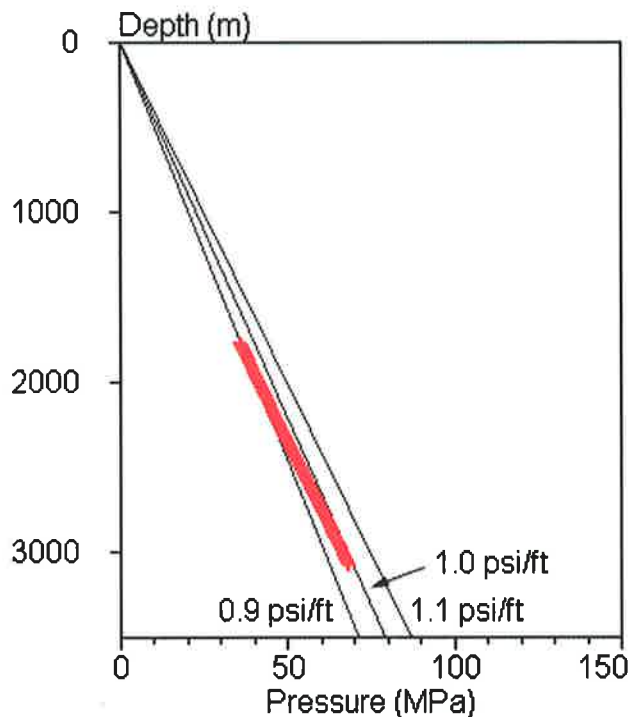
Figure 5.3. Depth plot showing S_v calculated at Swan Lake-1 (Hillis, 1996).

wellbore breakouts at Swan Lake-4 using the techniques described in Section 3.4 (Figure 5.4; Mildren, 2001). This orientation is significantly different to stress orientations observed in wells both to the north and south of the Swan Lake Field which exhibit an S_{Hmax} orientation of approximately 100°N, but the 124°N orientation is highly consistent within Swan Lake-4 (Figure 5.4).

5.2.3. Minimum Horizontal Stress Magnitudes

The minimum horizontal stress magnitude was determined from six LOTs and nine minifracture test closure pressures from wells in and adjacent to the Swan Lake Field (Figure 5.5; Appendix B; See Section 3.5 for a discussion of the relationship between these tests and S_{hmin}).

The minimum horizontal stress magnitude gradient increases with depth from 15 MPa/km at 600 m to 22.2 MPa/km at 3200 m, reflecting the change in S_v with depth (Figure 5.5). This suggests that either S_{hmin} is indeed equal to S_v or that S_{hmin} is greater than S_v and the LOPs and closure pressures are from transverse (horizontal) fractures, and consequently measure S_v. This value of S_{hmin} is revisited in Section 5.3.1.
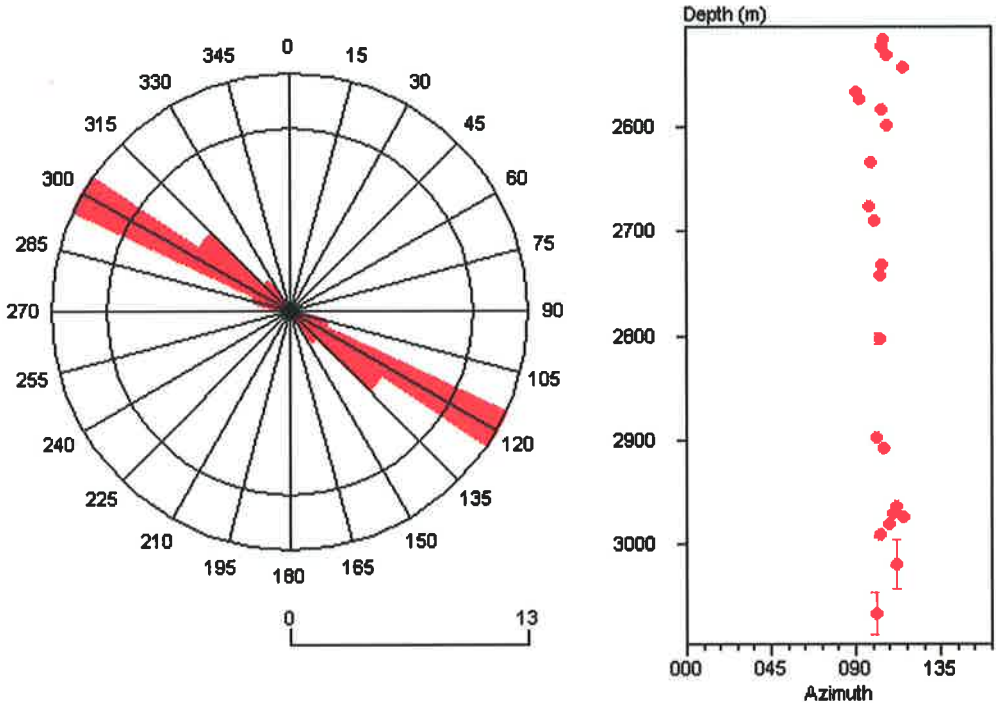
Figure 5.4. Un-weighted rose diagram of breakout inferred S_{Hmax} orientation and plot of breakout inferred S_{Hmax} orientation versus depth, from Swan Lake-4 image log (Mildren, 2001).
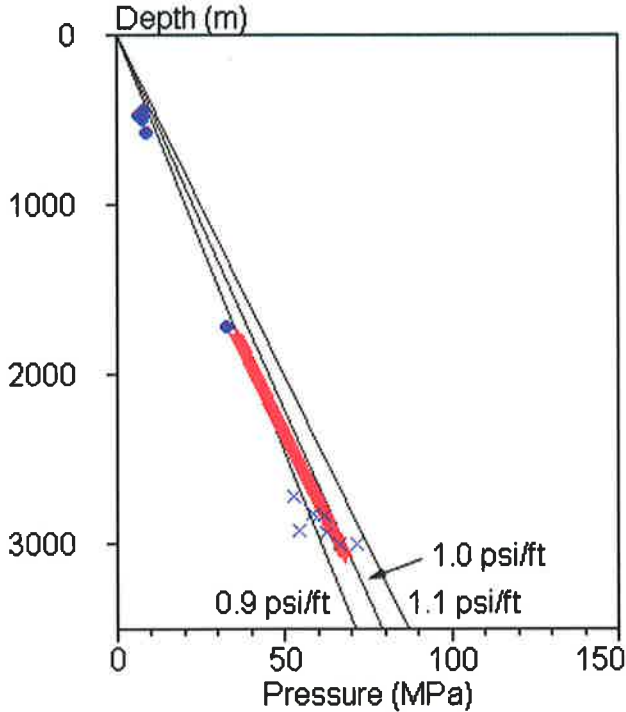
Figure 5.5. Depth plot showing six LOTs (•) and nine minifracture test P_c (✕) from wells in and adjacent to the Swan Lake Field and S_v (+) calculated at Swan Lake-1.

5.2.4. Pore Pressure

Pore pressures were determined from 56 WFIT measurements and 76 DST measurements made in wells adjacent to the Swan Lake Field, and mud weights in 27 wells in and adjacent to the Swan Lake Field (Figure 5.6). Section 3.7 summarises how these tests yield P_p. The pore pressure gradient from the WFITs and DSTs is 10.3 MPa/km, and 10.9 MPa/km from mud weights. The difference between the P_p gradient determined from mud weights and that determined from WFITs and DSTs is the result of mud weights typically being slightly over-balanced (Section 3.7). Consequently the P_p gradient of 10.3 MPa/km determined from WFITs and DSTs is used. The sequence is normally pressured.
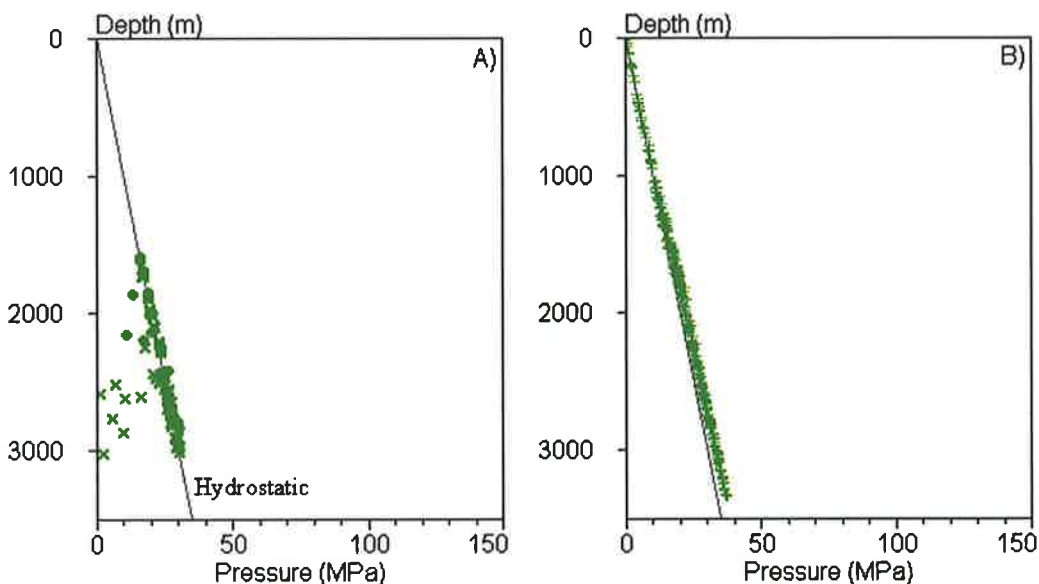
Figure 5.6. (A) Pore pressure from 56 WFITs (•) and 76 DSTs (✕) run in wells adjacent to the Swan Lake Field and (B) mud pressure (+) from 27 wells in and adjacent to the Swan Lake Field.

5.3. Non-Routine Stress Determination Techniques

The maximum horizontal stress is, as is often the case, the most difficult aspect of the in situ stress tensor to constrain in the Swan Lake Field. Maximum horizontal stress magnitudes can be determined using minifracture tests and/or the observation of wellbore failure (Section 3.6) or constrained using frictional limits to stress (Section 2.5). The minifracture tests conducted in the Swan Lake Field were conducted in cased and perforated holes. No fracture reopening pressure can be determined where minifracture tests are conducted in cased holes, and consequently no estimate of S_{Hmax}

can be made (Section 3.6.1). An image log was run in Swan Lake-4, in which 23 wellbore breakouts were observed. Maximum horizontal stress magnitudes can be determined from the occurrence of wellbore breakouts, if the compressive rock strength is known (Section 3.6.2). However, information on compressive rock strengths are not available for the Swan Lake Field. No conventional, vertical DITFs, such as can also be used to constrain S_{Hmax} (Section 3.6.3), were observed. However, unusual horizontal fractures were observed on the Swan Lake-4 image log. These crosscut bedding and are electrically conductive and hence were inferred to be open (Figures 5.7 and 5.8). These fractures are interpreted to be drilling-related, appearing similar to vertical DITFs in all aspects except their orientation. As discussed in this section, the interpretation of horizontal DITFs places close constraints on the stress regime of the Swan Lake Field and on the magnitude of S_{Hmax} in particular.

5.3.1. Horizontal DITFs

The possibility exists that the observed fractures are pre-existing natural fractures and not drilling-induced. However the wellbore stress state under which an existing horizontal fracture opens or a new drilling related horizontal fracture is created are the same, neglecting the tensile strength of unfractured rock which is likely to be negligible due to bedding related weakness. A horizontal DITF (HDITF) may only be initiated in a vertical wellbore if the axial wellbore stress is less than or equal to zero ($\sigma_{zz} \leq 0$) and the axial wellbore stress is less than or equal to the circumferential stress ($\sigma_{zz} \leq \sigma_{\theta\theta}$; Figure 5.9). The former condition permits horizontal fractures to develop and the latter is required otherwise conventional vertical DITFs would form.

The circumferential and axial stresses around a vertical wellbore can be written:

$$\sigma_{\theta\theta} = S_{Hmax} + S_{hmin} \text{ ñ } 2(S_{Hmax} - S_{hmin})\cos 2\theta - P_W - P_P \qquad \text{Eq. 3.9 and,}$$

$$\sigma_{zz} = S_V - 2\nu(S_{Hmax} - S_{hmin})\cos 2\theta - P_P \qquad \text{Eq. 3.10.}$$

The minimum values of the circumferential stress around the wellbore occur for the same value of θ as the minimum axial stress (i.e. $\theta = 0$). Consequently, the minimum of the circumferential and axial stresses can be written:

$$\sigma_{\theta\theta min} = 3S_{hmin} \text{ ñ } S_{Hmax} - P_W - P_P \qquad \text{Eq. 3.15 and,}$$
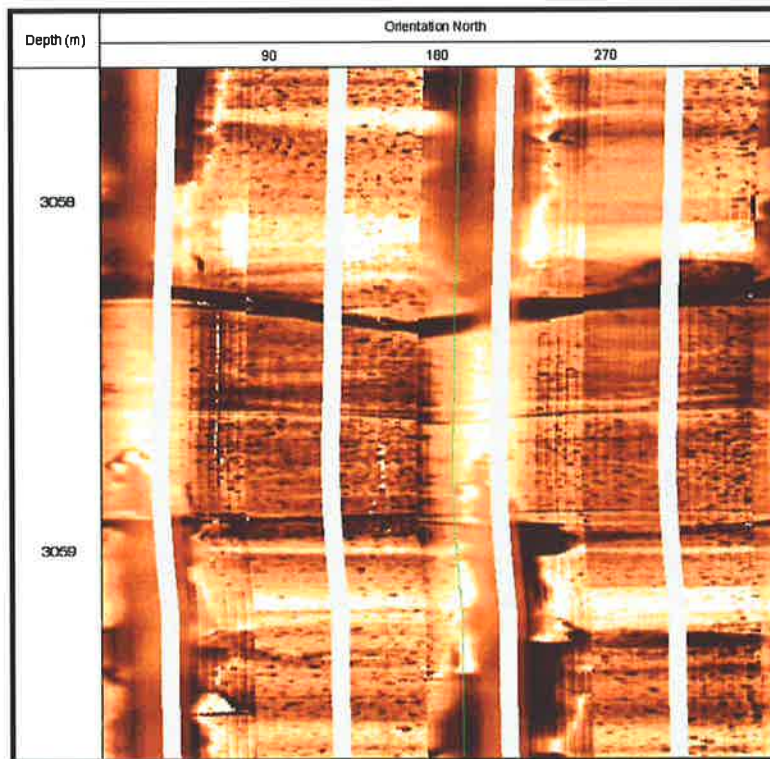
Figure 5.7. FMI image showing horizontal non-planar fracture cross cutting bedding. This is interpreted as HDITF.
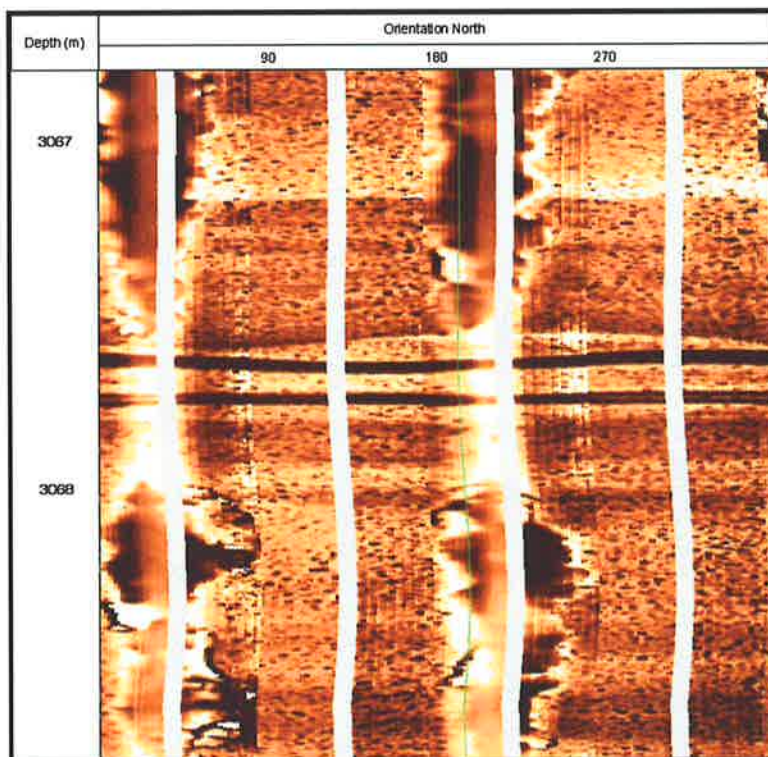
Figure 5.8. FMI image showing horizontal fractures cross cutting bedding. These are interpreted as HDITFs.

$$\sigma_{zzmin} = S_V - 2v(S_{Hmax} - S_{hmin}) - P_P \qquad\qquad \text{Eq. 5.2.}$$

Horizontal DITFs can occur if $\sigma_{zzmin} \leq 0$ and $\sigma_{zzmin} \leq \sigma_{\theta\theta min}$, or in terms of Equations 3.15 and 5.2:

$$S_V - 2v(S_{Hmax} - S_{hmin}) - P_P \leq 0 \qquad\qquad \text{Eq. 5.3 and,}$$

$$S_V - 2v(S_{Hmax} - S_{hmin}) - P_P \leq 3S_{hmin} \text{ ñ } S_{Hmax} - P_W - P_P \qquad \text{Eq. 5.4.}$$

Equation 5.4 reduces to:

$$S_V + S_{hmin}(2v - 3) + S_{Hmax}(1-2v) + P_W \leq 0 \qquad\qquad \text{Eq. 5.5.}$$

Equations 5.3 and 5.5 can be plotted as lines on the allowable region diagram (Section 4.5.4; Figure 5.10), facilitating determination of the stress region in which horizontal DITFs may form.
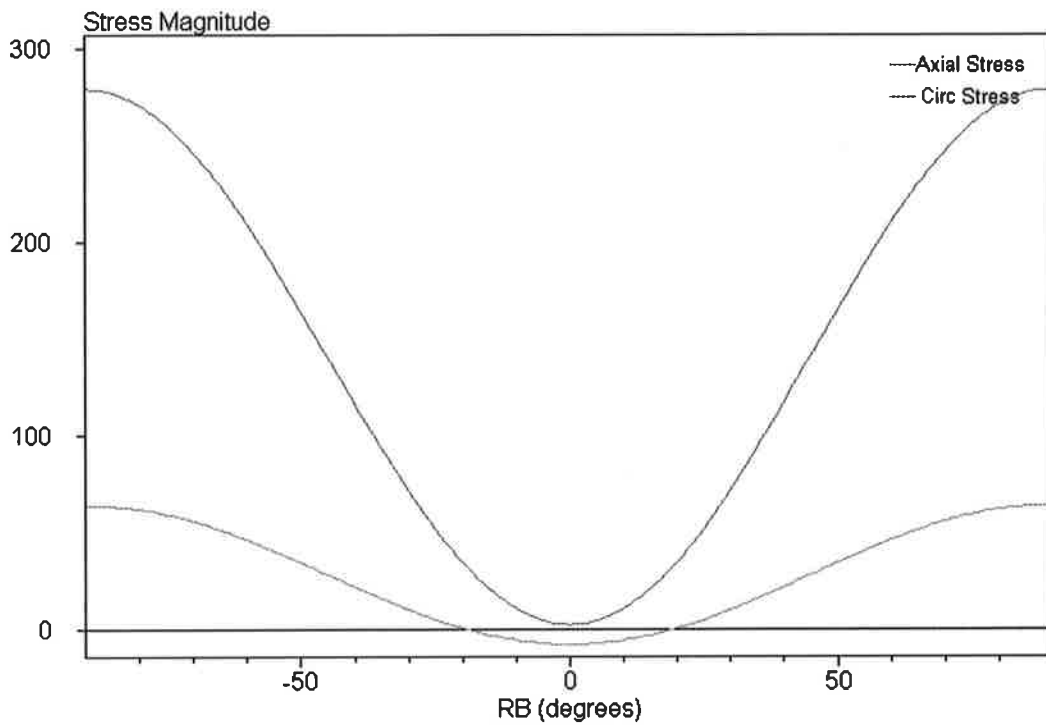
Figure 5.9. Wellbore stresses diagram showing the axial stress less than zero and less than the circumferential stress.
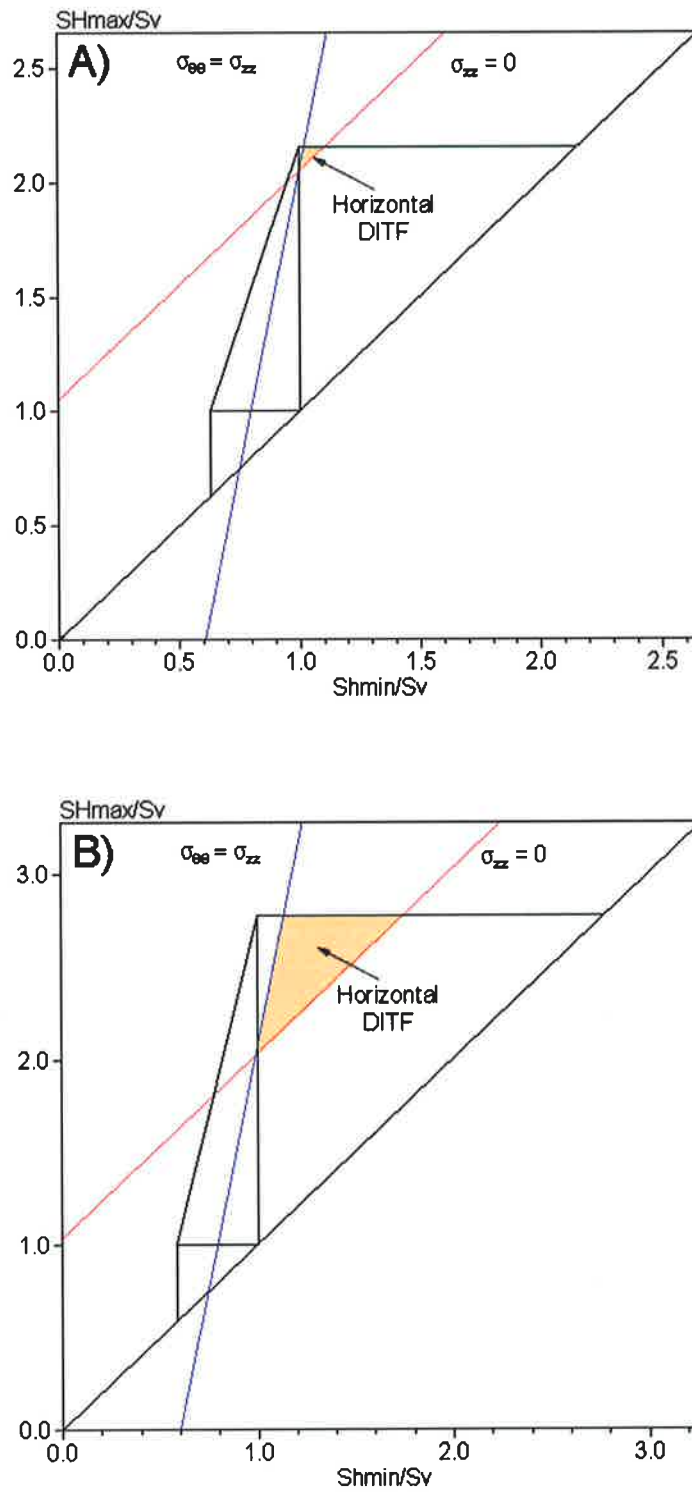
Figure 5.10. Allowable region diagrams with line representing axial stress equal to zero (–) and line representing the axial stress equal to the circumferential stress (–). The region in which horizontal DITFs may form is shaded. Allowable region calculated for $\mu = 0.6$ (A) and 0.8 (B), $\nu = 0.26$ and with P_p, P_w and S_v equivalent to that found in the Swan Lake Field at 3200 m.

The requirement that $\sigma_{zzmin} \leq 0$ and $\sigma_{zzmin} \leq \sigma_{\theta\theta min}$ constrains a restricted area on the allowable region diagram (Figure 5.10). The observation of HDITFs thus requires that the stress regime range from the boundary of strike-slip and thrust faulting to thrust faulting (Figure 5.10). The above analysis not only predicts the formation of HDITFs, but suggests that they can develop only in a restricted set of stress states and are diagnostic of the relative in situ stress magnitudes ($S_v \leq S_{hmin} < S_{Hmax}$). Furthermore the high value of S_{hmin} required for HDITFs to develop (close to or greater than S_v) is consistent with independent estimates of S_{hmin} from the LOTs and minifracture tests (Figure 5.5).

5.4. The Swan Lake Field In Situ Stress Tensor

The observation of HDITFs combined with S_{hmin} from LOTs and minifracture tests, S_v from the Swan Lake-1 density log and P_p from WFITs and DSTs (Sections 5.2 and 5.3) indicate the stress regime at the depth of interest in the Swan Lake Field is as shown in Table 5.1. The values in Table 5.1 are used in the following sections in considering the implications of the in situ stress tensor for hydraulic fracture stimulation and under-balanced drilling.

5.5. Implications

5.5.1. Fracture Stimulation

Fracture stimulation involves creating a large artificial fracture by increasing the fluid pressure in the wellbore until the tensile strength of the reservoir rocks and in situ stresses are overcome (Hubbert and Willis, 1957). The induced fracture propagates away from the wellbore, opening against the minimum principal stress (Hubbert and Willis, 1957). The induced fracture is vertical and propagates in the S_{Hmax} direction, if S_{hmin} is the minimum principal stress, but is horizontal if S_v is the minimum principal stress.

Hydraulic fractures may form vertically (axial to vertical wellbores) even if S_v is the minimum far field principal stress, because of the minimization of circumferential stresses at the azimuth of S_{Hmax}. In such cases the fracture forms vertically at the wellbore wall, but as it propagates into the far field, away from the influence of the

wellbore on the in situ stress tensor, it twists to horizontal (Figure 5.11). Such fracture tortuosity can severely impede fluid flow along the fracture and can indeed prevent the placement of proppant in the fracture.

Stress Component	Value
S_{Hmax} Orientation	124°N
S_v	22.2 MPa/km
S_{hmin}	22.2 MPa/km
P_p	10.3 MPa/km
S_{Hmax}	45.5 MPa/km

Table 5.1. Swan Lake Field in situ stress tensor at 3200 m.

Several fracture stimulations have been undertaken in the Swan Lake Field. High treatment pressures, an inability to place the designed amount of proppant and little or no increase in gas deliverability have resulted from these fracture stimulations.

As discussed above, the in situ stress tensor at Swan Lake is on the boundary between strike-slip and normal (i.e. $S_v \approx S_{hmin}$), and may result in the formation of HDITFs (Section 5.3.1) at the wellbore wall, if the well is approximately in balance (Figure 5.12). As the wellbore pressure increases above P_p, vertical fractures are more likely to form at the wellbore wall (Figure 5.13). Consequently, horizontal and or vertical fractures may form at the wellbore wall. As these fractures propagate away from the wellbore they become subject to the far field stresses, under which they may rotate to vertical or horizontal (as $S_v \approx S_{hmin}$), resulting in complex fracture geometry. Furthermore it is tentatively suggested that the lack of difference between S_v and S_{hmin} leads to a lack of strong stress-based directionality in the induced fracturesí, leading to variable geometry along the fracture and a strong influence on the fracture orientation from pre-existing rock fabric. The difficulties experienced conducting fracture stimulations in the Swan Lake Field are consistent with complex fracture geometries and with the observed in situ stress tensor.
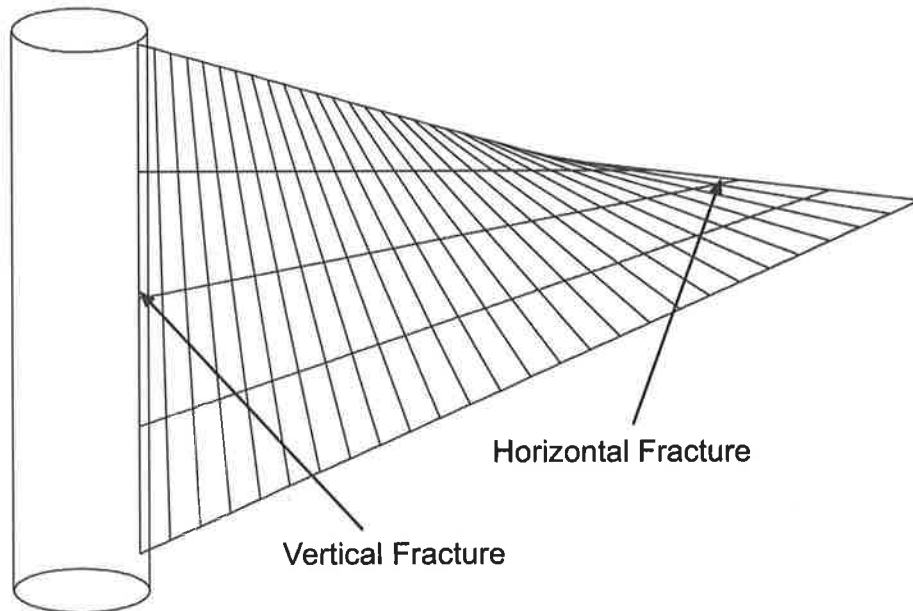
Figure 5.11. Fracture twisting from vertical at the wellbore wall to horizontal as it propagates into the far field in situ stress tensor.
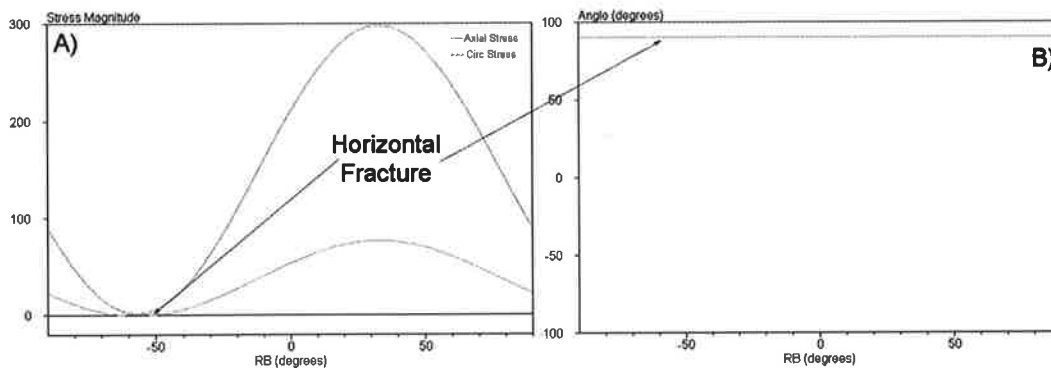
Figure 5.12. Wellbore stresses for a vertical in balance well in the Swan Lake Field. A) Wellbore stresses, with minimum axial stress < 0 and minimum axial stress < minimum circumferential stress, potentially resulting in horizontal DITF. B) Orientation of maximum wellbore stress (90° to the minimum stress), indicating fracture formation to be at 90° to the wellbore axis (i.e. horizontal).
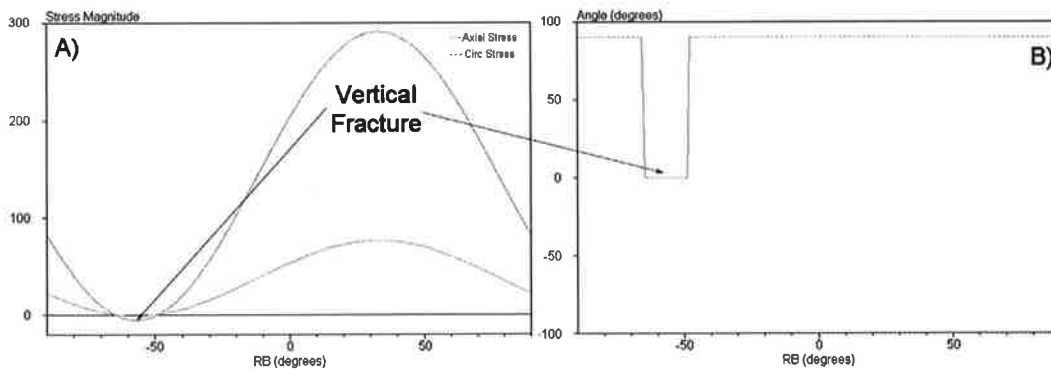
Figure 5.13. Wellbore stresses for a vertical slightly over-balanced well in the Swan Lake Field. A) Wellbore stresses, with minimum circumferential stress < 0 and minimum axial stress > minimum circumferential stress, resulting in vertical fractures. B) Orientation of maximum wellbore stress (90° to the minimum stress), indicating fracture formation to be at 0° to the wellbore axis (i.e. vertical).

One solution to stress-based fracture stimulation problems at Swan Lake that has been canvassed is to stimulate from horizontal wells deviated in the S_{hmin} direction. Fractures in such wells would form horizontally and axial to the wellbore. However this approach is not recommended.

1. Given that $S_v \approx S_{hmin}$ fracture tortuosity problems may again occur with fractures forming horizontally at the wellbore wall but twisting to vertical and striking in the S_{Hmax} direction in the far field.

2. Even if a horizontal fracture is successfully placed from a horizontal well, such may not significantly increase gas deliverability because horizontal permeability is generally greater than vertical permeability (Piplapure, 1969) and further improvement in horizontal permeability may not yield a large gain in deliverability.

The above concerns, combined with the additional cost of stimulating a horizontal well, have led to this strategy not being applied.

The author believes that any hydraulic fracture stimulation is likely to be problematic where $S_3 \approx S_2$. Fracture tortuosity, strongly influenced by pre-existing rock fabric, is (almost) inevitable in such an environment. There is no wellbore trajectory that can be fractured from to avoid such problems where $S_3 \approx S_2$. This recognition, and the phenomena of pore pressure/stress coupling, has led to an alternative strategy to improve the success of fracture stimulation in such environments. Producing from a

well depletes the reservoir pressure, which in turn reduces S_{hmin}. This phenomenon is known as pore pressure/stress coupling and has been widely described, for example in the Ekofisk Field North Sea (Teufel et al., 1991; see also summaries in Addis, 1997 and Hillis, 2000). The vertical stress is unaffected by such depletion, hence production prior to fracture stimulation presents the opportunity to reduce S_{hmin} with respect to S_v and create a difference between S_3 and S_2. Such has been adopted for fracture stimulation in high S_{hmin} areas of the Cooper Basin and has improved the success of treatments in such areas (Chipperfield, pers. comm.). Improvement in the effectiveness of fracture stimulations, in high stress regions, due to depletion has also been observed in the Mereenie Field (Chapter 6).

Summary
The in situ stress tensor in the Swan Lake Field is unsuitable for fracture stimulations to improve gas deliverability. Reservoir depletion prior to fracture stimulation may reduce the problems encountered. However, other solutions such as under-balanced drilling and/or targeting open natural fractures may prove to be more cost effective methods of improving gas deliverability.

5.5.2. Wellbore Stability for Under-Balanced Drilling
Drilling fluids can negatively impact on near wellbore permeability (Porter, 1989), especially in the already low permeability reservoirs of the Swan Lake Field. Consequently, under-balanced drilling has been proposed and undertaken in the Swan Lake Field. Swan Lake-2 was successfully gas drilled (vertically) below unstable coals. The operator has proposed under-balanced drilling of highly deviated (> 50°) wells at Swan Lake to improve reservoir and fracture intersection, and thus deliverability. The stability of such wellbores must be addressed with knowledge of the in situ stress tensor, and this is described in the following section.

Wellbore Stability Analysis
Mud weight and drilling trajectory are the critical variables for controlling mechanical wellbore stability. If mud weight is too low for a given trajectory, wellbore breakout may cause the wellbore to collapse. If the mud weight is too high, fluid may be lost into drilling-induced fractures. These stability problems can be addressed by setting

appropriate mud weights for a given wellbore trajectory. The in situ stress tensor and rock properties dictate safe drilling trajectories and mud weights.

As discussed above, the in situ stress tensor is well constrained in the Swan Lake Field, but little information on rock properties exists. When considering wellbore failure, several factors can influence the effective rock strength. These include not only the true rock strength, but also mud chemistry and its influence on rock strength (Mody and Hale, 1993) and thermal effects of colder drilling mud contacting hotter formation rocks (Coussy et al., 1991). Furthermore wellbore pressure may vary from the weight of the static mud column due to surge and swab pressures (Brudy and Zoback, 1999). Ideally rock strengths used in wellbore stability predictions should incorporate all of these factors. This can be achieved by using previous drilling experience to determine èpseudoí rock strength. This èpseudoí rock strength can be used to investigate wellbore stability in a comparative manner using an existing well as a benchmark and yielding wellbore stability predictions calibrated to that previous drilling experience. èPseudoí rock strength can be conservatively determined using the Swan Lake Field in situ stress tensor and assuming the successfully gas drilled Swan Lake-2 well was on the verge of failure (i.e. on the verge of breakout formation; Figure 5.14). This èpseudoí rock strength can then be used to predict wellbore stability of future wells relative to experience at Swan Lake-2.

Assuming the Swan Lake in situ stress tensor and P_w from the successfully gas drilled Swan Lake-2, a èpseudoí rock strength of 475 MPa is required to prevent the formation of wellbore breakout at Swan Lake-2, (Figure 5.14). However, a compressive rock strength as low as 330 MPa is feasible, below which complete wellbore collapse occurs, assuming wellbore collapse occurs when breakout width is greater than 90° (Moos and Peska, 1998; Figure 5.15). Consequently, the minimum compressive rock strength in Swan Lake-2 is 330 MPa at 3200 m. However, assuming the Swan Lake in situ stress tensor, P_w from the conventionally drilled Swan Lake-4 and the minimum compressive rock strength (330 MPa), no wellbore breakout is predicted at Swan Lake-4 (Figure 5.16). This lack of predicted breakout is inconsistent with the observation of wellbore breakouts in the conventionally drilled Swan Lake-4.

Figure 5.14. Wellbore stresses and breakout failure envelope calculated using the Swan Lake in situ stress tensor, $P_w = 7$ MPa and $C = 475$ MPa.
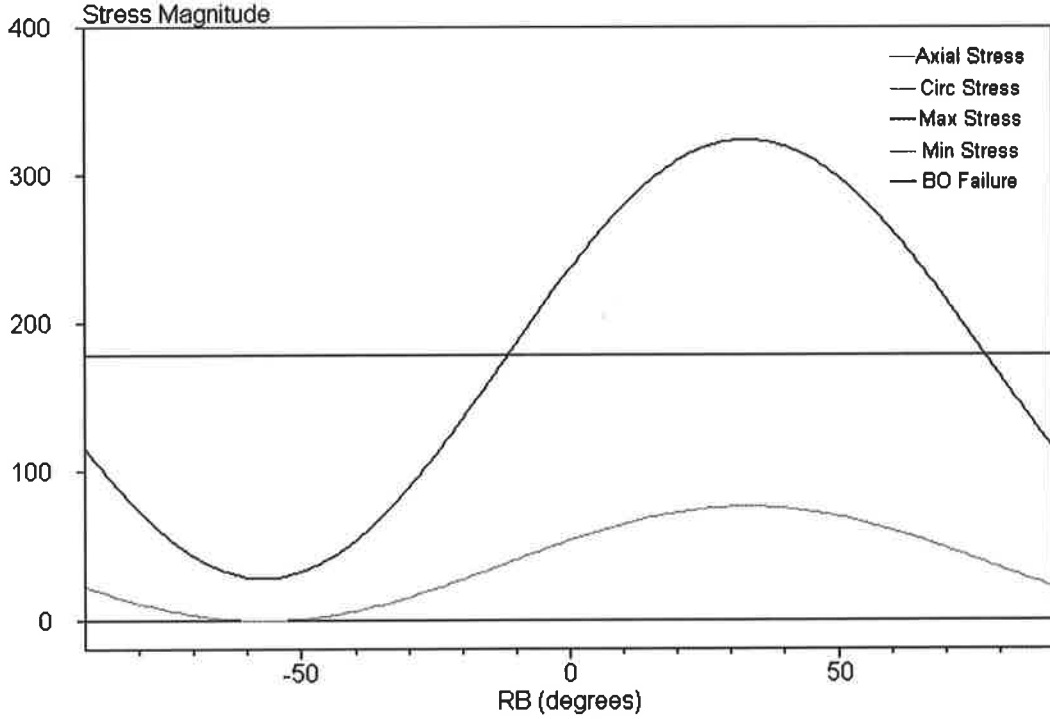
Figure 5.15. Wellbore stresses and breakout failure envelope calculated using the Swan Lake in situ stress tensor, $P_w = 7$ MPa and $C = 330$ MPa.
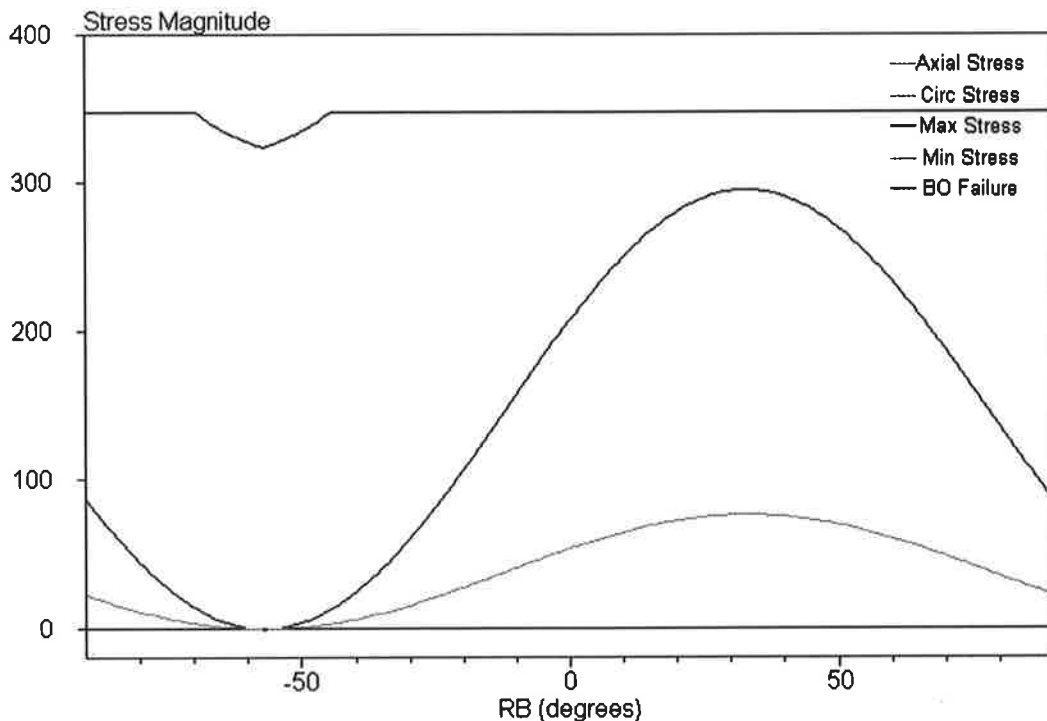
Figure 5.16. Wellbore stresses and breakout failure envelope for the Swan Lake-4 (P_w = 36 MPa and C = 330 MPa), indicating no breakout formation.

The discrepancy between the prediction of no breakouts and the observation of breakouts at Swan Lake-4 may be explained by near wellbore depletion. The compressive rock strengths above are determined assuming impermeable rocks (i.e. no pressure contact between the wellbore and formation; Figure 5.17). Under-balanced drilling does not produce a mud cake, keeping the well in pressure contact with the formation, and may lead to pore fluids flowing into the wellbore, resulting in near wellbore depletion (Figure 5.17; Section 3.6.2). The rate and amount of depletion depends on the difference in P_w and P_p, and the formation permeability. Assuming near wellbore depletion, a ëpseudoí rock strength of 350 MPa is determined (Figure 5.18). However, a compressive rock strength as low as 205 MPa is feasible, below which complete wellbore collapse occurs, assuming wellbore collapse occurs when breakout width is great than 90° (Moos and Peska, 1998; Figure 5.19). Thus, the minimum compressive rock strength in Swan Lake-2 is 205 MPa at 3200 m, assuming near wellbore depletion. Significant breakout is predicted in the conventionally drilled Swan Lake-4, assuming a minimum compressive rock strength of 205 MPa (Figure 5.20). Consequently, the occurrence of breakouts in Swan Lake-

4, the successful drilling of Swan Lake-2 and the resulting implications for rock strength affirm near wellbore depletion while drilling.

The risk of wellbore breakout and DITF formation are calculated in terms of required mud weight using the SWIFT software (Chapter 4) for the Swan Lake Field in situ stress tensor, a ëpseudoí rock strength of 350 MPa and assuming near wellbore depletion while drilling (Figure 5.21).
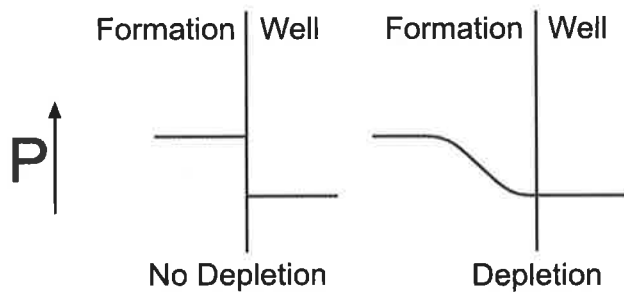
Figure 5.17. Pressure profiles across the wellbore wall for no depletion and depletion while drilling.
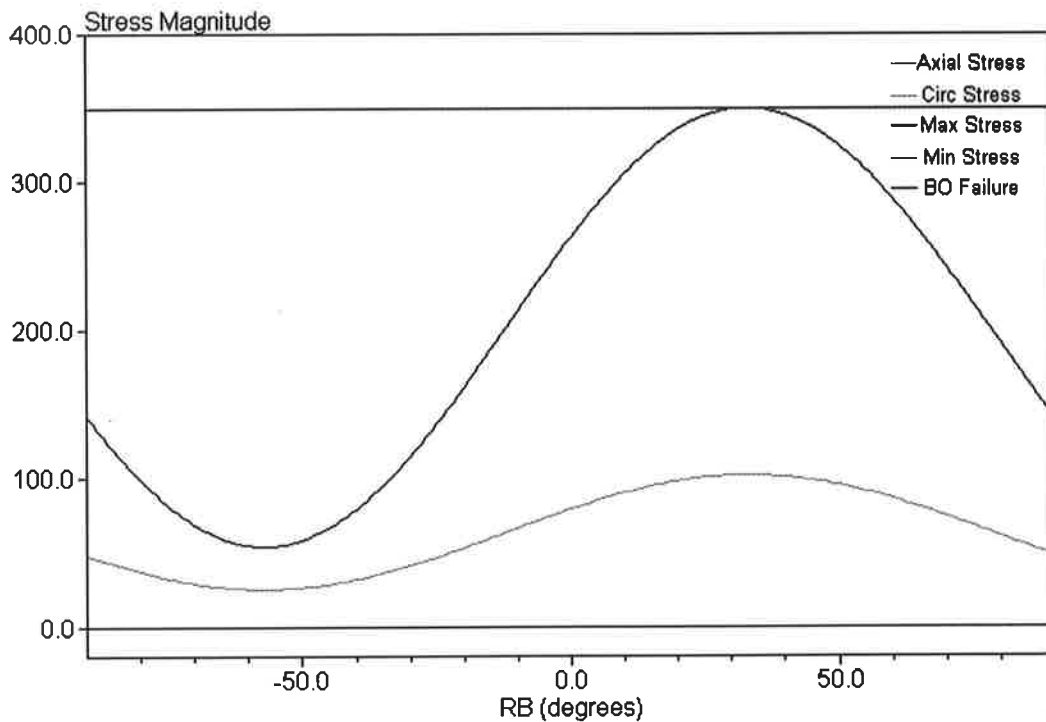
Figure 5.18. Wellbore stresses and breakout failure envelope calculated using the Swan Lake in situ stress tensor $P_p = 7$ MPa, $P_w = 7$ MPa and $C = 350$ MPa.
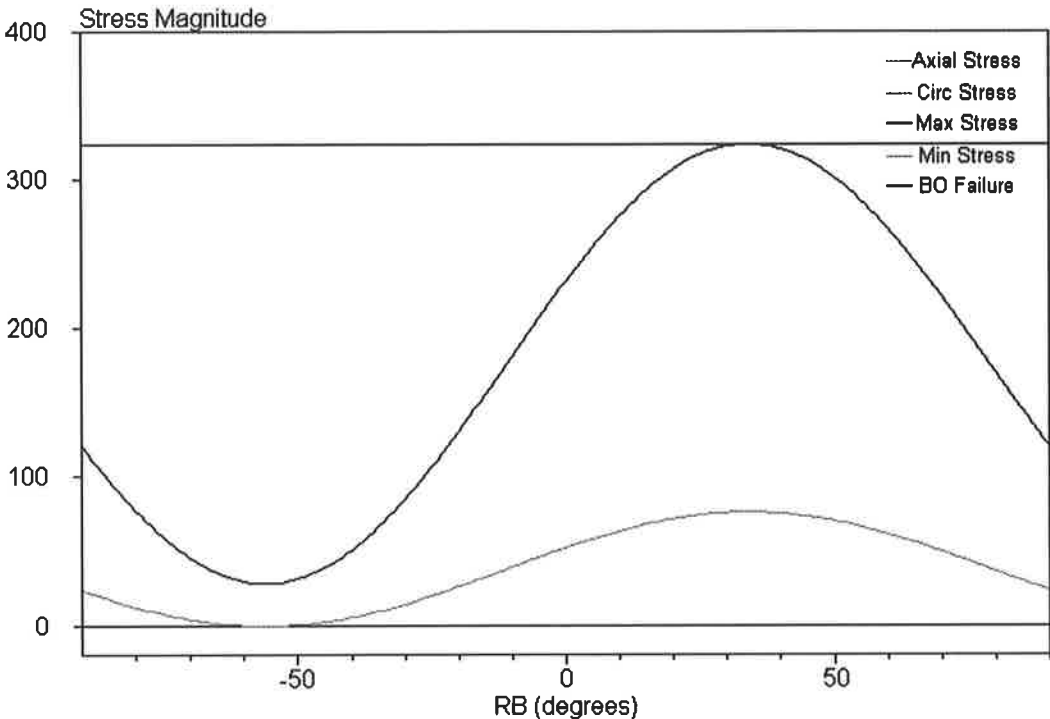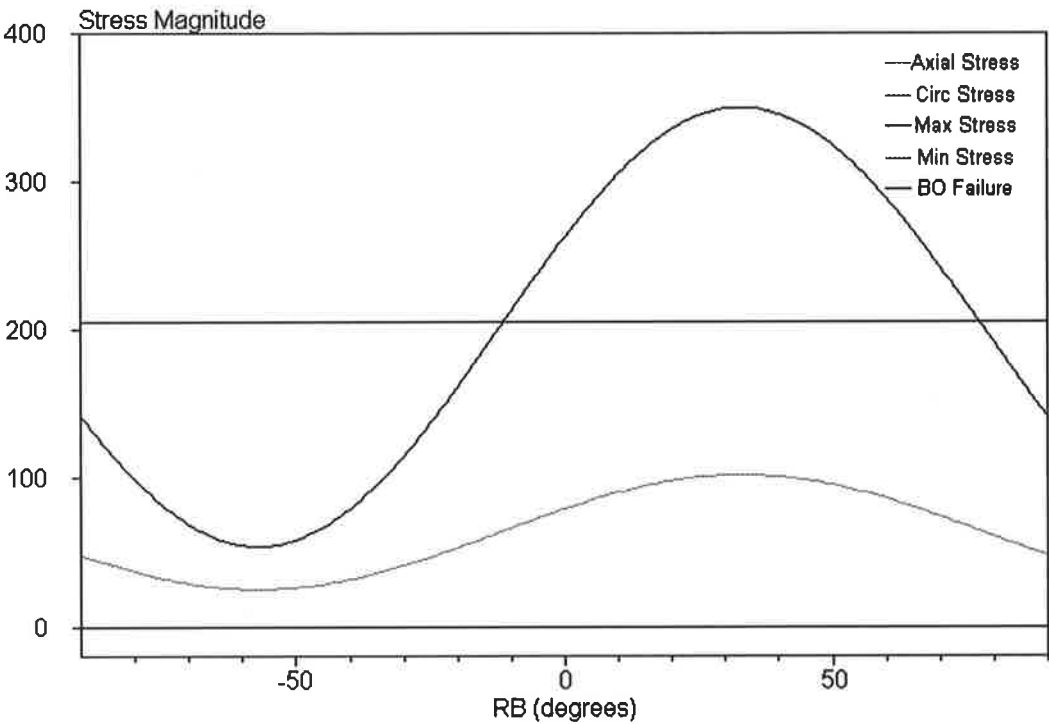
Figure 5.19. Wellbore stresses and breakout failure envelope calculated using the Swan Lake in situ stress tensor P_p = 7 MPa, P_w = 7 MPa and C = 205 MPa.
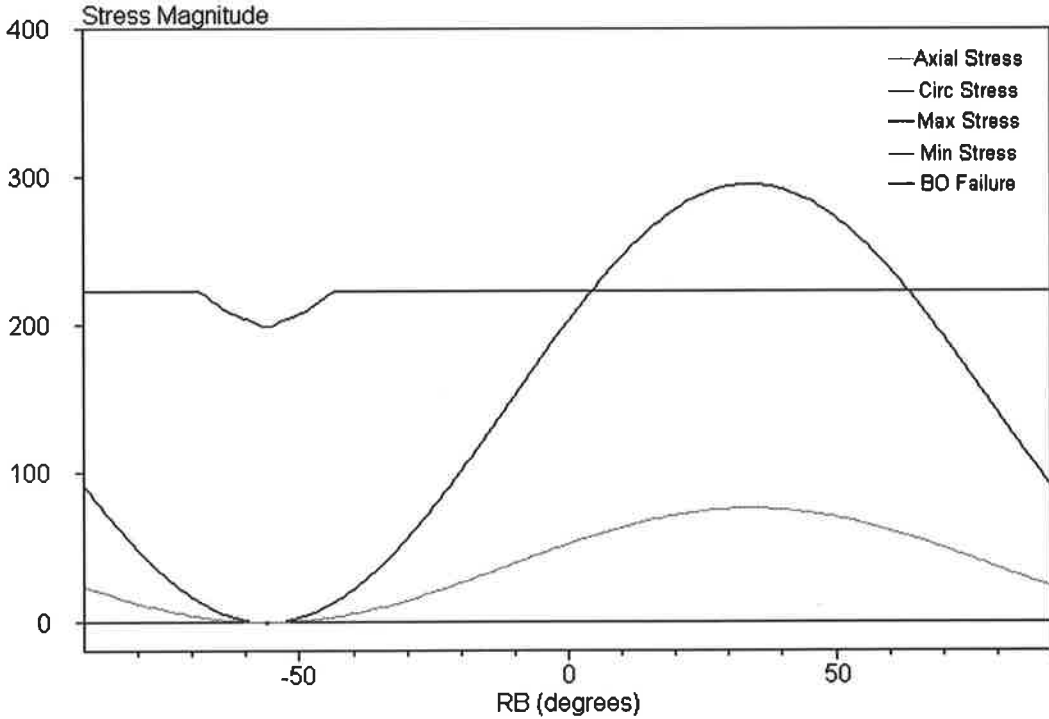
Figure 5.20. Wellbore stresses and breakout failure envelope for the Swan Lake-4 (P_w = 36 MPa and C = 205 MPa) indicates significant breakout formation.

Wellbore Stability Predictions

The highest risk of breakout development is in wells deviated towards 033°N and 213°N (minimum horizontal stress direction). All deviation angles at these azimuths (and the vertical well) have the same risk of breakout development (Figure 5.21). However, the risk of breakout development is no greater than that for Swan Lake-2, hence drilling and rock strength parameters being consistent, the least favourable trajectories will be no more prone to breakout than Swan Lake-2, and more favourable trajectories should be less prone to breakout.

The highest risk of DITF development is in wells deviated towards 033°N and 213°N (minimum horizontal stress direction). All deviation angles at these azimuths (and the vertical well) have the same risk of DITF development (Figure 5.22). DITFs will develop in a vertical well if the mud weight is greater than 9.4 ppg (worst case). Therefore wells drilled under-balanced have little risk of DITF development.

Summary

Under-balanced wells can be drilled in any trajectory in the Swan Lake area without stability problems greater than those encountered in the vertical, gas-drilled bottom section of Swan Lake-2, assuming drilling and rock strength parameters the same as those encountered in Swan Lake-2.

5.6. Conclusion

The in situ stress tensor in the Swan Lake Field, determined using the SWIFT software and available data, is unsuitable for fracture stimulation, but suitable for deviated under-balanced drilling. However, fracture stimulation may be successful if the well is depleted, altering the in situ stress tensor in the vicinity of the wellbore, prior to stimulation. Given that, with knowledge of the in situ stress tensor and appropriate planning, both strategies may be successful, the ultimate choice between fracture stimulation and under-balanced drilling as techniques for improving gas deliverability in the low permeability reservoir, requires investigation of the increase in production resulting from each of these techniques with respect to the cost of the techniques.
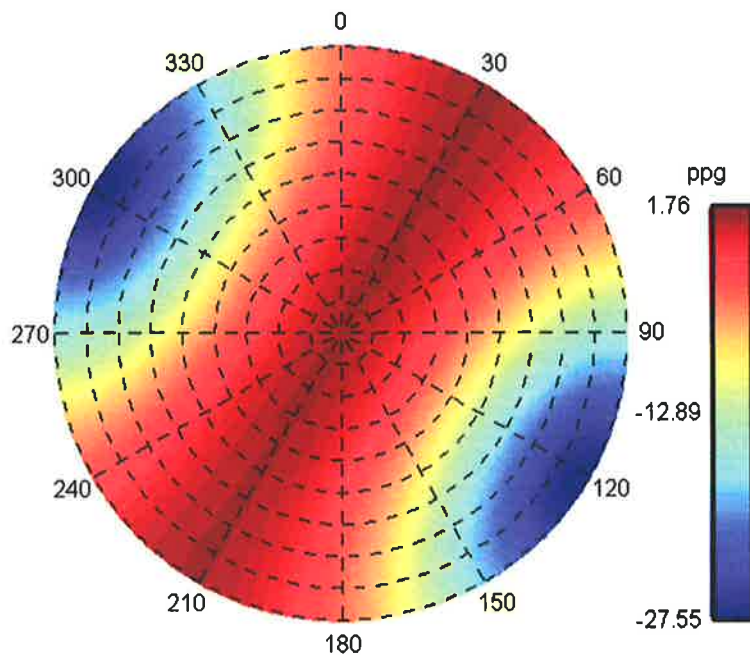
Figure 5.21. Polar diagram of wellbore trajectories coloured by minimum mud weight required to prevent compressional failure worse than that experienced at Swan Lake-2. Red indicates relatively high risk and blue indicates relatively low risk. A vertical well plots at the centre of the polar diagram and has the greatest risk of failure.
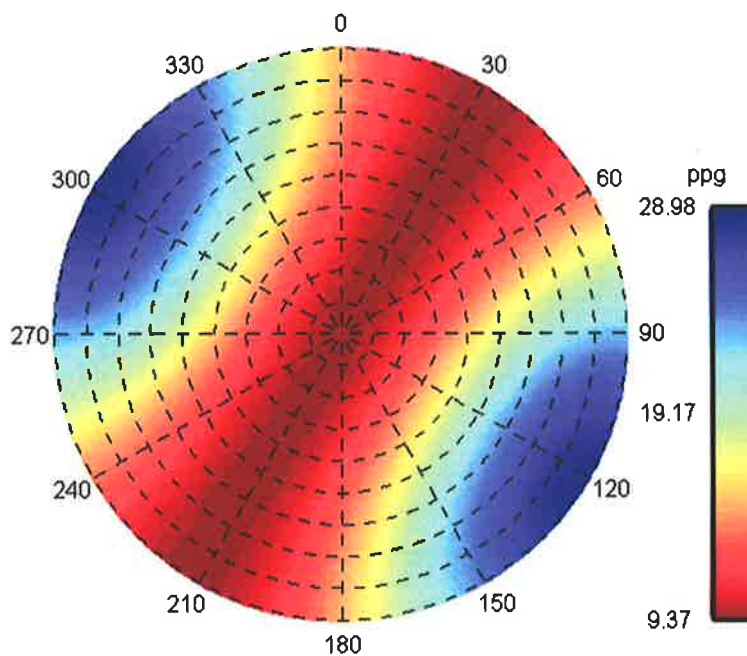
Figure 5.22. Polar diagram of wellbore trajectories coloured by maximum mud weight (ppg), above which DITF will occur. Red indicates relatively high risk and blue indicates relatively low risk. A vertical well plots at the centre of the diagram and has the greatest risk of failure (i.e. the lowest maximum mud weight).

6. Mereenie Field, Central Australia: Fracture Stimulation and Natural Fracture Intersection

6.1. The Problem

The Mereenie Field, Amadeus Basin, central Australia (Figure 6.1) contains an unexploited gas cap, in the Ordovician Stairway and Pacoota Sandstones (Figure 6.2), which the operator wishes to develop. This gas cap is characterised by permeabilities of typically 5-10 mD, which are further lowered during production by fines migration. Targeting hydraulically conductive natural fractures and fracture stimulation have been proposed as techniques for overcoming this problem. Many previous fracture stimulations in the field have encountered problems and resulted in little improvement in production. Furthermore, neither the extent of natural fracturing, nor their propensity to be open and hydraulically conductive were known prior to this study. The aim of this study was to determine the in situ stress tensor and fracture populations in the Mereenie Field and investigate the implications for fracture stimulation and the targeting of conductive natural fractures.

The extent to which natural fractures are hydraulically conductive is strongly influenced by the aperture of the fracture. Indeed the flow through a fracture is proportional to the cube of its aperture (eg see review by Cook, 1992). The in situ
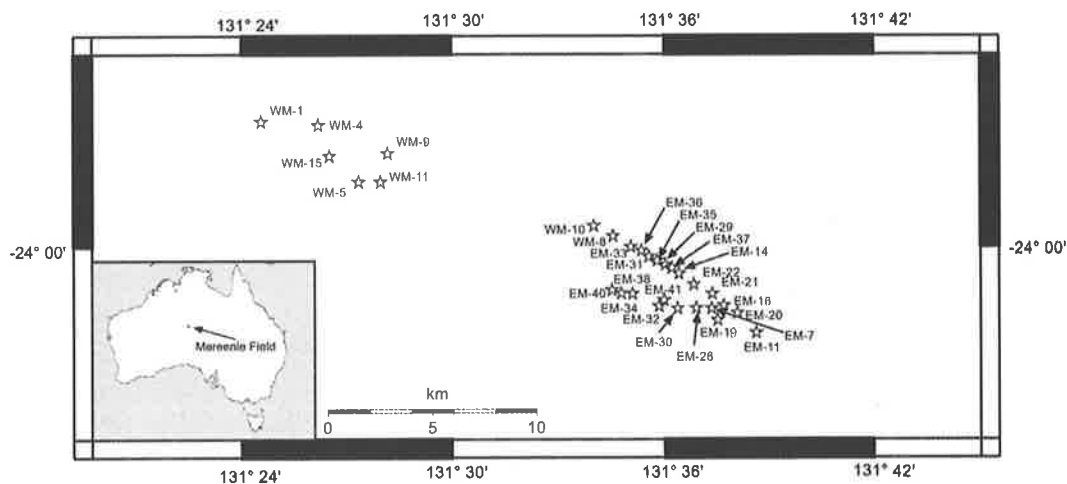
Figure 6.1. Mereenie Field location map. WM: West Mereenie; EM: East Mereenie.

stress tenor can act to close (reduce the aperture of) or open (increase the aperture of) natural fractures, while asperities, mineralisation and cementation may act to physically prop fractures open or hold them closed. Barton et al. (1995) found fractures carrying fluid, in the Cajon Pass scientific drill hole, to be generally critically stressed (i.e. subject to an in situ stress state that would induce failure), while fractures not carrying fluid were found not to be generally critically stressed. Consequently, the in situ stress tensor can be used to predict fracture sets most likely to be hydraulically conductive and this is undertaken in this chapter.

AGE		GROUP	FORMATION
Cainozoic			Surficial Deposits
Devonian	L	Pertnjara	Brewer Conglomerate
	M		Hermannsburg Sandstone
			Parke Siltstone
	E		
Silurian		Larapinta	Mereenie Sandstone
Ordovician	L		Carmichael Sandstone
	M		Stokes Siltstone
			Stairway Sandstone
	E		Horn Valley Siltstone
			Pacoota Sandstone
Cambrian	L	Pertaoorta	Goyder Formation
			Petermann Sandstone
			Deception Formation
	M		Illara Sandstone
			Temple Formation
	E		Chandler Formation
(Ediacaran)			Arumbera Sandstone
Late Proterozoic		Adelaidean	Pertataka Formation
			Aralka Formation
			Areyonga Formation
			Bitter Springs Formation — Loves Creek Member / Gillen Member
			Heavitree Quartzite

Figure 6.2. Stratigraphy of the Mereenie Field (after Oaks et al., 1991).

Twenty-nine wells in the field had been fracture stimulated at the time of this study. Productivity data was available for 26 of these wells (Table 6.1). Eight fracture stimulations resulted in flow rates of less than 120 barrels of oil per day. Five unproductive fracture stimulations exhibit P_c gradients greater than 18.1 MPa/km (0.8 psi/ft; Table 6.1). However treatments have been successfully pumped at fracture gradients ranging from 15.8 to 27.2 MPa/km (0.7 to 1.2 psi/ft; Santos and NSI, 1997).

The association of unproductive treatments and high in situ stresses suggests that fracture twisting away from the wellbore, as discussed in the previous chapter (Section 5.5.1), may be the cause of fracture stimulation problems (Santos and NSI, 1997).

This chapter determines the in situ stress tensor in the Mereenie Field by combining the available data with routine and non-routine stress determination techniques. Knowledge of the in situ stress tensor is applied to fracture stimulation and the targeting of open natural fractures.

6.2. Routine Stress Determination Techniques

6.2.1. Vertical Stress

The vertical stress in the Mereenie Field has previously been determined by Hillis and Mildren (1995), using the techniques described in Section 3.2, and is given by:

$$S_v = 0.018619 \times z^{1.0396} \qquad \text{Eq. 6.1,}$$

for East Mereenie, and:

$$S_v = 0.018525 \times z^{1.0363} \qquad \text{Eq. 6.2,}$$

for West Mereenie, where S_v is in MPa and z is depth in metres.

6.2.2. Horizontal Stress Orientations

The maximum horizontal stress orientations across the field were determined from 153 breakouts and 53 DITFs interpreted from resistivity image logs in 16 wells using the techniques described in Section 3.4 (Hillis et al., 1999; Figures 6.3 and 6.4).

Well	Zone	Pre-Frac Rate (bopb)	Post-Frac Rate (bopd)	P_c Grad (psi/foot)
East Mereenie-29	P3	70	340	-
East Mereenie-28	P3	60	180	0.57
East Mereenie-19	P3	25	65	0.56
East Mereenie-16	P3	140	380	0.49
East Mereenie-21	P3	55	140	0.52
East Mereenie-11	P3	110	190	0.57
East Mereenie-7	P3	60	150	0.49
West Mereenie-5	P3	25	175	0.61
East Mereenie-14	P3	30	150	0.58
East Mereenie-20	P3	20	150	0.53
East Mereenie-30	P3	-	240	0.56
East Mereenie-6	P1	5	35	-
East Mereenie-22	P3	40	75	0.55
East Mereenie-31	P3	-	375	0.60
West Mereenie-4	P3	-	5	1.00
East Mereenie-33	P3	-	500	0.60
East Mereenie-34	P3	-	110	0.84
East Mereenie-32	P3	-	230	0.67
West Mereenie-8	P3	-	350	0.72
West Mereenie-10	P3	-	25	1.03
West Mereenie-11	P3	-	80	0.96
West Mereenie-9	P3	-	35	0.86
East Mereenie-35	P3	165	500	0.71
East Mereenie-36	P3	90	380	0.72
East Mereenie-37	P3	60	360	0.70
East Mereenie-38	P4	25	150	-
East Mereenie-38	P3	80	220	0.69

Table 6.1. Pre and post-fracture productivity (bopd) in order of fracture stimulation date.
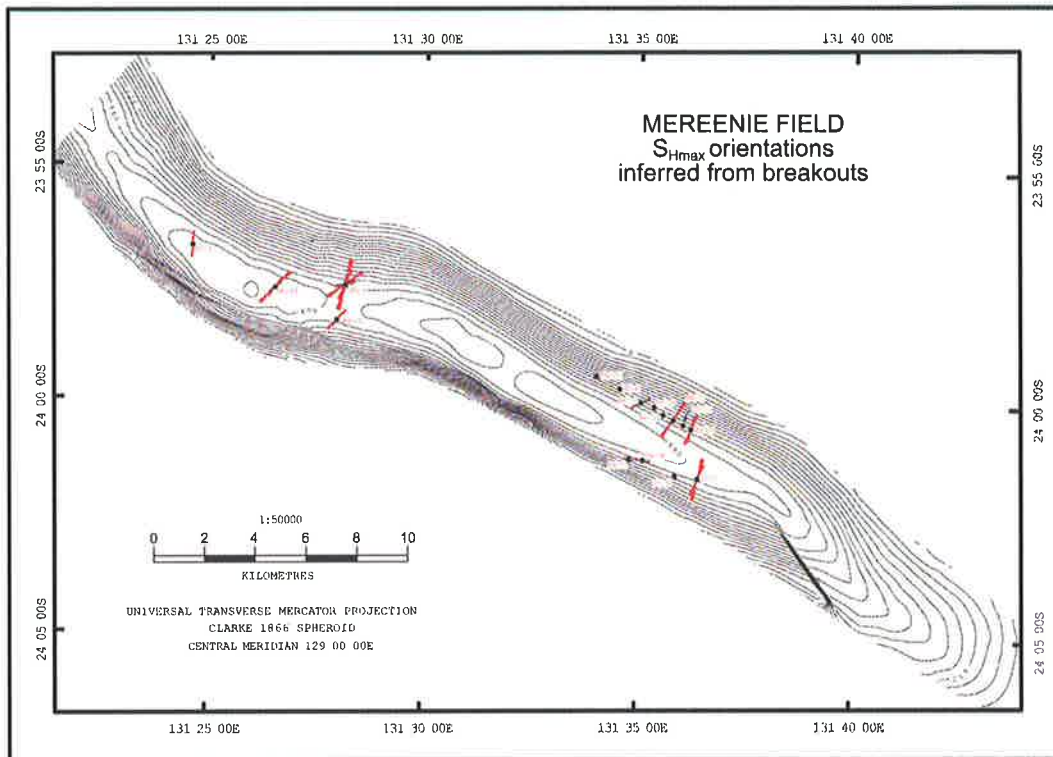
Figure 6.3. Maximum horizontal stress orientations inferred from breakouts in the Mereenie Field (from Hillis et al., 1999).
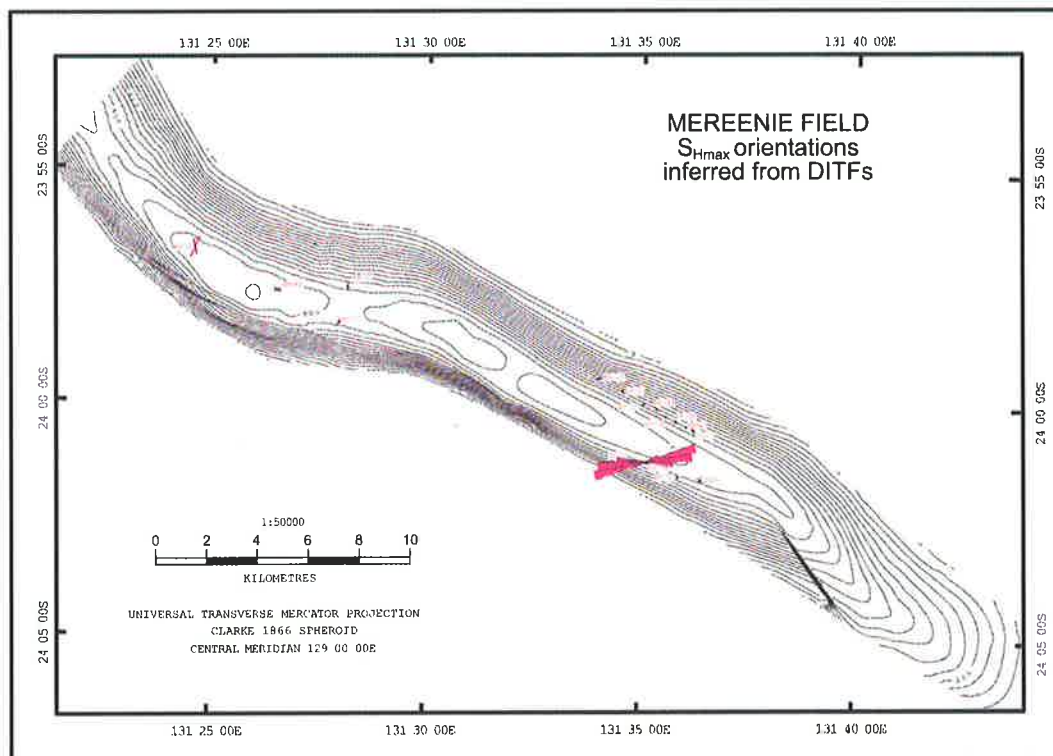
Figure 6.4. S_{Hmax} orientations inferred from DITFs (from Hillis et al., 1999).

Maximum horizontal stress directions inferred from breakouts are broadly consistent across the field, implying an S_{Hmax} direction of approximately 035∞N (Figure 6.5), orthogonal to the trend of the Mereenie anticline (Figure 6.3). Significant variations in the orientation of the maximum horizontal stress with depth are superimposed on this broad regional trend (Figure 6.6; Hillis et al., 1999). This is most pronounced in West Mereenie-9 well where breakout-inferred maximum horizontal stress rotates from approximately 080∞N at 950 m in the Middle Stairway Sandstone to approximately 010∞N at 1450 m in the Pacoota P3 Sandstone (Figure 6.6).
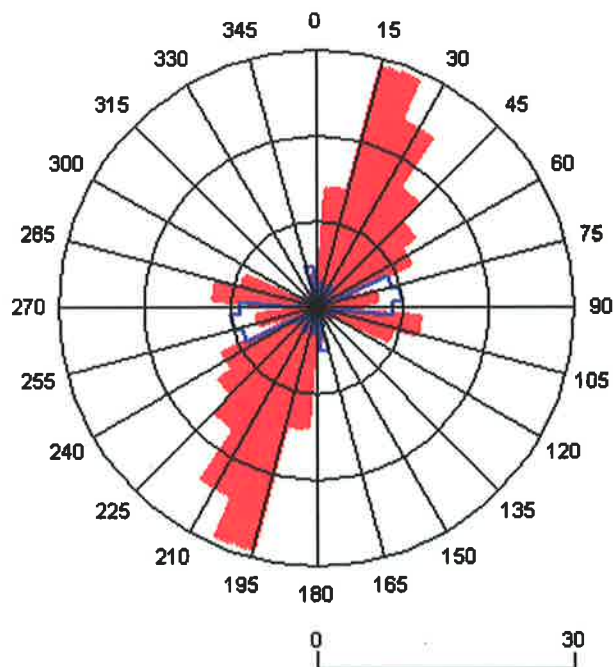
Figure 6.5. Rose diagram of S_{Hmax} orientations inferred from breakouts (red) and DITFs (blue) for the Mereenie Field.

The southern flank of the East Mereenie structure (East Mereenie-34 and East Mereenie-38) is the only anomalous area with respect to the above trends. Maximum horizontal stress there is approximately east-west (Figure 6.3), but again shows variation with depth. Breakouts at 1100 m in the Middle Stairway Sandstone indicate that maximum horizontal stress is approximately 100∞N, while in the Pacoota Sandstone, DITFs (discussed below) indicate that maximum horizontal stress is oriented approximately 080∞N. The anomalous stress orientations in this area may be

due to the relative proximity of East Mereenie-34 and East Mereenie-38 to the main thrust.

The rotation of maximum horizontal stress to sub-parallel to the main thrust at East Mereenie-34 and East Mereenie-38 is consistent with the thrust behaving as a relatively weak inclusion in stronger material (Hillis et al., 1999).
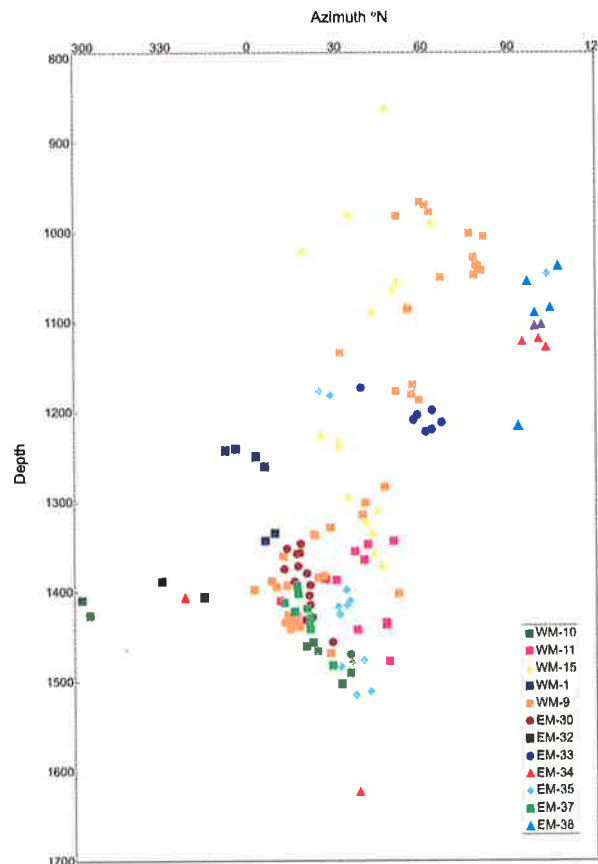
Figure 6.6. S_{Hmax} **orientations inferred from breakouts versus depth (from Hillis et al., 1999).**

DITFs are less frequent than breakouts across the Mereenie Field, and focused in two specific wells (Figure 6.4). East Mereenie-38, with 31 interpreted DITFs, and West Mereenie-1, with 9 interpreted DITFs, comprise 74% of the total of 54 DITFs interpreted across the field (Figure 6.4). Hence the information DITFs provide regarding in situ stress orientation is spatially limited (Figure 6.4). The field-wide summary of DITF azimuths (Figure 6.5) is strongly controlled by the pattern in East Mereenie-38 where DITFs in the Pacoota P3 and P4 Sandstone suggest that maximum horizontal stress there is oriented approximately 080∘N.

6.2.3. Minimum Horizontal Stress Magnitudes

The minimum horizontal stress magnitudes were determined from minifracture closure pressures, interpreted by Santos and NSI (1997) for 28 minifracture tests conducted in the Mereenie Field (Figure 6.7; Appendix C). Closure pressures were also determined by the author for the minifracture tests in East Mereenie-40 and East Mereenie-41, which were undertaken subsequent to the Santos and NSI (1997) analysis. Closure pressures for these wells were picked using the double tangent method on suitably scaled pressure/time plots (Figure 6.8; Enever, 1993). Closure pressures for the wells previously interpreted by Santos and NSI (1997) were also verified using the double tangent method, which yields similar results to those of Santos and NSI (1997). East Mereenie-39 was also fracture stimulated subsequent to the Santos and NSI (1997) analysis, however, the original data from the minifracture test in this well could not be obtained from Halliburton, and only a fracture gradient was available from the Halliburton report on the fracture stimulation at East Mereenie-39.
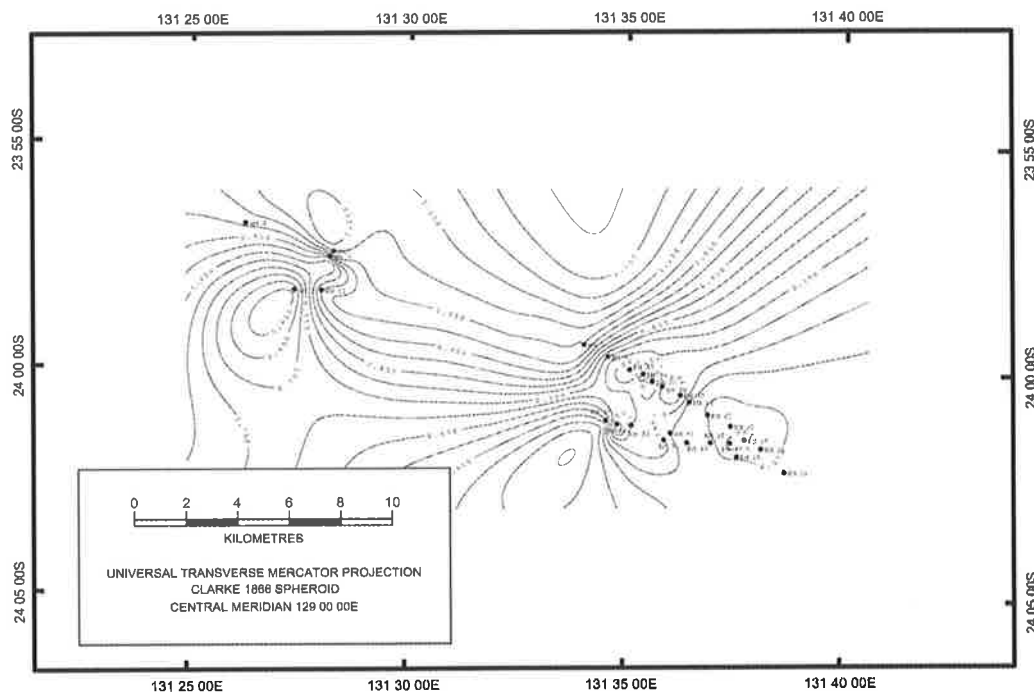
Figure 6.7. Minimum horizontal stress gradients (psi/ft) inferred from minifracture closure pressures.
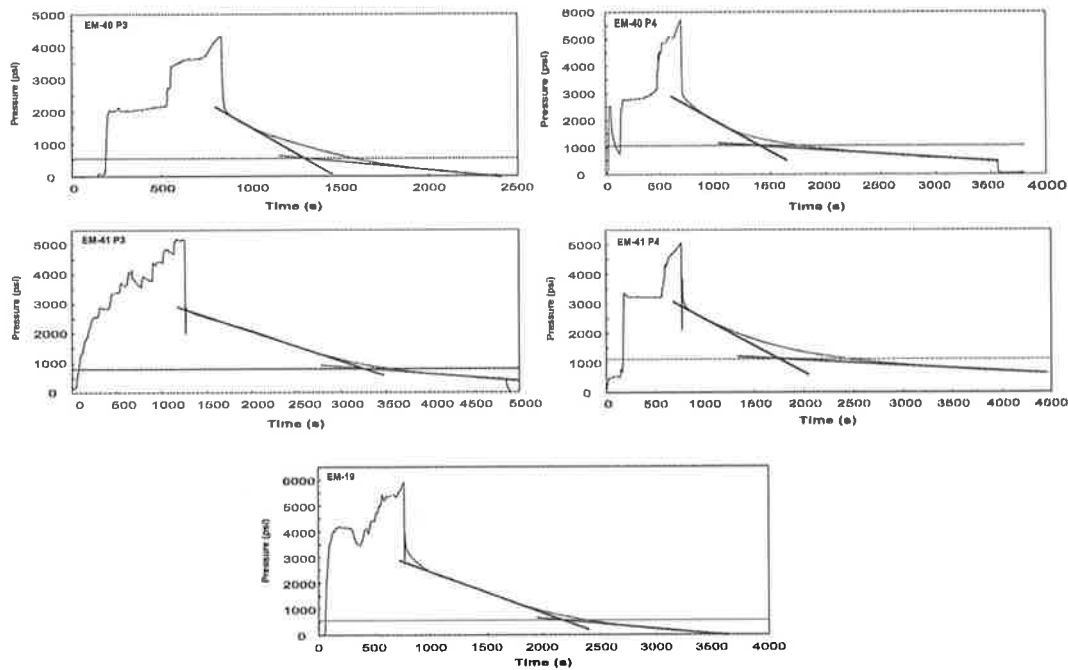
Figure 6.8. Pressure time plots for minifractures conducted in East Mereenie-40, East Mereenie-41 and East Mereenie-19.

The most notable aspect of interpreted minimum horizontal gradients across the Mereenie Field is their variability: 11.1 MPa/km to 23.3 MPa/km (0.49 psi/ft to 1.03 psi/ft) over a small distance (Figure 6.7) and depth (Figure 6.9). Typically, fracture gradient-type relations can describe minimum horizontal stress data reasonably successfully within a field. Such relations are unsuccessful in describing minimum horizontal stress in the Mereenie Field. Variations in reservoir pressure gradients (5.4-8.8 MPa/km, 0.24-0.39 psi/ft) can account for some, but far from all of this variation[1]. The extreme variation in minimum horizontal stress is interpreted to be in part linked to the structure, and associated changes in mechanical properties of the Mereenie anticline and its controlling thrust (Hillis et al., 1999).

The extreme variability of S_{hmin} requires the stress tensor to be determined at the local well-scale and not at the wider field-scale.

---

[1] Taking a typical pore pressure/stress coupling ratio of $\Delta S_{hmin}/\Delta P_p = 0.6$ (eg Addis, M.A., 1997; Hillis, R.R., 2000) and 4 MPa of reservoir depletion might account for 2.4 MPa S_{hmin} variation. See also Section 5.5.1.
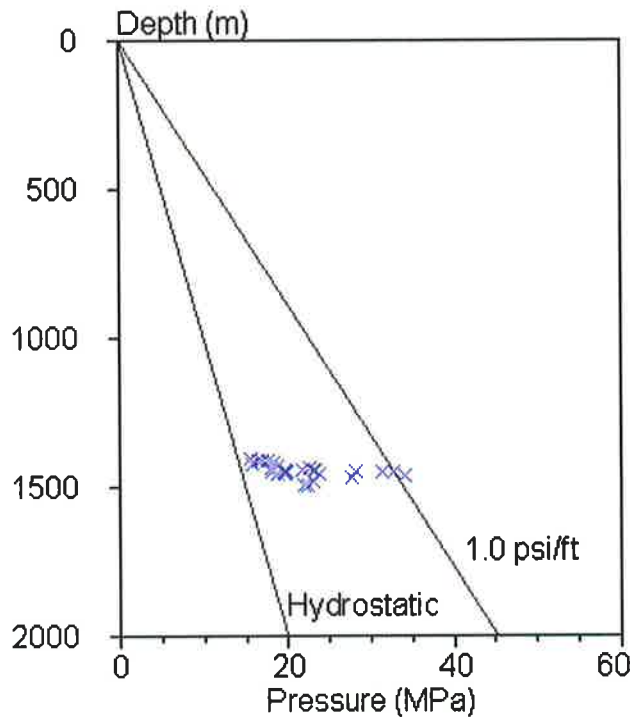
Figure 6.9. S_{hmin} inferred from minifracture P_c versus depth.

6.2.4. Pore Pressure

Pore pressures coincident with minifracture test depths were obtained from Santos and NSI (1997; Figure 6.10). The reservoir pressure gradient varies from 5.4 MPa/km to 8.8 MPa/km (0.24-0.39 psi/ft). This variation may have a significant impact on the in situ stress magnitudes (Section 6.2.3; Hillis, 2000). Mud weights in the Mereenie field are typically approximately 9 ppg, however higher mud weights have been used (e.g. the maximum mud weight in West Mereenie-1 was 11.9 ppg and in East Mereenie-38 was 11.0 ppg; Hillis et al., 1999). These mud weights (9 - 11.9 ppg) do not represent the measured reservoir pressures and hence, cannot be used to approximate reservoir pressures, but may be representative of pore pressures in shallower un-depleted zones.

6.3. Non-Routine Stress Determination Techniques

The maximum horizontal stress is, as is commonly the case, the most problematic aspect of the in situ stress tensor to constrain in the Mereenie Field. Maximum horizontal stress magnitude can be determined using minifracture tests and/or the observation of wellbore failure (Section 3.6) or constrained using frictional limits to
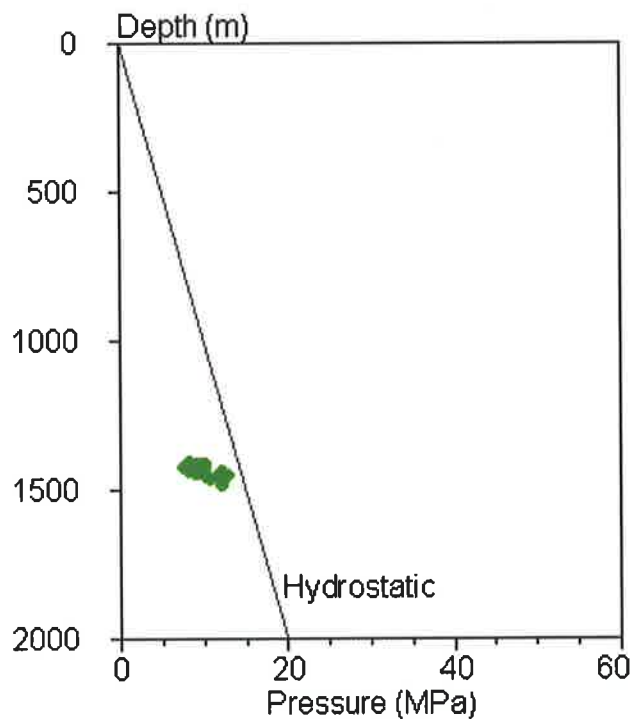
Figure 6.10. Pore pressure versus depth in the Mereenie Field.

stress (Section 2.5). The minifracture tests in the Mereenie Field were conducted in cased holes through perforations. No fracture reopening pressure can be determined where minifracture tests are conducted in cased holes (Section 3.6.1), hence S_{Hmax} can not be determined from these tests. Image logs were run in 16 wells, resulting in 153 wellbore breakouts and 53 DITFs being interpreted (Hillis et al., 1999). The maximum horizontal stress magnitude can be determined from observations of wellbore breakouts, if the compressive rock strength is known. However, no information on compressive rock strengths is available. Large numbers of DITFs were observed in two wells: East Mereenie-38, with 31 interpreted DITFs, and West Mereenie-1, with 9 interpreted DITFs, comprising 75% of the total of 53 DITFs interpreted across the field (Figure 6.4; Table 6.2). East Mereenie-38 and West Mereenie-1 were both drilled with higher mud weights than is typical for the Mereenie Field. Mud weights up to 11 ppg were used in East Mereenie-38, and up to 11.9 ppg in West Mereenie-1, as opposed to the 9 ppg more commonly used (Hillis et al., 1999). These higher mud weights are almost certainly responsible for the common occurrence of DITFs in these wells (Section 3.3.4). As discussed in this section, the occurrence of DITFs is used herein to constrain S_{Hmax}.

6.3.1. DITF Occurrence

The observation of DITFs provides the best method for determining S_{Hmax} in the Mereenie Field, in particular in wells in which information is available on the remainder of the components of the stress tensor. Of the nine wells in which DITFs were observed, six have information on S_{hmin} from minifracture tests (Table 6.2). However, the minifracture tests in East Mereenie-37 and 38 were conducted subsequent to a 4-6 week period of production, depleting these wells and perturbing the in situ stress tensor by means of pore pressure stress coupling (Addis, 1997; Hillis, 2000). Consequently, the stress state in these wells when the minifracture tests were conducted may have been different to that causing DITFs to form during drilling and these wells are not used in the stress analysis. However, East Mereenie-30, West Mereenie-9 and West Mereenie-11 were not produced prior to the minifractures being conducted (Hillis et al., 1999) and are analysed herein. No minifracture was conducted in West Mereenie-1 nor is P_p known in the well, precluding the observation of DITFs in this well from being used for S_{Hmax} determination.

Well Name	Number of DITFs
East Mereenie[1]-30	2
East Mereenie-34	1
East Mereenie[2]-37	1
East Mereenie[2]-38	31
Wes Mereenie-10	1
West Mereenie-1	9
West Mereenie[1]-11	2
West Mereenie-15	4
West Mereenie[1]-9	2

Table 6.2. Table of the number of DITFs interpreted in individual wells. [1] indicates wells in which minifractures were conducted prior to the wells being depleted, [2] indicates wells in which minifractures were conducted after depletion.

The occurrence of 75% of the observed DITFs in two wells with elevated mud weights, while the other seven wells in which DITFs were observed contain an average of 2 DITFs, suggests that wells drilled with 9 ppg mud are on the verge of DITF formation.

The occurrence of DITFs can be combined with frictional limits to constrain the maximum horizontal stress. The appropriate value for μ varies between 0.6 and 1 (Brace and Kohlstedt, 1980; McGarr, 1980; Zoback and Healy, 1984). However, the observation that in-balance wells are on the verge of DITF formation suggests that a μ in the low end of this range is appropriate for the Mereenie Field. Consequently a μ of 0.6 is used in this analysis.

West Mereenie-9

Two DITFs were interpreted in West Mereenie-9 at depths of 1414 m and 1455 m (Hillis et al., 1999). At intermediate depth of 1435 m S_v is 34.6 MPa, P_p is 12.1 MPa, P_w is 15.1 and S_{hmin} is 27.8 MPa. The shaded region in Figure 6.11 represents the stress states for which DITFs may form using the known S_v, P_p, and P_w. The vertical line at the known S_{hmin} in West Mereenie-9 further reduces the allowable values of S_{Hmax} (Figure 6.11). The minimum value of S_{Hmax} is constrained by the minimum value for which DITFs may occur (Section 3.6.3), while the maximum value is constrained by frictional limits (Section 3.6.4). The minimum value of S_{Hmax} for which DITFs can occur is 56.3 MPa (Figure 6.12; Table 6.3). The maximum value of S_{Hmax} from frictional limits (for $\mu = 0.6$) is 60.5 MPa (Figure 6.11; Table 6.3).

West Mereenie-11

Two DITFs were interpreted in West Mereenie-11 at depths of 1034 m and 1508 m (Hillis et al., 1999). The minifracture test was conducted at a depth of 1448 m. At this depth S_v is 35.0 MPa, P_p is 12.1 MPa, P_w is 15.3 and S_{hmin} is 31.3 MPa. The shaded region in Figure 6.13 represents the stress states for which DITFs may form using the known S_v, P_p, and P_w. The vertical line at the known S_{hmin} in West Mereenie-11 further reduces the allowable values of S_{Hmax} (Figure 6.13). As in West Mereenie-9, the minimum value of S_{Hmax} is constrained by the minimum value for which DITFs may occur (Section 3.6.3), while the maximum value is constrained by frictional limits (Section 3.6.4). The minimum value of S_{Hmax} for which DITFs can

occur is 66.5 MPa (Figure 6.14; Table 6.4). The maximum value of S_{Hmax} from frictional limits (for $\mu = 0.6$) is 72.5 MPa (Figure 6.13; Table 6.4).

Component	Value
Depth	1435 m
S_v	34.6 MPa
S_{hmin}	27.8 MPa
P_p	12.1 MPa
P_w	15.1 MPa
S_{Hmax}	56.3 (DITF) – 60.5 (frictional limit) MPa
S_{Hmax} orientations	039°N

Table 6.3. Stress tensor in West Mereenie-9 at a depth of 1435 m.
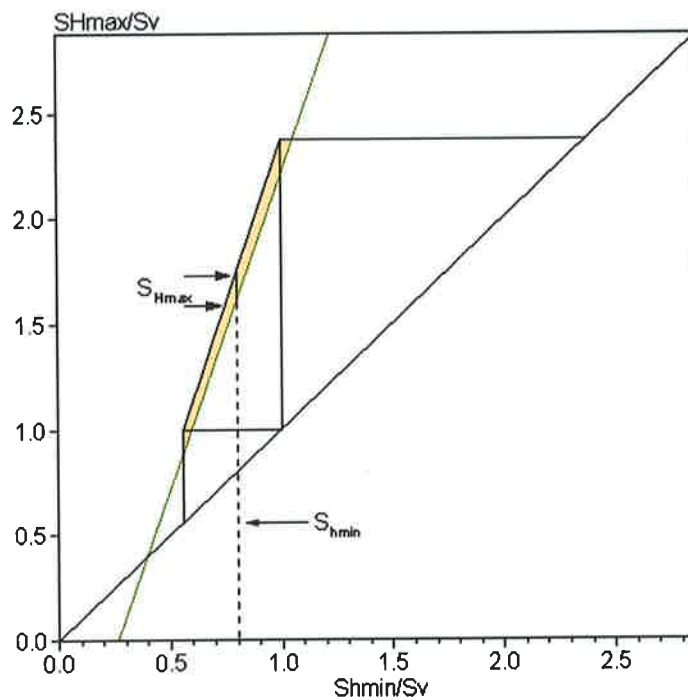
Figure 6.11. Allowable region: shaded area represents stress states in which DITFs can occur in West Mereenie-9.
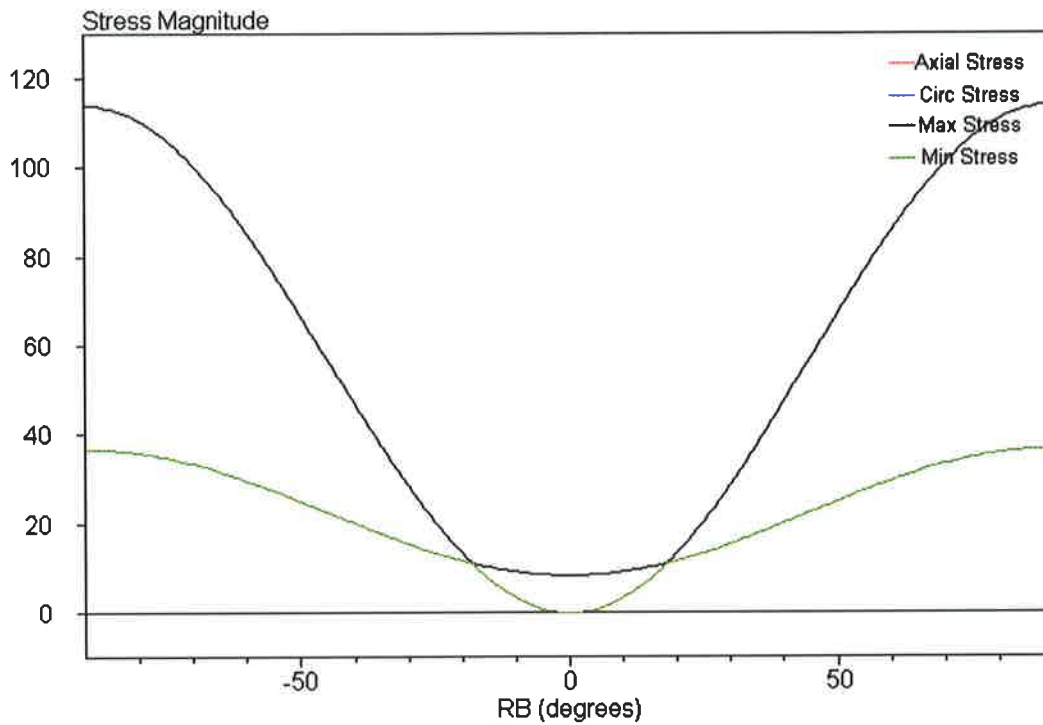
Figure 6.12. Wellbore stresses in West Mereenie-9, for $S_v = 34.6$ MPa, $P_p = 12.1$ MPa, $P_w = 15.1$, $S_{hmin} = 27.8$ MPa and $S_{Hmax} = 56.3$ MPa, S_{Hmax} is the only unknown and is determined to be of magnitude such that wellbore stress state is on the verge of DITF formation.
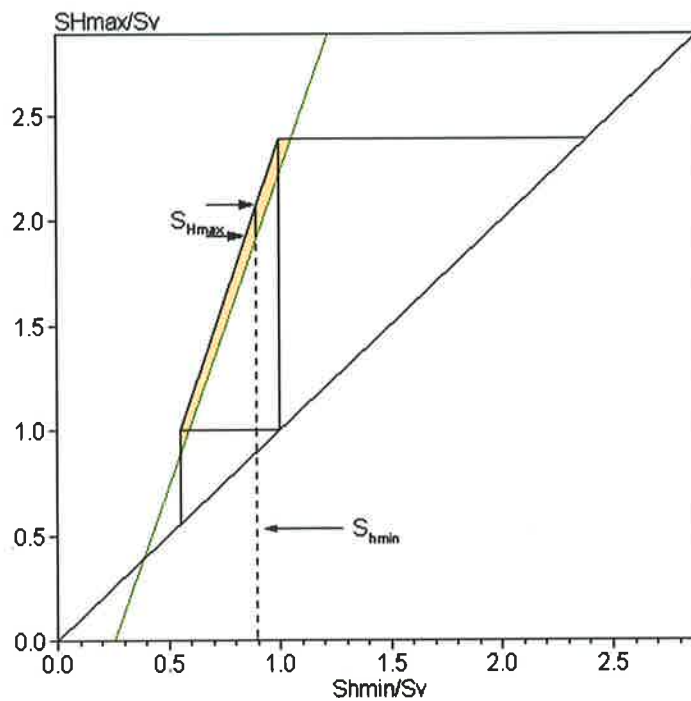
Figure 6.13. Allowable region: shaded area represents stress states in which DITFs can occur in West Mereenie-11.
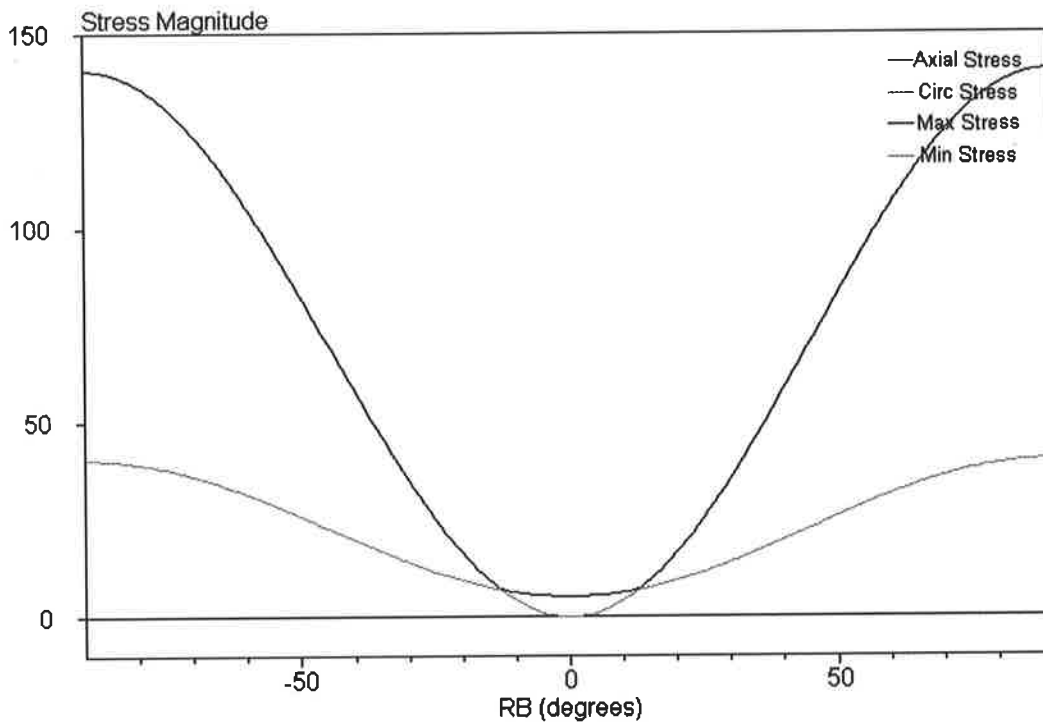
Figure 6.14. Wellbore stresses in West Mereenie-11, for S_v = 35.0 MPa, P_p = 12.1 MPa, P_w = 15.3, S_{hmin} = 31.3 MPa and S_{Hmax} = 66.5 MPa, S_{Hmax} is the only unknown and is determined to be of magnitude such that wellbore stress state is on the verge of DITF formation.

Component	Value
Depth	1448 m
S_v	35.0 MPa
S_{hmin}	31.3 MPa
P_p	12.1 MPa
P_w	15.3 MPa
S_{Hmax}	66.5 (DITF) – 72.5 (frictional limit) MPa
S_{Hmax} orientations	038°N

Table 6.4. Stress tensor in West Mereenie-11 at a depth of 1448 m.

East Mereenie-30

Two DITFs were interpreted in East Mereenie-30 at depths of 1216 m and 1415 m (Hillis et al., 1999). The minifracture test was conducted at a depth of 1442 m. At this depth S_v is 35.8 MPa, P_p is 9.3 MPa, P_w is 15.2 and S_{hmin} is 18.2 MPa. The shaded region in Figure 6.15 represents the stress states for which DITFs may form using the known S_v, P_p, and P_w. The vertical line at the known S_{hmin} in Figure 6.15 further reduces the allowable values of S_{Hmax}. As in West Mereenie-9 & 11 the minimum value of S_{Hmax} is constrained by the minimum value for which DITFs may occur (Section 3.6.3), while the maximum value is constrained by frictional limits (Section 3.6.4). The minimum value of S_{Hmax} for which DITFs can occur is 30.1 MPa (Figure 6.16; Table 6.5). The maximum value of S_{Hmax} from frictional limits (for $\mu = 0.6$) is 36.3 MPa (Figure 6.15; Table 6.5).
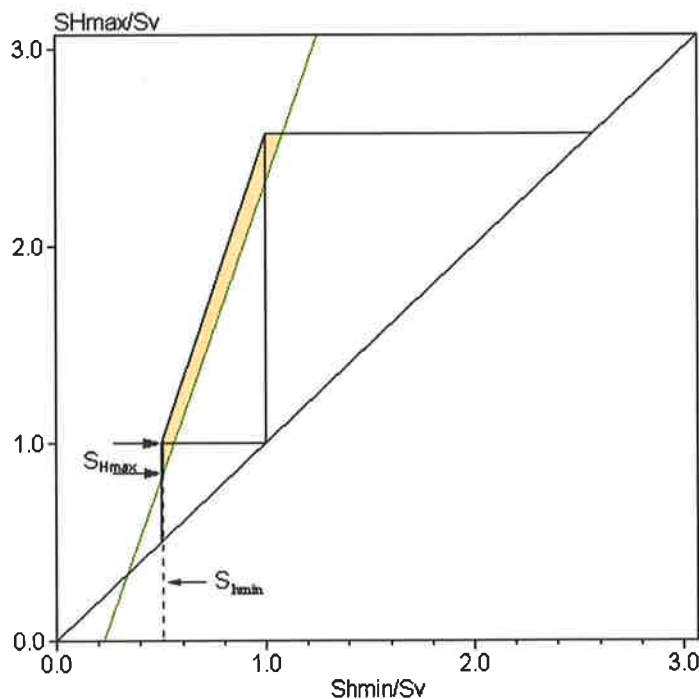
Figure 6.15. Allowable region: shaded area represents stress states in which DITFs can occur in East Mereenie-30.
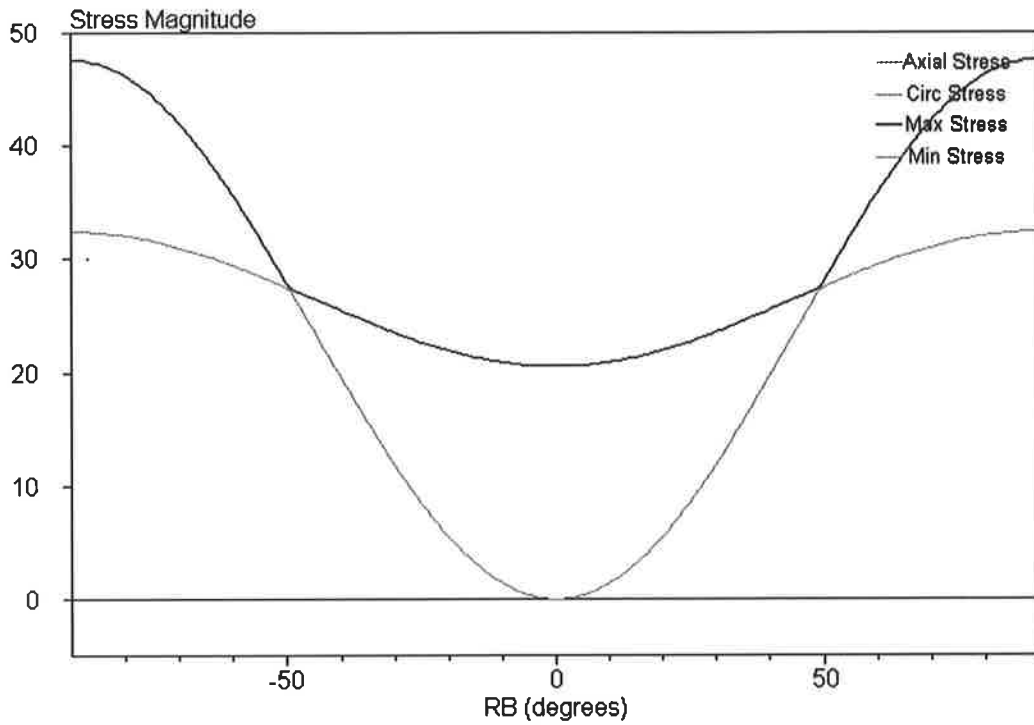
Figure 6.16. Wellbore stresses in East Mereenie-30, for $S_v = 35.8$ MPa, $P_p = 9.3$ MPa, $P_w = 15.2$, $S_{hmin} = 18.2$ MPa and $S_{Hmax} = 30.1$ MPa, S_{Hmax} is the only unknown and is determined to be of magnitude such that wellbore stress state is on the verge of DITF formation..

Component	Value
Depth	1442 m
S_v	35.8 MPa
S_{hmin}	18.2 MPa
P_p	9.3 MPa
P_w	15.2 MPa
S_{Hmax}	30.1 (DITF) – 36.3 (frictional Limit) MPa
S_{Hmax} orientations	020°N

Table 6.5. Stress tensor in East Mereenie-30 at a depth of 1442 m.

6.4.   The Mereenie Field In Situ Stress Tensor

The stress tensor determined in the West Mereenie-9 (Table 6.3), West Mereenie-11 (Table 6.4) and East Mereenie-30 (Table 6.5) wells varies significantly. The minimum horizontal stress varies from 18.2 MPa in East Mereenie-30 to 31.3 MPa in West Mereenie-11 at approximately the same depth. However, the stress state in each of the wells is restricted to a small (shaded) region of the allowable region diagram (Figures 6.11, 6.13, 6.15 and 6.17). Across the field, stress regimes vary from the boundary of normal/strike-slip ($S_v \approx S_{Hmax} > S_{hmin}$) to the boundary of strike-slip/reverse ($S_{Hmax} > S_{hmin} \approx S_v$), all lying relatively close to frictional limit in the strike-slip regime.

The significant variation in S_{hmin} (P_c) across the field (Figure 6.7; Section 6.2.3) makes it impossible to characterize the field in terms of a single stress tensor. This variation is in part due to large variations in P_p resulting from depletion, but may also be due to the structure and resulting variations in mechanical properties (Hillis et al., 1999).
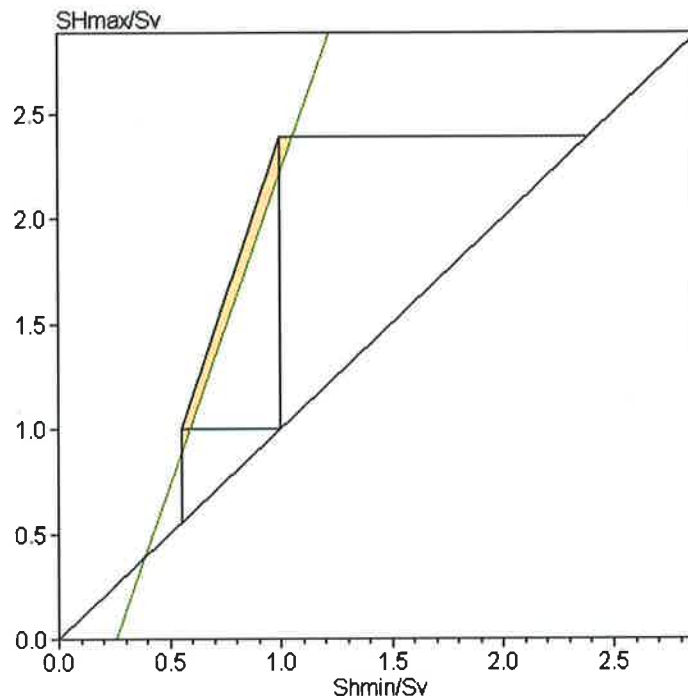
Figure 6.17. Allowable region: Shaded area represents stress states in which DITFs can occur (Mereenie Field).

6.5. Implications

6.5.1. Fracture Stimulation

Fracture stimulation is used, in the Mereenie Field, to improve deliverability and overcome low permeability resulting from fines migration. Wells in which fracture stimulations have resulted in poor post-stimulation production are characterised by high treatment pressures and high closure pressures (Santos and NSI, 1997; Hillis et al., 1999).

Five fracture stimulations in wells in the Mereenie Field with high P_c gradients (0.8-1.0 psi/ft) have been unsuccessful, resulting in flow rates less than 120 BOPD. The mean flow rate in these wells is 50 BOPD, while the mean flow rate in 19 wells stimulated with P_c gradients less than 0.8 psi/ft is 250 BOPD.

Successful stimulations have been carried out throughout the field, including the highly stressed West Mereenie region, in wells flowed for 4-6 weeks prior to fracture stimulations being undertaken. This success is attributed to depletion of the reservoir resulting in a decrease in the horizontal stress magnitudes (Addis, 1997; Santos and NSI, 1997; Hillis et al., 1999; Hillis, 2000; Section 5.5.1), leading to the formation of a single vertical fracture. This flow period also concentrates fines in the vicinity of the wellbore resulting in little or no fines migration towards the induced fracture, further improving production (Santos and NSI, 1997).

Although, closure pressures throughout the field are less than the overburden stress, suggesting vertical fractures are induced during fracture stimulation, high horizontal stress magnitudes are the main diagnostic of problematic fracture stimulations in the field. Targeting of low stress regions to avoid such problems is extremely difficult given the very localised nature of stress variations. Consequently, depletion prior to fracturing, is the key issue to improving fracture stimulation treatments. Whether depletion prior to fracturing improves subsequent production rates by lowering the horizontal stress magnitudes (thereby creating simple fractures) and/or by concentrating fines near the wellbore prior to stimulation is not clear.

6.5.2. Targeting Open Natural Fractures

In order to assess the potential for targeting open natural fractures as a development strategy in the Mereenie Field, the ëfracture susceptibilityí method was developed and used. Targeting open natural fractures requires knowledge of the nature of pre-existing fracture populations (eg. orientation and density) and of their ability to carry fluids within the in situ stress field, neither of which were known in the Mereenie Field prior to this study. The fracture susceptibility technique allows information on pre-existing fracture orientation and density to be easily combined with the effect of the in situ stress field on the permeability of pre-existing fractures.

The technique follows the results of Barton et al. (1995) in recognising that critically stressed fractures (i.e. subject to an in situ stress state that would induce failure) tend to be open and hydraulically conductive. However, we incorporate the possibility that fractures may be cemented and have cohesive strength (Dewhurst et al., 1999) and the role of tensile and mixed mode failure as well as shear failure in fluid flow (Sibson, 1994).

The production of fracture susceptibility plots (Section 4.5.9) requires knowledge of the stress field, and fracture orientations and a known/assumed failure envelope. The susceptibility of an individual fracture to be open and permeable is determined by calculating the shear and normal stress acting on that fracture and measuring the change in P_p (ΔP_p) required to cause failure for the known failure envelope (Figure 6.18). This can be undertaken for all potential fracture orientations and the results plotted as a structural permeability plot (polar diagram of normals to fracture planes coloured by ΔP_p required to cause failure; Figure 6.19). Finally, as is undertaken below for the Mereenie Field, known fracture orientations can be superimposed on the structural permeability plot in order to assess which if any pre-existing fracture orientations are suitably oriented to be open and hydraulically conductive within the in situ stress field. Such a diagram is known as a fracture susceptibility plot.

The significant variation in the Mereenie Field in situ stress tensor necessitates a variety of stress states to be considered in the analysis. Four stress states have been chosen representing states, ranging from the boundary of normal faulting and strike-slip faulting to the boundary of strike-slip and thrust faulting, and all near frictional limit (Figure 6.20; Table 6.6). A variation in S_{Hmax} orientation from the regional
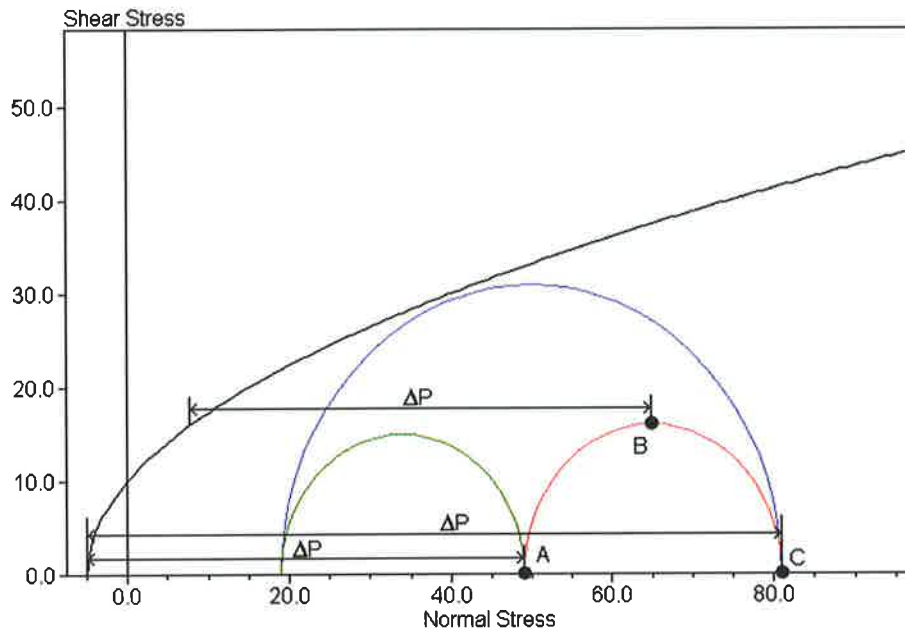
Figure 6.18. Mohr diagram with Griffith failure envelope showing three fractures (orientation of A, B and C as in Figure 6.19) and the change in P_p (ΔP) required to reactivate those fractures. From the stresses acting on each fracture it can be seen that the stress regime is strile-slip (A, the horizontal fracture is acted on by S_V' which is S_2 hence strike-slip stress regime) and that S_{Hmax} is oriented north-south (C, the vertical fractures striking east-west is acted on by S'_{Hmax}). The risk of reactivation for these fractures is shown in Figure 6.19.
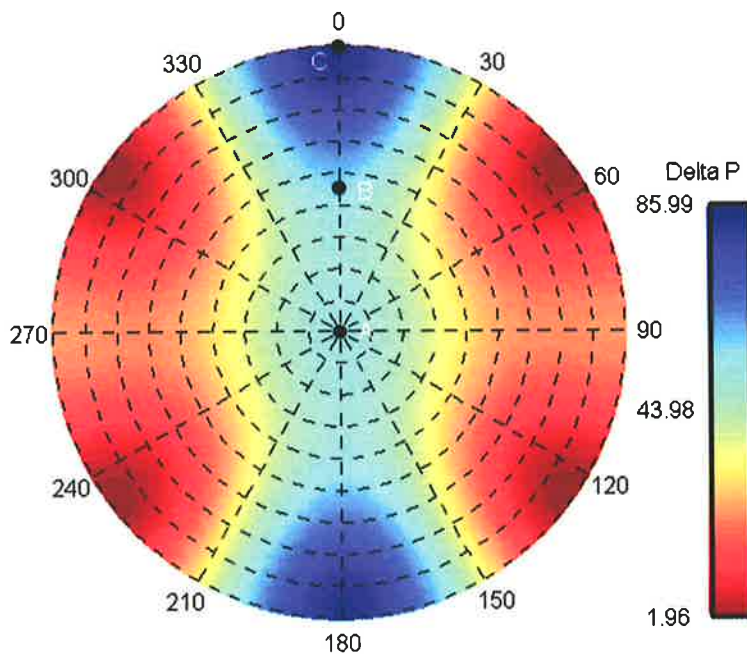
Figure 6.19. Structural permeability diagram: contoured polar diagram of normals to fracture planes coloured by the P_p change required to reactivate that fracture. The fracture/fault (A) is horizontal. The fracture/fault (B) is dipping 45° towards 180°N. The fracture/fault (C) is dipping 90° towards 180°N

035°N to ~090°N is observed in two closely spaced wells, East Mereenie-34 and 38, on the southern flank of the Mereenie structure (Figures 6.3 and 6.4). However, this variation in orientation is extremely spatially limited when compared to the field-wide 035°N trend and only the field-wide 035°N S_{Hmax} trend is considered here.
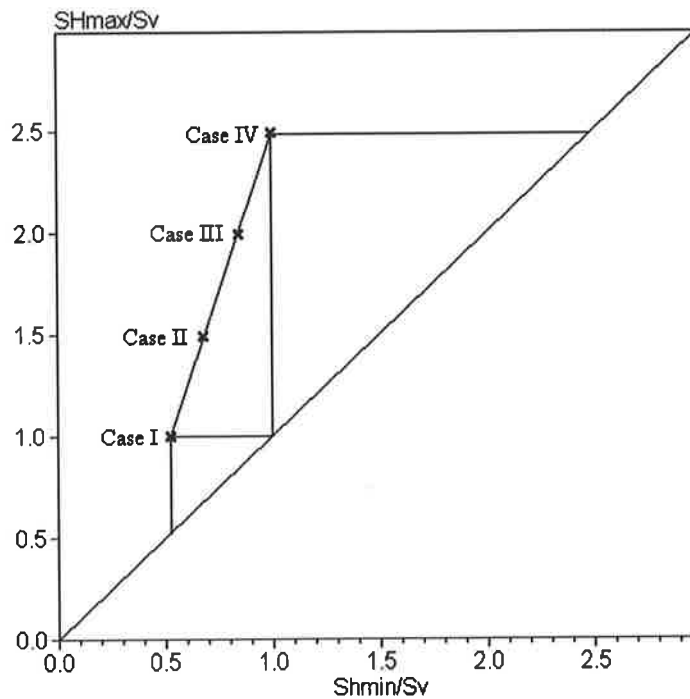
Figure 6.20. Allowable region diagram with stress cases used in structural permeability analysis.

Case	S_{Hmax} MPa/km	S_{hmin} MPa/km	S_v MPa/km	P_p MPa/km
1	24.5	13.0	24.5	7.3
2	36.6	16.7	24.5	7.3
3	48.8	20.7	24.5	7.3
4	61.0	24.5	24.5	7.3

Table 6.6. Stress cases used in structural permeability calculations.

The failure envelope for fractures in the Mereenie Field is not known. A Griffith failure envelope was chosen such that the in situ stress tensor is on the verge of frictional failure (Figure 6.21).
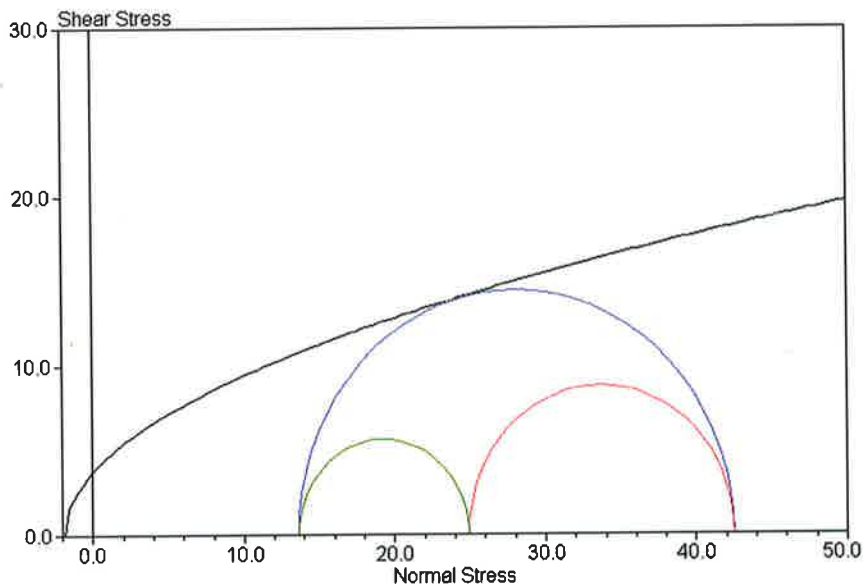
Figure 6.21. Griffith Failure envelope.

The failure envelope is combined with the four stress cases to produce structural permeability diagrams of fracture reactivation risk (Figure 6.22), enabling assesment of the likelihood of specific fracture orientations to be open and hydraulically conductive.

The orientation and abundance of fractures within the field can be investigated by examining core samples and image logs. Natural fractures, conductive on resistivity image logs, were interpreted in image logs from 16 wells in the Mereenie Field (Hillis et al., 1999; Figure 6.23). Hillis et al. (1999) interpreted the pattern of natural fracturing in the Mereenie Field as type 2 fold-related fracturing in the classification of Stearns and Friedman (1972). Type 2 fold-related fractures comprise tensile fractures parallel to the fold axis and orthogonal to bedding, and associated conjugate shear fractures also orthogonal to bedding (Figure 6.24). Observations from image log and core data suggest that natural fracture densities are relatively low in the Mereenie Field (Hillis et al., 1999). However, wells drilled in the Mereenie Field are typically drilled back into the structure at high angles to bedding, minimizing the chance of intersecting type-2 fold related fractures. Consequently fracture densities may be higher than indicated by image logs and core samples.

The observed fracture populations are combined with the in situ stress field and assumed failure envelope to produce fracture susceptibility plots for each of the four stress cases (Figure 6.25).
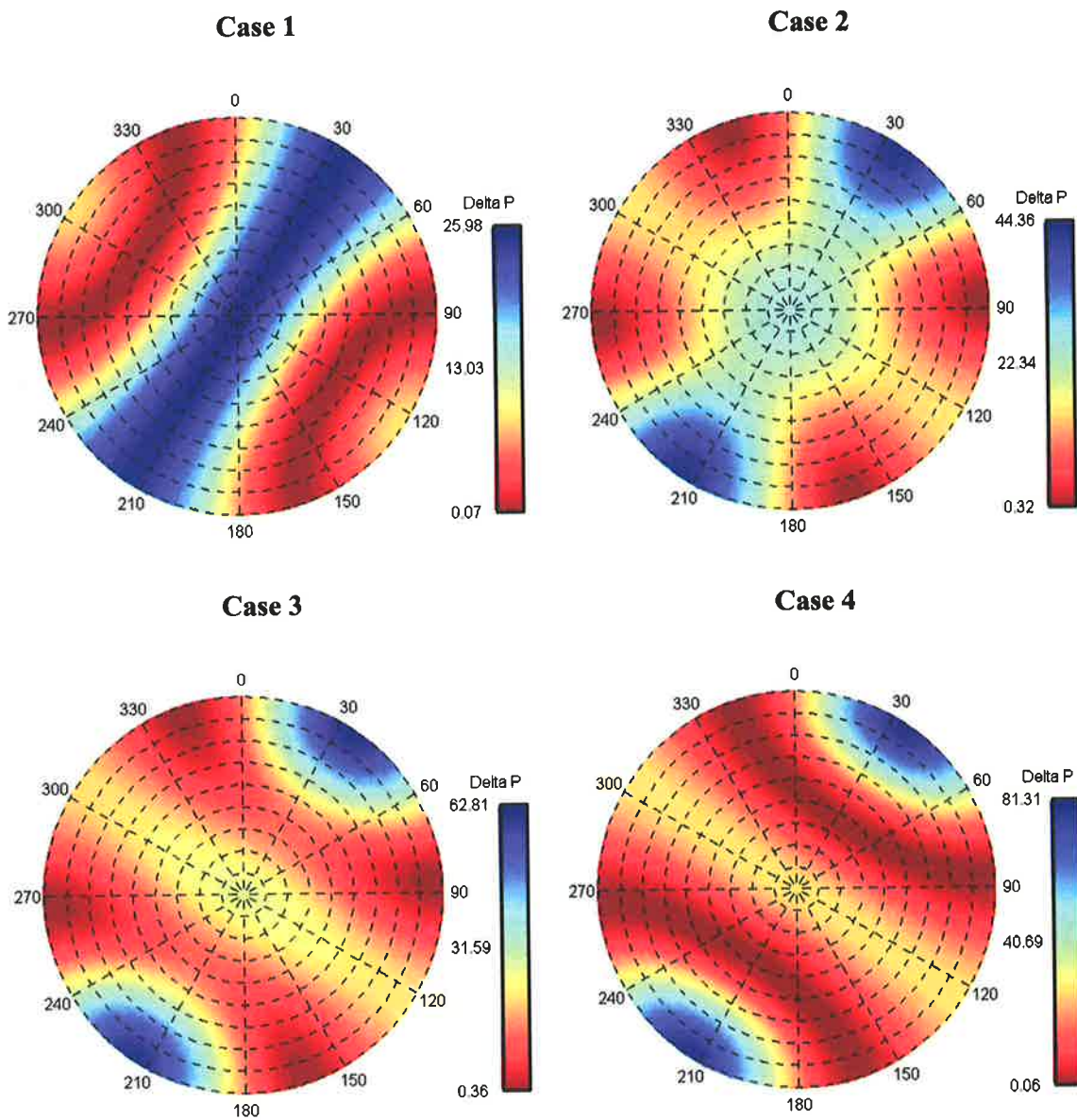
Figure 6.22. Structural permeability diagrams for stress cases in Table 6.6, using a Griffith failure envelopes.
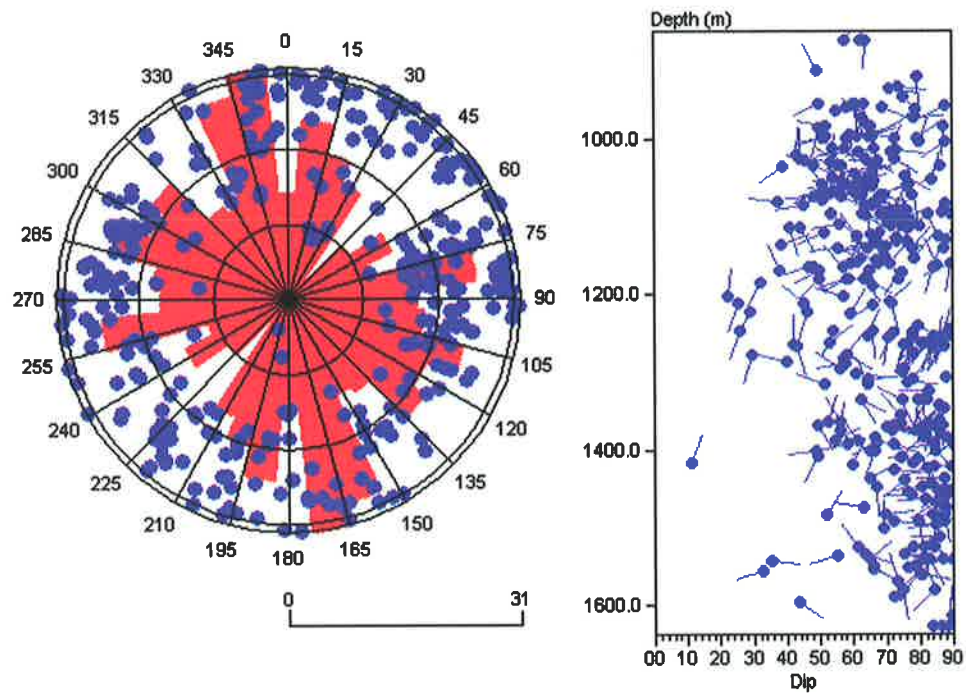
Figure 6.23. Stereonet, rose diagram and depth plot of conductive (on image log) fractures in the Mereenie Field. Stereonet is lower hemisphere poles to planes. Fractures are plotted on the depth plot with dip on the x-axis and the direction of the tadpole indicating the dip direction. The rose diagram (red) is calculated using fracture strikes.

IDEALIZED TYPE 2 ASSEMBLAGE

IDEALIZED TYPE 1 ASSEMBLAGE
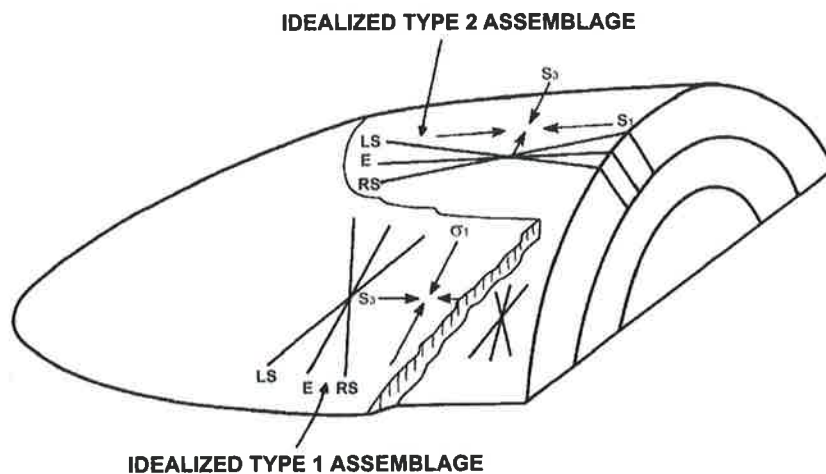
Figure 6.24. Idealised fold-related natural fracture types (after Stearns and Friedman, 1972)
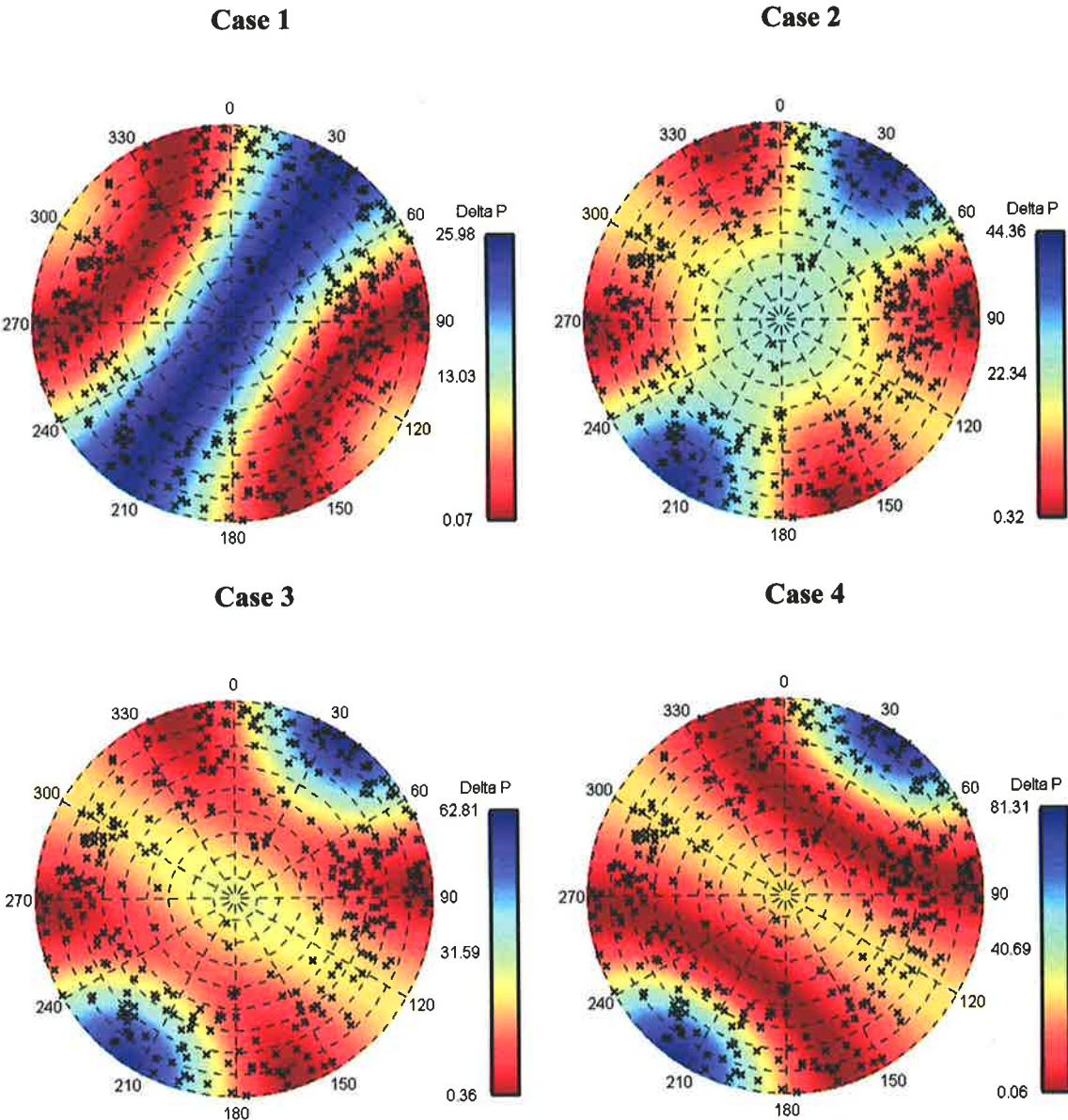
Figure 6.25. Fracture susceptibility plots for stress cases in Table 6.6, using a Griffith failure envelope and conductive (on image log) fractures in the Mereenie Field.

Vertical Fractures striking 000°N and 070°N are among the most likely to be open and conductive in all four stress cases (Figure 6.25). A limited number of fractures were interpreted to strike 070°N (Figure 6.25). However, a significant number of fractures were interpreted to be highly dipping and strike 000°N (Figure 6.25). Consequently, highly deviated wells drilled horizontally in the 090°N or 270°N directions are the most prospective in terms of natural fracture intersection in the Mereenie Field.

6.6. Conclusion

Although there is a relatively low fracture density in the Mereenie Field, the highly dipping north-south striking fracture sets are suitably oriented with respect to the in situ stress field to be open and productive. Given wells to-date have been drilled orthogonal to the pre-existing fracture sets, they may have been undersampled, and the sets suitably oriented within the in situ stress field remain feasible exploration targets. The highly variable nature of S_{hmin} means targeting low S_{hmin} zones, where fracture stimulations are more successful, is not feasible and as at Swan Lake, depletion prior to fracturing remains an important strategy.

7. Gulf of Thailand: Wellbore Stability and Fault Reactivation

7.1. The Problem

The Pattani Basin, Gulf of Thailand (Figure 7.1) is a region of active petroleum exploration and production, in which no information was available on the in situ stress field prior to this study. The in situ stress tensor is of interest in the Pattani Basin with respect to wellbore stability and hydrocarbon migration pathways. It is also relevant to an improved understanding of the contemporary tectonics of the basin, but that issue is not addressed in this thesis.

Production from offshore fields requires drilling wells in a wide variety of azimuths and deviations from fixed platforms. Wellbore trajectory, mud weight, the in situ stress field and rock strength are critical variables controlling wellbore stability. Wells drilled in different trajectories are subject to different stability problems.
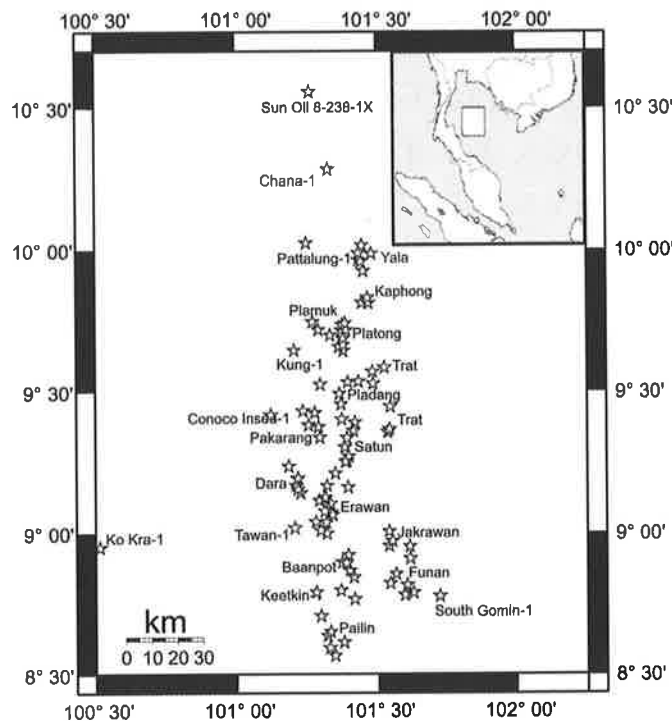
Figure 7.1. Gulf of Thailand location map.

Knowledge of the in situ stress tensor and appropriate planning can mitigate these problems through selection of appropriate mud weights, wellbore trajectories and even selection of the appropriate platform location for a particular target.

The Pattani Basin is dominated by northñsouth trending faults, which in places show northwest-southeast and northeast-southwest jogs and bends. The main oil and gas fields are located in open gently-dipping, faulted antiforms cut by numerous conjugate normal faults. The likelihood of different fault sets providing migration pathways, and associated exploration potential, can be assessed in terms of the reactivation potential of faults within the in situ stress field. As in naturally faulted reservoirs, faults close to failure are those most likely to provide migration pathways.

AGE	Regional Unit	Thicknes (up to)	Lithology		Enviroment	Pattani Basin
Late Miocene-Recent	IV	1700 m	Western graben area clay/shale/sandstone clay/shale, brown-grey varicoloured, silty sandstone, fine-very coarse grained, occasionally gravel.	Pattani & Malay Basins clay/shale/sandstone clay/shale, grey, silty sandstone, grey, fine-very coarse grained, channelised.	Flood plains with more mangrove swamp and marine deposits in upper part	V / MMU
Middle Miocene-Late Mid Miocene	III	1200 m	Shale/claystone, varicoloured, redbrown, silty and sandy. Sandstone, brown, varicoloured, fine-coarse grained, average thickness 5m, restricted lateral extent. Limestone streaks lignite are occasionally present.		FLood plains with local delta plain	IV
Early Miocene-Mid Miocene	II	800 m	Shale/grey, organic rich Sandstone, brown-grey, veryfine-medium grained, average thickness 4.5 m., significant lateral extent.		Lacustrine and restricted marine	III / II
Late Oligocene-Early Miocene	I	5000 m	Shale, brown-grey, varicoloured. Sandstone, brown-grey, veryfine-coarse grained, fining upward, channelised.		Alluvial and flood plains with ephemeral lacustrine conditions	I
Pre-Tertiary Basement			Mesozoic Clastics and Granites, Paleozoic Clastics and Carbonates			

MMU = Middle Miocene Uncomformity

Figure 7.2. Stratigraphy of the Gulf of Thailand (after Lian and Bradley, 1986).

This chapter determines the in situ stress tensor in the Pattani Basin by combining the available data with routine and non-routine stress determination techniques. Knowledge of the in situ stress tensor is applied to fault reactivation-related fluid migration and to wellbore stability.

7.2. Routine Stress Determination Techniques

7.2.1. Vertical Stress

Hillis et al. (2001) determined the vertical stress magnitude in the Pattani Basin from data acquired in 21 wells in seven fields in the Pattani Basin, using techniques described in Section 3.2 (Figure 7.3). The vertical stress in the Pattani Basin is closely approximated by the power law function:

$$S_V = 0.0085 \ z^{1.1257} \qquad\qquad Eq. \ 7.1,$$

where the vertical stress is in MPa and z is depth in meters below sea-level (Hillis et al., 2001).
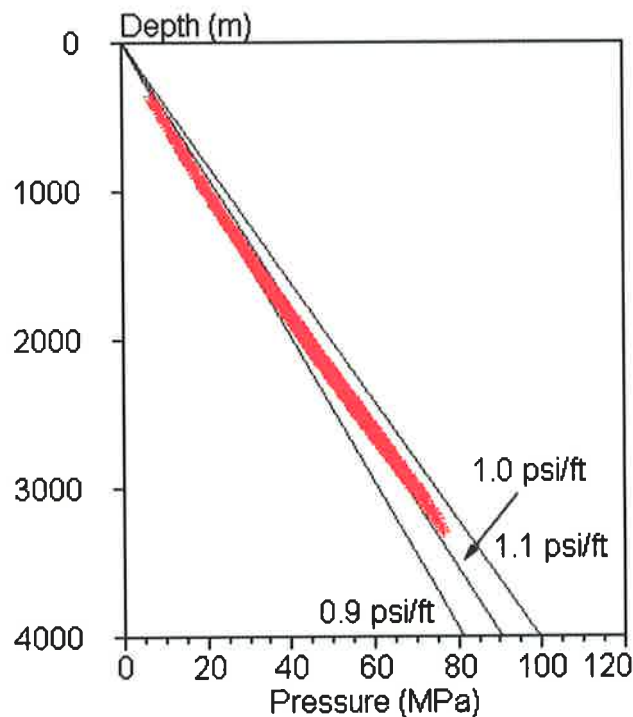
Figure 7.3. Vertical stress magnitude calculated in 21 wells in seven fields in the Pattani Basin (from Hillis et al., 2001).

The vertical stress magnitudes calculated are consistent throughout the Pattani Basin (Figure 7.3), and the mean values upon which Equation 7.1 is based are likely to be robust throughout the Pattani Basin. As is seen in most basins worldwide, there is a variation in the vertical stress gradient with depth from approximately 20 MPa/km at

1000 m to 23 MPa/km at 3000 m. This increase in vertical stress gradient with depth is related to increased rock density with depth due to sediment compaction.

7.2.2. Horizontal Stress Orientations

Horizontal stress orientations were inferred from wellbore breakouts interpreted using dipmeter log (HDT) data from 51 wells in the Pattani Basin. No image log data were available for the basin. Breakouts were interpreted using the methodology described in Section 3.4 and Table 3.1 (Hillis et al., 2001). A total of 298 breakouts were interpreted in 42 wells. Of the nine wells with no interpreted breakouts, four could not be interpreted due to tool problems (tool sticking or erroneous calipers), and three were highly deviated. The three logs run in wells deviated by more than 10° were found to be strongly key-seated and to exhibit no rotation. The results for the entire basin are shown in Figures 7.4 ñ 7.6. Figure 7.4 summarizes S_{Hmax} orientations inferred from breakouts for the entire basin as un-weighted and length-weighted rose diagrams. Figures 7.5 and 7.6 show S_{Hmax} orientations inferred from breakouts for individual wells across the basin, projected on the MMU horizon (B37-6) structural map and on the near top sequence 3 reflector (C61-3) structural map respectively.

Un-Weighted S_{Hmax} Directions
From Breakouts
Mean = 180 , S.D = 40.4

Length-Weighted S_{Hmax} Directions
From Breakouts
Mean = 178 , S.D = 38.6
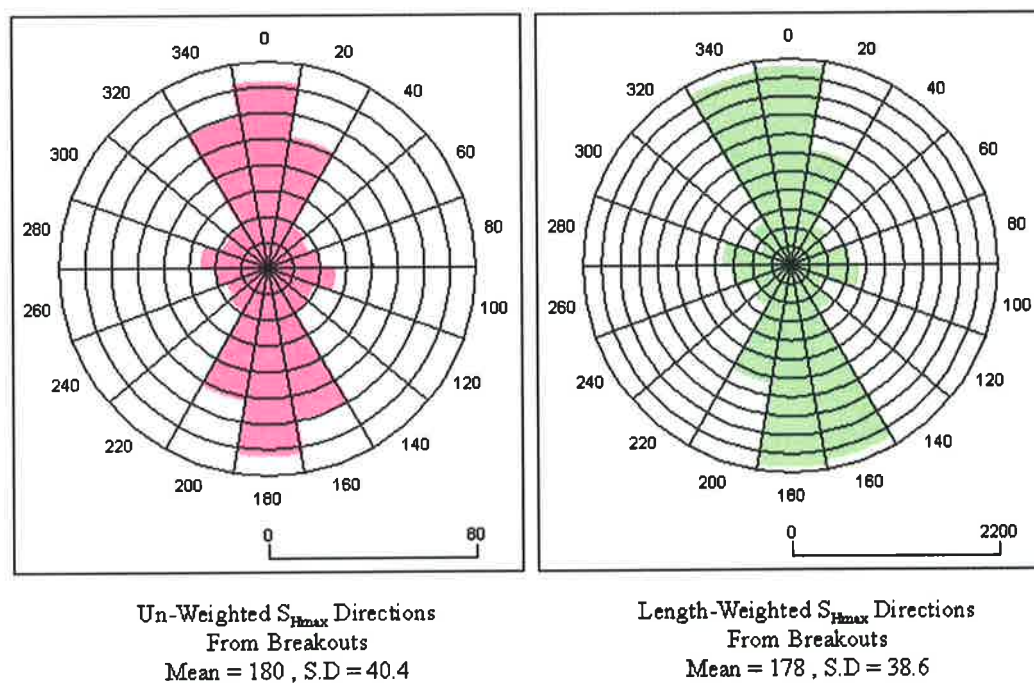
Figure 7.4. Summary of S_{Hmax} directions inferred from wellbore breakouts in the Pattani Basin (from Hillis et al., 2001).
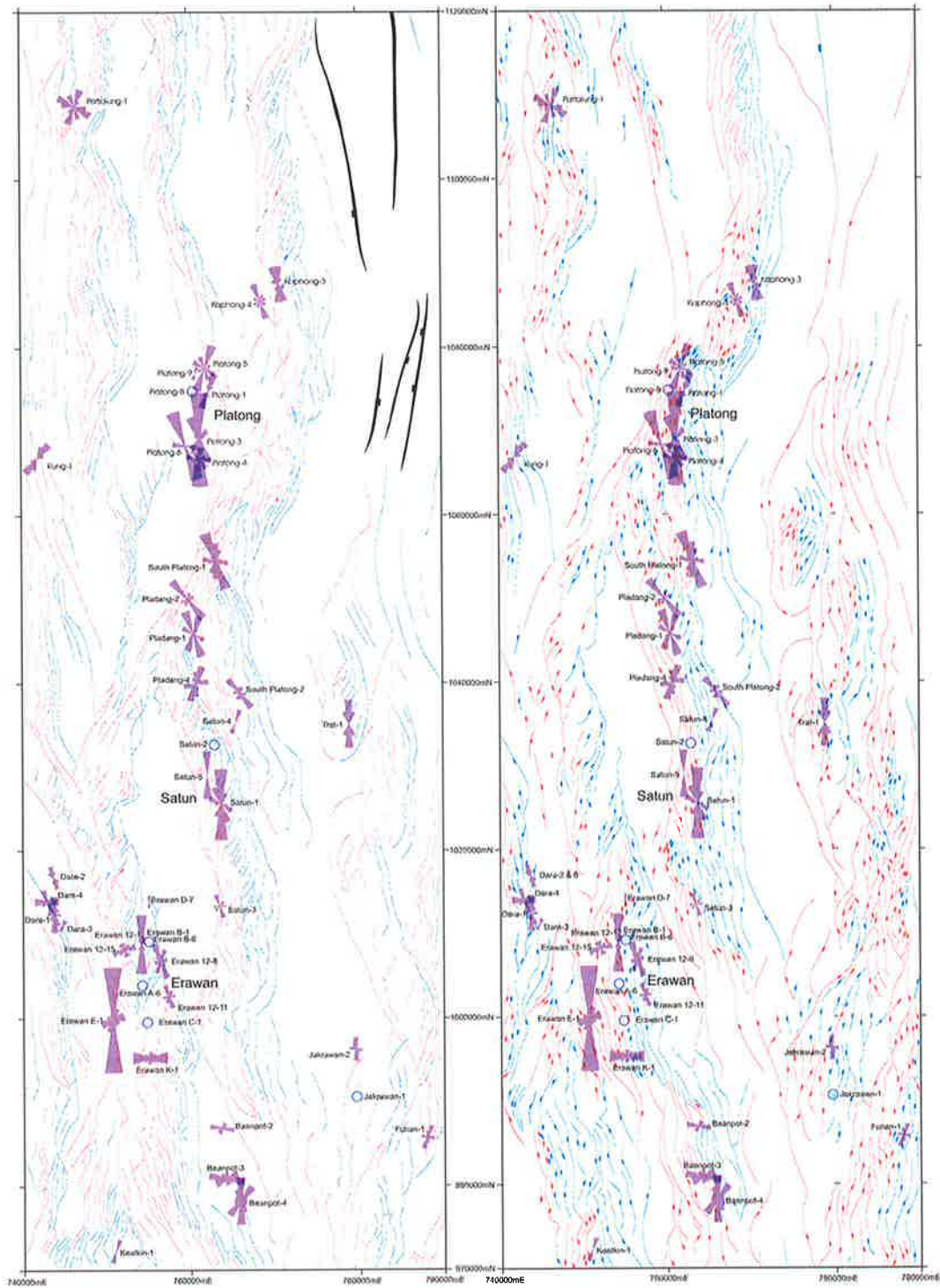
Figure 7.5. Un-weighted S$_{Hmax}$ orientations inferred from wellbore breakouts superimposed on (a) Structure at C61-3 (near top sequence 3). (b) Structure at B37-6 (i.e. MMU, or near top sequence 4) level (from Hillis et al., 2001).
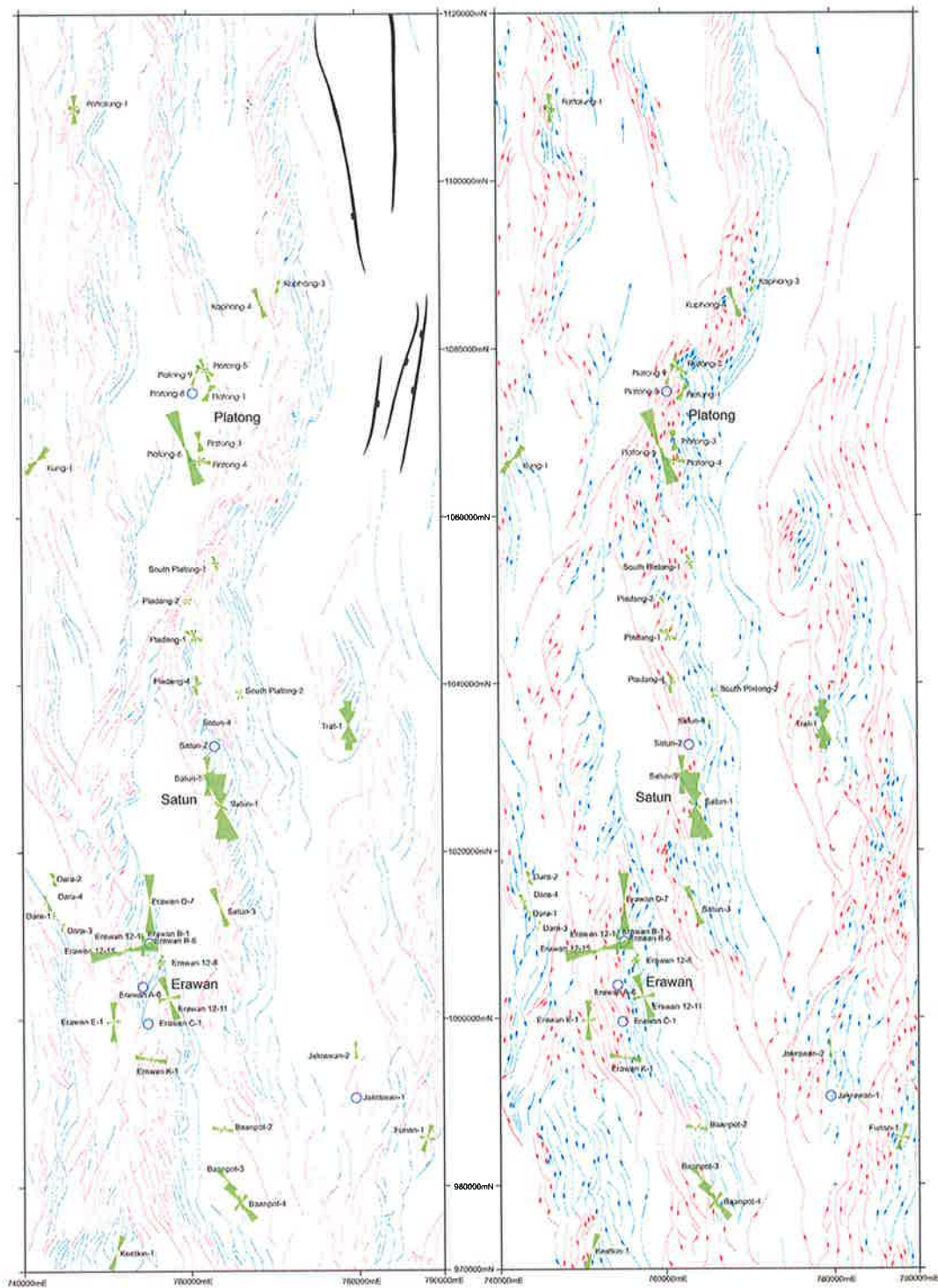
Figure 7.6. Length-weighted S_{Hmax} orientations inferred from wellbore breakouts superimposed on (a) Structure at C61-3 (near top sequence 3). (b) Structure at B37-6 (i.e. MMU, or near top sequence 4) level (from Hillis et al., 2001).

Breakout-inferred S_{Hmax} orientations are predominantly north-south, parallel to the structural grain of the basin (Hillis et al., 2001; Figures 7.5 and 7.6). The maximum horizontal stress orientation parallels variations in the structural grain from its regional north-south orientation in several regions of the basin. For example, the S_{Hmax} orientation between the Satun and Kaphong Fields is parallel to fault strike in nearly all wells, paralleling fault strikes that range from NNW-SSE to NE-SW (Figures 7.5 and 7.6). The fault strike-parallel nature of the S_{Hmax} direction is somewhat better developed with respect to near top sequence 3 (C61-3) structure than MMU (B37-6) structure.

The correlation between the structural grain and S_{Hmax} orientation is consistent across the basin, with the exception of four wells (Baanpot-2, Baanpot-3, Dara-4 and Erawan K-1). These wells exhibit east-west S_{Hmax} orientations that are perpendicular to the structural grain. The origin of these local perturbations is uncertain and may be the result of stresses locally rotated perpendicular to faults that have higher strengths than the surrounding rock (Bell, 1996b) or enlarged pre-existing natural fractures/drilling-induced tensile fractures are being mistaken for borehole breakouts (Dart and Zoback, 1989). Image logs would be required to unambiguously interpret whether the localised east-west S_{Hmax} orientations are genuine local deflections of the stress field, or due to enlarged pre-existing natural fractures and drilling-induced tensile fractures being mistaken for borehole breakouts (Hillis et al., 2001).

7.2.3. Minimum Horizontal Stress Magnitude

The minimum horizontal stress was determined from 112 leak-off test pressures from the entire basin and three minifracture tests from the Erawan Field (Figure 7.7).

Ideally pressure/time records for all leak-off tests would be checked to ensure consistent interpretation of leak-off pressures. However, pressure/time records were only available for 16 of the tests. Inspection of the available pressure/time records for the Pattani basin suggests that leak-off pressures have been consistently interpreted.

Three minifracture tests were undertaken in the Erawan Field (within the overpressured interval). Closure pressures for all three tests were available, while pressure time records were available for two of the tests. Consequently, closure pressures were interpreted from the two available pressure time records in accordance

with the techniques described in Section 3.5.2 (Figures 7.8 and 7.9). These interpreted fracture closure pressures (Erawan C-21: P_c = 48.6 MPa, Figure 7.10; Erawan C-23: P_c = 48.3 MPa, Figure 7.11) are consistent with those provided by the operator.
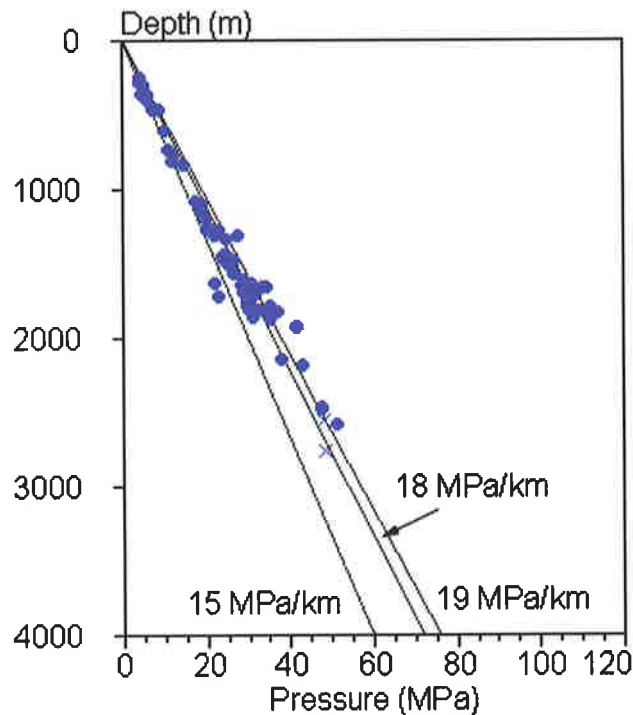
Figure 7.7. Depth plot showing 126 LOTs (●) and three minifracture test P_c (✕) from wells in and adjacent to the Pattani Basin.

The lower bound to leak-off pressures in the Pattani Basin suggests that the S_{hmin} gradient is 15 MPa/km (0.66 psi/ft) in the normally pressured sequences. There are a significant number of leak-off pressures in excess of the 15 MPa/km gradient, but most of these elevated leak-off pressures were from tests performed in deviated wells, where leak-off pressure does not yield S_{hmin} (as discussed further in Section 7.3.1), or overpressured sequences. The S_{hmin} gradient of 15 MPa/km is an appropriate lower bound to leak-off test pressures obtained in vertical wells through normally pressured sequences.

As is commonly seen worldwide (eg. Breckels and van Eeklen, 1982), minimum horizontal stress is elevated in the overpressured sequences and is reasonably described by a gradient of 19 MPa/km (0.84 psi/ft) in the overpressured interval for

the regional dataset and 18 MPa/km (0.80 psi/ft) in the overpressured interval for the Erawan Field. These values must be treated with caution as they are based on a limited amount of data.
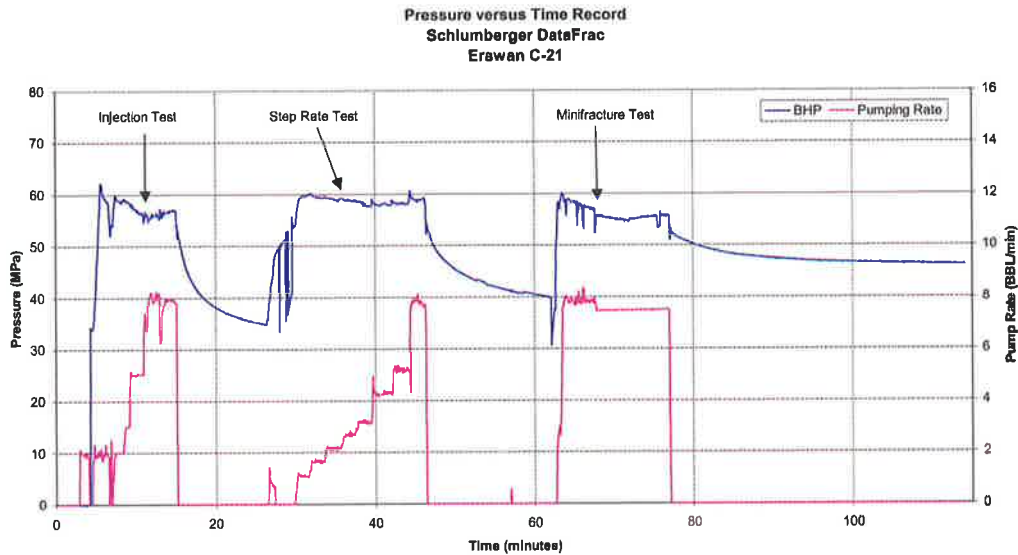
Figure 7.8. Pressure time record from Schlumberger DataFrac conducted in Erawan C-21 prior to main fracture treatment.
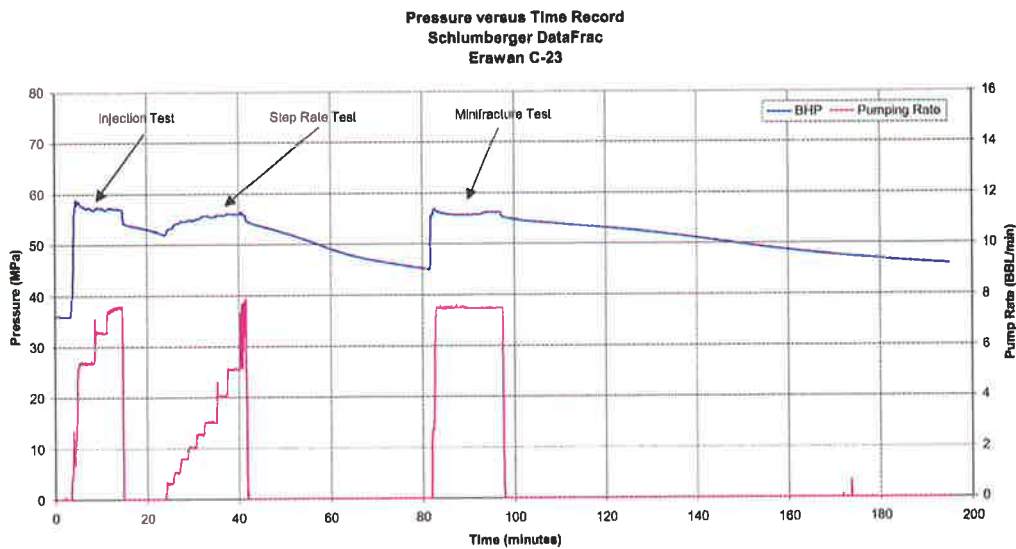
Figure 7.9. Pressure time record from Schlumberger DataFrac conducted in Erawan C-23 prior to main fracture treatment.

138
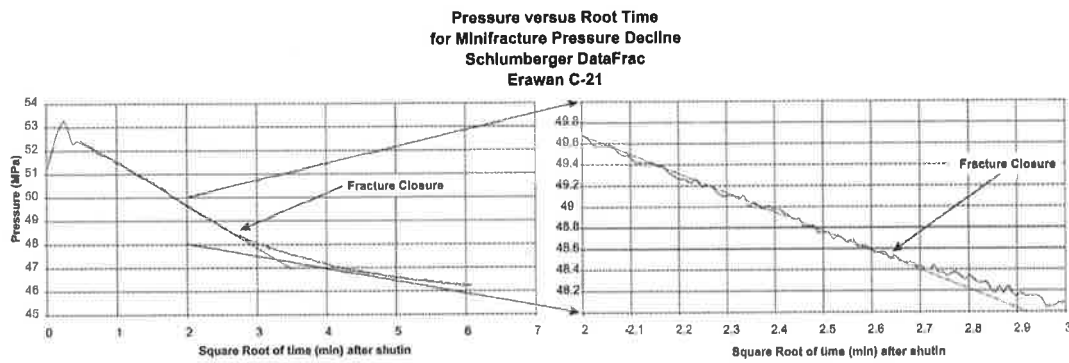
Figure 7.10. Pressure versus root of time after pumping stopped, used to determine P_c.
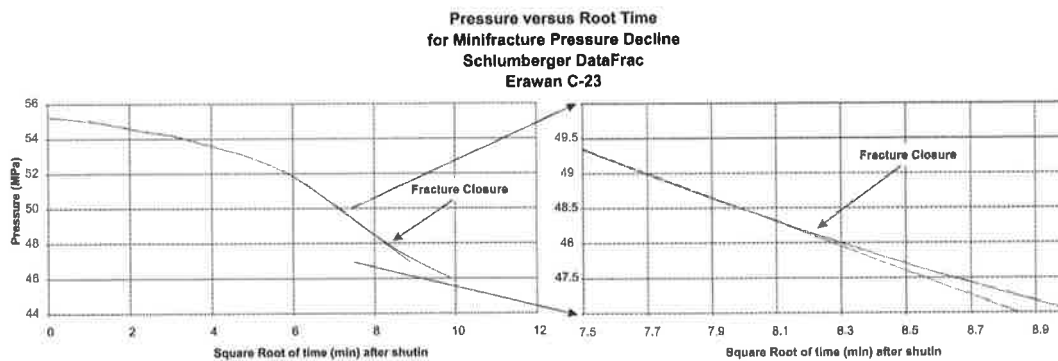
Figure 7.11. Pressure versus root of time after pumping stopped, used to determine P_c.

7.2.4. Pore Pressure

Pore pressures were determined from mud weights in 57 wells, 774 WFIT measurements in 47 wells and 50 DST measurements in 16 wells (Hillis et al., 2001; Figure 7.12). Section 3.7 summarises how these tests yield P_p. The P_p gradient varies from 10.0 MPa/km to 18.7 MPa/km. This represents a significant variation in P_p gradient. Given the variable P_p and S_{hmin} gradients (Section 7.2.3), three stress tensors were considered when investigating the implications of the in situ stress data. The three tensors considered were for normally pressured areas, for typical Pattani Basin regional overpressures and for overpressured zones in the Erawan Field.

7.3.   Non-Routine Stress Determination Techniques

The maximum horizontal stress, as is often the case, is the most problematic aspect of the in situ stress tensor to constrain in the Pattani Basin. Furthermore, many of the commonly applied methods for constraining S_{Hmax} could not be applied in the Pattani

Basin, due to a lack of data. The occurrence/non-occurrence of borehole breakouts (Section 3.6.2) and drilling-induced tensile fractures (Section 3.6.3) could not be utilised to constrain S_{Hmax} because neither image log nor rock strength data were available. Re-opening pressures interpreted from the minifracture tests (Section 3.6.1), could not be used because the minifracture tests were conducted in cased holes. Frictional limits can be used to constrain S_{Hmax} magnitudes where the S_v and/or S_{hmin} and P_p are known (Section 3.6.4). Frictional limits to S_{Hmax} calculated using known the known minimum stress S_{hmin} (Section 7.2.3) and P_p (Section 7.2.4) are listed in Table 7.1. However these provide only upper limits to S_{Hmax} in a strike-slip stress regime.
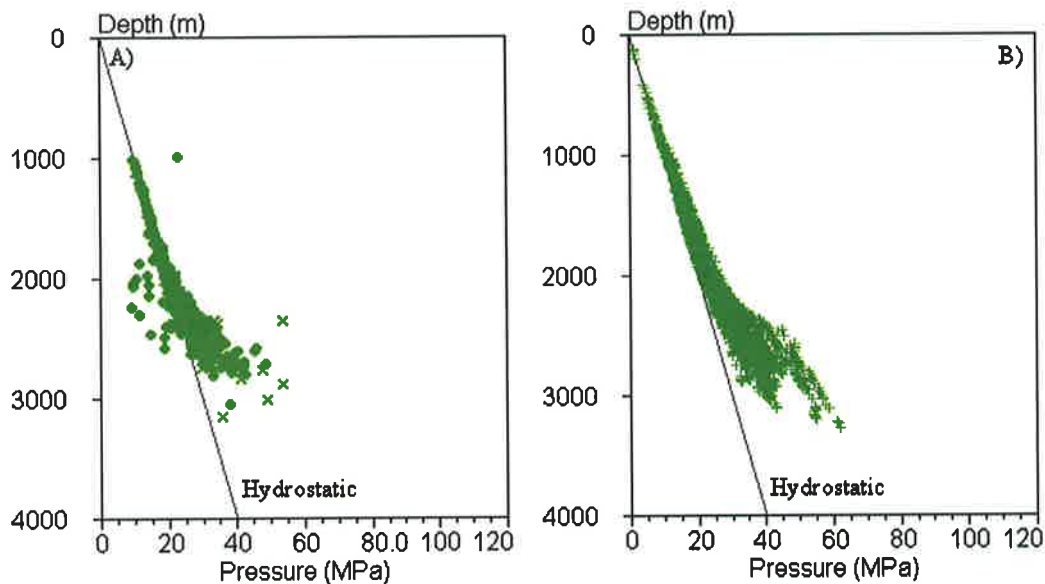
Figure 7.12. Pore pressure in the Pattani from 774 WFITs (•) and 50 DSTs (X)(A) and P_w (+) from 57 wells (B).

	S_{hmin} Gradient (MPa/km)	P_p Gradient (MPa/km)	S_{Hmax} Gradient from Frictional Limit (MPa/km)
Normally Pressured	15	10	25.5
Regional overpressured	19	14.5	28.5
Erawan Field overpressured	18	14	26.5

Table 7.1. Summary of frictional limits to S_{Hmax}.

In the absence of other available methods for constraining S_{Hmax}, modelling was undertaken of a systematic variation in leak-off pressures (LOP) with wellbore deviation that was observed in the data (Figure 7.13). Aadnoy (1990a) proposed a method for constraining the complete in situ stress tensor using leak-off pressure from wellbores of different deviations and azimuths. A variation of this technique developed by the author is used to constrain S_{Hmax} herein.
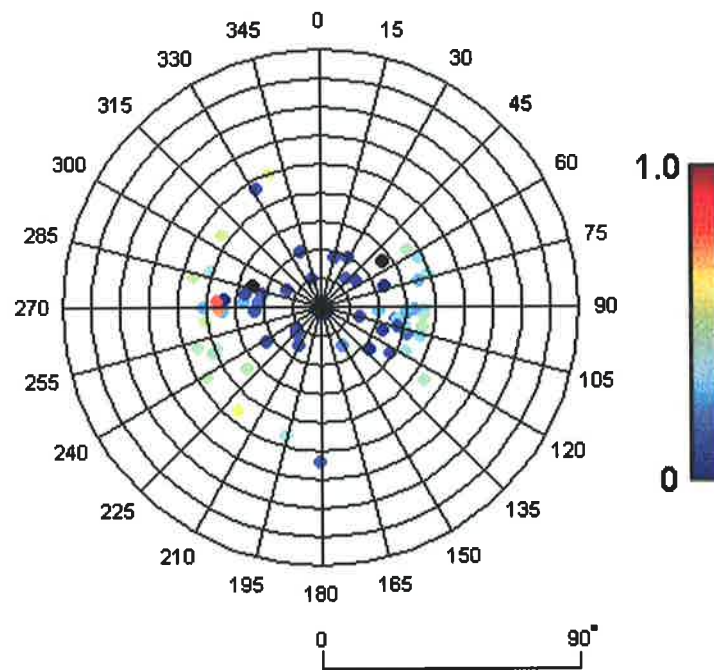
Figure 7.13. Polar diagram of wellbore azimuths and deviations for leak-off tests conducted above 1650 m (normally pressured), coloured by effective mud weight (emw). Blue (•) indicates a low emw while red (•) indicates a high emw.

7.3.1. Forward Modelling of Variation in Leak-Off Pressures

Aadnoy (1990a) proposed a method for inverting LOPs from wells of different orientations and deviations to constrain the complete in situ stress tensor. Aadnoy's (1990a) mathematical inversion can be unstable and is limited by the unreliability of leak-off pressures (inconsistent test procedures and interpretations), and the assumption that all leak-off pressures being considered are subject to the same stress field (Gj□hnes et al., 1998). Furthermore, Aadnoy's (1990a) inversion ignored all shear stress components. Gj□hnes et al. (1998) developed an inversion technique utilising all stress components and found significant errors resulting from shear

stresses being ignored. Gj□hnes et al. (1998) concluded that additional methods need to be combined with the LOP inversion, in order that uncertainty is reduced. In the technique used herein, the LOP variation with azimuth and deviation is forward modelled for a number of different S_{Hmax} scenarios in order to see which best fits the observed data. This forward modelling removes the potential numerical instability of the inversion.

Leak-off tests have been conducted in wells in the Pattani Basin with deviations of up to 53ʃ, and 85 leak-off tests have been conducted in wellbores with deviations greater than 15°. Leak-off tests conducted in the Pattani Basin display a systematic increase in LOP gradient with wellbore deviation that is considered to reflect the state-of-stress (Figure 7.13). However, this trend is superimposed on an increase in LOP gradient with depth (Figure 7.7). This increase in LOP gradient with depth is probably the result of the increase in P_p gradient with depth (Figure 7.12; Section 7.2.4; Breckels and van Eeklen, 1982). Consequently, only LOTs conducted in the normally pressured zone, above 1650 m, are considered in this analysis (in order to remove LOP variation due to P_p).

The inversions developed by Aadnoy (1990a) and Gj□hnes et al. (1998), and the forward modelling undertaken herein rely on the relationship between the fracture initiation pressure and hence leak-off pressure, and the minimum stress (σ_{tmin}) at the wellbore wall. The minimum wellbore stress is in turn controlled by the in situ stress tensor and the wellbore trajectory (Section 4; Equations 4.1 - 4.11). Consequently, fracture initiation pressure varies systematically with wellbore deviation and azimuth within a given stress field.

Given Equations 4.1 - 4.11, if S_{Hmin}, S_v, and P_p have been constrained the only unknown in forward modelling LOPs is S_{Hmax} (Section 7.2).

The variation of LOP with wellbore azimuth and deviation was predicted for five cases of S_{Hmax}, with S_{Hmax} ranging from S_{hmin} to frictional limit (Table 7.2; Figure 7.14). The aim of the forward model is not to match the actual LOP, but the relative variation in LOPs with deviation and azimuth. Hence, the scales on the forward models (Figure 7.14), and the observed data (Figure 7.13), are all normalised to the range 0-1 and illustrate relative increases in LOP.

Case	S$_{Hmax}$ (MPa)	S$_v$ (MPa)	S$_{hmin}$ (MPa)	P$_p$ (MPa)	S$_{Hmax}$ Orientation
I	15	20	15	10	000∫N
II	17.5	20	15	10	000∫N
III	20	20	15	10	000∫N
IV	22.8	20	15	10	000∫N
V	25.5	20	15	10	000∫N

Table 7.2. The five cases for which forward models of fracture initiation (leak-off) pressures were determined. The cases cover the range of possible values of S$_{Hmax}$ within frictional limits. S$_v$, S$_{hmin}$, and P$_p$ are independently constrained, and are the same in all five cases.

Case I predicts decreasing LOPs with increasing deviation (Figure 7.14). This is the opposite of the observed increase in LOP with deviation and hence S$_{Hmax}$ C S$_{hmin}$. This is further supported by the common occurrence of breakouts in vertical wells indicating significant anisotropy between S$_{Hmax}$ and S$_{hmin}$. Case V predicts no significant variation in leak-off pressure for the range of deviations seen in the Pattani Basin (Figure 7.14), and hence is also not a reasonable case. Case V is at the frictional limits to stress, and the absence of seismicity in the Gulf of Thailand is consistent with the stresses being somewhat below their frictional limit.

Case II predicts an increase in LOPs in wells deviated towards 250-290∫N and 070-110∫N, and no change or a decrease in LOPs in wells deviated in other directions (Figure 7.14). This is inconsistent with observation and hence Case II is not valid.

Cases III and IV show the best match to the observed leak-off pressure data. Given the common occurrence of breakouts in vertical wells in the Pattani Basin, it is likely that there is significant anisotropy between S$_{Hmax}$ and S$_{hmin}$, and hence Case IV is the preferred case.
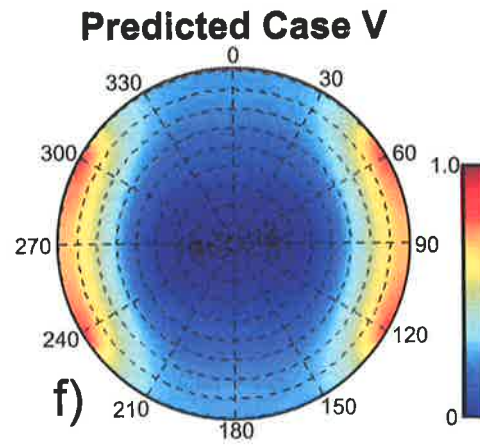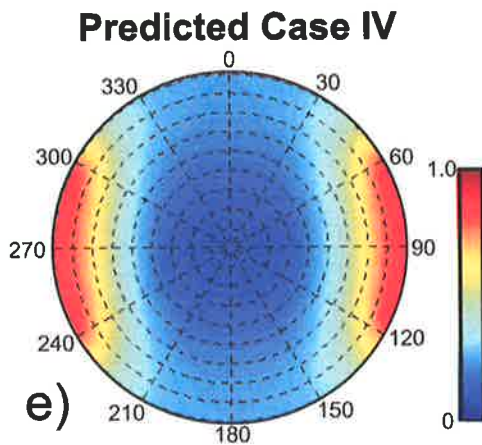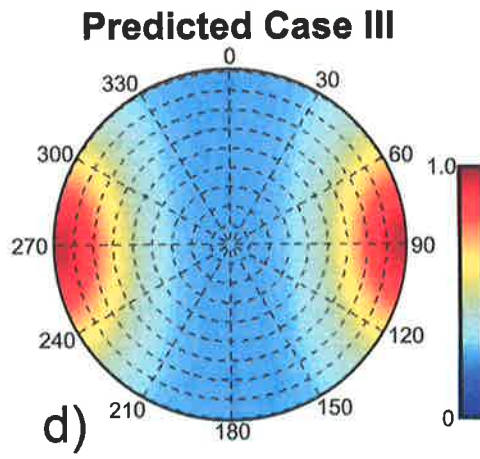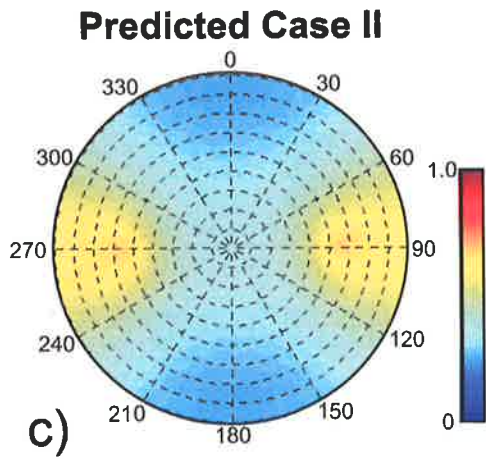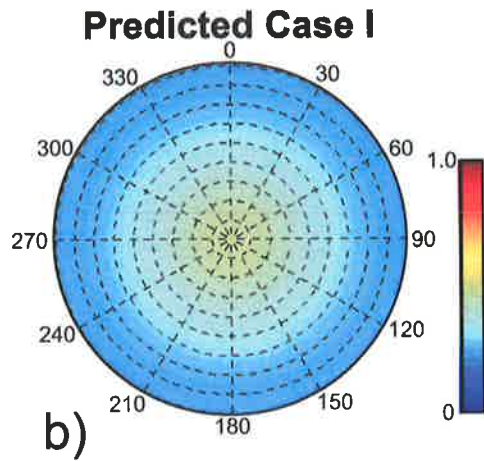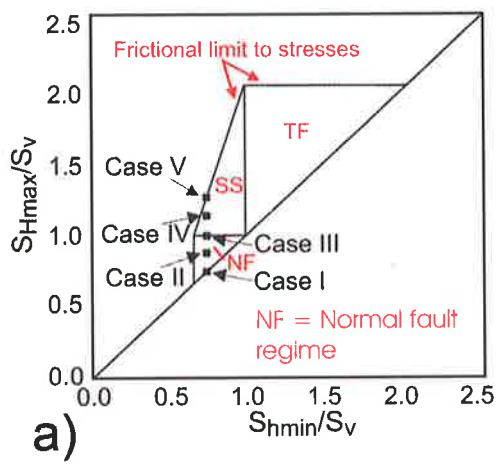
Figure 7.14. a) Cases I-V for which leak-off pressures variation with deviation and azimuth was forward modelled. b) - f) Predicted variation of leak-off pressure with deviation and azimuth for cases I-V respectively. Observed variation of leak-off pressure shown in Figure 7.13.

7.4. Gulf of Thailand In Situ Stress Tensor

The Gulf of Thailand in situ stress tensor has been determined using variation in LOPs with deviation and azimuth combined with S_v from density logs and checkshot surveys (Section 7.2.1), S_{Hmax} orientation from wellbore breakouts (Section 7.2.2), S_{hmin} from LOTs and minifractures (Section 7.2.3) and P_p from WFITs and DSTs (Section 7.2.4). The normally pressured zone is subject to a strike-slip stress regime in which S_{Hmax} is only slightly greater than S_v (Table 7.3). The maximum horizontal stress is not constrained in the overpressured zone which is subject to a range of possible stress states represented by the vertical line in Figure 7.15. However, the lack of seismicity and continued occurrence of wellbore breakouts in the over pressured interval suggests a stress regime similar to that of the normally pressured zone, i.e. a strike-slip faulting regime close to the boundary of normal faulting regime (Table 7.3).

Stress Component	Normally Pressured	Over Pressured
S_{Hmax} Orientation	000°N	000°N
S_v	20 MPa/km	23 MPa/km
S_{hmin}	15 MPa/km	18 MPa/km
P_p	10 MPa/km	14 MPa/km
S_{Hmax}	~20 - ~22.8 MPa/km	18< - < 26.5 MPa/km
Most Likely S_{Hmax}	22.8 MPa/km	24.6 MPa/km

Table 7.3. Pattani Basin in situ stress tensor for normally pressured and overpressured zones.

The vertical stress gradient in the normally pressured scenario is taken to be that at approximately 1 km depth, and in the overpressured scenario, approximately that at 3 km depth, but in situ stress gradients are used in order that the stress data are essentially depth-independent. The values summarised in Table 7.3 are used in the following sections in considering the implications of the in situ stress tensor for fault reactivation-related hydrocarbon migration and wellbore stability.
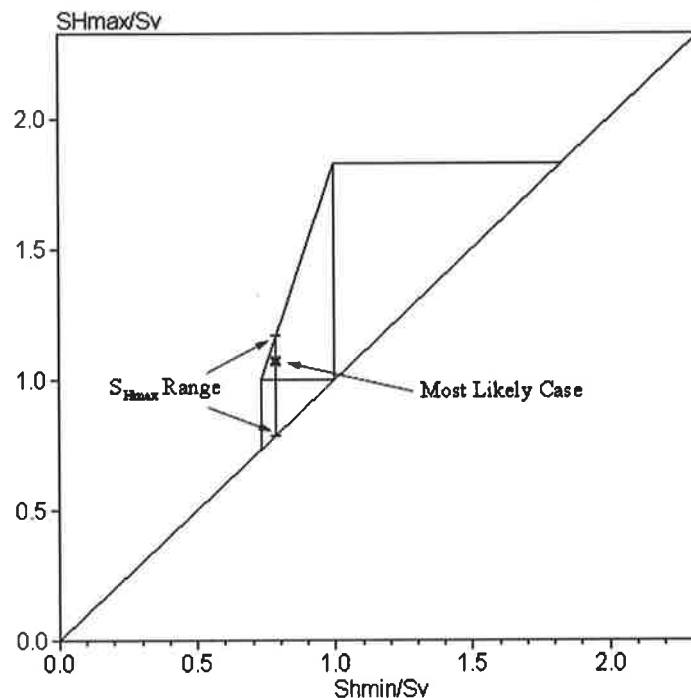
Figure 7.15. Allowable region diagram showing possible variation in S_{Hmax} and the most likely value.

7.5.   Implications

7.5.1.   Wellbore Stability

The normally pressured and overpressured in situ stress scenarios (Table 7.3) within the Pattani Basin were selected in order to investigate the implications for wellbore stability in the area.

Wellbore stability is assessed in terms of the risk of wellbore collapse due to breakout formation, and risk of lost circulation due to the formation of fractures in the wellbore wall (DITF risk). Breakout risk is calculated in terms of the rock strength (uniaxial, C_0) required to prevent breakout formation normalised to S_v (Section 4.5.10). Drilling induced tensile fracture risk is expressed in terms of the maximum mud weight, above which DITFs will be initiated.

Breakout risk is greatest for vertical wells in both of the stress scenarios considered (Figures 7.16 and 7.17). Vertical wells, drilled in the Pattani Basin, have been successfully drilled. Hence, wells of any trajectory can be successfully drilled, with respect to breakout-related instability, given the same rock strength and drilling
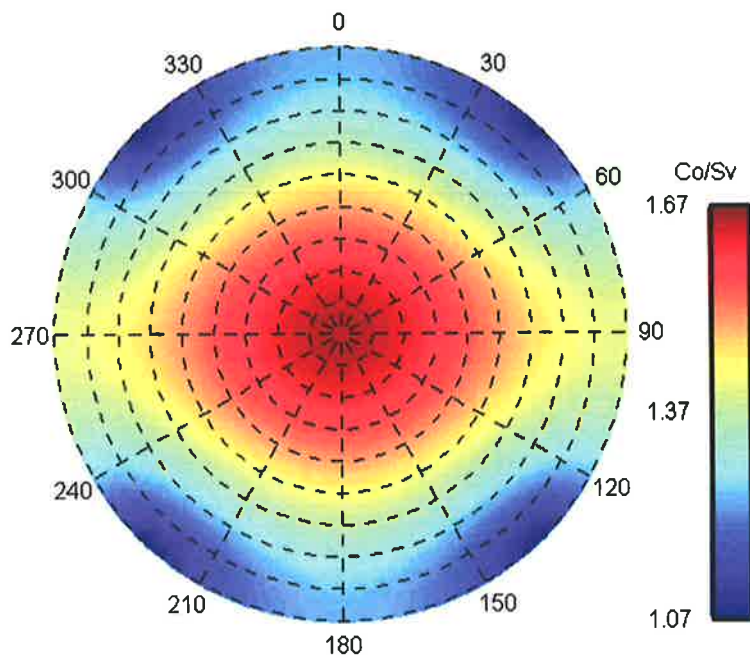
Figure 7.16. Polar diagram of wellbore trajectories coloured by uniaxial rock strength normalised by S_v, required to prevent compressional failure for the normally pressured zone. Red indicates relatively high risk and blue indicates relatively low risk. A vertical well plots at the centre of the polar diagram and has the greatest risk of failure.
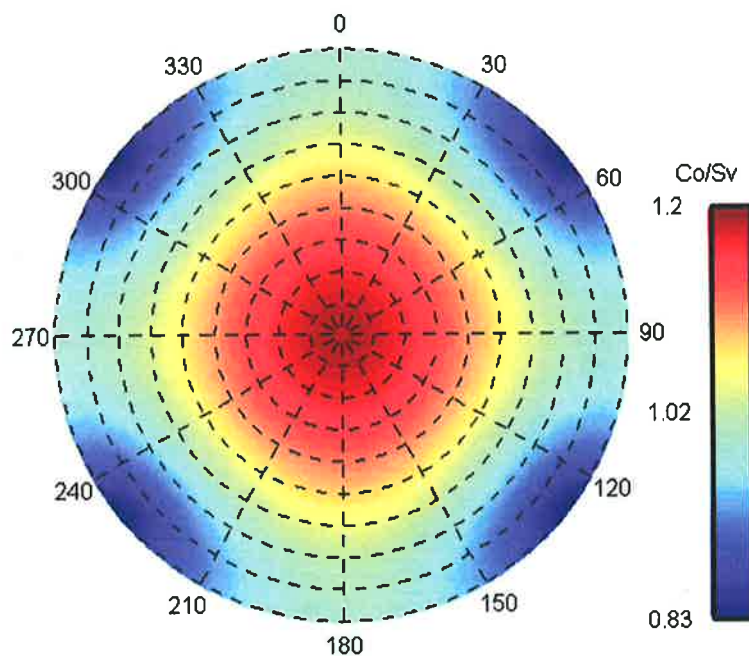
Figure 7.17. Polar diagram of wellbore trajectories coloured by uniaxial rock strength normalised by S_v, required to prevent compressional failure for the overpressured zone. Red indicates relatively high risk and blue indicates relatively low risk. A vertical well plots at the centre of the polar diagram and has the greatest risk of failure.

parameters as encountered in the vertical wells. The successful drilling of wells of a variety of deviations and azimuths, further confirms the predictions of the wellbore stability analysis.

The most stable horizontal drilling trajectories, with respect to breakout-related instability in both scenarios investigated, are approximately NE, SE, SW and NW. Highly deviated wells drilled in these azimuths should be relatively immune from breakout development.

The risk of DITF occurrence, like that of breakout occurrence, is greatest in vertical wells in both of the stress scenarios considered in the Pattani Basin (Figures 7.18 and 7.19). Hence DITFs form at the lowest mud weight in vertical wells. DITF risk reduces only slightly for wells deviated in the S_{Hmax} direction, but decreases significantly for wells deviated in the S_{hmin} direction, i.e. DITF risk is lowest for wells highly deviated in the east or west direction. This is likely to be of greatest significance in overpressured zones, partly because the risk of forming DITFs in the overpressured zones is higher than that in the normally pressured intervals, but also because the safe mud weight envelope is generally narrower in overpressured intervals. In overpressured zones, where an elevated mud weight is required, wells deviated in the S_{hmin} direction, are less likely to see mud loss due to the fracture gradient being exceeded.

All the wellbore stability results above should be considered as relative values of stability for different trajectories, rather than absolute values. No rock strength data are available, nor have the results been calibrated against drilling experience to take account of factors such as surge and swab pressures and stresses induced by the cooling effect of drilling mud on the wellbore wall. Such calibration needs to be undertaken in order to make predictions of appropriate mud weights for particular wellbore trajectories in particular regions of the Pattani Basin.
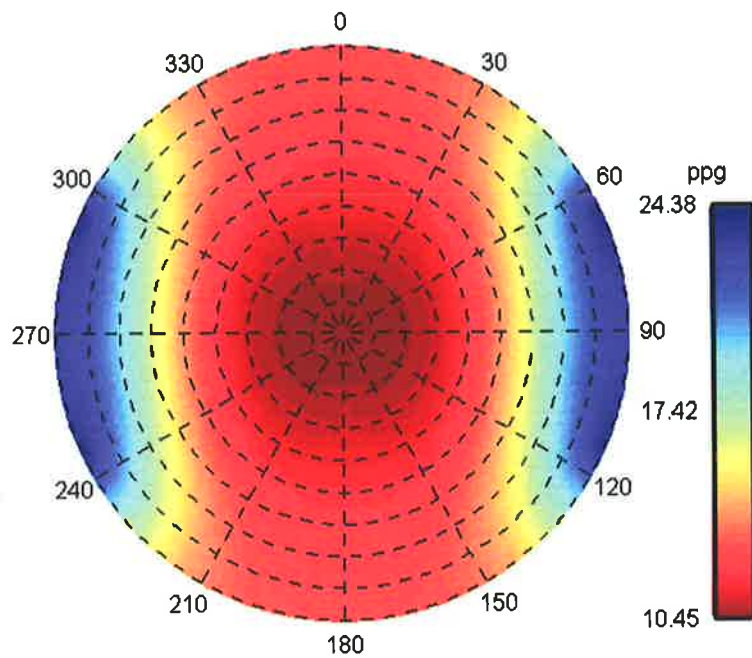
Figure 7.18. Polar diagram of wellbore trajectories coloured by maximum mud weight (ppg), above which DITF will occur for the normally pressured zone. Red indicates relatively high risk and blue indicates relatively low risk. A vertical well plots at the centre of the diagram and has the greatest risk of failure (i.e. the lowest maximum mud weight).
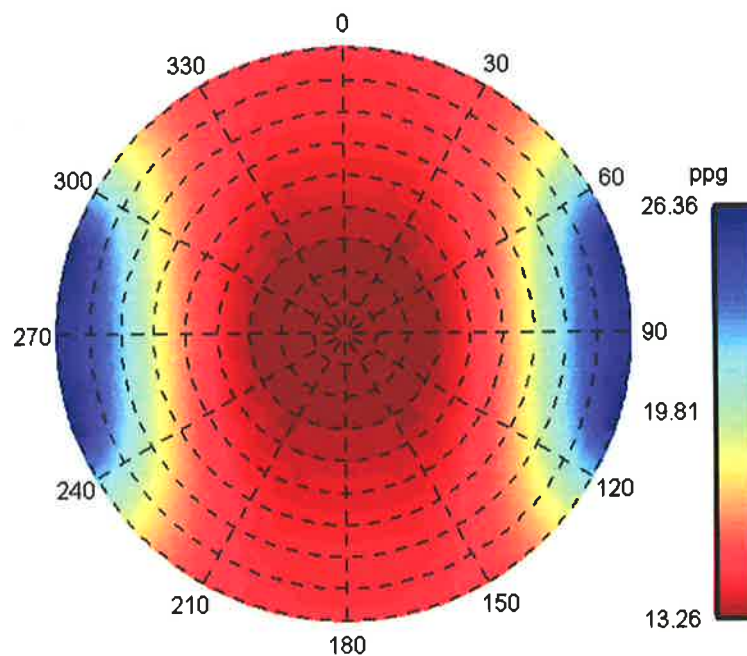
Figure 7.19. Polar diagram of wellbore trajectories coloured by maximum mud weight (ppg), above which DITF will occur for the overpressured zone. Red indicates relatively high risk and blue indicates relatively low risk. A vertical well plots at the centre of the diagram and has the greatest risk of failure (i.e. the lowest maximum mud weight).

7.5.2. Fault Reactivation

The implications of the in situ stress tensor in the Pattani Basin for fault reactivation and hydrocarbon migration pathways are discussed in this section for both normally and over pressured scenarios (Table 7.3).

As discussed in Section 6.5.2, fault reactivation is closely linked to subsurface fluid flow and hence the migration, accumulation, breaching and re-migration of hydrocarbons. There is abundant evidence that active faults and fractures, i.e. those subject to stresses close to those that induce failure, provide high permeability conduits for fluid flow during deformation (Sibson, 1994; Barton et al., 1995). Furthermore, active faults and fractures provide conduits for fluid flow even in shaly systems (Dewhurst et al., 1999).

Although in the Pattani Basin we are concerned with predicting faults that are likely to provide hydrocarbon migration pathways (and thereby refining exploration models), as opposed to looking for hydraulically conductive fractures in low permeability reservoirs, the methodology is the same as that used in the Mereenie Field (Section 6.5.2). The known in situ stress field is combined with an assumed failure envelope to determine the likelihood of reactivation of fault orientations (Figures 6.21 and 6.22). The in situ stress field and failure envelope used are shown in Figures 7.20 and 7.21.

Significant vertical fluid migration is observed in the Pattani Basin. Despite the lack of present day seismicity in the Pattani Basin, the stress field may be locally disturbed, and reactivation and fluid flow along reactivated faults may be induced by episodic P_p build-up (Sibson, 1992). The risk of fault reactivation is expressed as the ratio $\Delta P_p/S_v$, i.e. the increase in P_p required to cause failure normalised to S_v (Figures 7.22 and 7.23). Hence at 1 km depth (S_v=20 MPa) in the normally pressured scenario, the plane most likely to be reactivated requires a P_p increase of only 1.4 MPa for reactivation, whereas the plane least likely to be reactivated requires a P_p increase of 12.8 MPa, assuming the failure envelope shown in Figure 7.20. At 1 km depth in the overpressured case the plane most likely to be reactivated requires a P_p increase of only 0.9 MPa for reactivation, whereas the plane least likely to be reactivated requires a P_p increase of 10.6 MPa (Figure 7.23). In the normally pressured scenario, vertical faults striking approximately 30°east or west of N-S are the most likely to be
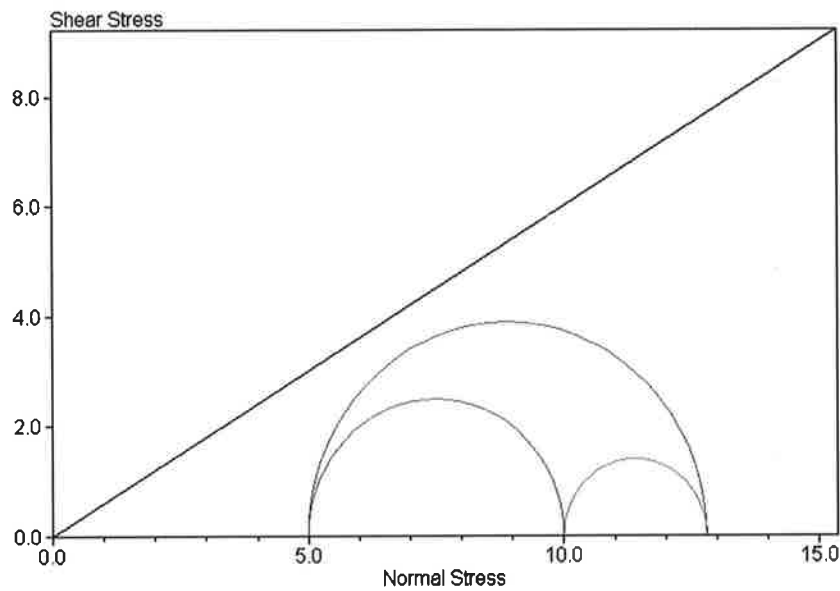
Figure 7.20. Mohr circle diagram with failure envelope used in normally pressured scenario.
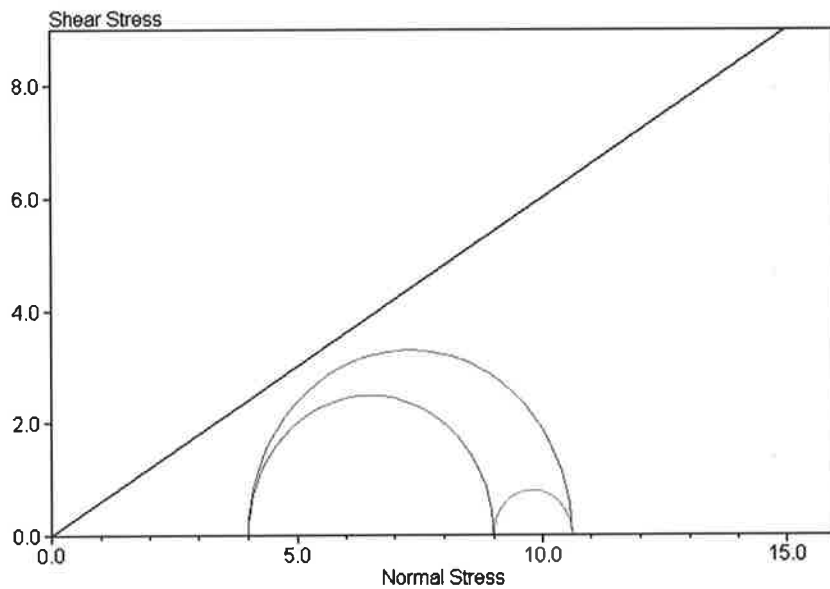
Figure 7.21. Mohr circle diagram with failure envelope used in overpressured scenario.

reactivated (Figure 7.22). N-S oriented vertical faults are located between that conjugate shear pair and are also likely to be reactivated and hydraulically conductive within the in situ stress field. Faults striking N-S and those striking 30∞east or west of N-S show little reduction in their risk of reactivation with decreasing dip until shallow dips (<40∞) are attained. E-W striking faults of any dip (and horizontal planes) are the least likely to be reactivated.
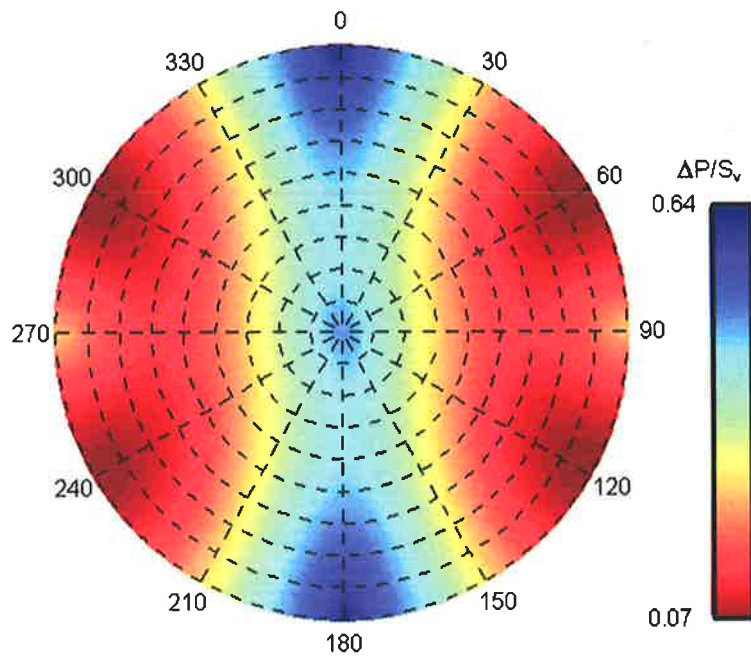
Figure 7.22. Polar diagram of poles to planes coloured by change in P_p normalised to S_v, above which fracture reactivation will occur for the normally pressured zone. Red indicates relatively high risk and blue indicates relatively low risk.
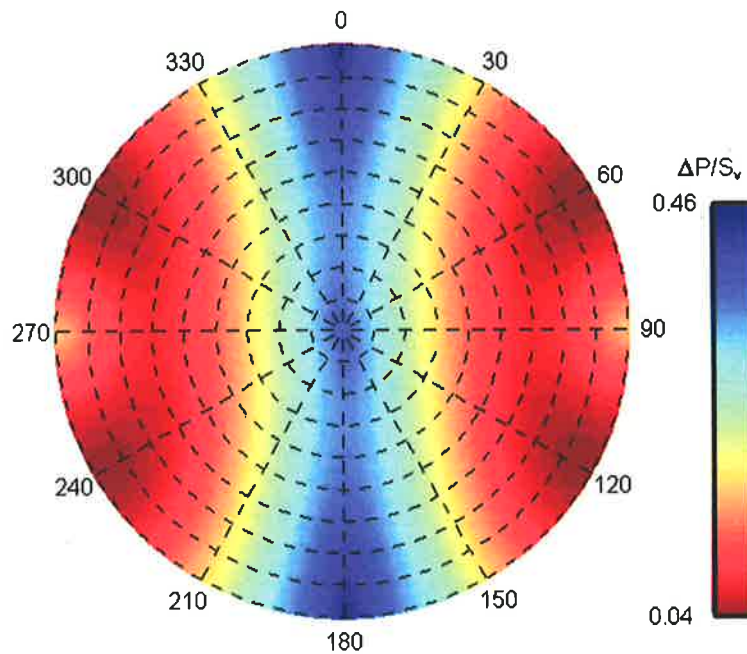
Figure 7.23. Polar diagram of poles to planes coloured by change in P_p normalised to S_v, above which fracture reactivation will occur for the overpressured zone. Red indicates relatively high risk and blue indicates relatively low risk.

The orientations of faults most likely to be reactivated are the same for the overpressured scenario as for the normally pressured scenario, but in the overpressured scenario, a slightly lesser increase in P_p is required for reactivation (Figure 7.23). Hence, the existing structural grain (N-S trending faults, which in places show NW-SE and NE-SW jogs and bends) is suitably oriented for reactivation (Figures 7.5 and 7.6). At 1 km depth, and assuming the failure envelope of Figure 7.20, vertical NW-SE (330oα) and NE-SW (030oα) trending faults require an increase in P_p of only slightly in excess of 1 MPa, or a gas column of approximately 110 m (for a density contrast with respect to water of 0.9 g/cm^3) for reactivation/seal breach.

It should be re-iterated that if migration occurred in a palaeo-stress field that differed from that of the present-day, then the above predictions are not relevant to such an earlier phase of migration/breach. It should also be noted that reactivation risk, hence risk of seal breach is a three-dimensional problem and care must be taken not to make predictions based on fault strike alone.

7.6. Conclusion

Stable wells (without breakouts or DITFs) can be drilled in all trajectories, in the Pattani Basin, provided rock strength and drilling parameters as previously encountered in the basin and the stress regime as described herein. The most unstable drilling trajectory with respect to both breakout and DITF formation is a vertical well, and vertical wells have been successfully drilled in the basin.

The in situ stress tensor and dominant fault orientations in the Pattani Basin are suitably oriented for fault reactivation given a small increase in P_p. Hence they may provide conduits for vertical hydrocarbon migration in the basin.

8. Otway Basin, South Australia: Fault Seal Risk

8.1. The Problem

The Penola Trough, Otway Basin, South Australia (Figures 8.1 and 8.2) is a northwest-southeast oriented rift feature. The producing fields and prospects are bound by a series of complex planar faults (Cockshell, 1995). Residual columns (traps in which hydrocarbons were present, but have migrated out of subsequent to being charged) have been encountered, and have been interpreted as being breached due to fault reactivation (Jones et al., 2000).

Jones et al. (2000) demonstrated, using mercury injection capillary pressure analysis, that the capillary properties the cap seal rocks in the Penola Trough were
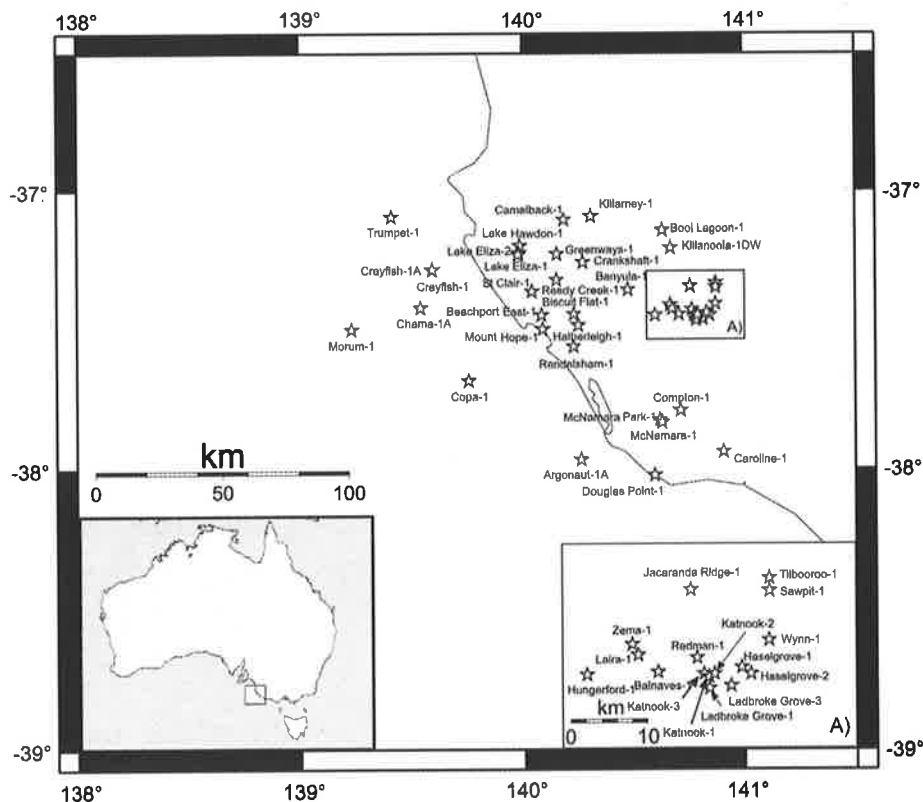
Figure 8.1. Otway Basin location map.

Otway Basin
Outer — Inner

Time Ma	Chronostratigraphy Senes	Div.	Stage	Spore Pollen Zones	seismic sequence	Rock Unit (Outer Seaward SW — Inner Landward NE)
10 / 25 / 36	MIOC	Early	Sarravallian	T. bellus	Megasequence III — T2	Pliocene Limestones / Recent Volcanics; Gambier Lst.; Gellibrand; Compton Congl.; HEYTSBURY GP.
	OLIG	Late / Early	Burdigalian to Rupelian	P. tucerulatus		
	EOCENE	Late	Priabonian	N. asperus	T1	Narrawaturk Marl; Mepunga Sst.; NIRR. GP.
		Middle	Bartonian			
			Lutetian	P. asperopolus		Dilwyn Formation; WANGERRIP GROUP
54		Early	Ypresian	M. diversus		Pember Mudstone
	PAL	Late	Thanelian	L. balmer		Pebbe Point Fm.
65		Early	Danian			K/T Shale
73	CRETACEOUS	Late	Maastrichtian	F. longus	Megasequence II — UK2	Timboon Sandstone; Paaratte Formation; Condensed Section; SHERBROOK GROUP
			Campanian	T. Illei		
				N. senctus		
83 / 87 / 88			Santonian	T. apoxyexinus		Belfast Mudstone; SHIPWRECK S-G
			Coniaclan			Flaxman Fm.
91			Turonian	P. mawsonii	UK1	Warra Sandstone; Copa Fm.
97			Cenomanian	H. uniforma		
		Early	Albian	P. pannosus	Megasequence I — LK3	Eumeralla Formation; Unnamed Sst.
				C. paradoxa		
				C. striatus		
113			Aptian	C. hughesii		Windermere Sst. Mbr.
119			Barremian	P. notensis		
125			Hauterivian	Upper F. wonthaggiensis	LK2	Katnooke Sandstone; OTWAY SUPERGROUP; CRAYFISH GROUP
131			Valanginian	Lower F. wonthaggiensis		Laira Formation
138				Upper C. australiensis	LK 1	Pretty Hill Formation
144			Berriasian	L C. australiensis		Casterton Formation
	JUR	Late	Thitonian	R. watherooensis		
150			Kimmeridgian		Basement	
	PZ					KANMANTOO GROUP EQUIVALENTS

Figure 8.2. Otway Basin stratigraphy (after Moore et al., 2000).

sufficient to hold back significant hydrocarbon columns. Jones et al. (2000) also demonstrated that, at least in several traps, juxtaposition and fault damage processes promote fault sealing, i.e. there is no juxtaposition of permeable formations across trap-bounding faults and fault damage (grain diminution) processes have yielded fault rocks that can hold back significant hydrocarbon columns (up to ~100 m of gas). Hence Jones et al. (2000) inferred that fault reactivation post-charge, within the in situ stress field, was the most likely cause of trap breach. This chapter constrains the in situ stress tensor of the Otway Basin in order to assess whether fault reactivation is the cause of seal failure, and if so which fault geometries are less likely to be reactivated and breached.

8.2. Routine Stress Determination Techniques

8.2.1. Vertical Stress

Vertical stress profiles were calculated for six wells in the Otway Basin, Argonaut-1A, Chama-1A, Copa-1, Crayfish-1, Katnook-2 and Ladbroke Grove-1 using the techniques described in Section 3.2 (Figure 8.3; Appendix D). Five of the wells had density correction logs (DRHO) enabling spurious data to be removed (i.e. values for which DRHO $\geq$ 0.2 g/cc; Section 3.2). S_v was calculated, in these five wells, using the corrected density logs and the average density to the top of the density log calculated from checkshot velocity surveys using the Nafe-Drake sonic velocity/density transform (Ludwig et al., 1970; Section 3.2). The sixth well, Crayfish-1, had no DRHO log and was consequently corrected using a de-spiking filter (Section 3.2). S_v was calculated, in Crayfish-1, using the de-spiked density log and the average density to the top of the density run calculated from a checkshot velocity survey.

The vertical stress profiles in the Otway Basin show significant variation. In particular S_v is significantly higher in Katnook-2 and significantly lower in Argonaut-1A (Figure 8.3 and Table 8.1). The author believes that difference reflects different uplift across the basin (and thus differential erosion of low density, near surface sediments), which has been subject to neotectonic activity (Dickinson et al., 2001).

Well	S$_v$ Gradient 1 km depth (MPa/km)	S$_v$ Gradient 2 km depth (MPa/km)	S$_v$ Gradient 3 km depth (MPa/km)
Argonaut-1A	18.5	20.0	21.0
Chama-1	18.8	21.1	-
Copa-1	18.6	20.6	21.4
Crayfish-1	19.7	21.3	22.1
Katnook-2	-	21.7	22.9
Ladbroke Grove-1	-	-	21.6

Table 8.1. Vertical stress gradients at different depths for the wells in which S$_v$ was calculated.
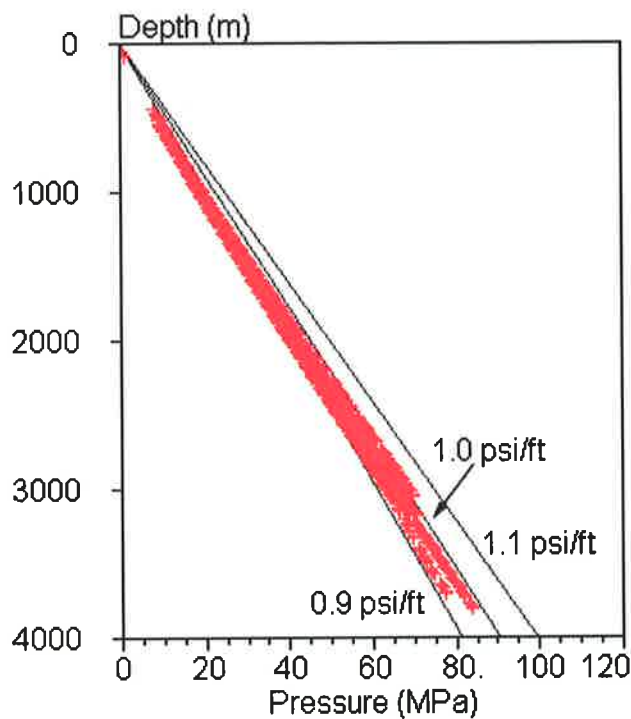
Figure 8.3. Vertical stress profiles for the Otway Basin. Calculated using Argonaut-1A, Chama-1A, Copa-1, Crayfish-1, Katnook-2 and Ladbroke Grove-1.

Excluding Katnook-2 and Argonaut-1A, S$_v$ is consistent in the remaining four wells (Figure 8.4; Table 8.1). The vertical stress magnitude in these four wells is closely approximated by the power law function:

$$S_V = 0.0077 \, z^{1.13085} \qquad\qquad \text{Eq. 8.1,}$$

where the vertical stress is in MPa and z is depth in meters below sea-level.
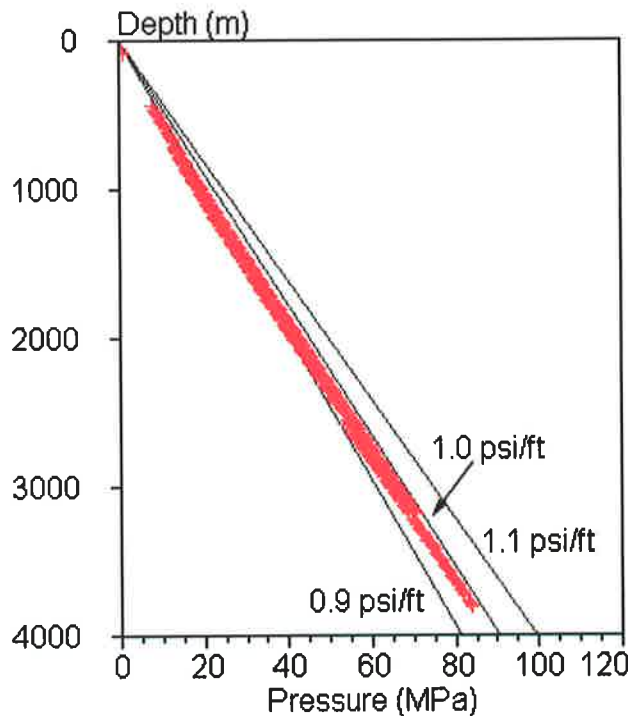
Figure 8.4. Vertical stress profiles for the Otway Basin. Calculated using Chama-1A, Copa-1, Crayfish-1 and Ladbroke Grove-1.

8.2.2. Horizontal Stress Orientation

Horizontal stress orientations were determined as outlined in Section 3.4 from 216 breakouts and 16 DITFs interpreted from image logs run in Haslegrove-1, Jacaranda Ridge-1, Killanoola-1DW and Wynn-1, and dipmeter logs run in Hungerford-1, Redman-1 and Rendelsham-1 (Figures 8.5 ñ 8.12; Appendix E). The mean declination corrected S_{Hmax} orientation is 123∫N (Table 8.2).

The S_{Hmax} orientations determined from the seven wells are relatively consistent across the Otway Basin, with variations in mean orientation from 107°N to 133°N (Table 8.2 and Table 8.3). The most anomalous S_{Hmax} orientation, of 107°N, was obtained at Killanoola-1DW.

Killanoola-1DW has the highest deviation (up to 20°) in the study. However, this deviation does not account for the 16° difference from the regional S_{Hmax} orientation

trend. The low standard deviation and high quality of the breakouts observed in Killanoola-1DW suggest there is a genuine variation in S_{Hmax} orientation at this location.

Source	Un-Weighted			Length-Weighted		
	Mean	SD	Number	Mean	SD	Total Length (m)
Breakouts	123°N	16.8°	216	121°N	11.6°	1232.8
DITFs	123°N	5.5°	16	-	-	-

Table 8.2. S_{Hmax} orientation inferred from breakouts and DITFs. SD: standard deviation.
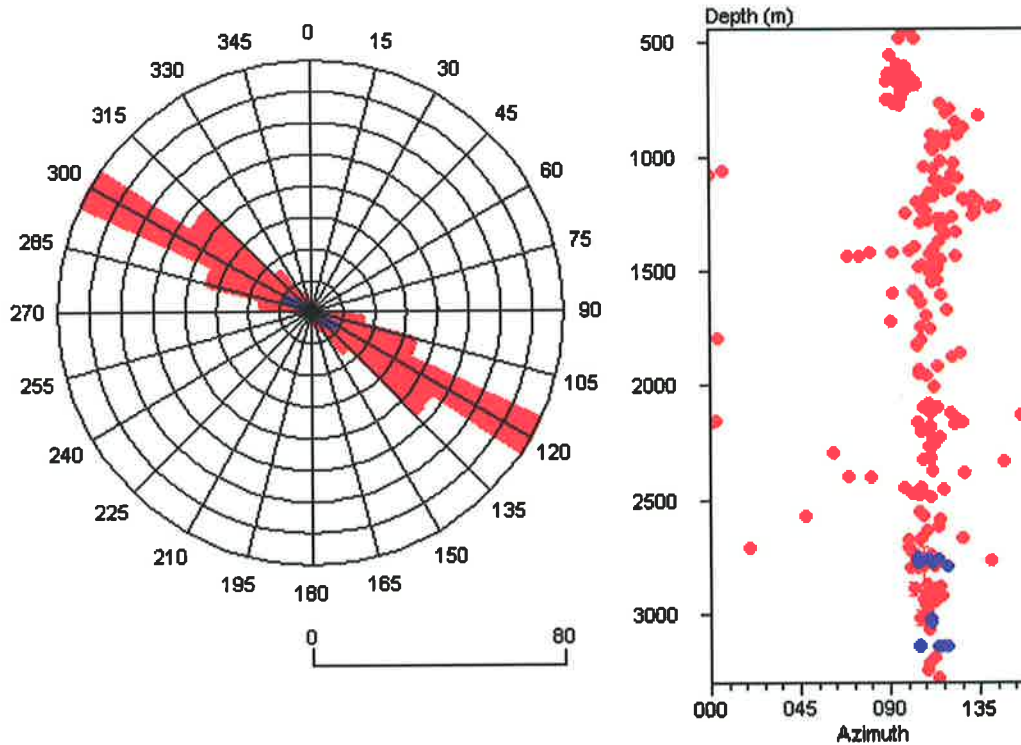
Figure 8.5. Un-weighted S_{Hmax} orientations determined from 216 breakouts (•) and 16 DITFs (•) from image logs in four wells and dipmeter logs from 3 wells.
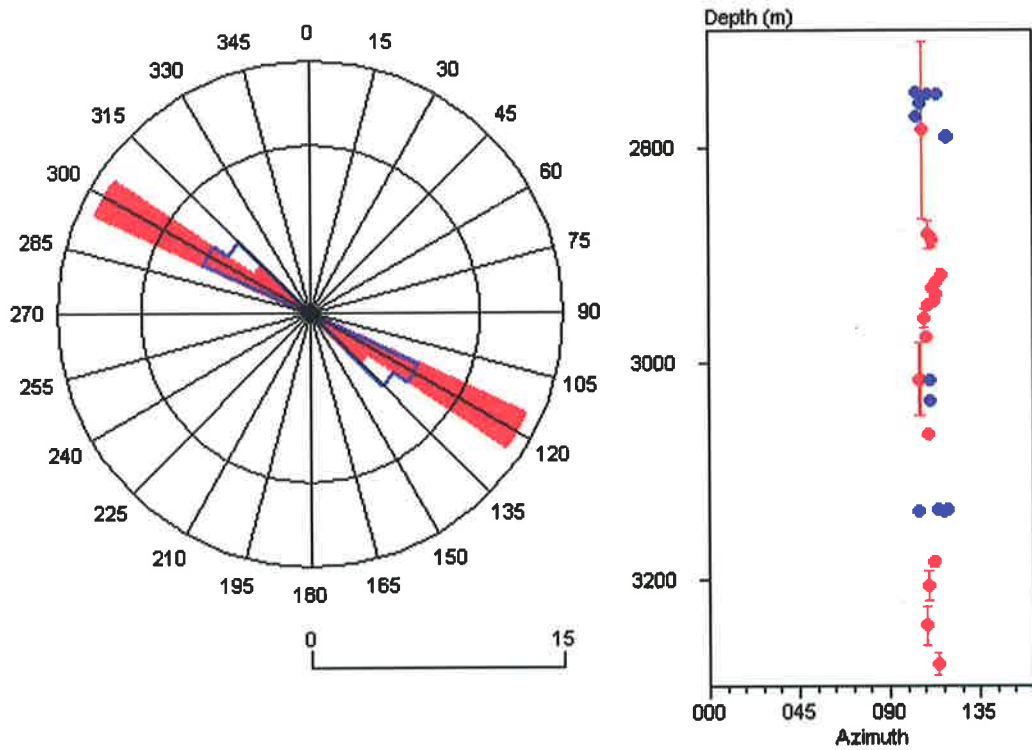
Figure 8.6. Un-weighted S_{Hmax} orientations determined from breakouts (•) and DITFs (•) interpreted in image log in Haselgrove-1.
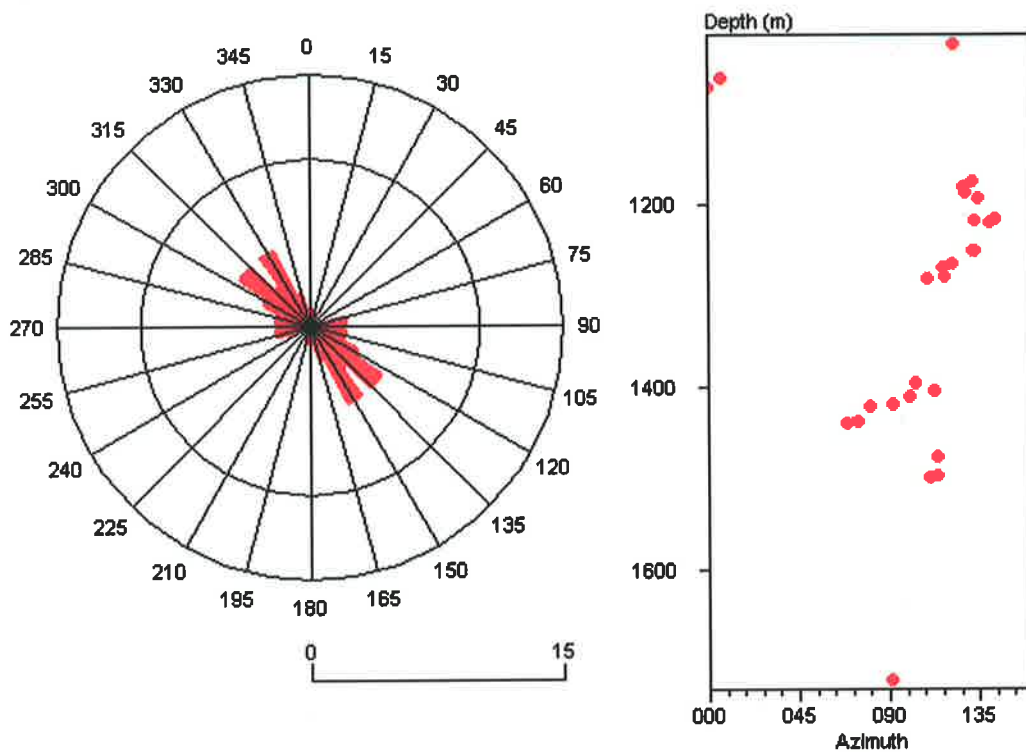
Figure 8.7. Un-weighted S_{Hmax} orientations determined from breakouts (•) interpreted in dipmeter log in Hungerford-1.

160
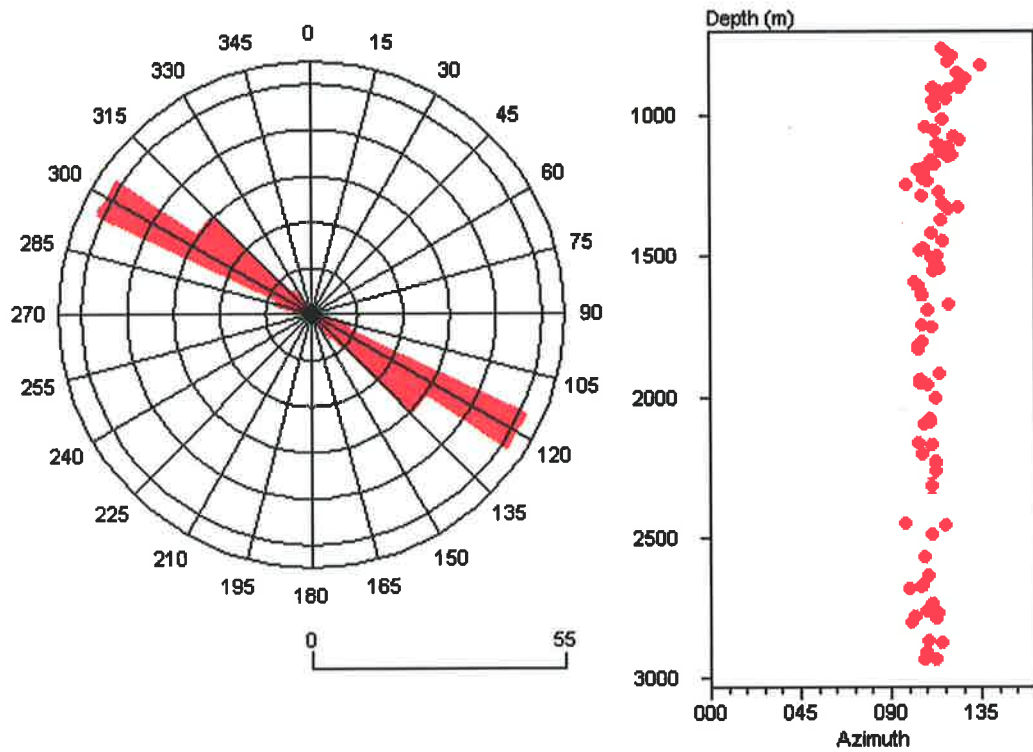
Figure 8.8. Un-weighted S_{Hmax} orientations determined from breakouts (•) interpreted in image log in Jacaranda Ridge-1.
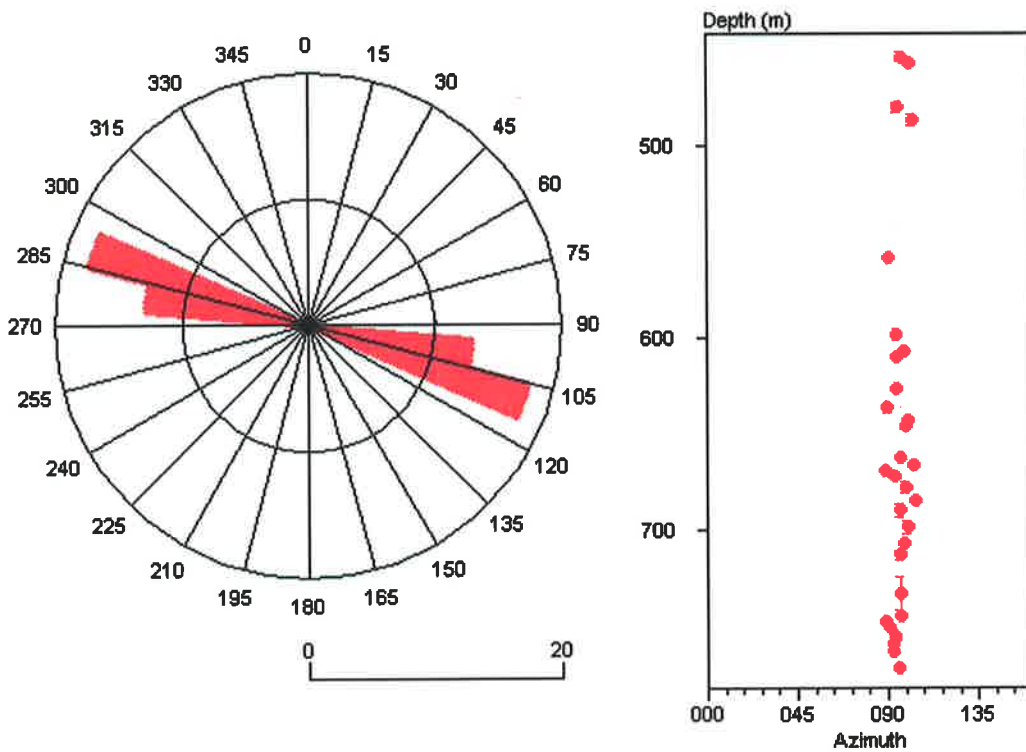
Figure 8.9. Un-weighted S_{Hmax} orientations determined from breakouts (•) interpreted in image log in Killanoola-1DW.

161
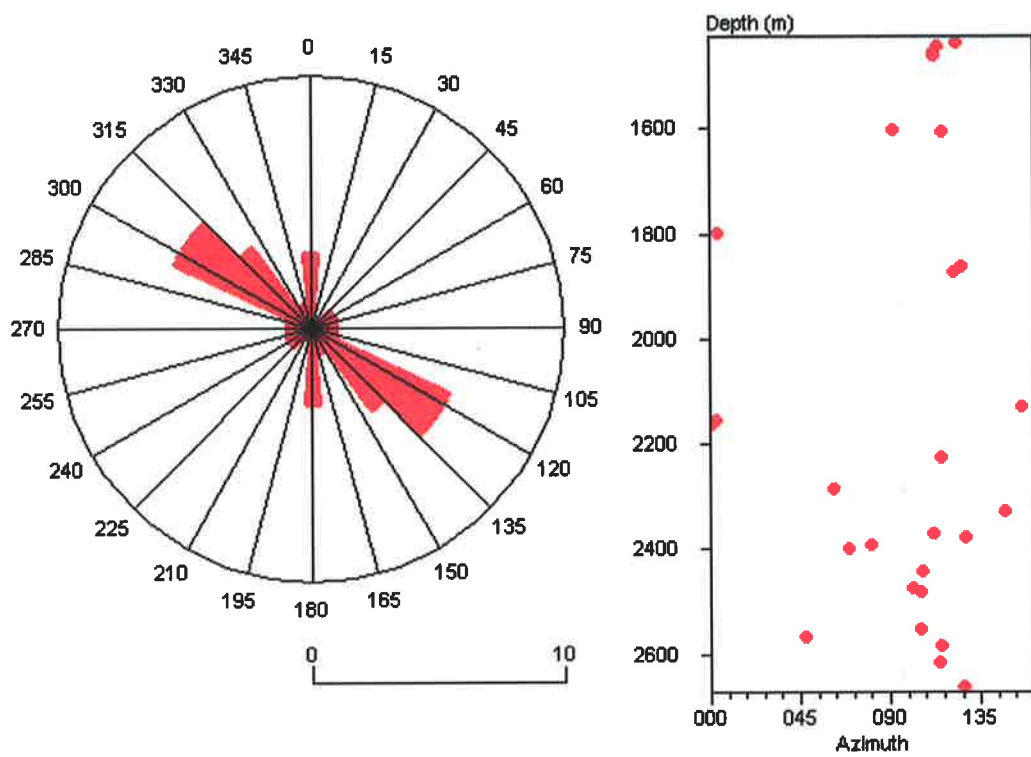
Figure 8.10. Un-weighted S_{Hmax} orientations determined from breakouts (•) interpreted in dipmeter log in Redman-1.
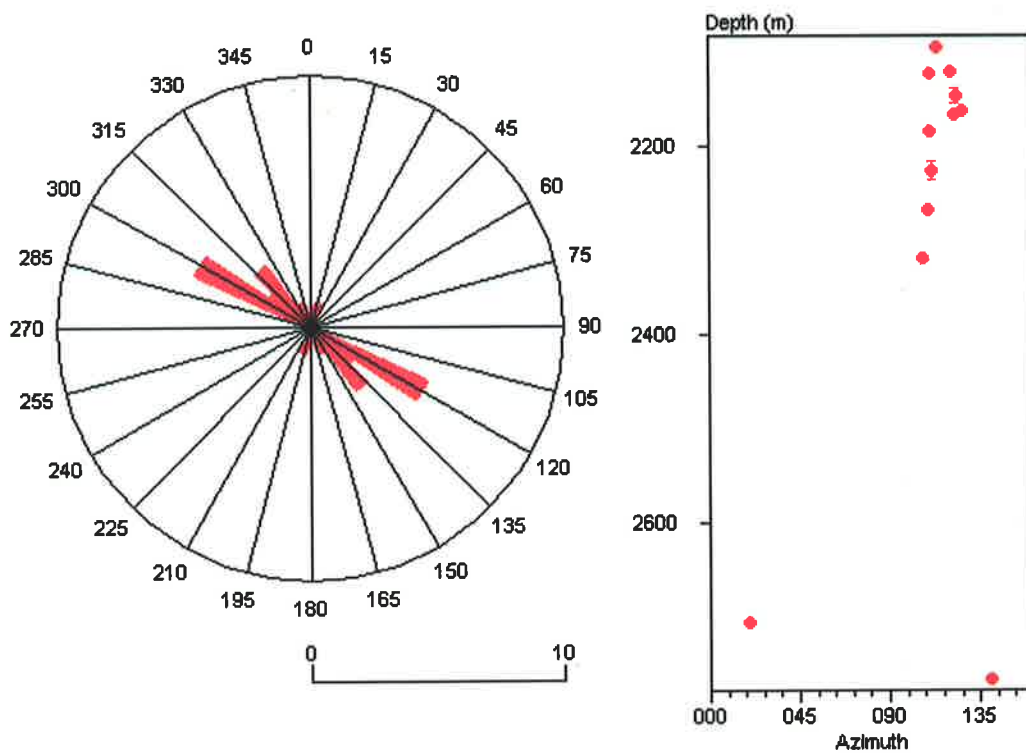
Figure 8.11. Un-weighted S_{Hmax} orientations determined from breakouts (•) interpreted in dipmeter log in Rendelsham-1.

162
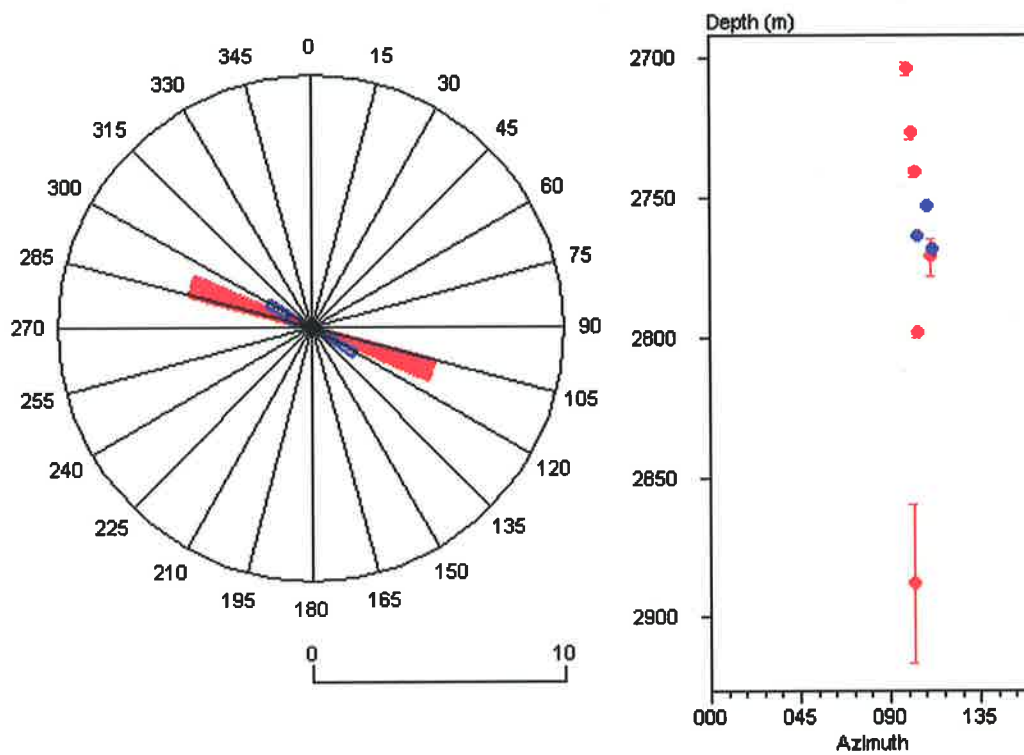
Figure 8.12. Un-weighted S$_{Hmax}$ orientations determined from breakouts (•) and DITFs (•) interpreted in image log in Wynn-1.

Well	Un-Weighted			Length-Weighted		
	Mean	SD	Count	Mean	SD	Length (m)
Haselgrove-1	123°N	3.1°	18	120°N	2.9°	430.02
Hungerford-1	132°N	26.0°	27	127°N	28.1°	32.31
Jacaranda Ridge-1	124°N	7.3°	95	125°N	8.0°	468.19
Killanoola-1DW	107°N	4.3°	31	107°N	3.8°	97.33
Redman-1	129°N	31.1°	27	127°N	38.5°	59.43
Rendelsham-1	133°N	19.5°	12	131°N	12.4°	60.81
Wynn-1	115°N	4.1°	6	114°N	3.8°	84.72

Table 8.3. Breakout inferred S$_{Hmax}$ orientations from 7 wells in the Otway Basin.

The standard deviation of breakouts within an individual well interpreted from image logs ranges from 2.9° to 8.0°, while the standard deviation for breakouts interpreted from dipmeter logs ranges from 12.4° to 38.5° (Table 8.3). Furthermore, combining the results from image logs results in a breakout inferred S_{Hmax} orientation of 120°N and a standard deviation of 9.5°, while combining the results from dipmeter logs results in a breakout inferred S_{Hmax} orientation of 131°N and a standard deviation of 27.0°. This highlights the improved accuracy and confidence in determining S_{Hmax} orientations afforded by image logs over dipmeter logs.

8.2.3. Minimum Horizontal Stress Magnitude

The minimum horizontal stress magnitude was determined from leak-off tests (LOTs) and four extended leak-off tests (XLOTs; Section 8.3). Leak-off test data was collected for all non-confidential wells drilled after 1980 in the Otway Basin, from well completion reports and mud logs stored at Primary Industries and Resources South Australia (PIRSA; Appendix F). This resulted in data from 15 LOTs and 13 FITs in the Otway Basin (Figure 8.13). These LOTs are relatively consistent and indicate an S_{hmin} gradient of ~15 MPa/km. All the tests were recorded as effective mud weights and no original pressure/time records were found. Nonetheless consistency of the LOPs with depth suggests a consistent method of interpretation.

Given the significance of the fault seal issue in the Otway Basin, and the importance of having good in situ stress data to predict fault reactivation potential, five XLOTs were conducted in exploration wells drilled by Origin Energy. The procedures, problems and results of these tests are discussed in Section 8.3.1.

8.2.4. Pore Pressure

Pore pressures in the Otway Basin were determined from 10 DSTs, 90 WFITs and mud weights from 33 wells (Section 3.7). DST measurements were obtained from PIRSAís PEPS database, while WFITs and mud weights were obtained from well completion reports and mud logs from non-confidential wells drilled after 1980, stored at PIRSA (Figure 8.14). The 90 WFITs and 10 DSTs indicate a P_p gradient of 9.8 MPa/km, while the P_w gradient is ~11 MPa/km from 33 wells. Neither overpressures nor virgin under-pressures have been observed in the Otway Basin
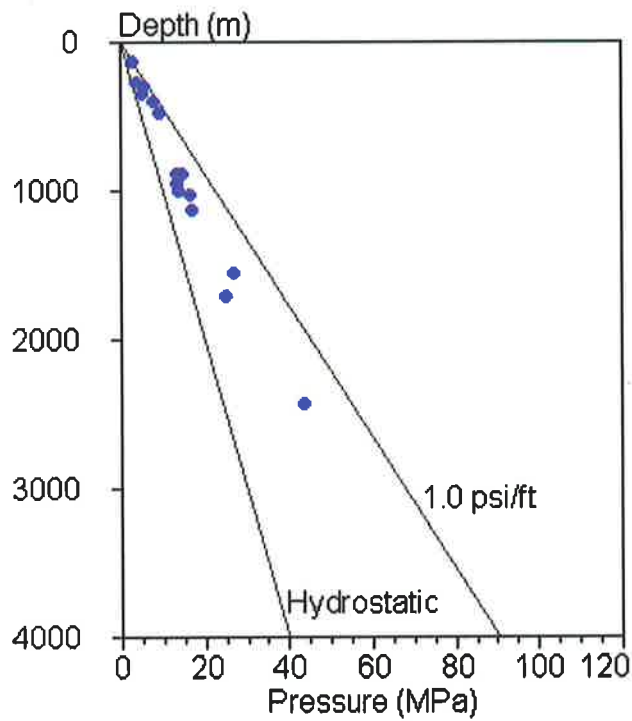
Figure 8.13. Depth plot showing 15 LOTs (●) from wells in the Otway Basin.
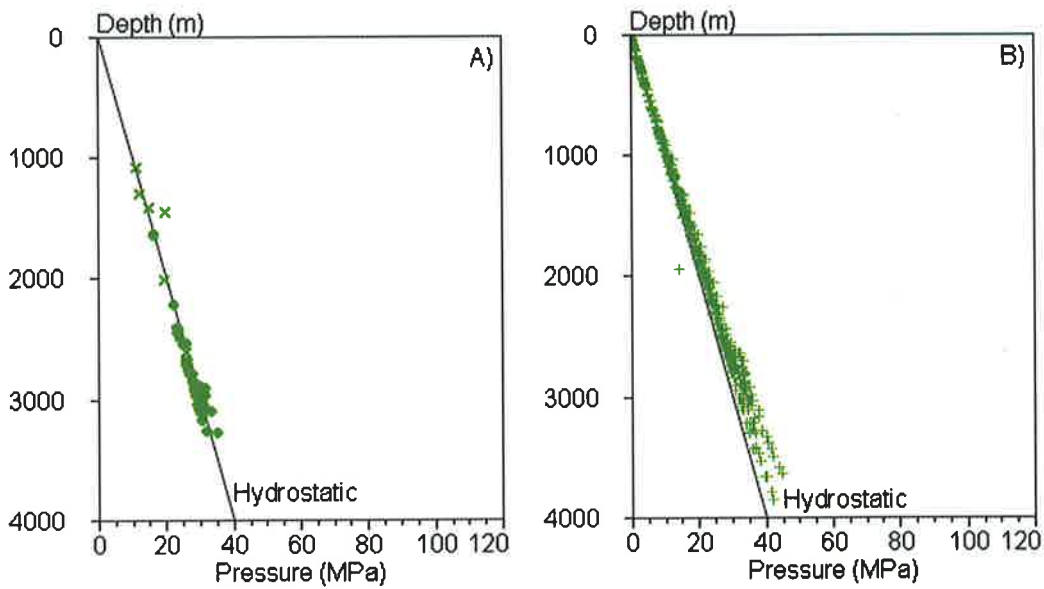
Figure 8.14. Pore pressure in the Otway Basin from (A) 90 WFITs (●) and 10 DSTs (×) and (B) P_w (+) from 33 wells.

8.3. Non-Routine Stress Determination Techniques

The maximum horizontal stress is, as is commonly the case, the most problematic aspect of the in situ stress tensor to constrain in the Penola Trough. Maximum horizontal stress magnitudes can be determined using XLOTs and/or the observation of wellbore failure (Section 3.6) or constrained using frictional limits to stress (Section 2.5). Five XLOTs were conducted in open holes in the Otway Basin. Extended leak-off tests can yield S_{hmin}, and may be used to determine S_{Hmax}, if fracture re-opening pressure can be interpreted (Section 3.6.1). However, in the Otway Basin fracture reopening pressures cannot be interpreted from the XLOTs (discussed in this section). Nonetheless the XLOTs are discussed in this section because they are a non-routine method of stress determination and indeed because the author was directly involved with the planning and rigsite execution of these tests.

Image logs were run in Haslegrove-1, Jacaranda Ridge-1, Killanoola-1DW and Wynn-1. Breakouts and DITFs were observed on these logs. Maximum horizontal stress magnitude can be constrained from the occurrence of wellbore breakouts, if the compressive rock strength is known (Section 3.6.2). In this case compressive rock strengths are available for the interval where breakouts occured in Jacaranda Ridge-1 (Dewhurst et al., 2001). Furthermore, S_{Hmax} can be constrained from observations of DITFs (Section 3.6.3). This section discusses XLOTs in the Otway Basin, and the use of the occurrence of DITFs and breakouts to constrain S_{Hmax}.

8.3.1. Extended Leak-Off Tests

Five XLOTs were conducted to better understand the stress tensor in the Penola Trough. These were conducted, in time order, in Wynn-1, Jacaranda Ridge-1, Ladbroke Grove-3, McNamara Park-1 and Balnaves-1. The author was directly involved in the planning and rig site execution of the tests at Jacaranda Ridge-1, McNamara Park-1 and Balnaves-1. Procedures were modified sequentially in the tests to yield better results.

The determination of S_{Hmax} from XLOTs requires the interpretation of an accurate Pr (Section 3.5.2). However, the occurrence of DITFs in the Otway Basin (Section 8.2.2) implies that the minimum wellbore stress is close to zero and hence Pr is close to zero, making interpretation difficult. Consequently no fracture reopening pressures

are interpreted and no estimate of S_{Hmax} is made from the XLOTs. They are, however, used to obtain improved estimates of S_{hmin}.

Wynn-1

The rig crew conducted the XLOT at Wynn-1 using the cement pumps and the resulting data was supplied for interpretation. Figure 8.15 displays the pressure and volume pumped versus time. The first cycle indicates that fluid was pumped into the wellbore increasing the pressure, but it is unclear whether a fracture was initiated or a problem occurred at the surface resulting in fluid return and a sharp pressure drop. Consequently, the second cycle may have either initiated or reopened a fracture, and P_r cannot be confidently interpreted.

Wynn-1 XLOT
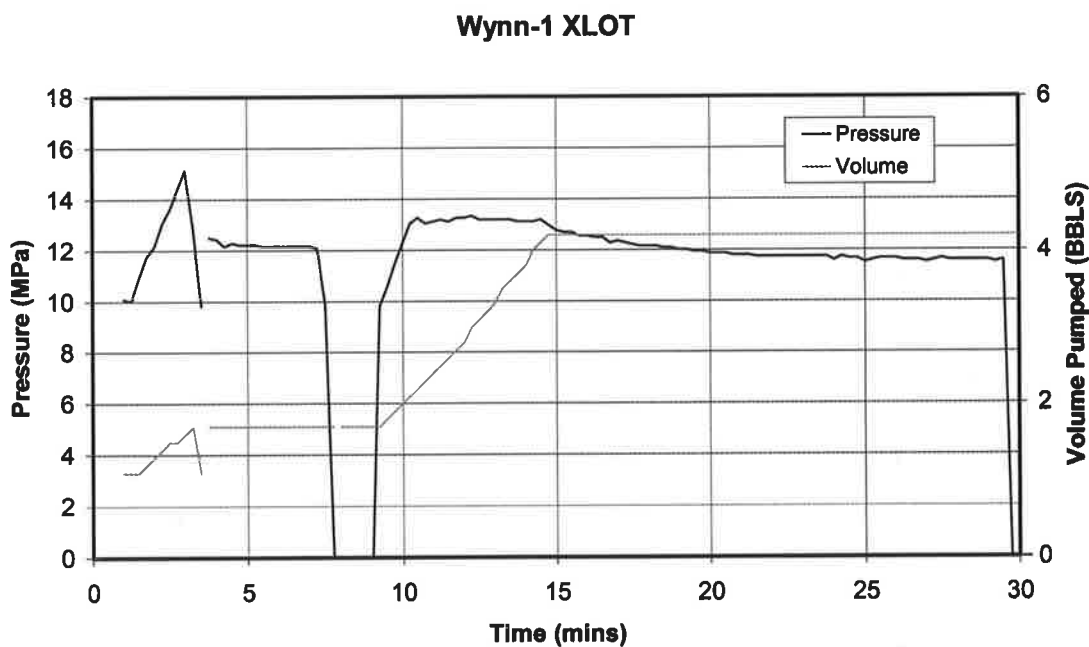
Figure 8.15. Down hole pressure and Volume pumped versus time for the XLOT conducted at 952 m in Wynn-1.

The pressure record indicates that in the second cycle a fracture was either initiated or reopened and then propagated away from the wellbore. Pumping was then ceased and the resulting pressure decline can be seen in Figure 8.15. A plot of pressure versus the square root of time since pumping stopped is used to interpret P_c (Section 3.5.2; Figure 8.16), as fracture closure is not obvious on the pressure time record (Figure 8.15). The pressure versus root time plot displays a linear pressure decay with a break

in gradient at 11.7 MPa (Figure 8.16). Consequently, S_{hmin} is interpreted to be 11.7 MPa at a depth of 952 m, corresponding to an S_{hmin} gradient of 12.3 MPa/km. However this value for S_{hmin} is below frictional limit ($\mu = 0.6$) for the well-constrained S_v and may be due to a poor cement job above the freshly drilled formation. This combined with the problems encountered in the first cycle of the test makes the estimate of S_{hmin} obtained in Wynn-1 unreliable.

Wynn-1 XLOT
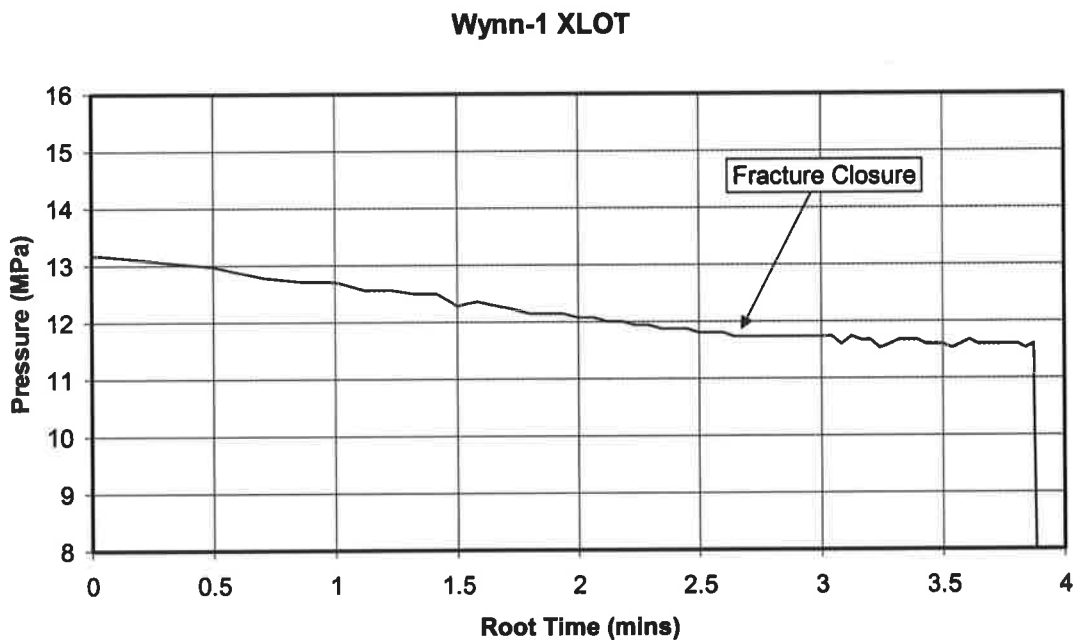
Figure 8.16. Down hole pressure versus the square root of time since pumping stopped for the XLOT conducted at Wynn-1. The interpreted P_c is 11.7 MPa.

Jacaranda Ridge-1

The XLOT at Jacaranda Ridge-1 was conducted using analogue surface pressure gauges, a digital data recorder and a pressure transducer, and the pressure-testing pump, all supplied by the rig contractor. The pressure-testing pump is a high-pressure pump (rated to 5000 psi), but is only capable of pumping at ~0.11 bbl/min, and was used instead of the cement pumps to reduce the cost of conducting the XLOT. The analogue pressure gauges were connected to the pressure-testing pump, while the pressure transducer was connected directly to the wellhead. The digital data recorder recorded pressure measurements from the pressure transducer every two seconds.

The test was conducted at a depth of 750 m in ~3 m of new hole in the Eumeralla Formation. The test procedure is given in Table 3.1.

1.	Pumping was begun at < 0.1 bbl/min.
2.	The pump rate was increased to approximately 0.1 bbl/min.
3.	Leak-off was observed and an additional ~0.2 bbl pumped.
4.	Pumping was stopped, the well shut in and pressure decay monitored.
5.	When pressure stabilised the pressure was vented off.
6.	Pumping was resumed.
7.	Fracture reopening was observed and pumping was continued to propagate fracture.
8.	The pump rate was halved
9.	The pump rate halved again
10.	The pressure stabilised, pumping was stopped and the well shut in while the pressure decay was monitored.
11.	The pressure stabilised and was vented off.

Table 8.4. Procedure used during the XLOT conducted at Jacaranda Ridge-1.

The apparent leak-off observed on the analogue pressure gauges during the first cycle was in fact due to a malfunction in the pump (the pump rate of which declined) and did not represent actual leak-off (Figure 8.17). Consequently, leak-off did not occur in the first cycle. A fracture was initiated and propagated away from the near wellbore stress concentration in the second cycle. However, no P_r can be interpreted without a definite leak-off in the first cycle. The pressure decline in the second cycle is dominated by radial flow, suggesting a relatively permeable formation. A plot of the pressure versus the root of time since pumping was stopped was used to remove the affect of the radial flow and assist in the interpretation of P_c (Section 3.5.2; Figure 8.18). The surface pressure at which the fracture closure is interpreted as 2.0 MPa, however P_c is not obvious on the pressure versus root time plot. This corresponds to a down hole pressure of 9.6 MPa for a mud weight of 8.6 ppg and a depth of 750 m. Consequently, S_{hmin} is interpreted to be 9.6 MPa at a depth of 750 m, corresponding to an S_{hmin} gradient of 12.8 MPa/km. However this value for S_{hmin} is below frictional

limit ($\mu = 0.6$) for the well-constrained S_v. This combined with the problems encountered in the first cycle of the test makes the estimate of S_{hmin} obtained in Jacaranda Ridge-1 unreliable.

Jacaranda Ridge-1 XLOT
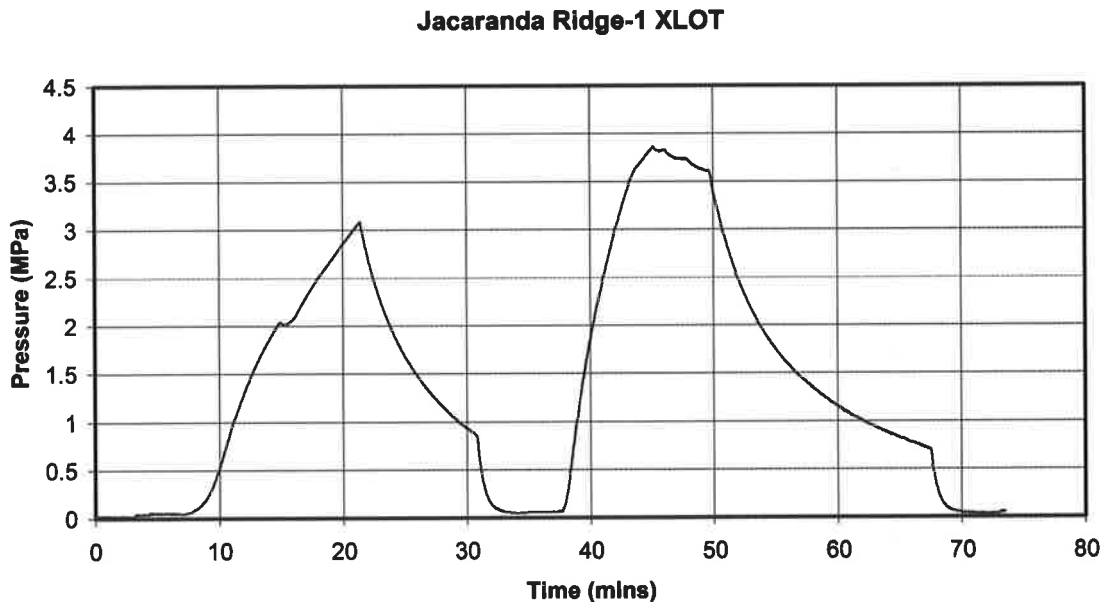
Figure 8.17. Surface pressure recorded during Jacaranda Ridge-1 XLOT conducted at 750 m.

The two main problems encountered at Jacaranda Ridge-1 were the incorrect interpretation of leak-off as the test was being conducted and difficulty in interpreting P_c. The inability to recognise leak-off in real time in the first cycle was a direct result of using inappropriate analogue pressure gauges. The gauges were rated to 5000 psi, while the maximum pressure reached during the test was 600 psi. The proposed solution to this problem was to link the data recorded directly to a laptop with the necessary software to visualise pressure versus time in real time, allowing the test to be conducted correctly. This approach was used in the remaining XLOTs.

The difficulty in interpreting P_c was due to the significant radial flow resulting from high formation permeability. The high permeability also reduces the rate of pressurisation, lengthening the total time for the test. Combining an increased pump rate with pumping a larger volume of fluid to propagate the fracture further can overcome these problems. The larger fluid volume increases the size of the fracture resulting in a more obvious fracture closure. The higher pumping rates can mitigate

the loss of fluid to the formation increasing the rate of pressurisation and maximising the size of the induced fracture for the volume of fluid pumped. However, the pumps used have a maximum pump rate of ~0.11 bbls/min and hence only an increase in the volume pumped to propagate the fracture could be implemented in subsequent tests.

Jacaranda Ridge-1 XLOT
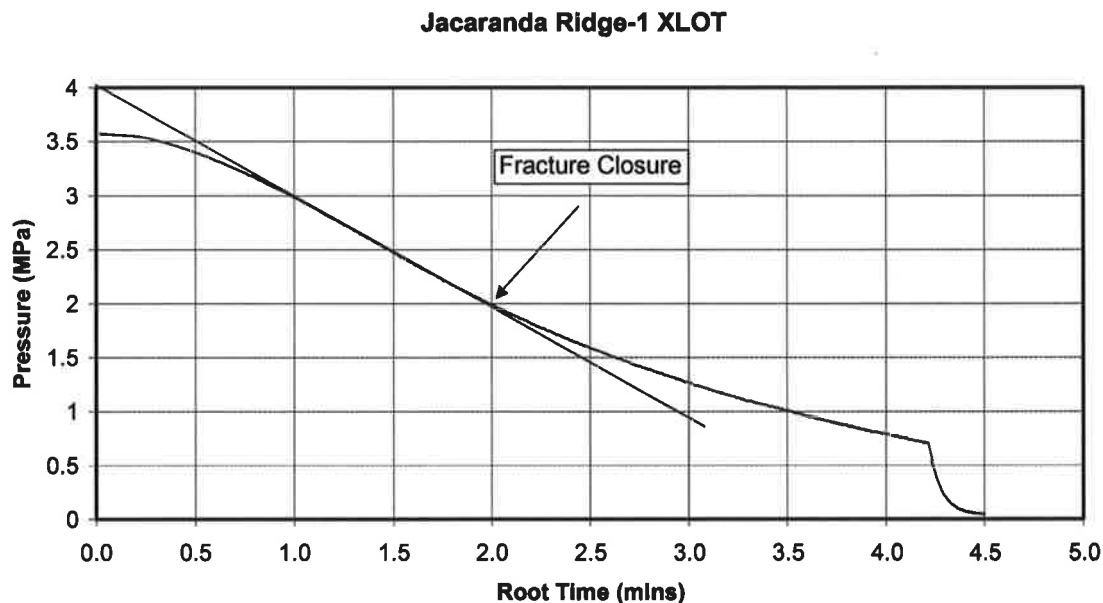
Figure 8.18. Surface pressure versus the square root of time since pumping stopped for the XLOT conducted at Jacaranda Ridge-1. The interpreted P_c is 2.0 MPa.

Ladbroke Grove-3

Peter Boult of Origin Energy conducted the XLOT at Ladbroke Grove-3 and the resulting data was supplied to the author for interpretation. The test was conducted using a pressure transducer connected directly to a laptop, and the pressure-testing pump. The laptop connected to the pressure transducer enabled the pressure time record to be visualised in real time, allowing the test to be conducted correctly. However, the pressure transducer was connected to the high-pressure line, at the pump end, connecting the pump to the wellhead. This led to errors in the pressure readings, particularly while pumping, due to the frictional losses associated with fluid flow down the high-pressure line. The error associated with the pressure reading during the pressure decline is negligible as little to no fluid flows along the high-pressure line. Thus, only the pressure recorded during the pumping phases needs to be corrected. The pressure loss can be determined from the pressure drop

immediately after pumping is stopped or the pump rate is changed. The correct
pressure can be calculated by subtracting the magnitude of the pressure drop for a
particular pumping rate from the pressure measured while pumping at that rate. The
test was conducted at a depth of 820 m in ~3 m of new hole, using the procedures
described in Section 3.5.2. The corrected pressure versus time record is shown in
Figure 8.19.

Ladbroke Grove-3 XLOT
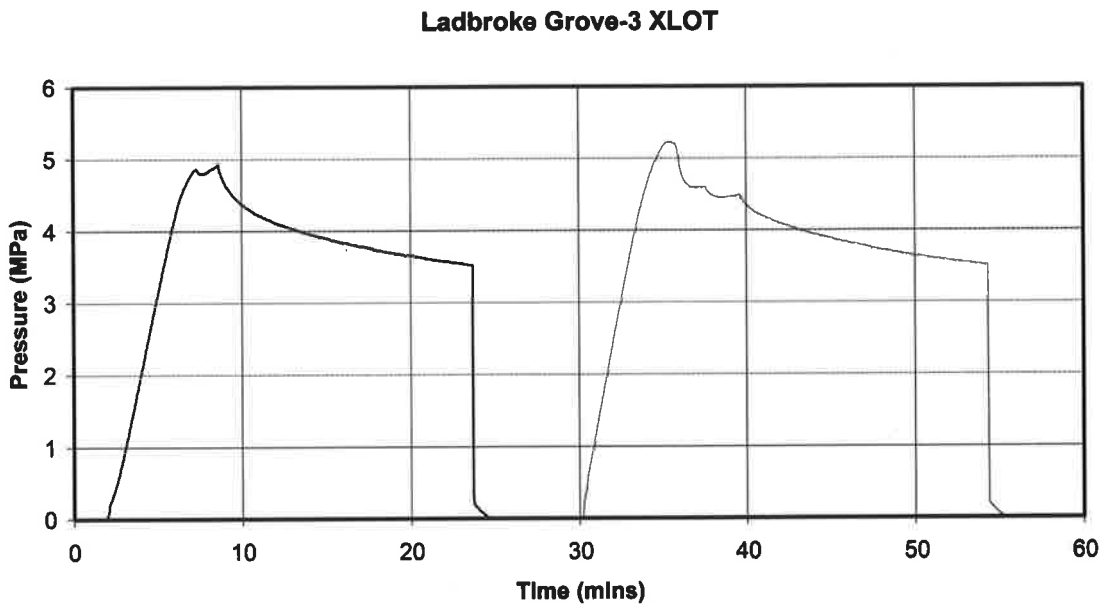
Figure 8.19. Surface pressure recorded during Ladbroke Grove-3 XLOT conducted at 820 m.

A fracture was initiated in the first cycle and propagated in the second cycle, making
interpretation of P_c possible (Figure 8.19). The pressure declines from both cycles are
affected by radial flow. Consequently, plots of pressure versus the square root of time
since pumping stopped are used to interpret P_c for the first and second cycles (Figures
8.20 and 8.21). The surface pressure at which fracture closure is interpreted is
4.38 MPa in the first cycle and 4.29 MPa in the second cycle. These equate to down
hole pressures of 12.7 MPa for the first cycle and 12.6 MPa for the second cycle, for a
mud weight of 8.6 ppg and a depth of 820 m. The fracture has been propagated
further into the far field stresses (beyond the wellbore effect) in the second cycle. A
gradual lowering of P_c in later cycles of some tests has been observed (Enever and
Wooltorton, 1982; Gronseth and Kry, 1982; Hickman and Zoback, 1982) and is
attributed to the reduction in magnitude of viscous pressure losses within the

hydraulic fracture as it propagates (Hickman and Zoback, 1982). Consequently, the estimate S_{hmin} determined from the second cycle is more reliable than that of the first cycle. The minimum horizontal stress at 820 m in Ladbroke Grove-3 is interpreted to be 12.6 MPa, corresponding to an S_{hmin} gradient of 15.4 MPa/km.

Figure 8.20. Surface pressure versus the square root of time since pumping stopped for the first cycle of the XLOT conducted at Ladbroke Grove-3. The interpreted P_c is 4.38 MPa.

Figure 8.21. Surface pressure versus the square root of time since pumping stopped for the second cycle of the XLOT conducted at Ladbroke Grove-3. The interpreted P_c is 4.29 MPa.

McNamara Park-1

The XLOT at McNamara Park-1 was conducted using a pressure transducer connected directly to a laptop, and the wellhead. The laptop connected to the pressure transducer enabled the pressure versus time record to be visualised in real time, allowing the test to be conducted correctly. The pressure transducer was connected directly to the wellhead to eliminate the errors in the pressure readings due to frictional losses encountered at Ladbroke Grove-3. The test was conducted at a depth of 547 m in ~3 m of new hole, using the procedures described in Section 3.5.2. The pressure versus time record is shown in Figure 8.22.

McNamara Park-1 XLOT
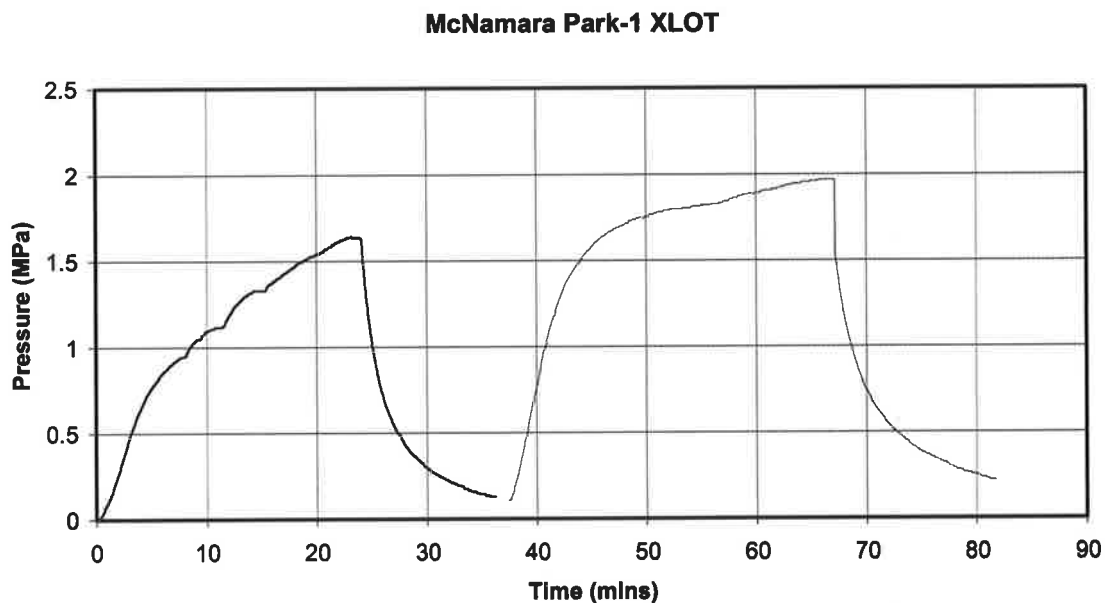
Figure 8.22. Surface pressure recorded during McNamara Park-1 XLOT conducted at 547 m.

Fracture initiation was not achieved in McNamara Park-1, despite pumping for 30 minutes in the second cycle (as opposed to ~10 minutes for the other XLOTs), at a pump rate of ~0.1 barrels/minute which had been successfully used in the previous tests. The inability to fracture the formation precludes P_c from being interpreted and hence no stress estimate can be made.

The inability to fracture the formation may be the result of high formation permeability, which is evidenced by the slow rate of pressurisation and the rapid rate of pressure decline after the cessation of pumping. The casing shoe is normally set in

a shaly zone, however at McNamara Park-1, the last drill cuttings indicated a sandy formation. Thus it seems likely casing was set in a permeable sand.

The use of higher pumping rates and drilling mud as opposed to water may alleviate the problem. Higher pumping rates enable the fluid loss to the formation to be overcome, while the use of drilling mud may result in the formation of a mud cake, reducing the fluid loss to the formation.

Balnaves-1

The XLOT at Balnaves-1 was conducted using a pressure transducer connected directly to a laptop, and the wellhead. The test was conducted at a depth of 860 m in a well-compacted silty sand with a mud weight of 8.55 ppg in ~3 m of new hole, using the procedures described in Section 3.5.2. The pressure versus time record is shown in Figure 8.23.

A pump rate of ~0.1 bbls/min resulted in a linear and rapid pressure build up suggesting little fluid loss to the formation (Figure 8.23). Formation breakdown was achieved and a fracture propagated away from the wellbore into the far field stress tensor. This fracture was further propagated in the second cycle of the test.

Plots of pressure versus root time after pumping stopped are used to aid the interpretation of P_c (Section 3.5.2; Figures 8.24 and 8.25). The pressure versus root time plot for the first cycle shows fracture closure at 4.7 MPa as witnessed by a sharp change in slope (Figure 8.24). The pressure versus root time curve for the second cycle exhibits a less clear P_c at ~4.8 MPa (Figure 8.25). The reason for a more ambiguous P_c in the second cycle is not known. Enever (1993) suggested that an increase in P_p in the vicinity of the fracture in later cycles can cause an increase in P_c resulting from poroelasticity and that in this case the first cycle provides the most reliable P_c. Consequently the P_c in the first cycle is used, which is unambiguous and gives a reliable estimate of S_{hmin} of 13.4 MPa at 860 m, corresponding to an S_{hmin} gradient of 15.5 MPa/km.
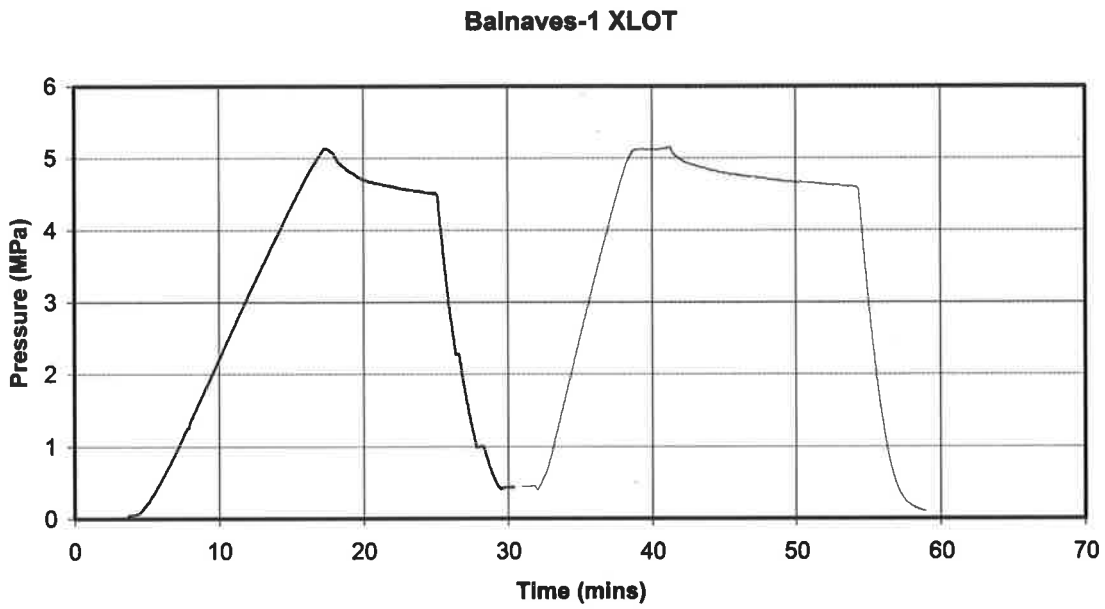
Balnaves-1 XLOT

Figure 8.23. Surface pressure recorded during Balnaves-1 XLOT conducted at 860 m.

Balnaves-1 XLOT
1st Cycle
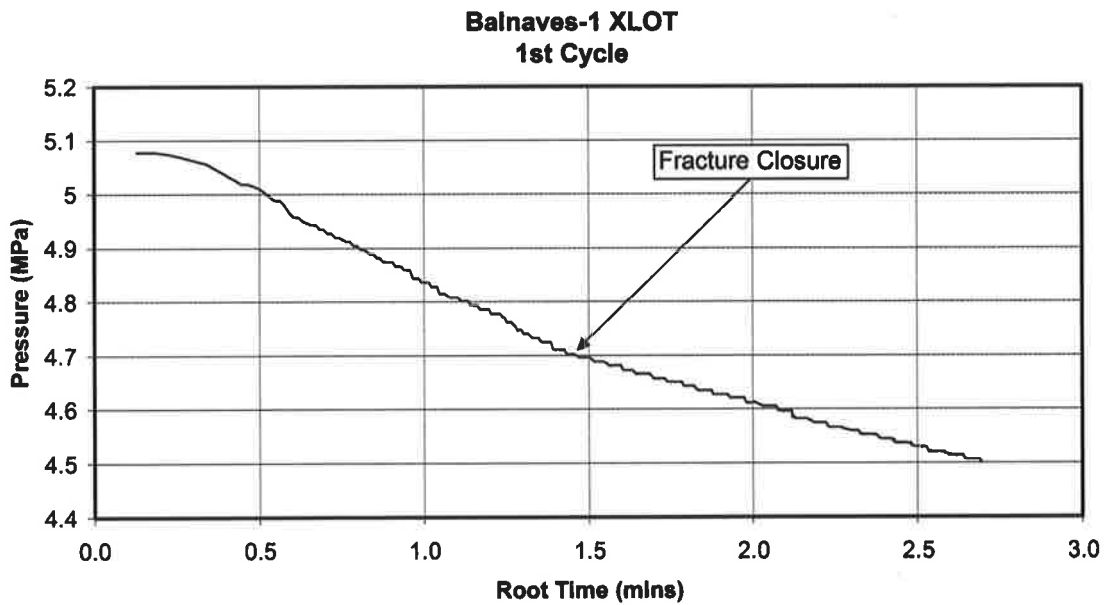
Figure 8.24. Surface pressure versus the square root of time since pumping stopped for the first cycle of the XLOT conducted at Balnaves-1. The interpreted P_c is 4.7 MPa.
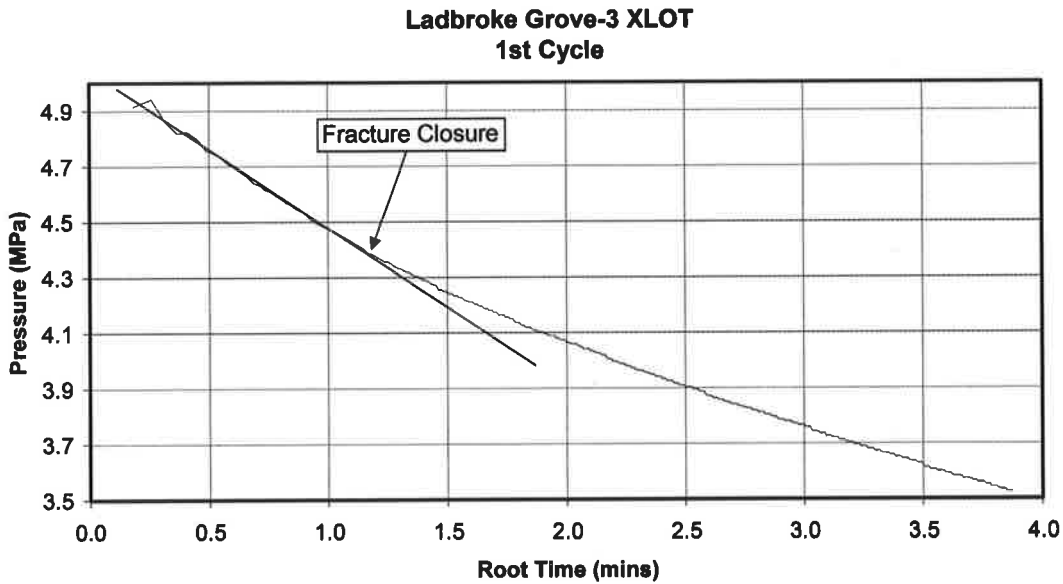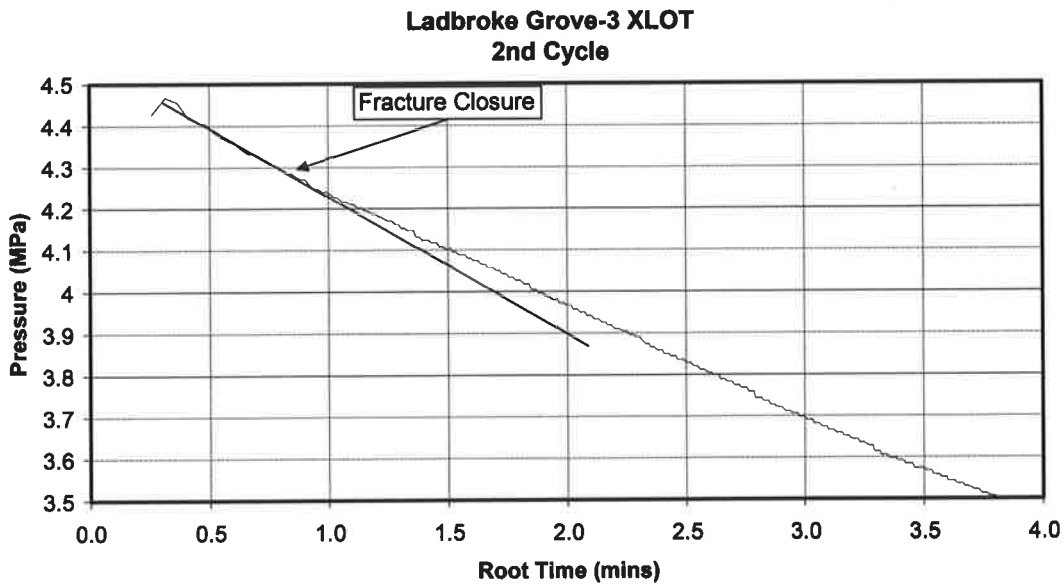
Balnaves-1 XLOT
2nd Cycle
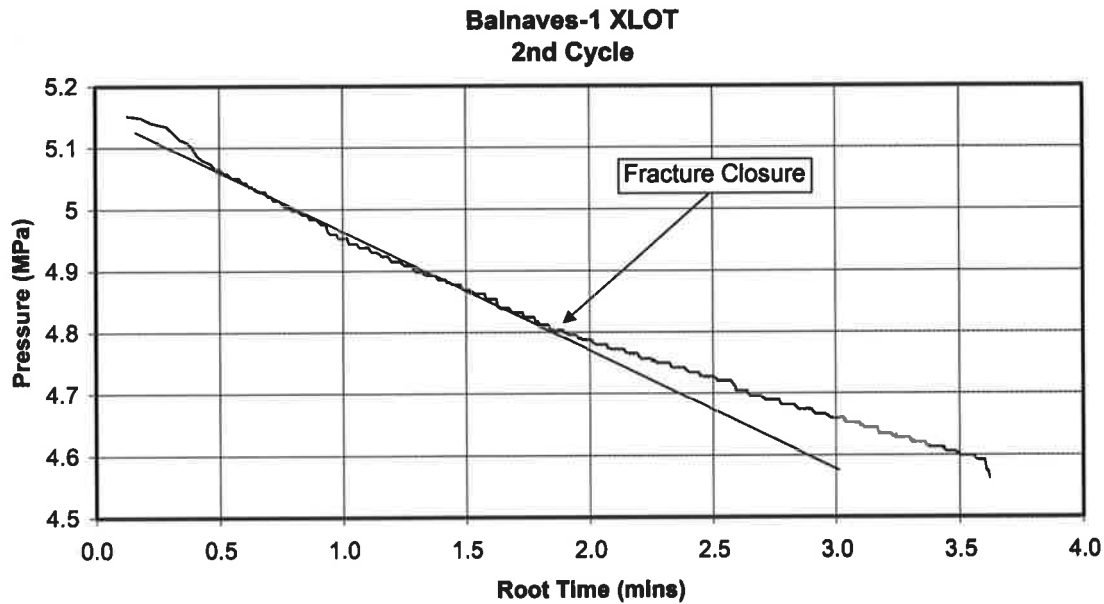
Figure 8.25. Surface pressure versus the square root of time since pumping stopped for the second cycle of the XLOT conducted at Balnaves-1. The interpreted P_c is 4.8 MPa.

8.3.2. DITF Occurrence

Drilling-induced tensile fractures were observed in two of the four wells in which image logs were available, Haselgrove-1 and Wynn-1. Information on P_p, P_w and S_{hmin} is available for Haselgrove-1, as are regional S_v profiles. Hence, the occurrence of DITFs in Haslegrove-1 can be used to constrain S_{Hmax}. Given that the S_{hmin} determined in Wynn-1 is unreliable, in the absence of S_{hmin}, the occurrence of DITFs in Wynn-1 cannot be used to constrain S_{Hmax}.

The maximum P_w gradient in Haslegrove-1 is 11.3 MPa/km. This value is typical for the Otway Basin and is slightly higher than the P_p gradient.

The occurrence of DITFs can be combined with frictional limits to constrain the maximum horizontal stress. The appropriate value for μ varies between 0.6 and 1 (Brace and Kohlstedt, 1980; McGarr, 1980; Zoback and Healy, 1984). However, the limited number of DITFs interpreted and the restriction of those DITFs to two wells indicates that in-balance wells are on the verge of DITF occurrence. This suggests that a μ in the low end of this range is appropriate for the Otway Basin. Consequently a μ of 0.6 is used on this analysis.

Haselgrove-1

Thirteen DITFs were interpreted in Haselgrove-1 at depths of 2750 m to 3137 m (Section 8.2.2). The LOT was conducted at a depth of 888 m indicating an S_{hmin} gradient of 15.0 MPa/km. The single LOT at Haselgrove-1 yields an S_{hmin} consistent with the XLOTs conducted at Ladbroke Grove-3 and Balnaves-1, and the regional LOT trend (Figure 8.26). This combined with the lack of overpressure in the region and the lack of any significantly deeper estimates of S_{hmin} makes 15.0 MPa/km the most reliable estimate of the S_{hmin} gradient. At a depth of 2750 m, the depth at which DITFs were observed, the S_{hmin} gradient is 15.0 MPa/km, the S_v gradient is 21.7 MPa/km, the P_p gradient is 9.8 MPa/km and the P_w gradient is 11.3 MPa/km (Table 8.5; Figure 8.27). The shaded region in Figure 8.28 represents the stress states for which DITFs may form using the known S_v, P_p, and P_w. A vertical line for the known S_{hmin} further reduces the allowable values of S_{Hmax}. The minimum value of S_{Hmax} is constrained by the minimum value for which DITFs may occur (Section 3.6.3), while the maximum value is constrained by frictional limits (Section 3.6.4). The minimum value of S_{Hmax} for which DITFs can occur is 23.9 MPa/km (Figure 8.28). The maximum value of S_{Hmax} from frictional limits (for $\mu = 0.6$) is 26.0 MPa/km (Figure 8.28).

Component	Value
Depth	2750 m
S_v	21.7 MPa/km
S_{hmin}	15.0 MPa/km
P_p	9.8 MPa/km
P_w	11.3 MPa/km
S_{Hmax}	23.9 (DITF) – 26.0 (frictional limit) MPa/km
S_{Hmax} orientations	123°N

Table 8.5. Stress tensor in Haselgrove-1 at a depth of 2750 m.

8.3.3. Breakout Occurrence

Breakouts were observed in the four wells in which image logs were available, Haselgrove-1, Jacaranda Ridge-1, Killanoola-1DW and Wynn-1. S_{Hmax} can be constrained using the occurrence of breakouts and rock strength. However, rock
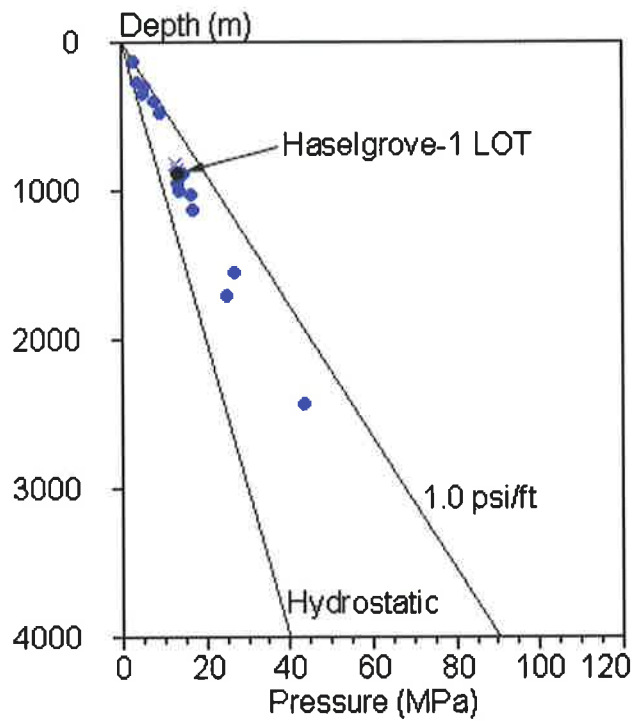
Figure 8.26. Depth plot of XLOT P$_c$ from Balnaves-1 and Ladbroke Grove-3, and LOPs from the entire Otway Basin.
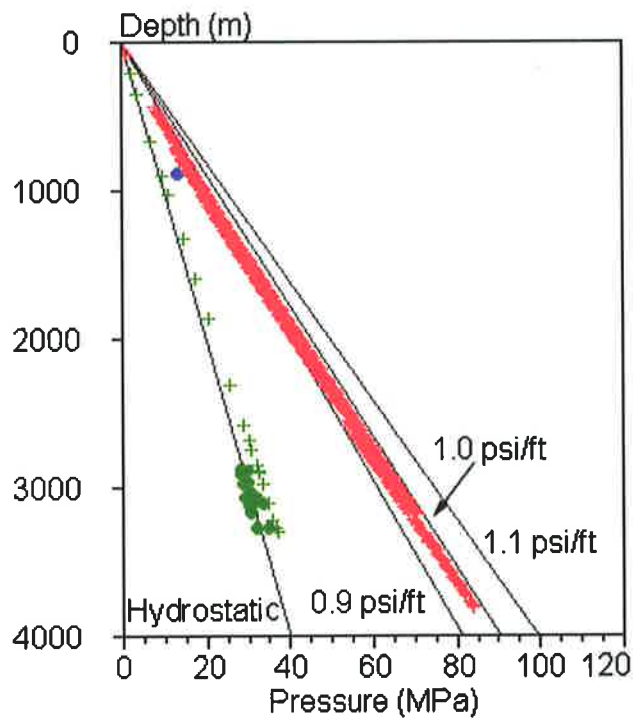
Figure 8.27. Depth plot showing, LOT (•), mud weights (+) and WFITs (•) from Haselgrove-1, and S$_v$ (+) from four wells in the Otway Basin.
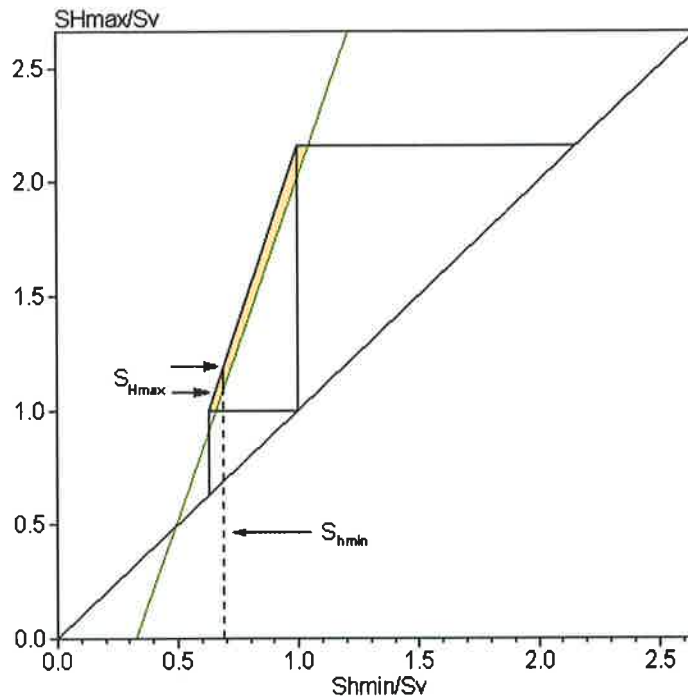
Figure 8.28. Allowable region: Shaded area represents stress states in which DITFs can occur (Haselgrove-1).

strengths were only available for Jacaranda Ridge-1 (Dewhurst et al., 2001).

Information on P_p, P_w and S_v are not available specifically for Jacaranda Ridge-1. However, regional values are used. As at Wynn-1, the XLOT ar Jacaranda Ridge-1 is considered to yield an unreliable S_{hmin} (below frictional limit) and the regional S_{hmin} gradient of 15 MPa/km is used.

Three samples were collected in Jacaranda Ridge-1 for the purpose of laboratory rock testing. These samples consist of a phyllosilicate fault rock from a depth of 2634.2 m, a cataclasite from a depth of 2636.5 m and a reservoir sample from a depth of 2636.85 m, coincident with observed breakout. Failure envelopes were determined for each of these three samples (Dewhurst et al., 2001; Figure 8.29). The reservoir rocks have a uniaxial compressive rock strength of 54 MPa (Figure 8.30). At 2635 m, the depth of rock test data and breakout occurrence, S_v = 56.9 MPa, S_{hmin} = 39.5 MPa, P_w = 29.0 MPa and P_p = 25.8 MPa (Sections 8.2 and 8.3.1). For this stress tensor, S_{Hmax} must exceed 54.5 MPa in order for breakouts to develop (Figure 8.31). This is the value for which breakouts will begin to form for a uniaxial rock strength of 54 MPa. Breakouts are well developed in Jacaranda Ridge-1, and the rock strength relevant in the context of breakout formation is $C_0 \leq C \leq 1.36C_0$ (Moos and Zoback,

1990; Section 3.3.3). Thus $S_{Hmax} = 54.5$ MPa is a conservative lower bound to S_{Hmax}. The equivalent minimum S_{Hmax} gradient is 20.7 MPa/km (normal fault regime). However, the rock strength data and breakout occurrence are consistent with the lower bound to S_{Hmax} of 23.9 MPa/km, indicating a strike-slip fault regime, determined using the observation of DITFs in Haselgrove-1 (Section 8.3.2) as breakouts are also predicted for this value.
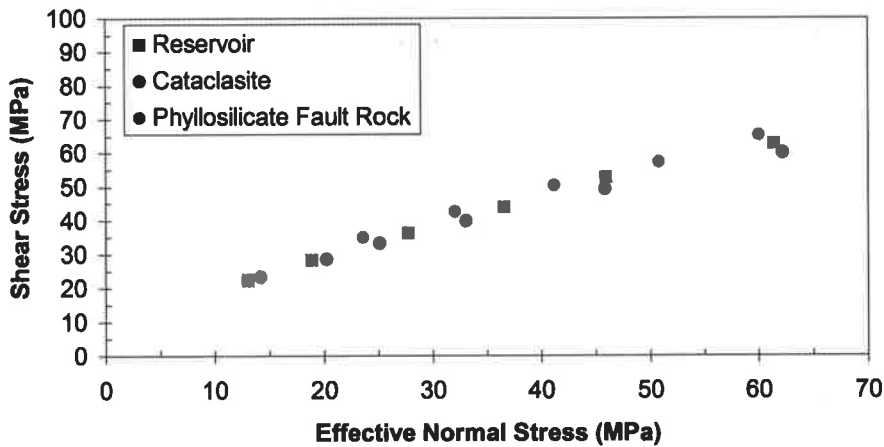
Figure 8.29. Failure envelope for rock samples taken from Jacaranda Ridge-1 (after Dewhurst et al., 2001).
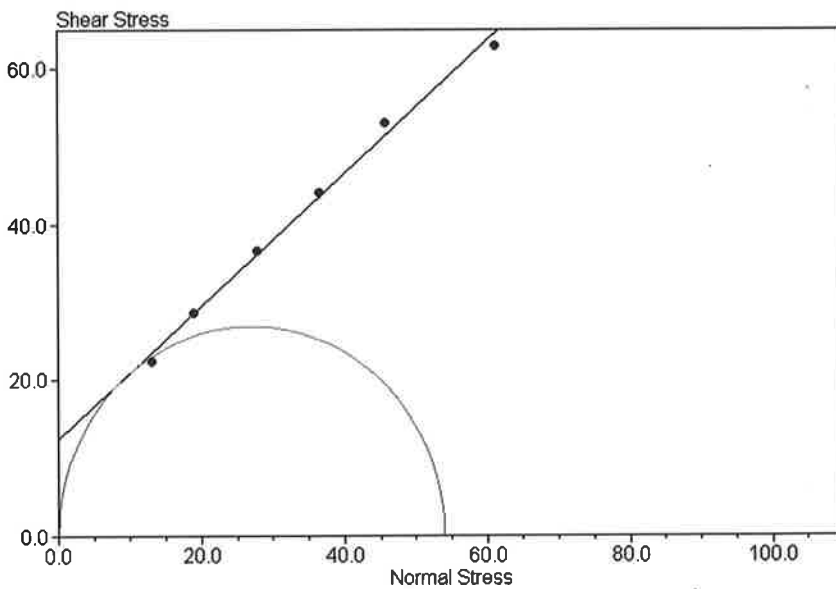
Figure 8.30. Failure envelope for reservoir sample from 2636.85 m with Mohr circle showing a uniaxial compressive rock strength of 54 MPa.
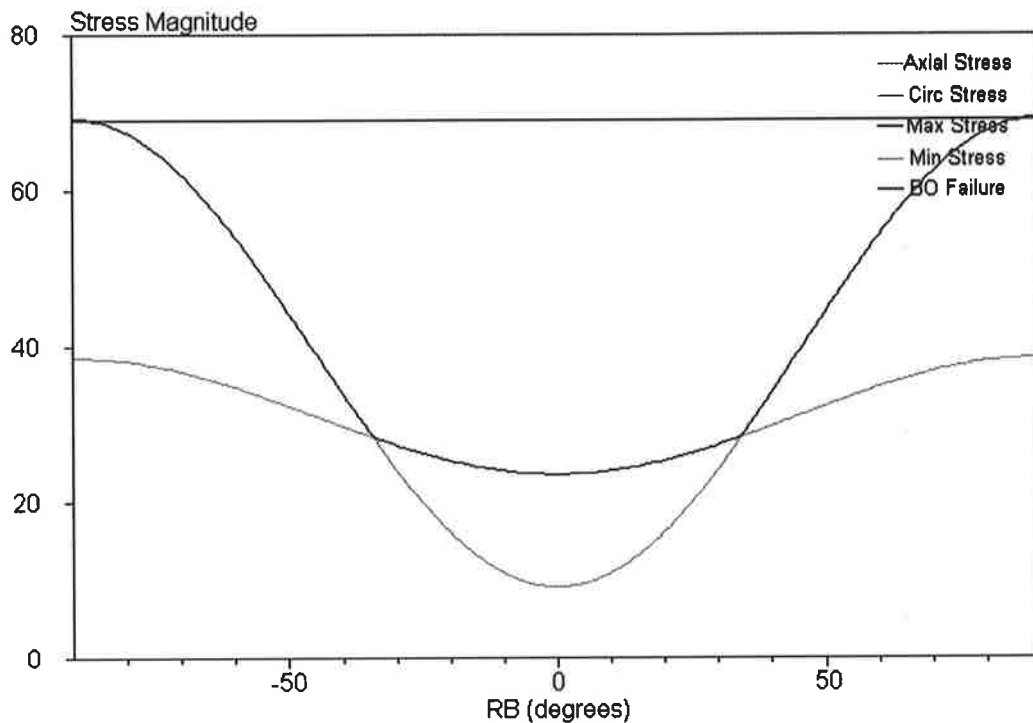
Figure 8.31. Wellbore stresses at a depth of 2635 m, with S_v = 56.9 MPa, S_{hmin} = 39.5 MPa, P_w = 29.0 MPa, P_p = 25.8 MPa and S_{Hmax} = 54.5 MPa and a failure line for a uniaxial compressive rock strength of 54 MPa.

8.4. Otway Basin Stress Tensor

The observation of DITFs combined with S_{hmin} determined from LOTs and XLOTs, S_v from four density logs and P_p from WFITs and DSTs indicate a strike-slip stress regime close to frictional limit with stress magnitudes as summarised in Table 8.6. Given that both S_{Hmax} determined from the occurrence of DITFs and breakouts are lower bounds to S_{Hmax}, the higher lower bound yielded by DITF occurrence is used in the following discussion of the implications of the in situ stress field because it provides a tighter constraint on S_{Hmax}.

8.5. Implications

8.5.1. Fault Reactivation and Seal Breach

The implications of the in situ stress tensor in the Penola Trough for fault reactivation and seal breach are discussed in this section for the range of in situ stresses outlined in Section 8.4 (Table 8.6). Two cases are investigated, the lower bound to S_{Hmax}

obtained from the observation of DITFs and the upper bound to S_{Hmax} obtained from friction limits (Table 8.6).

Stress Component	Value
S_{Hmax} Orientation	123°N
S_v	21.7 MPa/km
S_{hmin}	15.0 MPa/km
P_p	9.8 MPa/km
S_{Hmax}	23.9 (DITF) – 26.0 (Frictional Limit) MPa/km

Table 8.6. Otway Basin in situ stress tensor at 2700 m.

Fault reactivation is closely linked to subsurface fluid flow and hence the migration, accumulation, breaching and re-migration of hydrocarbons. There is abundant evidence that active faults and fractures, i.e. those subject to stresses close to those that induce failure, provide high permeability conduits for fluid flow during deformation (Sibson, 1994; Barton et al., 1995). Reactivation can breach fault-bound traps even if there is fault juxtaposition- and/or fault damage-related seal. Furthermore, active faults and fractures provide conduits for fluid flow even in shaly systems (Dewhurst et al., 1999).

As discussed in the introduction to this chapter (Section 8.1), prior work by Jones et al. (2000) suggested that the capillary properties of cap seals in the Otway Basin are such that they should hold back significant hydrocarbon columns. Across-fault juxtaposition relations and fault damage processes also suggest faults should be sealing. Hence reactivation of faults bounding traps seemed the most likely cause of seal breach (Jones et al., 2000).

Although in the Otway Basin we are concerned with predicting faults that are likely to have been reactivated and caused seal breaching, the methodology is the same as that used to predict hydraulically conductive fractures in the tight reservoirs of the Mereenie Field (Section 6.5.2)

The investigation of fault reactivation requires knowledge of the in situ stress tensor and of the failure envelope of the fault. The failure envelope for the fault bounding the trap at Jacaranda Ridge-1 was determined by Dewhurst et al. (2001; Figure 8.32) and the in situ stress tensor is given in Section 8.4 (Figure 8.32). Note that many previous studies of faults reactivation have assumed that the failure envelope for fault rocks are described by cohesionless Byerlee (1978)-type friction laws (Morris et al., 1996; Ferrill et al., 1999; Wiprut and Zoback, 2000). The lab tests of Dewhurst et al. (2001) show that fault rocks are not cohesionless and cohesion, which is incorporated herein, has a significant influence on fault reactivation potential.
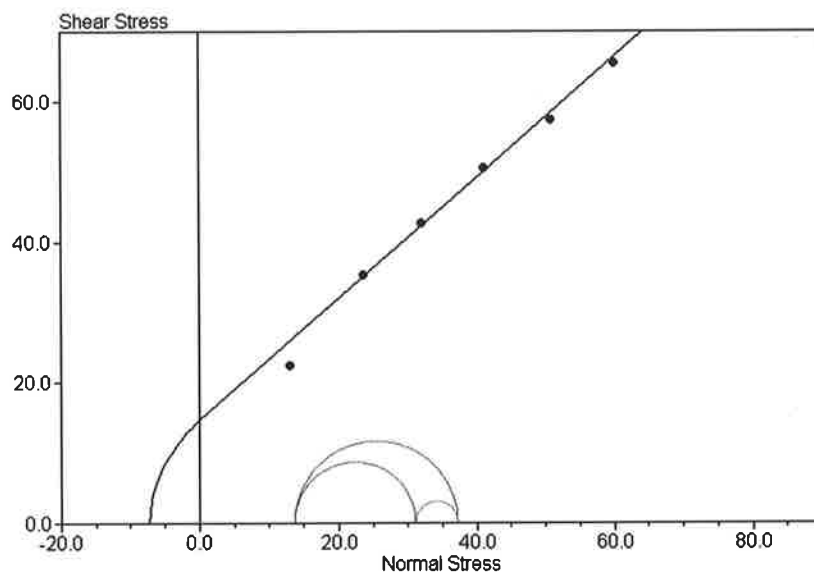
Figure 8.32. Mohr circles representing the Otway Basin in situ stress tensor (S_{Hmax} = 63.0 MPa, from observation of DITFs) and fault failure envelope from (Dewhurst et al., 2001).

The risk of fault reactivation is expressed as the ratio $\Delta P_p/S_v$, i.e. the increase in P_p required to cause failure normalised to S_v (Figures 8.33 and 8.34).

Vertical faults striking ~123°N are the most likely to be reactivated, with $\Delta P/S_v$ = 0.37 for both the upper and lower bound S_{Hmax} cases (Figures 8.33 and 8.34). This corresponds to a P_p difference of 21.1 MPa, at a depth of 2635 m (the fault depth in Jacaranda Ridge-1). Vertical faults striking 033°N are the least likely to be reactivated, with $\Delta P/S_v$ = 0.78 using the lower bound to S_{Hmax} (Figure 8.33) and $\Delta P/S_v$ = 0.88 using the upper bound to S_{Hmax} (Figure 8.34). The pore pressure change required to cause fault reactivation for faults of all orientations is large.
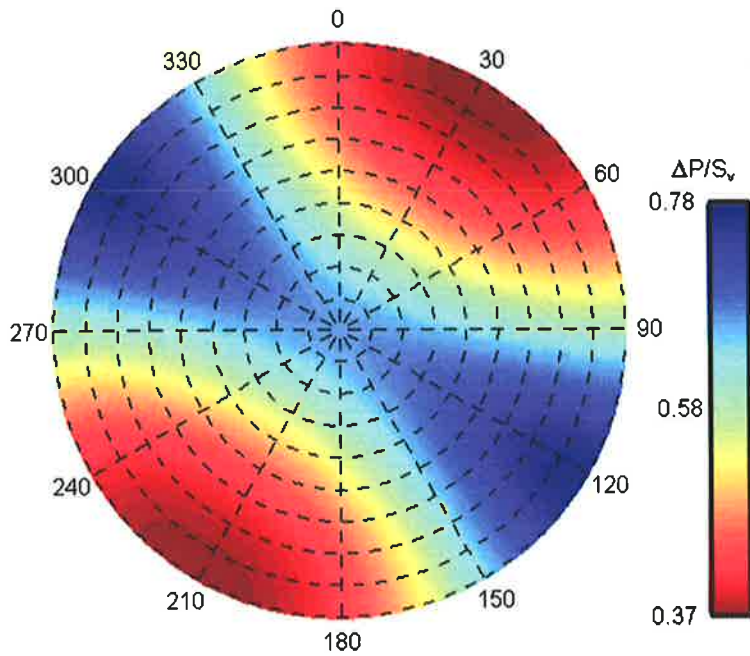
Figure 8.33. Polar diagram of poles to planes coloured by change in P_p normalised to S_v, above which fracture reactivation will occur for the lower bound to S_{Hmax} determined from observations of DITFs. Red indicates relatively high risk and blue indicates relatively low risk.
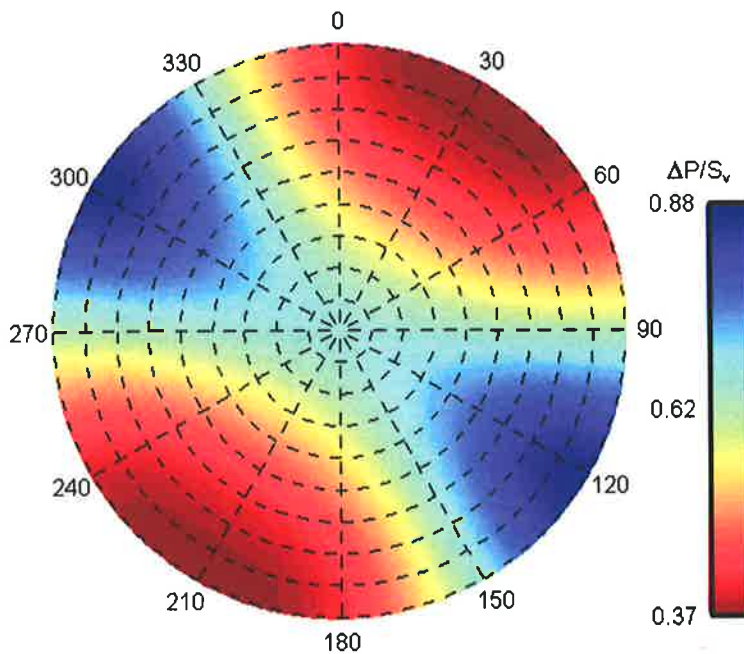
Figure 8.34. Polar diagram of poles to planes coloured by change in P_p normalised to S_v, above which fracture reactivation will occur for the upper bound to S_{Hmax} determined from friction limits. Red indicates relatively high risk and blue indicates relatively low risk.

Consequently, the risk of fault seal failure in the Penola Trough is relatively low, suggesting that seal breach in the Penola Trough is not due to fault reactivation, assuming all faults have a similar failure envelope to that of Jacaranda Ridge-1.

During the course of this study Origin Energy has drilled several prospects in the Penola Trough, targeting fault-bound traps with different fault orientations. These wells have intersected residual hydrocarbon columns. These results tentatively suggest that fault orientation (and thus reactivation potential) do not control seal integrity in the Otway Basin. This is consistent with the rather large increase in P_p required to cause fault reactivation in the area. It should be re-iterated that if migration/breach occurred in a palaeo-stress field that differed from that of the present-day, then the above predictions based on the in situ stress field are not relevant to such an earlier phase of migration/breach. However, the variation in breached fault orientations suggests that seal failure is due neither to contemporary or paleo fault reactivation. Boult et al. (2002) has similarly concluded that fault reactivation may not be responsible for seal breach in the Otway Basin. Boult et al. (2002) have observed extensive fracturing of the cap seal units in the Otway Basin on image logs not analysed in this study. Combined with the results of the analysis herein, and evidence for strong faults (Dewhurst et al., 2001), this has led Boult et al. (2002) to suggest that pervasive fracturing of previously intact cap rock, rather than fault reactivation, may be responsible for seal breach. Although beyond the scope of this thesis, it will be interesting to test this hypothesis against in situ stress variation across the Otway Basin and to look for ì low stressî areas where cap seals may be unfractured.

8.6.   Conclusion

The in situ stress tensor in the Penola Trough, combined with failure envelopes for fault rocks (Dewhurst et al., 2001) suggest that seal breach in the Penola Trough is not due to fault reactivation. This conclusion is supported by recent drilling experience in the Penola Trough, in which fault-bound traps with a variety of different fault orientations are breached. Pervasive fracturing of previously intact cap rock (which may be weaker than fault rocks) may be responsible for seal breach. This hypothesis requires further testing using in situ stress data and modelling.

9. Concluding Statement

The aims of this thesis were to apply existing, and develop new techniques for in situ stress determination from oil field data, and to utilise these techniques within several case studies of the varied significance of in situ stress data to petroleum exploration and production.

Existing stress determination techniques, and new techniques, have been implemented using the SWIFT software developed as part of this thesis. These techniques have been applied to case studies in four regions of petroleum exploration and production: the Swan Lake Field, South Australia; the Mereenie Field, Northern Territory; the Gulf of Thailand; and, the Otway Basin, South Australia. Techniques for in situ stress determination have been used and developed depending on the available dataset in each case study, resulting in:

- modest advancement in stress determination techniques (especially horizontal DITFs and forward modeling of LOPs);
- significant advancement in knowledge of the stress tensor in the four study areas;
- better understanding of the stress-related problems in the study areas, and;
- some solutions to stress-related problems in each of the case studies and identification of other areas requiring further research.

Appendix A
Functions and Parameters in the SWIFT Stress Classes

A1. Class Stress

Function	Returns	Description
CopySt()	stress*	Creates a copy of an instance of stress and returns a pointer to it
GetSHmax()	double	returns the magnitue of S_{Hmax}
GetShmin()	double	returns the magnitue of S_{hmin}
GetSv()	double	returns the magnitude of S_v
GetPp()	double	returns the P_P
GetHazi()	double	returns the wellbore azimuth (degrees)
GetDevi()	double	returns the wellbore deviation (degrees)
GetOrient()	double	returns the orientation of S_{Hmax} (degrees; see Section 4.2)
GetBeta()	double	returns the dip (β) of S_{Hmax} (degrees; see Sectio 4.2)
GetGamma()	double	returns γ (degrees; see Section 4.2)
GetSig11()	double	returns S_{11} from the transformed matrix (see Section 4.2)
GetSig12()	double	returns S_{12} from the transformed matrix (see Section 4.2)
GetSig13()	double	returns S_{13} from the transformed matrix (see Section 4.2)
GetSig22()	double	returns S_{23} from the transformed matrix (see Section 4.2)
GetSig23()	double	returns S_{23} from the transformed matrix (see Section 4.2)
GetSig33()	double	returns S_{33} from the transformed matrix (see Section 4.2)
GetNorm()	double	returns the normal stress acting on a plane whose dip direction and dip is set using SetHazi() and SetDevi()

Function	Returns	Description
GetShear()	double	returns the shear stress acting on a plane whose dip direction and dip is set using SetHazi() and SetDevi()
GetPois()	double	returns Poissonís Ratio
GetMu()	double	returns the coefficient of friction
GetMui()	double	returns the internal coefficient of friction
GetCo()	double	returns the uniaxial compressive rock strength
GetT()	double	returns the tensile rock strength
GetDepth()	double	returns the Depth
GetFMu()	double	returns the $f(\mu)$ (see Section 2.5)
GetFMui()	double	returns the $f(\mu_i)$ (see Section 2.5)
GetGriffithOnly()	int	returns 0 for a Griffith failure envelop 1 for a composite Griffith-Coulomb failure envelope 2 for a Coulomb failure envelope
GetGriffShear(double)	double	returns shear stress value of the Griffith failure envelope for a given normal stress value
GetGriffNorm(double)	double	returns normal stress value of the Griffith failure envelope for a given shear stress value
GetCoulombShear(double)	double	returns shear stress value of the Cloulmb failure envelope for a given normal stress value
GetCoulombNorm(double)	double	returns normal stress value of the Coulomb failure envelope for a given shear stress value
GetGriffCoulShear(double)	double	returns shear stress value of the Griffith-Coulomb failure envelope for a given normal stress value
GetGriffCoulNorm(double)	double	returns normal stress value of the Griffith-Coulomb failure envelope for a given shear stress value
GetWBCoulombShear(double)	double	returns shear stress value of the Coulomb failure envelope for a given normal stress value using the internal coefficient of friction

Function	Returns	Description
GetWBCoulombNorm(double)	double	returns normal stress value of the Coulomb failure envelope for a given shear stress value using the internal coefficient of friction
GetWBGriffCoulShear(double)	double	returns shear stress value of the Griffith-Coulomb failure envelope for a given normal stress value using the internal coefficient of friction
GetWBGriffCoulNorm(double)	double	returns normal stress value of the Griffith-Coulomb failure envelope for a given shear stress value using the internal coefficient of friction
SetSHmax(double or int)	-	Sets the magnitude of S_{Hamx}
SetShmin(double or int)	-	Sets the magnitude of S_{hmin}
SetSv(double or int)	-	Sets the magnitude of S_v
Set12(double)	-	Sets the value of S_{12} (see Section 4.2)
Set13(double)	-	Sets the value of S_{13} (see Section 4.2)
Set23(double)	-	Sets the value of S_{23} (see Section 4.2)
SetPp(double or int)	-	Sets the value of P_p
SetHazi(double or int)	-	Sets the hole azimuth/dip direction of the plane (degrees)
SetDevi(double or int)	-	Sets the hole deviation/dip of the plane (degrees)
SetOrient(double or int)	-	Sets the orientation of S_{Hmax} (degrees)
SetGamma(double or int)	-	Sets γ (degrees; see Section 4.2)
SetBeta(double or int)	-	returns the dip (β) of S_{Hmax} (degrees; see Section 4.2)
SetPois(double)	-	Sets Poissonís Ratio
SetMu(double)	-	Sets the coefficient of friction
SetMui(double mue)	-	Sets the coefficient of internal friction
SetCo(double)	-	Sets the uniaxial compressive rock strength
SetT(double)	-	Sets the tensile rock strength

Function	Returns	Description
SetDepth(double)	-	Sets the depth
SetuseCo(bool)	-	controls whether C_0 is used in failure calculations.
SetGriffithOnly(int)	-	Determines the failure envelope used 0 for a Griffith failure envelop 1 for a composite Griffith-Coulomb failure envelope 2 for a Coulomb failure envelope

A2. Class CStress

Function	Returns	Description
CopySt()	cstress*	Creates a copy of an instance of cstress and returns a pointer to it
GetSigZZ()	TMatrix*	returns the axial stress around the wellbore as a pointer to a (1,181) TMatrix
GetSigTT()	TMatrix*	returns the circumferential stress around the wellbore as a pointer to a (1,181) TMatrix
GetThauTZ()	TMatrix*	returns the shear stress around the wellbore as a pointer to a (1,181) TMatrix
GetSigTMax()	TMatrix*	returns the maximum wellbore stress around the wellbore as a pointer to a (1,181) TMatrix (see Section 4.2)
GetSigTmin()	TMatrix*	returns the minimum wellbore stress around the wellbore as a pointer to a (1,181) TMatrix (see Section 4.2)
GetW()	TMatrix*	returns the angle between the maximum wellbore stress and the wellbore axis as a pointer to a (1,181) TMatrix (degrees; see Section 4.2)
GetOriCoMax()	int	returns the angle at which the rock strength required to prevent breakout formation is a maximum (degrees)

Function	Returns	Description
GetBOWidth()	int	returns the predicted width of breakout formation
GetOriMaxSigTMax()	int	returns the angle at which the maximum wellbore stress is a maximum (degrees)
GetOriMinSigTmin()	int	returns the angle at which the minimum wellbore stress is a mminimum (degrees)
GetSigRR()	double	returns the radial stress
GetPw()	double	returns the mud pressure
GetCO()	TMatrix*	returns the rock strength required to prevent breakout formation around the wellbore as a pointer to a (1,181) TMatrix
GetBOFL()	TMatrix*	returns the limit to the maximum wellbore stress above which breakout will occur around the wellbore as a pointer to a (1,181) TMatrix
GetMinSigZZ()	double	returns the minimum axial stress
GetMaxSigZZ()	double	returns the maximum axial stress
GetMinSigTT()	double	returns the minimum circumferential stress
GetMaxSigTT()	double	returns the maximum circumferential stress
GetMinSigTMax()	double	returns the minimum of the maximum wellbore stress
GetMaxSigTMax()	double	returns the maximum of the maximum wellbore stress
GetMinSigTmin()	double	returns the minimum of the minimum wellbore stress
GetMaxSigTmin()	double	returns the maximum of the minimum welbore stress
GetMaxCo()	double	returns the maximum of the rock strength rewuired to prevent breakout around the wellbore
CalcSigZZRb(double)	double	returns the axial stress for a given relative bearing
CalcSigTTRb(double)	double	returns the circumferential stress for a given relative bearing
CalcThauTZRb(double)	double	returns the shear stress for a given relative bearing

Function	Returns	Description
CalcSigTMaxRb(double)	double	returns the maximum wellbore stress for a given relative bearing
CalcSigTminRb(double)	double	returns the minimum wellbore stress for a given relative bearing
CalcWRb(double)	double	returns the angle between the maximum wellbore stress and the wellbore axis for a given relative bearing
P1azToRb(double p1az, double hazi, double devi)	double	converts P1AZ to a relative bearing for a given P1Az Hazi and DEVI
SetPw(double)	-	sets the wellbore fluid pressure
GetMaxBOFL()	double	returns the maximum of the limit to the maximum wellbore stress above which breakout will occur
GetMinBOFL()	double	returns the minimum of the limit to the maximum wellbore stress above which breakout will occur
GetSigTMaxRB(int)	double	returns the maximum wellbore stress for a given relative bearing
GetBOFLRB(int)	double	returns the limit to the maximum wellbore stress above which breakout will occur for a given relative bearing

A3. Class WBFStress

Function	Returns	Description
SetDip(double)	-	sets the dip of a fracture (degrees)
SetDipDirect(double dd)	-	sets the dip direction of a fracture (degrees)
SetRB(double rb)	-	sets the relative bearing at which the normal and/orshear stress on the fracture are to be calculatesd
GetRB()	double	returns the relative bearing
GetWbfNorm()	double	returns the normal stress acting on a fracture under the wellbore stress concentration
GetWbfShear()	double	returns the shear stress acting on a fracture under the wellbore stress concentration

Function	Returns	Description
GetNWRisk()	TMatrix*	returns the maximum value of μ required to prevent fracture reactivation for a given fracture and wellbore azimuths and deviation increments of 5 degrees as a pointer to a (19,72) TMatrix
GetRiskWidth()	TMatrix*	returns the width of a fracture around the wellbore predicted to reactivate for a given value of μ and wellbore azimuths and deviation increments of 5 degrees as a pointer to a (19,72) TMatrix

Appendix B
Swan Lake Area Leak-Off and Minifracture Test Data

B1. Leak-Off Data

Well Name	Latitude	Longitude	Measured Depth (m)	Casing	Mud Weight (ppg)	Effective Mud Weight (ppg)	HAZI	DEVI	Pressure (MPa)	Test Type	Date	Lithology
Cowralli-3	27.88642	140.021	1713.6	9.63	9.2	16.1	0	2.75	32.43	LOT	4/4/1989	sandstone
Gidgealpa-38	27.91601	140.049	467.87	9.63	8.6	11.6	0	0.5	6.38	LOT	3/3/1990	siltstone
Gidgealpa-39	27.92671	140.056	490.12	9.63	8.9	12.8	0	0.25	7.37	LOT	6/19/1990	siltstone
Gidgealpa-47	27.95214	140.044	434.35	9.63	9	16.1	0	0.5	8.22	LOT	5/26/1991	claystone
Pelican-2	27.80353	140.079	457.21	9.63	8.8	13.6	0	0.75	7.31	LOT	2/16/1988	siltstone
Pelican-4	27.80925	140.104	574.86	9.63	8.8	13.1	0	0.5	8.85	LOT	11/2/1989	silt/sandstone

B2. Minifracture Data

Well Name	Latitude	Longitude	TVD SS(m)	Pc (MPa)	Pp (MPa)
Cowralli-1	27.87734	140.0174	2931.414	62.20128	29.06396
Meranji-15	27.84788	140.0668	2916.326	54.40699	29.37432
Meranji-7	27.85453	140.0703	2719.73	52.69998	27.13969
Swan Lake-2	27.84438	140.1428	2811.932	58.53925	28.2685
Swan Lake-4	-27.85241	140.1261	2817.724	60.62394	29.31225
Swan Lake-4	-27.85241	140.1261	2992.831	71.53311	29.57851

Appendix C
Mereenie Fracture Data

Well Name	Latitude	Longitude	Formation	TVD (m)	Reservoir Pressure (MPa)	Reservoir Pressure Gradient (MPa/km)	Closure Pressure (MPa)	Closure Pressure Gradient (MPa/km)	Source
East Mereenie-11	-24.036778	131.64412	P3 120/130	1415.03	8.55	6.04	18.24	12.89	NSI
East Mereenie-14	-24.011156	131.60738	P3 120/130	1427.68	10.05	7.04	18.83	13.19	NSI
East Mereenie-16	-24.024947	131.62867	P3 120/130	1402.99	8.2	5.84	15.51	11.05	NSI
East Mereenie-19	-24.031231	131.62576	P3 120/130	1437.13	8.27	5.75	18.06	12.57	NSI
East Mereenie-20	-24.02825	131.63507	P3 120/130	1409.7	9.65	6.85	16.89	11.98	NSI
East Mereenie-21	-24.019881	131.62329	P3 120/130	1411.07	8.83	6.26	16.55	11.73	NSI
East Mereenie-22	-24.015839	131.61449	P3 120/130	1410.16	10	7.09	17.58	12.47	NSI
East Mereenie-28	-24.026108	131.61568	P3 120/130	1452.37	10.2	7.02	18.79	12.94	NSI
East Mereenie-30	-24.026242	131.60668	P3 120/130	1442.16	9.31	6.46	18.24	12.65	NSI
East Mereenie-31	-24.003736	131.59312	P3 120/130	1454.2	11.55	7.94	19.65	13.51	NSI
East Mereenie-32	-24.025272	131.59786	P3 120/130	1442.47	8.96	6.21	21.72	15.06	NSI
East Mereenie-33	-23.999461	131.58443	P3 120/130	1448.1	10	6.91	19.72	13.62	NSI
East Mereenie-34	-24.019675	131.57986	P3 120/130	1465.94	12.07	8.23	27.74	18.92	NSI
East Mereenie-35	-24.0055	131.59703	P3 230/250	1439.72	12.07	8.38	23.24	16.14	NSI

Well Name	Latitude	Longitude	Formation	TVD (m)	Reservoir Pressure (MPa)	Reservoir Pressure Gradient (MPa/km)	Closure Pressure (MPa)	Closure Pressure Gradient (MPa/km)	Source
East Mereenie-36	-23.958861	131.46917	P3 230/250	1444.14	12.07	8.36	23.44	16.23	NSI
East Mereenie-37	-23.994719	131.57601	P3 230/250	1437.74	12.07	8.4	22.61	15.73	NSI
East Mereenie-38	-23.971292	131.45569	P3 230/250	1477.67	12.07	8.17	23.1	15.63	NSI
East Mereenie-40	-23.946742	131.43678	P3	1449.93			18.03	12.44	picked
East Mereenie-40	-23.971336	131.46603	P4	1494.74			21.99	14.71	picked
East Mereenie-41	-23.990325	131.5668	P3	1441.7			19.68	13.65	picked
East Mereenie-41	-24.026261	131.62303	P4	1494.74			22.47	15.03	picked
East Mereenie-7	-24.02265	131.60029	P3 120/130	1420.52	7.58	5.34	15.72	11.07	NSI
West Mereenie-10	-24.02265	131.60029	P3 120/130	1460.14	10.76	7.37	34.09	23.35	NSI
West Mereenie-11	-24.018311	131.57546	P3 120/130	1447.95	12.07	8.34	31.3	21.62	NSI
West Mereenie-4	-24.018311	131.57546	P3 120/130	1451.91	12.82	8.83	32.75	22.56	NSI
West Mereenie-5	-24.019911	131.58531	P3 120/130	1445.51	12.07	8.35	19.86	13.74	NSI
West Mereenie-8	-24.008711	131.60396	P3 120/130	1455.88	12.07	8.29	23.72	16.29	NSI
West Mereenie-9	-24.001028	131.58962	P3 120/130	1450.39	12.34	8.51	28.27	19.49	NSI

Appendix D
Otway Basin Vertical Stress

D1. Argonaut-1A

Latitude: -37.97012

Longitude: 140.2661

TVD (m)	Vertical Stress (MPa)	TVD (m)	Vertical Stress (MPa)	TVD (m)	Vertical Stress (MPa)	TVD (m)	Vertical Stress (MPa)	TVD (m)	Vertical Stress (MPa)
77.1	0.76	822.96	14.91	1143	21.56	1463.04	28.39	1783.08	35.33
518.16	8.72	838.2	15.22	1158.24	21.88	1478.28	28.72	1798.32	35.66
533.4	9.03	853.44	15.52	1173.48	22.2	1493.52	29.05	1813.56	35.99
548.64	9.34	868.68	15.82	1188.72	22.52	1508.76	29.38	1828.8	36.32
563.88	9.65	883.92	16.14	1203.96	22.84	1524	29.71	1844.04	36.65
579.12	9.94	899.16	16.46	1219.2	23.16	1539.24	30.04	1859.28	36.98
594.36	10.24	914.4	16.77	1234.44	23.49	1554.48	30.37	1874.52	37.32
609.6	10.53	929.64	17.08	1249.68	23.81	1569.72	30.7	1889.76	37.65
624.84	10.84	944.88	17.39	1264.92	24.13	1584.96	31.03	1905	37.98
640.08	11.15	960.12	17.7	1280.16	24.46	1600.2	31.36	1920.24	38.32
655.32	11.47	975.36	18.01	1295.4	24.78	1615.44	31.7	1935.48	38.65
670.56	11.79	990.6	18.32	1310.64	25.1	1630.68	32.03	1950.72	39.01
685.8	12.11	1005.84	18.64	1325.88	25.43	1645.92	32.36	1965.96	39.35
701.04	12.43	1021.08	18.98	1341.12	25.75	1661.16	32.69	1981.2	39.69
716.28	12.75	1036.32	19.31	1356.36	26.09	1676.4	33.02	1996.44	40.03
731.52	13.06	1051.56	19.63	1371.6	26.42	1691.64	33.35	2011.68	40.36
746.76	13.37	1066.8	19.95	1386.84	26.74	1706.88	33.67	2026.92	40.69
762	13.68	1082.04	20.27	1402.08	27.07	1722.12	34	2042.16	41.03
777.24	13.99	1097.28	20.6	1417.32	27.4	1737.36	34.32	2057.4	41.38
792.48	14.29	1112.52	20.93	1432.56	27.73	1752.6	34.65	2072.64	41.71
807.72	14.6	1127.76	21.25	1447.8	28.06	1767.84	34.99	2087.88	42.05

TVD (m)	Vertical Stress (MPa)	TVD (m)	Vertical Stress (MPa)	TVD (m)	Vertical Stress (MPa)	TVD (m)	Vertical Stress (MPa)	TVD (m)	Vertical Stress (MPa)
2103.12	42.39	2575.56	53.16	3048	64.09				
2118.36	42.73	2590.8	53.53	3063.24	64.45				
2133.6	43.07	2606.04	53.88	3108.96	65.45				
2148.84	43.42	2621.28	54.24	3124.2	65.77				
2164.08	43.76	2636.52	54.61	3139.44	66.04				
2179.32	44.09	2651.76	54.96	3154.68	66.35				
2194.56	44.43	2667	55.31	3200.4	67.19				
2209.8	44.78	2682.24	55.66	3230.88	67.74				
2225.04	45.12	2697.48	56.02	3246.12	68.03				
2240.28	45.47	2712.72	56.36	3261.36	68.32				
2255.52	45.81	2727.96	56.7	3276.6	68.6				
2270.76	46.16	2743.2	57.05	3291.84	68.88				
2286	46.5	2758.44	57.4	3322.32	69.47				
2301.24	46.84	2773.68	57.75	3337.56	69.75				
2316.48	47.2	2788.92	58.1	3398.52	70.88				
2331.72	47.55	2804.16	58.45	3413.76	71.17				
2346.96	47.9	2819.4	58.8	3429	71.47				
2362.2	48.25	2834.64	59.16	3444.24	71.75				
2377.44	48.61	2849.88	59.51	3459.48	72.07				
2392.68	48.96	2865.12	59.87	3474.72	72.39				
2407.92	49.31	2880.36	60.23	3489.96	72.66				
2423.16	49.66	2895.6	60.58	3505.2	72.97				
2438.4	50	2910.84	60.94	3535.68	73.62				
2453.64	50.35	2926.08	61.29	3550.92	73.97				
2468.88	50.7	2941.32	61.64	3566.16	74.32				
2484.12	51.06	2956.56	62	3581.4	74.68				
2499.36	51.41	2971.8	62.36	3642.36	76.12				
2514.6	51.76	2987.04	62.71	3657.6	76.47				
2529.84	52.11	3002.28	63.07	3672.84	76.84				
2545.08	52.47	3017.52	63.42	3688.08	77.2				
2560.32	52.81	3032.76	63.72	3703.32	77.56				

D2. Chama-1A

Latitude: -37.42546

Longitude: 139.5449

TVD (m)	Vertical Stress (MPa)	TVD (m)	Vertical Stress (MPa)	TVD (m)	Vertical Stress (MPa)	TVD (m)	Vertical Stress (MPa)	TVD (m)	Vertical Stress (MPa)
83.1	0.82	1097.28	21.02	1493.52	30.31	1920.24	40.35	2331.72	49.91
716.28	12.76	1112.52	21.37	1508.76	30.68	1935.48	40.71	2346.96	50.27
731.52	13.07	1127.76	21.72	1539.24	31.4	1965.96	41.47	2362.2	50.61
746.76	13.37	1143	22.07	1554.48	31.76	1981.2	41.84	2377.44	50.96
762	13.68	1158.24	22.43	1569.72	32.12	1996.44	42.21	2392.68	51.27
777.24	13.98	1173.48	22.79	1584.96	32.48	2011.68	42.58	2407.92	51.59
792.48	14.28	1188.72	23.15	1600.2	32.83	2026.92	42.95	2423.16	51.92
807.72	14.58	1203.96	23.5	1615.44	33.19	2042.16	43.28	2438.4	52.27
822.96	14.9	1219.2	23.85	1630.68	33.55	2057.4	43.65	2468.88	52.92
838.2	15.23	1234.44	24.21	1645.92	33.91	2072.64	44.03	2484.12	53.26
853.44	15.56	1249.68	24.57	1661.16	34.27	2087.88	44.38	2499.36	53.62
868.68	15.89	1264.92	24.93	1676.4	34.6	2103.12	44.73	2514.6	53.98
883.92	16.23	1280.16	25.3	1691.64	34.94	2118.36	45.08	2529.84	54.32
899.16	16.56	1295.4	25.67	1706.88	35.28	2133.6	45.45	2545.08	54.67
914.4	16.89	1310.64	26.03	1737.36	36	2148.84	45.78	2560.32	55.02
929.64	17.23	1325.88	26.39	1752.6	36.36	2164.08	46.12	2575.56	55.37
944.88	17.56	1341.12	26.75	1767.84	36.73	2179.32	46.46	2590.8	55.73
960.12	17.9	1356.36	27.1	1783.08	37.09	2194.56	46.8	2606.04	56.13
975.36	18.23	1371.6	27.46	1798.32	37.44	2209.8	47.14	2621.28	56.46
990.6	18.57	1386.84	27.81	1813.56	37.79	2225.04	47.49	2636.52	56.75
1005.84	18.92	1402.08	28.17	1828.8	38.15	2240.28	47.84	2651.76	57.09
1021.08	19.27	1417.32	28.52	1844.04	38.52	2255.52	48.17	2667	57.43
1036.32	19.62	1432.56	28.89	1859.28	38.88	2270.76	48.49	2682.24	57.8
1051.56	19.97	1447.8	29.24	1874.52	39.25	2286	48.83	2697.48	58.19
1066.8	20.31	1463.04	29.6	1889.76	39.62	2301.24	49.16	2712.72	58.58
1082.04	20.66	1478.28	29.96	1905	39.98	2316.48	49.53	2727.96	58.97

D3. Copa-1

Latitude: **-37.68695**

Longitude: **139.7575**

TVD (m)	Vertical Stress (MPa)	TVD (m)	Vertical Stress (MPa)	TVD (m)	Vertical Stress (MPa)	TVD (m)	Vertical Stress (MPa)	TVD (m)	Vertical Stress (MPa)
92.3	0.92	1402.08	27.44	1798.32	36.38	2194.56	45.81	2758.44	58.31
1021.08	19.04	1417.32	27.78	1813.56	36.74	2209.8	46.16	2773.68	58.69
1036.32	19.35	1432.56	28.12	1828.8	37.1	2225.04	46.52	2788.92	59.08
1051.56	19.68	1447.8	28.46	1844.04	37.47	2240.28	46.88	2804.16	59.46
1066.8	20.01	1463.04	28.8	1859.28	37.82	2255.52	47.26	2819.4	59.84
1082.04	20.34	1478.28	29.14	1874.52	38.17	2270.76	47.64	2834.64	60.23
1097.28	20.67	1493.52	29.48	1889.76	38.52	2286	48	2849.88	60.59
1112.52	21.01	1508.76	29.82	1905	38.87	2301.24	48.36	2865.12	60.97
1127.76	21.34	1524	30.16	1920.24	39.23	2316.48	48.72	2880.36	61.35
1143	21.67	1539.24	30.5	1935.48	39.58	2331.72	49.08	2895.6	61.73
1158.24	22	1554.48	30.83	1950.72	39.95	2346.96	49.46	2910.84	62.1
1173.48	22.33	1569.72	31.17	1965.96	40.32	2362.2	49.84	2941.32	62.85
1188.72	22.67	1584.96	31.51	1981.2	40.68	2377.44	50.22	2956.56	63.22
1203.96	23.01	1600.2	31.86	1996.44	41.04	2392.68	50.6	2971.8	63.59
1219.2	23.34	1615.44	32.2	2011.68	41.4	2407.92	50.98	2987.04	63.97
1234.44	23.69	1630.68	32.56	2026.92	41.77	2423.16	51.37	3002.28	64.35
1249.68	24.03	1645.92	32.91	2042.16	42.14	2590.8	54.06	3017.52	64.72
1264.92	24.38	1661.16	33.26	2057.4	42.51	2621.28	54.85	3032.76	65.1
1280.16	24.73	1676.4	33.61	2072.64	42.88	2636.52	55.23	3048	65.47
1295.4	25.07	1691.64	33.95	2087.88	43.24	2651.76	55.62	3063.24	65.85
1310.64	25.41	1706.88	34.3	2103.12	43.61	2667	56.01	3078.48	66.23
1325.88	25.75	1722.12	34.65	2118.36	43.98	2682.24	56.38	3093.72	66.61
1341.12	26.1	1737.36	34.99	2133.6	44.34	2697.48	56.77	3108.96	66.98
1356.36	26.43	1752.6	35.34	2148.84	44.71	2712.72	57.15	3124.2	67.35
1371.6	26.77	1767.84	35.68	2164.08	45.07	2727.96	57.54	3139.44	67.73
1386.84	27.11	1783.08	36.03	2179.32	45.45	2743.2	57.93	3154.68	68.1

TVD (m)	Vertical Stress (MPa)	TVD (m)	Vertical Stress (MPa)	TVD (m)	Vertical Stress (MPa)	TVD (m)	Vertical Stress (MPa)	TVD (m)	Vertical Stress (MPa)
3169.92	68.48	3672.84	80.71						
3185.16	68.86	3688.08	81.04						
3215.64	69.61	3703.32	81.43						
3230.88	69.99	3718.56	81.82						
3246.12	70.36	3733.8	82.21						
3261.36	70.74	3764.28	82.96						
3276.6	71.12	3779.52	83.32						
3291.84	71.51	3794.76	83.7						
3307.08	71.9								
3322.32	72.27								
3337.56	72.64								
3352.8	73.01								
3368.04	73.38								
3398.52	74.14								
3413.76	74.52								
3429	74.89								
3444.24	75.27								
3459.48	75.64								
3474.72	76								
3489.96	76.37								
3505.2	76.73								
3520.44	77.1								
3535.68	77.48								
3550.92	77.85								
3566.16	78.22								
3581.4	78.6								
3596.64	78.97								
3611.88	79.34								
3627.12	79.71								
3642.36	80.08								
3657.6	80.47								

D4. Crayfish-1

Latitude: **-37.28799**

Longitude: **139.5986**

TVD (m)	Vertical Stress (MPa)	TVD (m)	Vertical Stress (MPa)	TVD (m)	Vertical Stress (MPa)	TVD (m)	Vertical Stress (MPa)	TVD (m)	Vertical Stress (MPa)
51.5	0.51	822.96	15.84	1219.2	24.59	1615.44	33.69	2011.68	42.9
441.96	8.01	838.2	16.17	1234.44	24.93	1630.68	34.04	2026.92	43.26
457.2	8.32	853.44	16.49	1249.68	25.27	1645.92	34.38	2042.16	43.6
472.44	8.62	868.68	16.82	1264.92	25.61	1661.16	34.72	2057.4	43.96
487.68	8.93	883.92	17.15	1280.16	25.95	1676.4	35.08	2072.64	44.31
502.92	9.23	899.16	17.48	1295.4	26.29	1691.64	35.44	2087.88	44.66
518.16	9.54	914.4	17.81	1310.64	26.64	1706.88	35.8	2103.12	45.01
533.4	9.85	929.64	18.14	1325.88	26.98	1722.12	36.15	2118.36	45.38
548.64	10.15	944.88	18.47	1341.12	27.33	1737.36	36.49	2133.6	45.74
563.88	10.46	960.12	18.81	1356.36	27.68	1752.6	36.84	2148.84	46.12
579.12	10.76	975.36	19.13	1371.6	28.03	1767.84	37.21	2164.08	46.47
594.36	11.07	990.6	19.47	1386.84	28.38	1783.08	37.57	2179.32	46.81
609.6	11.38	1005.84	19.81	1402.08	28.73	1798.32	37.91	2194.56	47.16
624.84	11.69	1021.08	20.15	1417.32	29.08	1813.56	38.25	2209.8	47.5
640.08	12.01	1036.32	20.48	1432.56	29.44	1828.8	38.59	2225.04	47.86
655.32	12.33	1051.56	20.83	1447.8	29.78	1844.04	38.93	2240.28	48.22
670.56	12.65	1066.8	21.17	1463.04	30.13	1859.28	39.29	2255.52	48.59
685.8	12.97	1082.04	21.5	1478.28	30.49	1874.52	39.66	2270.76	48.94
701.04	13.28	1097.28	21.84	1493.52	30.84	1889.76	40.03	2286	49.3
716.28	13.61	1112.52	22.18	1508.76	31.2	1905	40.39	2301.24	49.66
731.52	13.93	1127.76	22.52	1524	31.55	1920.24	40.76	2316.48	50
746.76	14.25	1143	22.87	1539.24	31.91	1935.48	41.13	2331.72	50.36
762	14.57	1158.24	23.21	1554.48	32.27	1950.72	41.5	2346.96	50.73
777.24	14.88	1173.48	23.55	1569.72	32.63	1965.96	41.85	2362.2	51.08
792.48	15.21	1188.72	23.9	1584.96	32.99	1981.2	42.19	2377.44	51.43
807.72	15.52	1203.96	24.25	1600.2	33.34	1996.44	42.54	2392.68	51.79

TVD (m)	Vertical Stress (MPa)	TVD (m)	Vertical Stress (MPa)	TVD (m)	Vertical Stress (MPa)	TVD (m)	Vertical Stress (MPa)	TVD (m)	Vertical Stress (MPa)
2407.92	52.15	2880.36	63.3						
2423.16	52.51	2895.6	63.65						
2438.4	52.87	2910.84	64.02						
2453.64	53.23	2926.08	64.4						
2468.88	53.59	2941.32	64.77						
2484.12	53.95	2956.56	65.13						
2499.36	54.32	2971.8	65.5						
2514.6	54.68	2987.04	65.85						
2529.84	55.03	3002.28	66.21						
2545.08	55.39	3017.52	66.57						
2560.32	55.75	3032.76	66.94						
2575.56	56.12	3048	67.31						
2590.8	56.47	3063.24	67.68						
2606.04	56.82	3078.48	68.05						
2621.28	57.18	3093.72	68.41						
2636.52	57.55	3108.96	68.79						
2651.76	57.91	3124.2	69.18						
2667	58.26	3139.44	69.55						
2682.24	58.63	3154.68	69.94						
2697.48	58.98	3169.92	70.32						
2712.72	59.34	3185.16	70.7						
2727.96	59.7								
2743.2	60.04								
2758.44	60.4								
2773.68	60.76								
2788.92	61.12								
2804.16	61.48								
2819.4	61.84								
2834.64	62.21								
2849.88	62.59								
2865.12	62.95								

D5. Katnook-2

Latitude: **-37.44948**

Longitude: **140.7897**

TVD (m)	Vertical Stress (MPa)	TVD (m)	Vertical Stress (MPa)	TVD (m)	Vertical Stress (MPa)	TVD (m)	Vertical Stress (MPa)	TVD (m)	Vertical Stress (MPa)
1158.24	23.41	1554.48	32.64	1950.72	42.28	2468.88	55.35	2926.08	66.86
1173.48	23.75	1569.72	33.01	1965.96	42.64	2514.6	56.5	2941.32	67.23
1188.72	24.1	1584.96	33.38	1981.2	43.01	2529.84	56.89	2956.56	67.6
1203.96	24.45	1600.2	33.75	2026.92	44.17	2545.08	57.27	2971.8	67.98
1219.2	24.8	1615.44	34.12	2057.4	44.94	2560.32	57.66	2987.04	68.35
1234.44	25.14	1630.68	34.49	2072.64	45.32	2575.56	58.05	3002.28	68.73
1249.68	25.49	1645.92	34.86	2103.12	46.09	2590.8	58.44	3017.52	69.09
1264.92	25.84	1661.16	35.23	2118.36	46.47	2606.04	58.82	3032.76	69.46
1280.16	26.19	1676.4	35.6	2133.6	46.85	2621.28	59.2	3048	69.85
1295.4	26.55	1691.64	35.97	2148.84	47.24	2636.52	59.58		
1310.64	26.9	1706.88	36.34	2179.32	48.01	2651.76	59.96		
1325.88	27.25	1722.12	36.71	2194.56	48.39	2667	60.35		
1341.12	27.6	1737.36	37.08	2209.8	48.77	2682.24	60.75		
1356.36	27.96	1752.6	37.46	2225.04	49.16	2727.96	61.91		
1371.6	28.31	1767.84	37.83	2270.76	50.32	2743.2	62.3		
1386.84	28.67	1783.08	38.21	2286	50.7	2758.44	62.69		
1402.08	29.03	1798.32	38.58	2301.24	51.09	2773.68	63.08		
1417.32	29.39	1813.56	38.96	2316.48	51.48	2788.92	63.47		
1432.56	29.75	1828.8	39.32	2331.72	51.88	2804.16	63.86		
1447.8	30.1	1844.04	39.7	2346.96	52.27	2819.4	64.25		
1463.04	30.47	1859.28	40.07	2362.2	52.65	2834.64	64.64		
1478.28	30.83	1874.52	40.45	2377.44	53.03	2849.88	65.02		
1493.52	31.19	1889.76	40.81	2392.68	53.42	2865.12	65.39		
1508.76	31.55	1905	41.18	2407.92	53.8	2880.36	65.75		
1524	31.91	1920.24	41.54	2438.4	54.58	2895.6	66.12		
1539.24	32.28	1935.48	41.91	2453.64	54.96	2910.84	66.49		

D6. Ladbroke Grove-1

Latitude: -37.46711

Longitude: 140.7822

TVD (m)	Vertical Stress (MPa)	TVD (m)	Vertical Stress (MPa)	TVD (m)	Vertical Stress (MPa)	TVD (m)	Vertical Stress (MPa)	TVD (m)	Vertical Stress (MPa)
2392.68	50.16	3108.96	67.37						
2438.4	51.33	3169.92	68.83						
2545.08	53.93	3246.12	70.7						
2560.32	54.29	3307.08	72.2						
2575.56	54.66	3352.8	73.36						
2590.8	55.02	3368.04	73.75						
2606.04	55.39	3383.28	74.14						
2636.52	56.1								
2651.76	56.46								
2667	56.82								
2682.24	57.19								
2712.72	57.92								
2727.96	58.29								
2834.64	60.83								
2849.88	61.19								
2865.12	61.56								
2880.36	61.92								
2895.6	62.3								
2910.84	62.68								
2926.08	63.06								
2956.56	63.79								
2971.8	64.14								
2987.04	64.5								
3017.52	65.23								
3048	65.95								
3078.48	66.67								

Appendix E
Otway Basin Horizontal Stress Orientations

E1. Haselgrove-1

Latitude: -37.44193

Longitude: 140.8305

Type	Top (m)	Bottom (m)	C1 (in)	C2 (in)	P1AZ	HAZI	DEVI	Dip	Dip Direction	S_{Hmax} Orientation
BO	2701.76	2866.83			306	62	2.63812	89	126	126
DITF	2749.705				304	67	2.00672	79	33	33
DITF	2750.66				303	67	2.02991	79	39	39
DITF	2751.173				303	66	2.04527	83	44	44
DITF	2759.987				309	64	2.22571	64	35	35
DITF	2771.353				310	61	2.49341	62	33	33
DITF	2789.715				308	57	2.84804	59	49	49
BO	2879.72	2892.37			220	46	3.82079	90	131	131
BO	2893.55	2869.16			220	46	3.8684	90	129	129
BO	2913.69	2924.53			135	48	4.03561	90	136	136
BO	2925.56	2927.11			132	48	4.26101	90	133	133
BO	2929.89	2932.96			130	48	4.44116	89	131	131
BO	2934.06	2937.79			133	48	4.5091	90	133	133
BO	2942.22	2943.99			130	48	4.57764	90	132	132
BO	2946.31	2947.07			129	48	4.62049	89	129	129
BO	2948.96	2967.71			127	48	4.79578	89	127	127

Type	Top (m)	Bottom (m)	C1 (in)	C2 (in)	P1AZ	HAZI	DEVI	Dip	Dip Direction	S_{Hmax} Orientation
BO	2974.68	2977.48			130	49	4.80036	89	128	128
BO	2981.76	3049.24			125	50	4.70424	89	125	125
BO	2981.76	3049.24			124	50	4.5709	89	124	124
DITF	3016.397				130	50	4.61144	82	220	40
DITF	3033.936				128	51	4.76794	89	40	40
BO	3064.67	3068.66			39	50	4.64569	89	129	129
DITF	3134.787				318	43	4.30702	69	224	44
DITF	3134.899				316	43	4.3208	75	224	44
DITF	3135.191				314	43	4.31905	75	229	49
DITF	3135.955				305	42	4.31073	77	227	47
DITF	3136.506				296	42	4.29721	69	214	34
BO	3179.69	3189.54			131	41	3.7422	90	312	132
BO	3192.96	3219.92			129	41	4.10003	90	129	129
BO	3224.26	3261.05			39	43	4.48484	90	128	128
BO	3268.63	3289.5			313	47	4.41222	90	134	134

E2. Hungerford-1

Latitude: -37.45039

Longitude: 140.5982

Type	Top (m)	Bottom (m)	C1 (in)	C2 (in)	P1AZ	HAZI	DEVI	Dip	Dip Direction	S_{Hmax} Orientation
BO	1025.5	1026.414	8.622	8.23	53	0	0	90	143	143
BO	1062.838	1063.6	8.176	8.691	14	0	0	90	194	14
BO	1073.048	1073.963	8.174	8.615	7	0	0	90	187	7
BO	1176.833	1177.9	8.109	8.885	154	0	0	90	154	154
BO	1182.776	1183.538	8.11	9.709	149	0	0	90	149	149
BO	1187.501	1189.482	8.139	9.094	150	0	0	90	150	150
BO	1194.816	1196.035	8.13	8.905	157	0	0	90	157	157
BO	1216.304	1217.676	8.109	9.273	166	0	0	90	166	166
BO	1220.267	1220.876	8.099	8.649	155	0	0	90	155	155
BO	1221.334	1221.943	8.146	8.679	163	0	0	90	163	163
BO	1250.442	1251.814	8.136	8.676	155	0	0	90	155	155
BO	1252.118	1252.88	8.26	8.637	154	0	0	90	154	154
BO	1264.768	1266.596	8.177	8.792	142	0	0	90	142	142
BO	1268.578	1270.406	8.166	8.9	137	0	0	90	137	137
BO	1279.855	1280.465	8.179	8.558	138	0	0	90	138	138
BO	1283.056	1283.665	8.264	8.667	129	0	0	90	129	129
BO	1396.289	1397.356	8.74	8.116	31	0	0	90	121	121
BO	1405.28	1406.195	9.101	8.258	42	0	0	90	132	132
BO	1409.852	1411.072	9.27	8.478	28	0	0	90	118	118

Type	Top (m)	Bottom (m)	C1 (in)	C2 (in)	P1AZ	HAZI	DEVI	Dip	Dip Direction	S$_{Hmax}$ Orientation
BO	1417.168	1418.387	9.145	8.695	19	0	0	90	109	109
BO	1420.216	1420.825	8.514	8.181	7	0	0	90	97	97
BO	1433.627	1438.656	8.638	8.108	180	0	0	90	270	90
BO	1438.961	1439.57	8.57	8.13	174	0	0	90	264	84
BO	1475.08	1475.994	8.852	8.261	44	0	0	90	134	134
BO	1494.282	1495.958	10.131	8.615	44	0	0	90	134	134
BO	1496.416	1497.33	9.606	8.293	40	0	0	90	130	130
BO	1719.072	1719.986	8.575	9.048	108	0	0	90	108	108

E3. Jacaranda Ridge-1

Latitude: -37.34845

Longitude: 140.7539

Type	Top (m)	Bottom (m)	C1 (in)	C2 (in)	P1AZ	HAZI	DEVI	Dip	Dip Direction	S_{Hmax} Orientation
BO	763.76	770.96			228	267	1.00089	90	316	136
BO	772.14	775.31			229	274	0.92319	89	317	137
BO	785.01	792.81			232	276	0.94435	89	321	141
BO	794.41	795.15			232	281	0.91036	89	320	140
BO	808.88	811.8			232	287	0.86422	89	319	139
BO	821.12	825.11			334	296	0.86612	89	337	157
BO	849.46	854.27			141	279	0.77928	89	324	144
BO	858.12	885.6			56	283	0.75223	89	328	148
BO	894.94	896.69			324	302	0.82101	89	324	144
BO	901.7	903.02			238	301	0.83372	89	325	145
BO	905.14	906.06			223	298	0.9483	89	311	131
BO	909.28	912.85			233	299	1.00294	89	319	139
BO	915.49	918.56			135	282	0.95078	89	314	134
BO	941.57	946.2			230	293	0.92934	89	318	138
BO	950.37	953.89			134	280	0.92379	89	311	131
BO	970.66	972.84			223	291	0.91697	89	312	132
BO	1017.01	1019.48			48	276	0.58998	90	316	136
BO	1040.67	1050.09			38	282	0.52468	90	307	127
BO	1053.81	1058.45			311	300	0.52869	90	312	132

Type	Top (m)	Bottom (m)	C1 (in)	C2 (in)	P1AZ	HAZI	DEVI	Dip	Dip Direction	S_{Hmax} Orientation
BO	1067.58	1082.41			232	293	0.37004	90	322	142
BO	1091.01	1093.85			60	202	0.27332	90	145	145
BO	1102.57	1105.95			44	178	0.49536	90	133	133
BO	1109.25	1114.21			319	167	0.5577	89	135	135
BO	1117.63	1118.5			229	181	0.63631	90	139	139
BO	1128.74	1132.42			316	167	0.82604	89	135	135
BO	1134.09	1143.8			229	171	0.85662	89	141	141
BO	1149.64	1155.51			225	168	1.00527	89	139	139
BO	1160.7	1161.39			223	164	0.91445	89	130	130
BO	1170.37	1174.76			223	158	0.87329	89	132	132
BO	1188.37	1192.15			216	149	0.9993	89	127	127
BO	1195.27	1198.77			214	144	0.98168	89	122	122
BO	1202.75	1205.47			216	140	1.0309	89	126	126
BO	1228.06	1231.43			217	125	1.04116	89	126	126
BO	1235.04	1236.51			220	124	1.11536	89	128	128
BO	1247.28	1251.95			205	118	1.16203	89	116	116
BO	1272.02	1272.6			227	112	1.12186	90	134	134
BO	1287.23	1292			126	111	1.34214	89	125	125
BO	1304.01	1322.46			315	104	1.3529	89	136	136
BO	1326.15	1330.54			235	112	1.13693	89	144	144
BO	1334.21	1337.71			141	114	1.2214	89	139	139
BO	1368.61	1376.33			45	106	1.47392	89	135	135
BO	1422.26	1423.94			219	88	1.3343	89	130	130

Type	Top (m)	Bottom (m)	C1 (in)	C2 (in)	P1AZ	HAZI	DEVI	Dip	Dip Direction	S_{Hmax} Orientation
BO	1448.08	1449.35			319	82	1.51879	89	136	136
BO	1471.05	1474.91			304	82	1.62444	89	126	126
BO	1479.71	1481.23			306	81	1.59334	89	124	124
BO	1495.85	1499.32			312	77	1.67882	89	133	133
BO	1505.26	1511.28			309	77	1.81973	89	130	130
BO	1524.52	1527.33			227	76	1.9303	89	132	132
BO	1531.54	1532.72			225	75	1.91223	89	133	133
BO	1543.15	1545.25			226	73	1.74296	89	134	134
BO	1548.91	1551.21			226	71	1.69883	89	131	131
BO	1587.88	1592.21			122	61	1.85705	89	120	120
BO	1598.23	1617.13			122	51	2.23878	89	122	122
BO	1619.15	1658.69			123	39	2.93689	90	125	125
BO	1671.11	1675.23			321	31	4.15549	89	319	139
BO	1693.92	1695.46			41	28	4.25683	89	308	128
BO	1741.06	1744.23			218	25	4.70548	89	305	125
BO	1751.43	1755.45			131	27	4.74653	89	310	130
BO	1802.36	1804.91			307	21	6.02409	88	305	125
BO	1812.13	1818.12			306	20	6.12455	89	303	123
BO	1823.05	1833.4			302	19	6.23998	88	303	123
BO	1918.07	1920.41			312	56	8.42334	88	134	134
BO	1930.64	1937.61			305	55	8.46477	87	124	124
BO	1948.04	1949.9			303	53	8.47977	87	124	124
BO	1958.1	1959.16			214	52	8.39869	88	128	128

Type	Top (m)	Bottom (m)	C1 (in)	C2 (in)	P1AZ	HAZI	DEVI	Dip	Dip Direction	S_{Hmax} Orientation
BO	1999.24	2013.71			138	51	8.43082	89	132	132
BO	2077.85	2080.89			130	45	7.56395	89	129	129
BO	2090.43	2094.09			130	43	7.69211	89	129	129
BO	2096.26	2097.12			126	42	7.74229	89	126	126
BO	2159.15	2166.54			32	44	7.99697	88	123	123
BO	2168.99	2176.36			42	47	7.53641	89	130	130
BO	2198.68	2209.03			305	48	6.4271	89	125	125
BO	2230.74	2231.95			134	54	5.34871	89	132	132
BO	2234.61	2235.33			132	53	5.3887	89	132	132
BO	2260.75	2261.75			308	45	5.82629	90	132	132
BO	2287.67	2342.23			130	59	5.25649	88	130	130
BO	2443.74	2446.65			212	52	4.77166	88	115	115
BO	2454.27	2456.29			143	56	4.4949	89	137	137
BO	2486.68	2488.06			126	56	4.1036	89	130	130
BO	2568.96	2570.52			40	55	3.90883	89	126	126
BO	2625.01	2639.75			305	40	3.664	90	128	128
BO	2668.54	2669.56			215	37	3.53223	89	124	124
BO	2675.47	2676.8			114	38	3.59039	89	117	117
BO	2684.7	2650.23			209	38	3.58903	90	125	125
BO	2734.6	2735.15			39	27	3.98209	89	310	130
BO	2757.06	2759.18			312	27	3.96097	90	307	127
BO	2765.99	2769.98			127	27	3.73904	89	313	133
BO	2775.75	2779.33			27	24	3.81442	89	300	120

Type	Top (m)	Bottom (m)	C1 (in)	C2 (in)	P1AZ	HAZI	DEVI	Dip	Dip Direction	S$_{Hmax}$ Orientation
BO	2780.89	2786.81			312	24	3.69706	89	312	132
BO	2793.02	2801.26			301	23	3.54013	90	298	118
BO	2863.29	2865.38			305	24	2.95443	90	308	128
BO	2874.02	2874.65			323	25	2.98013	88	315	135
BO	2903.64	2906.07			38	30	3.49845	90	307	127
BO	2927.88	2930.39			224	23	3.92847	89	312	132
BO	2932.3	2934.62			124	25	4.00296	89	306	126

E4. Killanoola-1DW

Latitude: -37.21025

Longitude: 140.6689

Type	Top (m)	Bottom (m)	C1 (in)	C2 (in)	P1AZ	HAZI	DEVI	Dip	Dip Direction	S_{Hmax} Orientation
BO	456.45	458.09						90	299	119
BO	478.03	482.94						89	113	113
BO	484.02	488.98						89	301	121
BO	557.11	559.86						90	108	108
BO	595.66	601.18						88	292	112
BO	607.08	607.72						87	296	116
BO	608.94	610.62						88	292	112
BO	625.73	627.28						88	292	112
BO	634.06	638.84						90	287	107
BO	642.68	643.16						87	298	118
BO	644.62	648.2						86	297	117
BO	662.03	662.79						87	294	114
BO	665.73	666.86						85	301	121
BO	668.94	670.18						89	106	106
BO	671.59	672.42						90	291	111
BO	675.06	680.51						88	297	117
BO	684.38	685.45						86	302	122
BO	686.31	693.77						89	294	114
BO	695.04	702.13						88	298	118

Type	Top (m)	Bottom (m)	C1 (in)	C2 (in)	P1AZ	HAZI	DEVI	Dip	Dip Direction	S_{Hmax} Orientation
BO	706.87	708.24						87	296	116
BO	711.55	715.93						89	294	114
BO	724.74	742.44						88	294	114
BO	744.49	745.74						88	294	114
BO	746.67	749.85						89	106	106
BO	750.68	751.62						89	108	108
BO	756.21	756.61						89	291	111
BO	757.57	757.87						89	291	111
BO	758.49	761.86						90	290	110
BO	764.03	764.73						89	290	110
BO	771.63	773.04						88	293	113

E5. Redman-1

Latitude: -37.43062

Longitude: 140.7632

Type	Top (m)	Bottom (m)	C1 (in)	C2 (in)	P1AZ	HAZI	DEVI	Dip	Dip Direction	S_{Hmax} Orientation
BO	1434.078	1436.211	8.392	9.114	144	0	0	90	144	144
BO	1442.612	1443.831	8.426	8.859	134	0	0	90	134	134
BO	1451.756	1454.499	8.503	10.779	132	0	0	90	132	132
BO	1457.547	1459.071	8.626	9.02	132	0	0	90	132	132
BO	1600.498	1601.718	8.481	9.298	109	0	0	90	109	109
BO	1604.766	1606.594	12.563	8.528	46	0	0	90	136	136
BO	1793.742	1798.618	8.614	9.009	11	0	0	90	191	11
BO	1859.274	1860.493	8.285	9.628	146	0	0	90	146	146
BO	1872.99	1874.209	8.382	9.238	142	0	0	90	142	142
BO	2125.669	2128.107	8.813	8.464	90	0	0	90	180	180
BO	2152.796	2154.32	8.73	8.475	100	0	0	90	190	10
BO	2158.892	2162.245	8.835	8.486	98	0	0	90	188	8
BO	2223.814	2228.082	9.373	8.483	45	0	0	90	135	135
BO	2284.47	2288.432	8.953	8.458	166	0	0	90	256	76
BO	2326.227	2327.446	8.774	8.408	80	0	0	90	170	170
BO	2368.29	2370.728	8.934	8.375	41	0	0	90	131	131
BO	2375.91	2377.434	8.822	8.413	58	0	0	90	148	148
BO	2390.54	2396.026	9.348	8.285	7	0	0	90	97	97
BO	2398.16	2400.598	9.158	8.489	174	0	0	90	264	84

Type	Top (m)	Bottom (m)	C1 (in)	C2 (in)	P1AZ	HAZI	DEVI	Dip	Dip Direction	S_{Hmax} Orientation
BO	2440.832	2442.356	8.973	8.556	35	0	0	90	125	125
BO	2471.617	2473.141	9.146	8.644	29	0	0	90	119	119
BO	2478.932	2480.456	9.083	8.572	34	0	0	90	124	124
BO	2549.646	2551.17	8.779	8.481	34	0	0	90	124	124
BO	2566.41	2568.848	9.172	8.296	150	0	0	90	240	60
BO	2582.564	2583.783	9.065	8.524	45	0	0	90	135	135
BO	2615.482	2617.006	10.768	8.456	44	0	0	90	134	134
BO	2661.202	2662.726	9.956	8.718	57	0	0	90	147	147

E6. Rendelsham-1

Latitude: -37.56293

Longitude: 140.2319

Type	Top (m)	Bottom (m)	C1 (in)	C2 (in)	P1AZ	HAZI	DEVI	Dip	Dip Direction	S$_{Hmax}$ Orientation
BO	2093.062	2095.805	8.16	8.778	134	0	0	90	134	134
BO	2118.97	2121.256	8.115	8.906	141	0	0	90	141	141
BO	2122.018	2124.151	8.098	9.089	130	0	0	90	130	130
BO	2139.391	2154.631	8.081	8.891	144	0	0	90	144	144
BO	2159.66	2166.518	8.16	9.002	147	0	0	90	147	147
BO	2166.976	2168.042	8.114	8.92	143	0	0	90	143	143
BO	2183.13	2184.502	8.197	10.92	130	0	0	90	130	130
BO	2215.896	2236.318	8.178	9.629	131	0	0	90	131	131
BO	2265.883	2268.626	8.696	9.543	129	0	0	90	129	129
BO	2318.309	2320.138	8.196	12.013	126	0	0	90	126	126
BO	2703.271	2704.795	8.784	9.355	29	0	0	90	209	29
BO	2765.45	2768.041	9.409	8.538	73	0	0	90	163	163

E7. Wynn-1

Latitude: -37.40916

Longitude: 140.8722

Type	Top (m)	Bottom (m)	C1 (in)	C2 (in)	P1AZ	HAZI	DEVI	Dip	Dip Direction	S$_{Hmax}$ Orientation
BO	2702.01	2706.87			299	203	5.19307	90	117	117
BO	2726.13	2729.09			298	204	5.35479	90	119	119
BO	2739.12	2742.75			300	204	5.53613	89	121	121
DITF	2752.786				305	204	5.88331	82	38	38
DITF	2763.769				303	206	5.97816	84	212	32
BO	2764.9	2778.38			307	205	5.8895	88	130	130
DITF	2768.402				307	205	5.90315	71	221	41
BO	2797.28	2799.96			300	206	5.89374	89	122	122
BO	2859.33	2916.44			299	200	5.73286	89	120	120
BO	2702.01	2706.87			299	203	5.19307	90	117	117

Appendix F
Otway Basin Leak-Off Test Data

Well Name	Lattitude	Longitude	Measured Depth (m)	Casing	Mud Weight (ppg)	Effective Mud Weight (ppg)	HAZI	DEVI	Pressure MPa	Test Type	Date	Lithology
Bool Lagoon-1	37.146	140.63	282.6	9.625		15.4	0	0	5.12	FIT		silt/claystona
Camelback-1	37.105	140.19	289.9	8.625		15.6	0	0.75	5.32	LOT		claystone
Compton-1	37.795	140.71	479.5	9.625		15.9	0	0.75	8.96	LOT		claystone
Copa-1	37.687	139.76	409	20		10.2	0	1.5	4.9	FIT		claystone
Copa-1	37.687	139.76	1024	13.38		13.7	0	0.75	16.49	LOT		clay/sandstone
Copa-1	37.687	139.76	2423	9.625		15.2	0	0	43.3	LOT		silt/claystone
Haselgrove-1	37.442	140.83	888	244		12.8	0	0.5	13.36	LOT		silt/claystone
Haselgrove-2	37.45	140.85	887	244		1.7	0	0.5	14.78	LOT		siltstone
Hatherleigh-1	37.486	140.25	885.8	9.625		1.77	0	1.25	15.37	FIT		sand/siltstone
Hungerford-1	37.45	140.6	1002	244		1.38	0	2	13.55	LOT		sand/claystone
Katnook-1	37.454	140.78	648	9.625		12.7	0	0.5	9.67	FIT		sand/coal
Katnook-2	37.45	140.79	1154	9.625		14.2	0	0.5	19.26	FIT		
Katnook-3	37.45	140.77	707.4	9.625		12.4	0	0.75	10.31	FIT		siltstone
Killarney-1	37.101	140.31	267.9	8.625		11.3	0	0.25	3.56	LOT		clay

Well Name	Lattitude	Longitude	Measured Depth (m)	Casing	Mud Weight (ppg)	Effective Mud Weight (ppg)	HAZI	DEVI	Pressure MPa	Test Type	Date	Lithology
Ladbroke Grove-1	37.467	140.78	1024	9.625		13.2	303	2.75	15.89	FIT		silt/claystone
Laira-1	37.427	140.68	1010	9.625		13.55	2	1	16.09	FIT		sand/silts
Lake Hawdon-1	37.199	139.99	392.9	9.625		16.6	0	0.25	7.67	LOT		
Mount Hope-1	37.5	140.09	124.8	178			0	0	2.89	LOT		
Reedy Creek-1	37.323	140.16	263	13.38		10.6	0	0.75	3.28	FIT		clay/sandstone
Reedy Creek-1	37.323	140.16	1574	9.625		14.1	0	1	26.09	FIT		claystone
Rendelsham-1	37.563	140.23	1124	244		12.7	0	1.5	16.78	LOT		sand/claystone
Sawpit-1	37.349	140.87	713.3	9.625		14	0	0.25	11.74	FIT		claystone
St Clair-1	37.364	140.04	262	13.38		12.2	0	0.75	3.76	FIT		claystone
St Clair-1	37.364	140.04	1705	9.625		12.5	0	0	25.05	LOT		claystone
Tilbooroo-1	37.334	140.87	347.3	13.38		1.44	0	0.5	4.9	LOT		siltstone
Tilbooroo-1	37.334	140.87	1549	9.625		14.84	0	1.25	27.02	LOT		siltstone
Wynn-1	37.409	140.87	952	244		12	20	0.5	13.43	LOT		sand/claystone
Zema-1	37.414	140.67	858.6	9.625		13	0	1.25	13.12	FIT		claystone
Ladbroke Grove-1	37.467	140.78	1024	9.625		13.2	303	2.75	15.89	FIT		silt/claystone

References

Aadnoy, B.S., 1990a, Inversion Technique to Determine the in-Situ Stress Field from Fracturing Data: Journal of Petroleum Science and Engineering, v. 4, p. 127-141.

Aadnoy, B.S., 1990b, In-Situ Stress Direction from Borehole Fractures: Journal of Petroleum Science and Engineering, v. 4, p. 143-153.

Aadnoy, B.S., and Chenevert, M.E., 1987, Stability of Highly Inclined Boreholes: SPE Drilling Engineering, v. 2, p. 364-374.

Addis, M.A., 1997, The Stress-Depletion Response of Reservoirs, 1997 SPE Annual Technical Conference and Exhibition; Formation Evaluation and Reservoir Geology; Part Ii., Volume 1997: SPE - Society of Petroleum Engineers of Aime: Dallas, TX, United States, Society of Petroleum Engineers of the American Institute of Mining, Metallurgical and Petroleum Engineers (AIME), p. 55-65.

Addis, M.A., Hanssen, T.H., Yassir, N., Willoughby, D.R., and Enever, J.R., 1998, A Comparison of Leak-Off Test and Extended Leak-Off Test Data for Stress Estimation, Eurock 98: Trondheim, Norway, Society of Petroleum Engineers.

Anderson, E.M., 1951, The Dynamics of Faulting and Dyke Formation with Applications in Britain, Edinburgh.

Asquith, G., and Gibson, C., 1983, Basic Well Log Analysis for Geologists: Tulsa, Oklahoma, The American Association of Petroleum Geologists.

Barton, C.A., 2000, Discrimination of Natural Fractures from Drilling-Induced Wellbore Failures in Wellbore Image Dataó Implications for Reservoir Permeability, SPE International Petroleum Conference and Exhibition in Mexico: Villahermosa, Mexico, SPE.

Barton, C.A., Zoback, M.D., and Burns, K.L., 1988, In Situ Stress Orientation and Magnitude at the Fenton Geothermal Site, New Mexico, Determined from Wellbore Breakouts: Geophysical Research Letters, v. 15, p. 467-470.

Barton, C.A., Zoback, M.D., and Moos, D., 1995, Fluid Flow Along Potentially Active Faults in Crystalline Rock: Geology, v. 23, p. 683-686.

Bell, J.S., 1996a, In Situ Stresses in Sedimentary Rocks (Part1): Measurement Techniques: Geoscience Canada, v. 23, p. 85-100.

Bell, J.S., 1996b, In Situ Stresses in Sedimentary Rocks (Part2): Application of Stress Measurements: Geoscience Canada, v. 23, p. 135-153.

Bell, J.S., and Gough, D.I., 1979, Northeast-Southwest Compressive Stress in Alberta: Evidence from Oil Wells: Earth and Planetary Science Letters, v. 45, p. 475-482.

Bennion, D.B., 1996, Underbalanced Operations Offer Pluses and Minuses: International Journal of Rock Mechanics and Mining Sciences, v. 33, p. 222A.

Borah, I., 1993, Drill Stem Tests, *in* Morton-Thomas, D., and Woods, A.M., eds., Development Geology Reference Manual: AAPG Methods in Exploration Series: Tulsa, Oklahoma, The American Association of Petroleum Geologists.

Boult, P., Camac, B.A., and Davids, A.W., 2002, 3d Fault Modelling and Assessment of Top Seal Structural Permeability-Penola Trough, Onshore Otway Basin: APPEA Journal, v. 42, p. 151-166.

Brace, W.F., 1960, An Extension of the Griffith Theory of Fracture to Rocks: Journal of Geophysical Research, v. 65, p. 3477-3480.

Brace, W.F., and Kohlstedt, D.L., 1980, Limits on Lithospheric Stress Imposed by Laboratory Experiments: Journal of Geophysical Research, v. 85, p. 6248-6252.

Bradley, W.B., 1979, Failure of Inclined Boreholes: Journal of Energy Resources Technology, v. 101, p. 232-239.

Breckels, I.M., and van Eeklen, H.A.M., 1982, Relationship between Horizontal Stress and Depth in Sedimentary Basins: Journal of Petroleum Technology, v. 34, p. 2191-2198.

Bredehoeft, J.D., Wolff, R.G., Keys, W.S., and Shuter, E., 1976, Hydraulic Fracturing to Determine the Regional in-Situ Stress Field Piceance Basin, Colorado: Geological Society of America Bulletin, v. 87, p. 250-258.

Brudy, M., and Zoback, M.D., 1993, Compressive and Tensile Failure of Boreholes Arbitrarily Inclined to Principal Stress Axes: Application to the Ktb Boreholes, Germany: International Journal of Rock Mechanics and Mining Science, v. 30, p. 1035-1038.

Brudy, M., and Zoback, M.D., 1999, Drilling-Induced Tensile Wall-Fractures: Implications for Determination of in-Situ Stress Orientations and Magnitudes: International Journal of Rock Mechanics and Mining Sciences, v. 36, p. 191-215.

Byerlee, J., 1978, Friction of Rocks, *in* Byerlee, D., and Wyss, eds., Rock Friction and Earthquake Prediction., Volume 116: Pure and Applied Geophysics: Basel, Switzerland, Birkhaeuser Verlag, p. 615-626.

Coblentz, D.D., Sandiford, M., Richardson, R.M., Zhou, S., and Hillis, R.R., 1995, The Origins of the Intraplate Stress Field in Continental Australia: Earth and Planetary Science Letters, v. 133, p. 299-309.

Cockshell, C.D., 1995, Petroleum Entrapment, *in* Morton, J.G.G., and Drexel, J.R., eds., Petroleum Geology of South Australia Volume 1: Otway Basin: Adelaide, South Australia, PIRSA.

Cook, N.G.W., 1992, Jaeger Memorial Dedication Lecture; Natural Joints in Rock; Mechanical, Hydraulic and Seismic Behaviour and Properties under Normal Stress: International Journal of Rock Mechanics and Mining Sciences and Geomechanics Abstracts, v. 29, p. 198-223.

Cooper, G.A., 1994, Directional Drilling: Scientific American, v. 270 (5), p. 56-61.

Coussy, O., Charlez, P., and Heugas, O., 1991, Response Thermoporoelastique D'un Forage, *in* Wittke, ed., Proceedings; Seventh International Congress on Rock Mechanics., Volume 7: Proceedings of the Congress of the International Society for Rock Mechanics, p. 699-702.

Dart, R.L., and Zoback, M.L., 1989, Wellbore Breakout Analysis within the Central and Eastern Continental United States: Log Analyst, v. 30, p. 12-25.

Detournay, E., and Roegiers, J.-C., 1986, Comment on "Well Bore Breakouts and in Situ Stress" by Zoback M.D., Moos D., Mastin L., and Anderson R.N.: Journal of Geophysical Research, v. 91, p. 14, 161-14,162.

Dewhurst, D.N., Jones, R.M., Hillis, R.R., and Mildren, S.D., 2001, Microstructural, Petrophysical and Geomechanical Characterisation of Fault Rocks from the Carnarvon and Otway Basins: Perth, Australia, CSIRO.

Dewhurst, D.N., Yang, Y., and Aplin, A.C., 1999, Permeability and Fluid Flow in Natural Mudstones, *in* Aplin, A.C., Fleet, J., and Macquaker, J., eds., Muds and Mudstone; Physical and Fluid-Flow Properties., Volume 158: Geological Society Special Publications: London, United Kingdom, Geological Society of London, p. 23-43.

Dickinson, J.A., Wallace, M.W., Holdgate, G.R., Daniels, J., Gallagher, S.J., and Thomas, L., 2001, Neogene Tectonics in Se Australia: Implications for Petroleum Systems: APPEA Journal, v. 41, p. 37-52.

Doe, T.W., Hustrulid, W.A., Leijon, B., Ingavald, K., and Strindell, L., 1983, Determination of Stress in the Stripa Mine, Sweden, Hydraulic Fracturing Stress Measurements: Washington D.C., National Academy Press, p. 119-129.

Enever, J.R., 1993, Case Studies of Hydraulic Fracture Stress Measurement in Australia, *in* Hudson, J.A., ed., Comprehensive Rock Engineering.

Enever, J.R., and Chopra, P.N., 1986, Experience with Hydraulic Fracture Stress Measurementsin Granite, International symposium of rock stress and rock stress measurement: Stockholm, Centek Lulea Sweden, p. 411-420.

Enever, J.R., and Wooltorton, B.A., 1982, Experience with Hydraulic Fracturing as a Means of Estimating in-Situ Stress in Australian Coal Basin Sediments, *in* Zoback, M.D., and Haimson, B.C., eds., Proceedings Workshop XVII; Workshop on Hydraulic Fracturing Stress Measurements.: Open-File Report - U. S. Geological Survey: Reston, VA, United States, U. S. Geological Survey, p. 62-102.

Enever, J.R., Yassir, N., Willoughby, D.R., and Addis, M.A., 1996, Recent Experience with Extended Leak-Off Tests for in-Situ Stress Measurement in Australia: APPEA Journal, p. 528-535.

Engelder, T., 1993, Stress Regimes in the Lithosphere: Princeton, N.J., Princeton University Press.

Evans, K., Engelder, T., and Plumb, R.A., 1989, Appalachian Stress Study 1: A Detailed Description of in Situ Stress Variation in Devonian Shales of the Appalachian Plateau: Journal of Geophysical Research, v. 94, p. 1729-1754.

Fairhurst, C., 1968, Methods of Determining in Situ Rock Stresses at Great Depths: Omaha, Mo. River Division Corps of Engineers.

Ferrill, D.A., Winterle, J., Wittmeyer, G., Sims, D., Colton, S., Armstrong, A., and Morris, A.P., 1999, Stressed Rock Strains Groundwater at Yucca Mountain, Nevada: GSA Today, v. 9, p. 1-8.

Finch, R.W., Skees, J.L., Aud, W.W., Johnson, J.L., Esphahanian, C., and Hansen, J.T., 1997, Evolution of Completion and Fracture Stimulation Practices in the Jonah Field, Sublette County, Wy, AAPG Rocky Mountain Section Meeting; Abstracts., Volume 81: AAPG Bulletin: Tulsa, OK, United States, American Association of Petroleum Geologists, p. 1223.

Fjaer, E., Holt, R.M., Horsrud, P., Raaen, A.M., and Risnes, R., 1992, Petroleum Related Rock Mechanics: Amsterdam, Elsevier, 269 p.

Gjønnes, M., Cruz, A.M.G.L., Horsrud, P., and Holt, R.M., 1998, Leak-Off Tests for Horizontal Stress Determination?: Journal of Petroleum Science and Engineering, v. 20, p. 63-71.

Griffith, A.E., 1924, Theory of Rupture, *in* Biezeno, C.B., and Burgers, J.M., eds., First International Congress on Applied Mechanics, Waltman Deft, p. 53-63.

Gronseth, J.M., 1982, Determination of the Instantaneous Shut-in Pressure from Hydraulic Fracturing Data and Its Reliability as a Measure of the Minimum Principal Stress, *in* Goodman, R.E., and Heuze, F.E., eds., The 23rd U.S. Symposium on Rock Mechanics: New York, Society of Mining Engineers, p. 183-89.

Gronseth, J.M., and Kry, P.R., 1982, Instantaneous Shut in Pressure and Its Relationship to the Minimum in Situ Stress, *in* Zoback, M.D., and Haimson, B.C., eds., Proceedings Workshop XVII; Workshop on Hydraulic Fracturing Stress Measurements.: Open-File Report - U. S. Geological Survey: Reston, VA, United States, U. S. Geological Survey, p. 147-166.

Gronseth, J.M., and Kry, P.R., 1983, Instantaneous Shut-in Pressure and Its Relationship to the Minimum in-Situ Stress, Hydraulic Fracturing Stress Measurements: Washington D.C., National Academy Press, p. 55-60.

Haimson, B., and Fairhurst, C., 1967, Initiation and Extension of Hydraulic Fractures in Rocks: Society of Petroleum Engineers Journal, p. 310-318.

Haimson, B.C., 1993, The Hydraulic Fracturing Method of Stress Measurement: Theory and Practice, *in* Hudson, J.A., ed., Comprehensive Rock Engineering, Volume 3: oxford NewYork Seoul Tokyo, Pergamon Press, p. 395-412.

Handin, J.W., 1958, Effects of Pore Pressure on the Experimental Deformation of Some Sedimentary Rocks: Geological Society of America Bulletin, v. 69, p. 1576-1577.

Heffer, K.J., and Dowokpor, A.B., 1990, Relationship between Azimuths of Flood Anistropy and Local Earth Stresses in Oil Reservoirs, *in* Buller, A.T., Berg, E., Hjelmeland, O., Kleppe, J., Torsaeter, O., and Aasen, J.O., eds., 2nd North Sea oil and gas reservoirs conference: North Sea oil and gas reservoirs; II, Proceedings of the North Sea oil and gas reservoirs conference: Trondheim, Norway, Graham & Trotman. London, United Kingdom, p. 251-260.

Hickman, S.H., and Zoback, M.D., 1982, The Interpretation of Hydraulic Fracturing Pressure-Time Data for in-Situ Stress Determination, *in* Zoback, M.D., and Haimson, B.C., eds., Proceedings Workshop Xvii; Workshop on Hydraulic Fracturing Stress Measurements.: Open-File Report - U. S. Geological Survey: Reston, VA, United States, U. S. Geological Survey, p. 103-146.

Hillis, R.R., 1996, Fms Log Image Interpretation and the Contemporary Stress Field of the Nappamerri Trough: Implications for Fracture Stimulation of Tight Gas Prospects and the Stability of Horizontal Wellbores: Adelaide, Australia, Department of Geology and Geophysics, University of Adelaide.

Hillis, R.R., 1998, Mechanisms of Dynamic Seal Failure in the Timor Sea and Central North Sea, The Sedimentary Basins of Western Australia, Volume 2, p. 313-324.

Hillis, R.R., 2000, Coupled Changes in Pore Pressure and Stress in Oil Fields and Sedimentary Basins, AAPG International Conference and Exhibition; Abstracts., American Association of Petroleum Geologists. Tulsa, OK, United States. 2000.

Hillis, R.R., and Mildren, S.D., 1995, The Contemporary Stress Regime of the Mereenie Field: Implications for the Stability of Horizontal Wells and the Orientation of Natural and Hydraulically-Induced Fractures.: Adelaide, University of Adelaide.

Hillis, R.R., Mildren, S.D., Meyer, J.J., and Flˆttman, T., 1999, In Situ Stress and Natural Fracturing in the Mereenie Field: Implications for Field Development: Adelaide, South Australia, National Centre For Petroleum Geology and Geophysics, University of Adelaide.

Hillis, R.R., Monte, S.A., Tan, C.P., and Willoughby, D.R., 1995, The Contemporary Stress Field of the Otway Basin, South Australia; Implications for Hydrocarbon Exploration and Production, *in* Anonymous, ed., Australian Petroleum Exploration Association Conference., Volume 35: The Apea Journal: Canberra, Australia, Australian Petroleum Production and Exploration Association, p. 494-506.

Hillis, R.R., Tingay, M.R.P., and Meyer, J.J., 2001, Gulf of Thailand in Situ Stress Study: Adelaide, Australia, National Centre for Petroleum Geology and Geophysics, University of Adelaide.

Hiramatsu, Y., and Oka, Y., 1962, Stress around a Shaft or Level Excavated in Ground with a Three-Dimensional Stress State: Memoirs of the Faculty of Engineering Kyoto University, v. XXIV(I), p. 56-76.

Hoek, E., and Brown, E.T., 1980, Underground Excavations in Rock: London, Institute of Mining and Metallurgy, 527 p.

Horner, R.B., Barclay, J.E., MacRae, J.M., Wetmiller, R.J., and Asudeh, I., 1994, Earthquakes and Hydrocarbon Production in the Fort St. John Area of Northeastern British Columbia, Agu 1994 Fall Meeting., Volume 75: Eos, Transactions, American Geophysical Union: Washington, DC, United States, American Geophysical Union, p. 472.

Hubbert, M.K., and Rubey, W.W., 1959, Role of Fluid Pressures in Mechanics of Overthrust Faulting: I. Mechanics of Fluid-Filled Porous Solids and Its Application to Overthrust Faulting: Geological Society of America Bulletin, v. 70, p. 115-166.

Hubbert, M.K., and Willis, D.G., 1957, Mechanics of Hydraulic Fracturing: Journal of Petroleum Technology, v. 9, p. 153-168.

Jaeger, J.C., and Cook, N.G.W., 1979, Fundamentals of Rock Mechanics: London New York, Chapman and Hall ; distributed in U.S. by Halsted Press, XXII, 593 p.

Jones, R.M., Boult, P., Hillis, R.R., Mildren, S.D., and Kaldi, J., 2000, Integrated Hydrocarbon Seal Evaluation in the Penola Trough, Otway Basin: APPEA Journal, p. 194-213.

Kirsch, G., 1898, Die Theorie Der Elastizitat Un Die Bedurfnisse Der Festigkeiteslehre: VDI Z, v. 42, p. 797-807.

Kunze, K.R., and Steiger, R.P., 1991, Extended Leakoff Tests to Measure in Situ Stress During Drilling, *in* Roegiers, ed., Rock Mechanics as a Multidisciplinary Science: Rotterdam, Balkema.

Lian, H.M., and Bradley, K., 1986, Exploration and Development of Natural Gas, Pattani Basin, Gulf of Thailand, Fourth Circum-Pacific Energy and Mineral Resource Conference: Singapore, p. 171-181.

Ludwig, W.J., Nafe, J.E., and Drake, C.L., 1970, Seismic Refraction, *in* Maxwell, A.E., ed., The Sea: Ideas and Observations on Progress in the Study of the Sea, Volume 4: New York, Wiley-Interscience, p. 53-84.

Mastin, L., 1988, Effect of Borehole Deviation on Breakout Orientations: Journal of Geophysical Research, v. 93, p. 9187-9195.

McGarr, A., 1980, Some Constraints on the Levels of Shear Stress in the Crust from Theory and Observation: Journal of Geophysical Research, v. 93, p. 6231-6238.

McGarr, A., and Gay, N.C., 1978, State of Stress in the Earth's Crust: Annuls of Review of Earth and Planetary Sciences, v. 6, p. 405-436.

Mildren, S.D., 2001, In Situ Stress and Fracture Assessment: Swan Lake Area: Adelaide, National Centre for Petroleum Geology and Geophysics.

Mildren, S.D., Hillis, R.R., Fett, T., and Robinson, P.H., 1994, Contemporary Stresses in the Timor Sea: Implications for Fault-Trap Integrity, *in* Purcell, P.G., and Purcell, R.R., eds., Sedimentary Basins of Western Australia: Perth, Australia.

Mody, F.K., and Hale, A.H., 1993, A Borehole Stability Model to Couple the Mechanics and Chemistry of Drilling Fluid Interaction, SPE/IADC Drilling Conference: Amsterdam, The Netherlands, p. 473-490.

Mohr, O., 1900, Welche Umst%ade Bedingen Die Elastizit%asgrenze Und Den Bruch Eines Materiales?: Zeitschrift des Vereines Deutscher Ingenieure, v. 44.

Moore, A.M.G., Stagg, H.M.J., and Norvik, M.S., 2000, Deep-Water Otway Basin: A New Assessment of the Tectonics and Hydrocarbon Prospectivity: APPEA Journal, v. 40, p. 66-85.

Moos, D., and Peska, P., 1998, Predicting the Stability of Horizontal Wells and Multi-Laterals -- the Role of in Situ Stress and Rock Properties SPE 50386, SPE International Conference on Horizontal Well Technology: Calgary, Albeterta, Canada, SPE.

Moos, D., and Zoback, M.D., 1990, Utilisation of Observations of Well Bore Failure to Constrain the Orientation and Magnitude of Crustal Stresses: Application to Continental, Deep Sea Drilling Project, and Ocean Drilling Program Boreholes: Journal of Geophysical Research, v. 95, p. 9305-9325.

Morris, A., Ferrill, D.A., and Henderson, D.B., 1996, Slip-Tendency Analysis and Fault Reactivation: Geology (Boulder), v. 24, p. 275-278.

Mount, V.S., and Suppe, J., 1987, State of Stress near the San Andreas Fault: Implications for Wrench Tectonics: Geology, v. 15, p. 1143-1146.

Nelson, R.A., 1985, Geologic Analysis of Naturally Fractured Reservoirs: Dallas, Texas, Gulf Publishing co., 320 p.

Oaks, R.Q., Jr., Deckelman, J.A., Conrad, K.T., Phillips, J.O., and Stewart, A.J., 1991, Sedimentation and Tectonics in the Northeastern and Central Amadeus Basin, Central Australia, *in* Korsch, R.J., and Kennard, J.M., eds., Geological and Geophysical Studies in the Amadeus Basin, Central Australia., Volume 236: Bulletin - Australia, Bureau of Mineral Resources, Geology and Geophysics: Canberra, A.C.T., Australia, Australian Geological Survey Organization, p. 73-90.

Peska, P., and Zoback, M.D., 1995, Compressive and Tensile Failure of Inclined Well Bores and Determination on in Situ Stress and Rock Strength: Journal of Geophysical Research, v. 100, p. 12791-12811.

Piplapure, A.R., 1969, Theory, Measurement and Applications of Anisotropic Permeability in Petroleum Reservoirs: Bulletin of the Oil and Natural Gas Commission, v. 6, p. 17-35.

Plumb, R.A., 1989, Fracture Patterns Associated with Incipient Wellbore Breakouts, *in* Maury, V., and Fourmaintraux, D., eds., Rock at Great Depth: Rotterdam, Balkema.

Plumb, R.A., and Cox, J.W., 1987, Stress Directions in Eastern North America Determined to 4.5 Km from Borehole Elongation Measurements: Journal of Geophysical Research, v. 92, p. 4805-4816.

Plumb, R.A., and Hickman, S.H., 1985, Stress-Induced Borehole Elongation: A Comparison between Four-Arm Dipmeter and the Borehole Televiewer in the Auburn Geothermal Well: Journal of Structural Geology, v. 90, p. 5513-5521.

Porter, K.E., 1989, An Overview of Formation Damage: J. Petroleum Technology, v. 41, p. 780-786.

Qian, W., and Pedersen, L.B., 1991, Inversion of Borehole Breakout Orientation Data: Journal of Geophysical Research, B, Solid Earth and Planets, v. 96, p. 20,093-20,107.

Santos, and NSI, 1997, Mereenie Field Hydraulic Fracturing Study, Santos.

Secor, D.T., 1965, Role of Fluid Pressure in Jointing: American Journal of Science, v. 263, p. 633-646.

Shirley, K., 2000, Horizontal Wells Now Common, AAPG Explorer.

Shlyapobersky, J., and Chudnovsky, A., 1994, Review of Recent Developments in Fracture Mechanics with Petroleum Engineering Applications, Rock Mechanics in Petroleum Engineering; Proceedings.: Rotterdam, Netherlands, A.A. Balkema, p. 381-389.

Sibson, R.H., 1974, Frictional Constraints on Thrust, Wrench and Normal Faults: Nature, v. 249, p. 542-544.

Sibson, R.H., 1992, Implications of Fault-Valve Behaviour for Rupture Nucleation and Recurrence, *in* Takeshi, M., Aki, K., Ohnaka, M., Ruff, L.J., and Spudich, P., eds., Earthquake Source Physics and Earthquake Precursors., Volume 211: Tectonophysics: Amsterdam, Netherlands, Elsevier, p. 283-293.

Sibson, R.H., 1994, Crustal Stress, Faulting and Fluid Flow, *in* Parnell, J., ed.,
Geofluids; Origin, Migration and Evolution of Fluids in Sedimentary Basins.,
Volume 78: Geological Society Special Publications: London, United Kingdom,
Geological Society of London, p. 69-84.

Sibson, R.H., 1996, Structural Permeability of Fluid-Driven Fault-Fractures Meshes:
Journal of Structural Geology, v. 18, p. 1031-1042.

Smolen, J.J., 1993, Wireline Formation Testers, *in* Morton-Thomas, D., and Woods,
A.M., eds., Development Geology Reference Manual: AAPG Methods in
Exploration Series: Tulsa, Oklahoma, The American Association of Petroleum
Geologists.

Stearns, D.W., and Friedman, M., 1972, Reservoirs in Fractured Rock, *in* King, R.E.,
ed., Stratigraphic Oil and Gas Fields, Volume 12, American Association of
Petroleum Geologists, p. 82-106.

Terzaghi, K., 1943, Theoretical Soil Mechanics: New York, John Wiley.

Teufel, L.W., Rhett, D.W., and Farrell, H.E., 1991, Effect of Reservoir Depletion and
Pore Pressure Drawdown on in Situ Stress and Deformation in the Ekofisk
Field, North Sea, *in* Roegiers, J.C., ed., Rock Mechanics as a Multidisciplinary
Science; Proceedings of the 32nd U.S. Symposium., Volume 32: Proceedings -
Symposium on Rock Mechanics: [location varies], United States, A.A.
Balkema, p. 63-72.

van Ruth, P., and Hillis, R.R., 2000, Estimating Pore Pressure in the Cooper Basin,
South Australia: Sonic Log Method in an Uplifted Basin: Exploration
Geophysics, v. 31, p. 441-447.

van Ruth, P., Hillis, R.R., Swarbrick, R., and Tingate, P., 2000, Mud Weights,
Transient Pressure Tests, and the Distribution of Overpressure in the North
West Shelf, Australia: PESA Journal, v. 28, p. 59-66.

Wiebels, G.A., and Cook, N.G.W., 1968, An Energy Criterion for the Strength of
Rock in Polyaxial Compression: International Journal of Rock Mechanics and
Mining Sciences, v. 5, p. 529-549.

Wiprut, D., and Zoback, M.D., 2000, Fault Reactivation and Fluid Flow Along a Previously Dormant Normal Fault in the Northern North Sea: Geology (Boulder), v. 28, p. 595-598.

Zemack, J., and Caldwell, R.L., 1967, The Borehole Televiewer -- a New Logging Concept for Fracture Location and Other Types of Borehole Inspection: Journal of Petroleum Technology, v. 25, p. 762-774.

Zoback, M.D., and Healy, J.H., 1984, Friction, Faulting and in Situ Stress: Ann Geophysics, v. 2, p. 689-698.

Zoback, M.D., Moos, D., and Anderson, R.N., 1985, Well Bore Breakouts and in Situ Stress: Journal of Geophysical Research, v. 90, p. 5523-5530.

Zoback, M.L., 1992, First- and Second-Order Patterns of Stress in the Lithosphere: The World Stress Map Project: Journal of Geophysical Research, v. 97, p. 11703-11728.

Zoback, M.L., and Zoback, M.D., 1980, State of Stress in the Conterminous United States: Journal of Geophysical Research, v. 85, p. 6113-6156.

Zoback, M.L., Zoback, M.D., Adams, J., Assumpcao, M., Bell, J.S., Bergman, E.A., Blumling, P., Brereton, N.R., Denham, D., Ding, J., Fuchs, K., Gay, N.C., Gregersen, S., Gupta, H.K., Gvishiani, A., Jacob, K., Klein, R., Knoll, P., Magee, M., Mercier, J.L., Muller, B.C., Paquin, C., Rajendran, K., Stephansson, O., Suarez, G., Suter, M., Udias, A., Xu, Z.H., and Zhizhin, M., 1989, Global Patterns of Tectonic Stress: Nature, v. 341, p. 291-298.